Implementing 3D electron diffraction at York to determine structures of challenging small molecule organometallic compounds

Emily Thompson

PhD

University of York

Chemistry

April 2024

Abstract

The elucidation of accurate 3D structures is of vital importance in chemistry and is fundamental to understanding the chemical and physical properties of a material. Thus far, X-ray crystallography has stood as the gold standard method for structure determination. However, obtaining sufficiently large crystals of quality suitable for single-crystal X-ray diffraction (SCXRD) experiments can prove prohibitively difficult. Three-dimensional electron diffraction (3DED) provides an alternative means for structure determination, enabling data collection from crystals of sub-micrometre size, which are too small to study by SCXRD. As such, 3DED is emerging as a valuable technique to explore a wide range of materials and is of particular interest to synthetic chemists studying small molecule organometallic compounds.

3D electron diffraction was implemented at the University of York and a data collection and processing workflow were established. 3DED was then utilised to determine the structures of a range of challenging small molecule organometallic complexes, exploring the possibilities and limitations of the technique. Specifically, 3DED was used to determine the structures of: (i) a beam and air sensitive σ-alkane species that was difficult to study via SCXRD (**Chapter 4**), (ii) bulky planar porphyrin complexes that could not be studied by SCXRD (**Chapter 5**), (iii) a series of manganese complexes and their precursor ligand where only a scarce quantity of material was available (**Chapter 6**), and (iv) palladium complexes derived directly from reaction mixtures, where further purification and recrystallisation had not been attempted (**Chapter 7**). Finally, this thesis also describes the identification and characterisation of a rare and previously undiscovered crystal form of a palladium complex (**Chapter 7**).

Contents

List of Tables

List of Figures

Acknowledgements

Completing this PhD has been more challenging than anticipated and I will be forever grateful to my supervisors, Dr Huw Jenkins, and Professor Fred Antson, for their continued support and patience throughout this journey. I would particularly like to thank Huw for sharing his knowledge with me and for all the time he has spent working with me on this project. Being a part of the Antson group, and YSBL as a whole, has been an amazing experience. I am incredibly happy, and lucky, to have had the opportunity to work (and have coffee) with so many wonderful individuals.

I would be remiss not to thank my independent panel member, Professor Ian Fairlamb, for his enthusiasm for this project and for the collaboration fostered as a result. In addition, I would like to thank my collaborators: Dr Laurence Doyle, Professor Andrew Weller, Dr Alice Jane McEllin, Professor Duncan Bruce, Dr Thomas Burden, Dr Neda Jeddi, Dr George Clarke, and Joe Goodall for providing such interesting samples to study. My thanks to Dr Jamie Blaza, Dr Johan Turkenburg, and Sam Hart for setting up and running the electron microscopy facility at York, and to Dr Adrian Whitwood for training and assistance in collecting PXRD data. My mentor, Kate Morris, has massively helped me in terms of planning this thesis and pushing me to actually get it written. Thank you for your support and encouragement!

I could not have got through this process without my family and friends. Thank you all for sticking by me when things got tough. To Kalum, you are a phenomenal human and friend. I am so proud of everything you have accomplished; you continue to astound me. To my parents, thank you for always cheering me on. Your love and support knows no bounds, and I am truly indebted to you both. To Ben, thank you for believing in me when I didn't believe in myself, and for reminding me (many times…) that I could in fact, do it.

Declaration

I declare that this thesis is a presentation of original work and I am the sole author, except where reference has been made to work contributed by others, as indicated below. This work has not previously been presented for an award at this, or any other, University. All sources are acknowledged as References.

Significant contributions to this project from other researchers:

- Dr Huw Jenkins authored the semi-automatic processing script used to process data.
- Dr Laurence Doyle synthesised **Compound 4.1** and **Compound 4.2** and prepared TEM grids of these samples, while working under the supervision of Professor Andrew Weller.
- Dr Alice Jane McEllin synthesised **Compounds 5.1 – 5.4** as part of their PhD project under the supervision of Professor Duncan Bruce.
- Dr Thomas Burden synthesised **Compounds 6.1 – 6.6** as part of their PhD project under the supervision of Professor Ian Fairlamb.
- Dr Neda Jeddi synthesised and prepared TEM grids of the samples presented in **Chapter 7** as part of their PhD project under the supervision of Professor Ian Fairlamb.
- Dr Theo Tanner collected and solved the single-crystal X-ray diffraction structure of **Compound 5.1**.

Some of the material presented in this thesis has previously been published in:

L. R. Doyle, E. A. Thompson, A. L. Burnage, A. C. Whitwood, H. T. Jenkins, S. A. Macgregor, and A. S. Weller, MicroED characterization of a robust cationic σ-alkane complex stabilized by the [B(3,5-$(SF_5)_2C_6H_3)_4$]$^-$ anion, via on-grid solid/gas single-crystal to single-crystal reactivity *Dalton Trans. J. Inorg. Chem.*, 2022, **51**, 3661–3665.

1   General introduction

1.1   History of electron diffraction

The field of electron crystallography emerged in the early twentieth century thanks to the groundbreaking work of Davisson and Germer[1,2] and Thomson and Reid.[3] (See also a historical account of the discoveries of Davisson and Germer published on the 50th anniversary.)[4] Their work earned Davisson and Thomson the Nobel Prize in Physics a mere 10 years later. The concept of electron diffraction was first demonstrated by Davisson and Germer in 1927.[1,2] They fired a parallel beam of electrons, accelerated by a potential of ~15-65 V, at a single crystal of nickel and observed that the electrons were reflected at discrete scattering angles, akin to X-ray scattering. This was a monumental discovery, as it substantiated that electrons could behave like waves, in addition to behaving like particles. From their experiments, Davisson and Germer,[1,2] were able to use Bragg's law[5] to calculate the wavelength of the electrons. See **Chapter 3, Section 3.1.2**. The calculated values were found to be in agreement with the theoretical value predicted by the de Broglie equation: $\lambda = \frac{h}{mv}$.[6] See **Chapter 2, Section 2.1.1**. These results experimentally confirmed the de Broglie hypothesis put forward in 1924.[6]

In the experiments of Thomson and Reid in the same year,[3] a higher energy electron beam, accelerated by a potential of ~13 kV, was fired at a polycrystalline celluloid film. They observed a central spot surrounded by diffuse continuous rings, similar to what would be observed when a polycrystalline material was bombarded with X-rays in powder X-ray diffraction (PXRD). Further work by Thomson utilised polycrystalline films of platinum,[7] gold, and aluminium.[8] The structure of these metals was known, allowing for a more accurate calculation of the wavelength of electrons using the de Broglie equation. As the electrons were accelerated by a high voltage (~13 kV), they travelled at ~22% the speed of light ($6.6362 * 10^7\ m/s$). This meant that relativistic effects had to be considered when calculating the de Broglie wavelength. See Equation (2.5). As such, these experiments not only further validated the de Broglie hypothesis[6] but also supported Einstein's theory of relativity.[9]

These discoveries led to numerous studies of crystalline materials via electron diffraction.[10–12] Notably, a large proportion of research on structural analysis by electron diffraction was taking place in the Former Soviet Union as early as 1937.[13–15] Unfortunately, these works did not receive as much interest or acclaim as deserved, and were often treated with outright suspicion.[16] Early research by Pinsker in

1937-1938 began to establish methods for independent, full structure determination from electron diffraction data.[13,14] Following this, Vainshtein and co-workers were able to develop a diffractometer capable of recording diffraction patterns.[15] Various types of diffraction patterns exist, these can be classified as, spot patterns, texture patterns, and polycrystalline patterns.[15] Spot patterns are obtained from a single crystal, their reflections appear as "spots". Polycrystalline patterns are obtained from multiple randomly oriented crystals, the resulting patterns appear as concentric rings, as in PXRD. Texture patterns are obtained from multiple crystals that are uniformly oriented with respect to the specimen support (i.e., all crystals are parallel to it), but randomly distributed with respect to one another. The resulting diffraction patterns are comprised of ring or arc reflections.[15] Using these texture patterns, Vainshtein and co-workers were able to solve the 3D structures of over 30 materials.[15] The book; *"Structure Analysis by Electron Diffraction"* published in English in 1964, details the experimental technique and the series of materials studied.[15]

Despite the initial excitement and progression of the field,[10–15,17–22] electron diffraction faced a significant setback due to the growing unease surrounding the dynamical scattering of electrons. Fears about the intrinsic multiple scattering events associated with electrons, stagnated the progress of the field. Electrons can be elastically scattered multiple times as they pass through a crystal. This breaks the approximation of the linear relationship between the squared structure factor amplitudes and the observed intensities ($|F_{hkl}| \propto \sqrt{I_{hkl}}$), that holds true when a single elastic scattering event (kinematical diffraction) occurs. As a result, the intensities of the observed reflections become redistributed, with the intensity of weak peaks becoming more intense, and the strong peaks becoming less intense.[23,24]. Further, dynamical scattering violates Friedel's law[25–27] (the intensities of the h, k, l reflections are equal to the intensities of the $\bar{h}, \bar{k}, \bar{l}$ reflections) and enables symmetry forbidden reflections, resulting from screw axes and glide planes, to be present in diffraction patterns.[16,28–30] See **Chapter 3, Section 3.2** for further information. There were concerns that as a result of dynamical effects, the intensities of the reflections would be entirely meaningless and unable to yield reliable crystal structures.[17]

It was long believed that due to dynamical scattering, electron diffraction was an inferior technique to its X-ray and neutron counterparts.[16,17,31] The negative association with electron diffraction only began to relent when Dorset and Hauptman released a paper in 1976, in which they were able to determine the structures of two organic compounds from electron diffraction data using *ab initio* phasing.[32] This work showed that it was possible to solve electron diffraction structures using the

kinematical approximation.[32] This demonstrated that the impact of multiple elastic scattering events was not as catastrophic as previously suspected, as structure determination from electron diffraction data was possible. In the 1990s, the scepticism was further dispelled when Dorset released a series of publications retroactively validating the research of early crystallographers such as Vainshtein.[33–39] Dorset was able to apply direct methods to the original data and replicate the structures assuming a kinematical approximation. This validation led to a boom in the field that was facilitated by the availability of superior transmission electron microscope (TEM) hardware.

1.2   Advances in data collection methodology

Once it was shown that electron diffraction data could be collected on a TEM,[23,32,38,40] there was a resurgence in the field that led to the development of a plethora of different data collection strategies, designed to minimise the dynamical effects of electrons. Up until 2007, electron diffraction data were typically collected with the crystal oriented on a low-index zone-axis.[15,23,40–42] A zone axis is a lattice row that is parallel to the intersection of at least two families of lattice planes. These are typically high symmetry orientations of a crystals. This was done to aid crystal indexing that required determination of unit cell parameters and orientation of crystallographic axes. Unfortunately, this strategy had unintended consequences due to the dynamical effects. When the crystal is oriented along a zone-axis, the probability of multiple scattering events increases, as many geometrically related reflections are excited simultaneously.[23,43] This causes the intensities of the reflections to become redistributed. As such, strong reflections appear less intense and weak reflections appear more intense.[23,24] This breaks the kinematical assumption of the linear relationship between the squared structure factor amplitudes and intensities (see **Chapter 3, Section 3.2.1**). This can hinder the crystal's symmetry determination, its indexing, structure determination and structure refinement.[44]

1.2.1   Precession electron diffraction

The technique, precession electron diffraction (PED), was developed to reduce dynamical scattering.[45,46] Initially data were still collected from crystals that were oriented so that one of the crystallographic axes (often a zone-axis) was oriented along one of the principal experimental axes i.e., either the beam or perpendicular to it. PED data are collected by rocking the beam around the optical axis in a conical fashion above the sample and then de-rocking it below the sample. The motion of the beam, replicates what would occur if the sample were precessed around a fixed electron beam.[45,46] More reflections are present in the resulting diffraction patterns, than if a non-precessed

beam were used i.e., in a standard still-frame zone-axis pattern.[45] This is because off-zone reflections are also recorded in addition to the in-zone reflections.[46] Another advantage to the precession technique, over still-frame zone-axis data collection, was that the intensities were averaged (integrated) over the sections encompassed by the precession motion. However, the key advantage of precession was the reduction in dynamical scattering. This was achieved because the motion of the beam excited reflections sequentially rather than simultaneously. As such, geometrically related reflections are not excited concurrently, and the probability of dynamical scattering occurrences is reduced.[45,46]

1.2.2   Automated diffraction tomography

The primary disadvantage of PED data collection was that it typically still required crystals to first be oriented on a zone-axis, and only a small number of off-zone reflections could be recorded. In 2007, Kolbe and coworkers[47,48] proposed that data should instead be collected while tilting the sample around the goniometer axis in discrete steps, with the goniometer axis and crystal orientation being arbitrary to one another. The advantage of this was that diffraction patterns were recorded from a randomly oriented crystal, so overlap with a zone-axis was unlikely and thus the probability of dynamical scattering was reduced. The technique developed by Kolb *et al.* in 2007 was coined automated diffraction tomography (ADT).[47] This data acquisition strategy involved collecting a series of diffraction patterns as the goniometer was tilted in discrete steps. As such, a larger portion of reciprocal space, conveniently typically away from a zone-axis, could be sampled compared to PED. The only limitation to this being the maximum tilt angles allowable by the goniometer, due to microscope configuration and pole piece positions. In reality, the maximum tilt range is further limited by the increased thickness of the crystal at high tilt angles and, other species on the grid entering the beam. The key disadvantage of ADT is that, despite having improved coverage of reciprocal space compared to zone-axis or PED, portions of reciprocal space are still missed in between tilt steps, as illustrated in **Figure 1.1**.

To combat this, in 2009 Mugnaioli *et al.* combined ADT with PED creating a hybrid technique known as precession-assisted electron diffraction tomography (PEDT).[49] The addition of precession, elevated the technique as the precession movement enabled the Ewald sphere to sweep reciprocal space in between the goniometer tilt steps, giving large reciprocal space coverage, and integrating the

intensities over the precession movement. As such, PEDT data can be processed using the kinematical approximation, despite not being truly kinematic. **Figure 1.2** illustrates the collection scheme for PEDT.
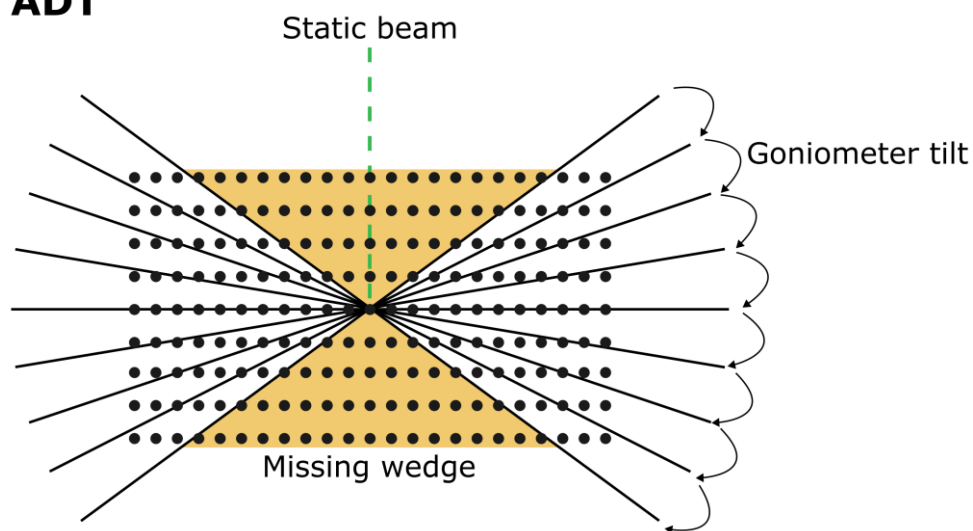
Figure 1.1. Data collection scheme for automated diffraction tomography. The crystal is randomly oriented with respect to the goniometer axis. The goniometer is tilted in discrete steps. A diffraction pattern is recorded after each tilt step. Data is recorded while the beam remains static. Black lines represent slices of reciprocal space at which diffraction patterns are recorded. In addition to the missing wedge of data due to the maximum tilt angle limitation (yellow wedge), the portions of reciprocal space between tilt steps are also not sampled (white space between black lines).
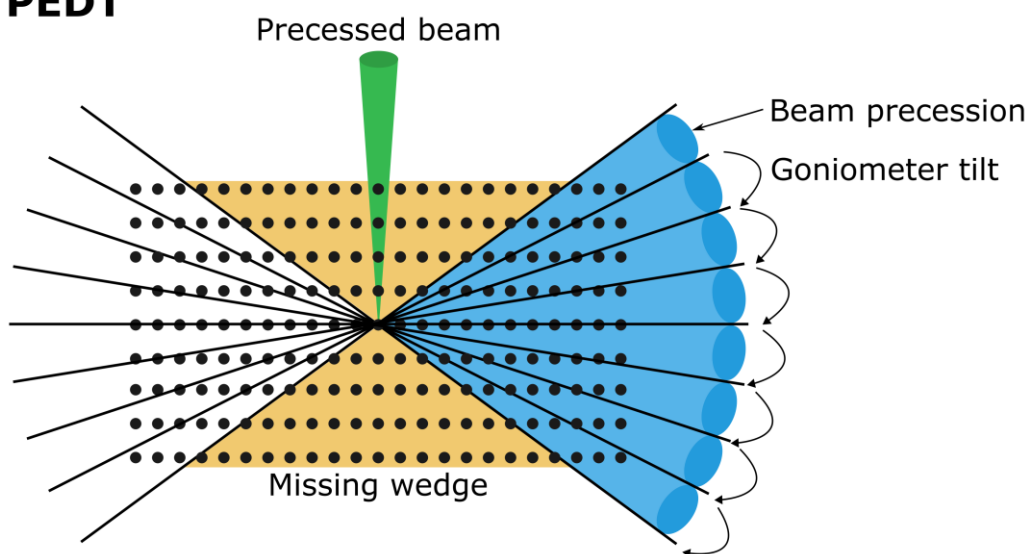
Figure 1.2. Data collection scheme for precession-assisted electron diffraction tomography. This collection scheme is a hybrid of ADT and PED. The goniometer is tilted in discrete steps (black lines) and the beam is precessed in a conical shape on the sample (blue cones), allowing for increased coverage of reciprocal space. The missing wedge of data is highlighted in yellow. For clarity, only half of the reciprocal space sampling (blue cones) is shown.

The coverage of such a high proportion of reciprocal space was a huge leap forward in the field of 3D electron diffraction, and PEDT was the first 3D electron diffraction technique to gain popularity and acceptance as a means of structure determination.[46,50] An additional advantage of PEDT was that dynamical refinement of the data was possible, as the dynamical effects could be modelled.[51–55] Detection of hydrogen atoms was also possible with this technique.[56] Unfortunately, however PEDT was a specialised technique that required additional instrumentation to enable beam precession.[57] The device required to achieve this does not come as standard with a typical TEM. Specialised software was also required to process PEDT data.

1.2.3   Rotation electron diffraction

An alternate data collection approach is rotation electron diffraction (RED).[58,59] This is another stepwise method in which the goniometer is tilted in discrete increments. To achieve improved reciprocal space sampling, the electron beam is tilted in small angular steps (< 0.1°) in between the goniometer tilt steps (2-3°).[43] See **Figure 1.3**. This allows for a greater precision than is attainable with discrete goniometer tilts alone. While this method does not require external hardware, custom software is required to synchronise the beam tilt and microscope hardware.[44]
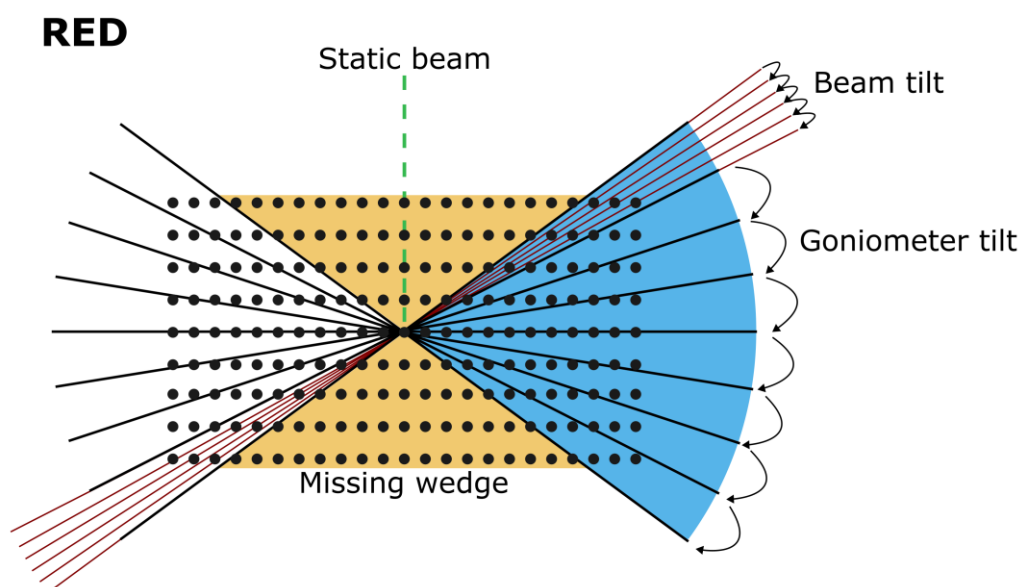
Figure 1.3. Data collection scheme for rotation electron diffraction. The goniometer is tilted in discrete steps. The electron beam is tilted in between the mechanical goniometer tilts. This allows for increased coverage of reciprocal space, beyond what the precision of the goniometer would allow through mechanical tilts alone. Black lines represent goniometer tilt, maroon lines represent beam tilt, sampled reciprocal space is shown in blue and the missing wedge is highlighted in yellow. For clarity, only the beam tilts for the first goniometer tilt, and only half of the reciprocal space sampling (blue) are shown.

1.2.4 Continuous rotation electron diffraction

These methodological advances culminated in continuous rotation electron diffraction. As the name suggests, this technique involved continuously collecting data while the crystal rotated in a static electron beam. **Figure 1.4** illustrates the data collection scheme for continuous rotation. Unlike PEDT or RED, no additional hardware or software were required for data collection. The key requirement was for goniometer stability and a constant, known rotation speed. As the crystal continuously rotates throughout data collection, the resulting diffraction patterns are integrated ranges of reciprocal space defined by the exposure time (t_{exp}) and goniometer rotation velocity (ω). The thickness of the reciprocal space wedges ($\Delta\eta_{exp}$) is defined by the following equation:

$$\Delta\eta_{exp} = \omega * t_{exp} \qquad\qquad (1.1)$$

An additional factor to take into consideration is the detector readout time (t_{dead}). This is the time in which the crystal is rotating but no data can be recorded as the prior data is being read out and stored.

$$\Delta\eta_{dead} = \omega * t_{dead} \qquad\qquad (1.2)$$

This modifies the thickness of the reciprocal space wedges such that:

$$\Delta\eta_{total} = \omega * \left(t_{exp} + t_{dead}\right) \qquad\qquad (1.3)$$

In modern, fast detectors the readout time becomes negligible. (See **Chapter 2, Figure 2.8**) However, in older, slow-scan detectors the diffraction patterns ($\Delta\eta_{exp}$) are separated by the angular range ($\Delta\eta_{dead}$). This needs to be carefully accounted for to allow successful data processing and avoid mistakes during data indexing.

Continuous rotation
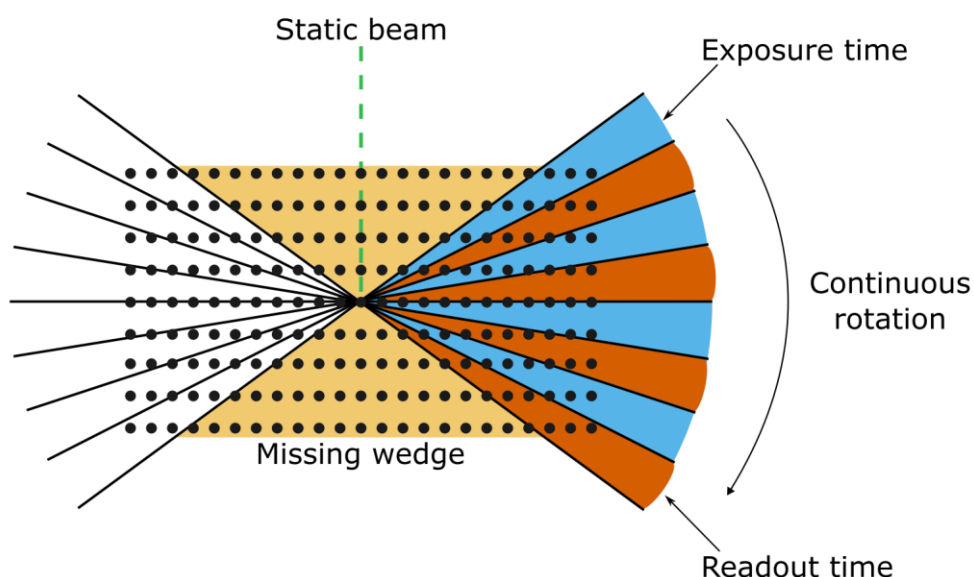
Figure 1.4. Data collection scheme for continuous rotation electron diffraction data collection. *The goniometer is continuously rotating while the beam remains static. Diffraction patterns are recorded while the sample is continuously rotating. The blue wedge represents the exposure time, the red wedge represents the readout time. Data are lost during readout time as the detector can record no further diffraction patterns. The shorter the readout time, the more reciprocal space can be sampled. For clarity, only half of the reciprocal space sampling (blue) and readout time (red) are shown.*

The continuous rotation technique for electron diffraction was developed almost concurrently by Nederlof *et al*. in 2013[60] and Nannenga *et al*. in 2014.[61] The rotation method had existed many years prior to this, and had been the standard approach for X-ray crystallography for several decades,[62,63] but had not previously been used for electron diffraction. Numerous different names and acronyms exist to describe this technique: microcrystal electron diffraction (microED),[61] integrated electron diffraction tomography (IEDT),[64] and continuous rotation electron diffraction (cRED).[65,66] Perhaps the most popularised of these terms is microED.[61] The abbreviation 3DED (three-dimensional electron diffraction) was formulated as a means to describe any electron diffraction data collection strategy involving the sampling of 3D reciprocal space by tilting the sample around an arbitrary axis.[43] Including ADT,[47,48] PEDT,[49] RED,[58,59] microED,[61] IEDT,[64] and cRED,[65,66] among others. 3DED is a helpful, generic, umbrella term which shall be used henceforth in this thesis to describe the continuous rotation technique.

1.3   Recent resurgence of 3DED

The development of 3DED provided an alternative means of structure determination in cases where X-ray diffraction was difficult or unsuitable. Obtaining crystals of sufficient size and quality for single-crystal X-ray diffraction (SCXRD) experiments can be prohibitive. For in-house SCXRD experiments, the volume requirement for crystals is on the order of $\sim 10^5$ μm^3,[50] with a minimum crystal side length of ~ 50 μm.[67] This volume requirement is reduced to $\sim 10^3$ μm^3 for synchrotron sources.[50] Electrons and X-rays interact with matter differently. X-rays are scattered by the electron density, whereas electrons, being charged particles with mass, interact with the electrostatic potential of molecules. The electrostatic potential is comprised of both the negatively charged electron clouds and the positively charged protons in atomic nuclei. As electrons are also charged, they interact with the matter more strongly, resulting in a significantly larger scattering cross section, allowing data collection from significantly smaller crystals than attainable with X-rays, in the volume range of 10^{-2} μm^3.[50] Further differences between electrons and X-rays are detailed in **Chapter 3, Section 3.2**.

Due to electrons interacting more strongly with matter than X-rays, they are also more likely to be elastically scattered multiple times. This is known as dynamical diffraction. The 3DED data collection protocol reduces dynamical effects as rotation of the crystal ensures that the geometrically related reflections are not excited simultaneously. See **Chapter 3, Section 3.2**. As 3DED data are collected in a means that is analogous to SCXRD, 3DED data can be processed using the same software and routines utilised in X-ray crystallography with minimal changes.[68–75] 3DED data can be treated assuming the kinematical approximation of scattering, despite this technically not holding true.

The development of the 3DED technique led to a resurgence in the field of electron crystallography. 3DED data could be collected with relative ease on standard TEMs.[60,61,63,67,76] The ability to collect data from such tiny crystals on the nanometre to sub-micrometre size range was a huge advantage of electron diffraction. In addition to this, 3DED could be used to determine the structures of species where multiple crystal forms or crystalline species are present in a single sample.[67,76–80]

3DED has been used to study a wide range of materials. Metal organic frameworks (MOFs) are an example of a group of materials that are particularly amenable to study via 3D electron diffraction. This is because MOFs are often synthesised as polycrystalline powders, comprised of crystals that are too small or of too poor quality to study using SCXRD.[81,82] MOFs have a wide variety of applications

including: catalysis, ion exchange, gas storage and separation, and as bio-medical agents.[83–89] For these applications, it is essential to know the structure of the MOF and its atomic arrangement in order to understand its physical and chemical properties.[81,82] 3DED has been successfully used to characterise the structures of numerous different MOFs, providing vital information on their structure-property relationships.[65,81,82,90–104]

Another area of interest in which the 3DED technique has been applied is macromolecular structure determination. Obtaining sufficiently large and high quality protein crystals for SCXRD can be difficult and time-consuming, if not entirely impossible.[105–111] It has been found that failed crystallisation trials, i.e. crystallisation attempts that failed to yield suitably large crystals for SCXRD experiments, may contain micrometre sized protein crystals,[112–114] potentially suitable for study via 3DED. These micrometre sized crystals may be more ordered and contain fewer defects than larger crystals of the same material.[115–117] In order to establish and validate 3DED as a technique to study proteins, standard proteins that have been well-studied and previously characterised by X-ray crystallography have been used. As such, a large proportion of the macromolecular structures that have been solved by 3DED are those of proteinase K,[116,118–123] lysozyme,[116,124–130] and catalase.[61,131–133] As of 2021, standard proteins such as these accounted for over 40% of the electron diffraction structures deposited in the protein databank (PDB).[50] Few novel protein structures have so far been solved using 3DED.[50,134]

A drawback of 3DED as a means to study protein crystals is sample preparation. Protein crystals contain channels filled with disordered solvent. These solvent molecules are often volatile and as such, the crystal structures are highly likely to collapse when exposed to the high vacuum present within a TEM. Protein crystals can also desolvate under ambient conditions, destroying their order and leading to a loss of diffraction.[135] To prevent desolvation, crystals require treatment. A traditional approach to this issue involved substituting the solvent with sugar solutions.[136] A more modern approach, that is typically used today, utilises vitrification.[137–140] The vitrification process involves rapidly freezing samples in liquid ethane to prevent formation of crystalline ice.[137–140] This preserves the solvent channels in the proteins in their disordered (amorphous) states and inhibits solvent removal under vacuum conditions.

An additional step, often utilised in protein sample preparation for 3DED, is focused ion beam (FIB) milling.[120,123,128,141–145] In this process, a focused beam of ions is repeatedly scanned over the crystal

surface removing layers of atoms to generate crystalline lamella of ~100 – 300 nm thickness, ideal for 3DED experiments.[145] This is a time consuming process that requires specialised equipment and extensive operator experience and expertise.[145] Another potential disadvantage of requiring a FIB milling step in protein sample preparation is that it requires relatively large crystals (that may be of suitable size for SCXRD) that are subsequently thinned to form lamella, this somewhat negates the benefit of not having to grow large crystals for SCXRD experiments.

In contrast, sample preparation for small molecule compounds for 3DED is often remarkably simple. Crystalline powders can be deposited directly onto grids (sometimes with prior grinding), cooled if required, and inserted directly into a TEM.[63,67,76] 3DED has successfully been used to characterise a wide range of small molecule compounds including: active pharmaceutical ingredients (APIs),[24,56,63,65,67,76,146–152] natural products,[76,153] supramolecular complexes,[154–156] organometallic compounds,[157,158] and organic compounds.[63,67,76,77,146,159–163] This thesis focuses exclusively on small molecules, specifically organometallic species.

In 2016, 3DED was used to determine the structures of beam-sensitive organic compounds.[63] A low flux electron beam (~0.013 e^- $Å^{-2}$ s^{-1}) was used, enabling data collection from beam-sensitive compounds at room temperature.[63] The data were then processed, and the structures determined *ab initio,* using standard X-ray crystallographic software (XDS[74] and SHELX[164–166]). Two papers, published in 2018, by Gruene *et al.*[67] and Jones *et al.*[76] ignited substantial excitement, particularly among synthetic chemists, about 3DED and highlighted the extraordinary potential of the technique as a means to study small molecules. The two papers demonstrated that 3DED could be an invaluable tool to synthetic chemists.[67,76] Structure determination from "seemingly amorphous" powders containing microcrystalline material was possible with minimal sample preparation on a commercially available instrument, already in use at many institutions.[67,76] Here, the term microcrystalline is used to mean comprised of small crystals.[67] "Micro" is perhaps a misleading misnomer here, as most of the crystals in such powders are typically on the nanometre size range.[76]

Gruene *et al.*[67] demonstrated the applicability of the technique on pharmaceutical products comprised of a blend of powders. They were able to determine the structure of paracetamol (acetaminophen) from a sample comprised of a mixture of other crystalline and non-crystalline species. The localisation of some hydrogen atoms was also achieved. They also demonstrated the

speed with which 3DED could be used to determine structures was comparable to that of X-ray crystallography, determining the structure of a methylene blue derivative, MBBF$_4$ in a mere 4 hours. In a similar vein, Jones *et al.*[76] were also able to determine the structure of paracetamol from a commercially available medication. In addition to this, they also studied ibuprofen and a series of other commercially available bioactive species. Structure determination from all the species studied was possible without any further synthesis or crystallisation attempts. Additionally, Jones *et al.*[76] created a heterogenous mixture of carbamazepine, biotin, cinchonine, and brucine. Heterogenous mixtures are typically not suitable for study via X-ray crystallography or nuclear magnetic resonance (NMR) spectroscopy.[76] However, using 3DED it was possible to rapidly determine the structures of all the small molecules present in the heterogenous mixture by collecting data from several different crystals on the TEM grid. These papers further demonstrated that for ideal cases, structure determination was possible in less than an hour.[67,76]

1.4 Applications of 3D electron diffraction in organometallic chemistry

A field in which 3DED could have a substantial impact is organometallic chemistry and the study of elusive transition metal complexes. The potential of 3DED to characterise reactive organometallic species was demonstrated in 2019 by Jones *et al.*[157] The structures of six transition metal complexes, including reactive intermediates, were determined using 3DED to illustrate the wide applicability of the technique. Remarkably, it was also possible to determine the first crystal structure of Schwartz's reagent (chloridobis(η^5-cyclopentadienyl)hydridozirconium).[157] Despite being an important and commonly used reagent, first prepared over 50 years ago,[167,168] no crystal structure of this compound had previously been obtained. The low solubility of Schwartz's reagent in common solvents, and its reactivity with polar chlorinated solvents, precluded structure determination by X-ray crystallography due to the inability to obtain suitably sized crystals.[169] Additionally, characterisation by NMR studies also proved difficult. Using 3DED Jones *et al.*[157] were able to determine the structure of Schwartz's reagent directly from a commercially available powder without any additional purification and crystallisation efforts. This, in combination with the determination of other transition metal structures, highlighted the power of 3DED as a structure determination technique where characterisation by other means is inaccessible. The interest in the 3DED technique from synthetic chemists continued to rise.[170,171]

1.5 Scope of the thesis

Following the success and excitement surrounding the papers released by Gruene *et al.*[67] and Jones *et al.*[76] in 2018, we wanted to ascertain whether it would be possible to collect our own 3DED data and eventually establish 3DED as a technique at the University of York. Initial studies, not presented in this thesis, were conducted on a Tecnai T12 microscope fitted with a Ceta 16M camera. Data collection with this instrument proved to be a manual and time-consuming process. Additionally, the stability of the side entry goniometer and the noisy camera proved less than ideal for data collection. See **Chapter 2** for further information on TEMs. Despite this, it was possible to replicate the work of Gruene *et al.*[67] and Jones *et al.*[76] and successfully determine the structure of paracetamol from data collected on the T12. Further test species, including biotin, were then studied on the T12.

There was substantial interest in 3DED from the Chemistry Department at the University of York. This led to several fruitful collaborations that were initially inspired by the Jones *et al.* paper entitled: "Characterization of Reactive Organometallic Species via MicroED".[157] We wanted to establish whether the previous successes of this technique with small molecule compounds[67,76,157] were as the result of using carefully selected test samples that diffracted well, [67,76,157] or whether 3DED could be applied more broadly to derive structural information in a high-throughput manner for most compounds synthesised in chemistry laboratories. If this proved to be possible it would allow us to investigate challenging and novel complexes that were difficult, if not impossible to characterise via X-ray crystallography.

The installation and commissioning of the Thermo Fisher Scientific Glacios microscope in April 2021, helped to rapidly accelerate progress. It allowed for a semi-automated data collection protocol to be established using the EPU-D software, making data collection considerably faster and easier. The data collection workflow is presented in **Chapter 9**. Initial experiments on the Glacios instrument, worked to replicate Jones *et al.*'s work[157] with [1,1-bis(diphenylphosphino)ferrocene]dichloronickel(II) and its palladium counterpart, [1,1-bis(diphenylphosphino)ferrocene]dichloropalladium(II). These samples were obtained directly from the supplier, Sigma-Aldrich. When structure determination from these compounds proved to be possible, we then investigated a range of materials synthesised in the lab by our collaborators.

The aim of these collaborations were to characterise the structures of challenging samples using 3DED, to explore the limitations of 3DED, and to establish the possibilities of the technique when working with novel organometallic samples. 3DED was used to determine the structures of: (i) a beam and air sensitive σ-alkane species that was difficult to study via SCXRD (**Chapter 4**), (ii) bulky planar porphyrin complexes that could not be studied by SCXRD (**Chapter 5**), (iii) a series of manganese complexes and their precursor ligand where only a scarce quantity of material was available (**Chapter 6**), and (iv) palladium complexes derived directly from reaction mixtures, where further purification and recrystallisation had not been attempted (**Chapter 7**).

1.6   Thesis aims

The aims of this PhD project were to:

1. Implement 3D electron diffraction as a technique at the University of York.

2. Establish a data collection and processing workflow for 3D electron diffraction data based on the available instrumentation at the University of York.

3. Explore the limitations of 3D electron diffraction in determining the structures of small molecule organometallic compounds.

4. Utilise 3D electron diffraction to study small molecule organometallic compounds, synthesised in the chemistry laboratories, which were precluded from structure determination using X-ray crystallography.

2 Introduction to Transmission Electron Microscopy

2.1 The transmission electron microscope

A transmission electron microscope (TEM) utilises a series of electromagnetic lenses to manipulate the path of a beam of accelerated electrons. The electron beam then strikes the sample and, depending on sample thickness, a portion of these electrons pass through the sample, interacting with it and being scattered as they do so. The transmitted electrons are then focused, and the image formed is magnified by further electromagnetic lenses to form an image or a diffraction pattern which can be observed on a phosphor screen or recorded on a detector. Electron microscopy is analogous to light microscopy, with a few key differences. Instead of using visible light, electron microscopy employs electrons. These have a much shorter wavelength, meaning samples can be imaged at much higher resolution. In light microscopy, glass lenses are used to deflect the photons in a beam of visible light, with electrons, electromagnetic lenses are required. The magnetic field generated by these lenses bends the electron beam. The degree to which the electron beam is deflected can be changed by altering the electric current supplied to the electromagnetic lens. The other key difference is that a vacuum is required in electron microscopy, this is to allow the electrons to pass to the sample and then to the detector unimpeded. If no vacuum was present the electrons would be scattered by air molecules in the column.

The TEM used for all work in this thesis was a Thermo Fisher Scientific Glacios microscope. A schematic of the optics of this microscope is given in **Figure 2.1**. Further details on the components of a TEM will be explored in subsequent sections. The Glacios was operated in bright field mode. In bright field images, areas where no diffraction of the beam has occurred appear bright, and areas that absorb or scatter electrons are darker. Bright field images are produced by the transmitted beam. In contrast, when using dark field mode, the transmitted beam is blocked by an aperture and scattered electrons create the image. In dark field images the areas where no diffraction has occurred appear black and, the areas where absorption or scattering have occurred appear white.

Electron Source	
Gun Lens	
Accelerator Stack	**Voltage (high tension)**
Gun Deflectors	**Gun shift, gun tilt**
Condenser Lens 1	**Spot size**
Condenser Lens 2	**Beam size, intensity, centring**
C2 Aperture	
Condenser Stigmators	**Condenser stigmatism**
Beam Deflectors	**Beam shift, beam tilt**
Mini-condenser Lens	**Micro/nanoprobe**
Upper Objective Lens	
Sample Stage	**Stage position, tilt, z-height**
Lower Objective Lens	**Focus**
Objective Aperture	
Objective Stigmators	**Objective stigmatism**
Image Deflectors	**Image shift, image tilt**
Selected Area Aperture	
Intermediate Lens	**Imaging/diffraction**
	Magnification
Projector Lens	**Magnification**
Screen	**Detectors**

Figure 2.1. Schematic diagram of the optics of a two-condenser transmission electron microscope. The components of a TEM are labelled on the left and the functions of the components are given on the right.

2.1.1 Electron source

Electrons are generated by an electron source, colloquially referred to as a gun. Various types of electron sources exist. The Glacios utilises an X-FEG (extreme field emission gun), created by FEI (Field Electron and Ion Company), as its source. This is a Schottky thermally assisted FEG. Field emission guns emit electrons by using a strong electrostatic field which is applied to a sharpened tip of a tungsten wire. As the field emission source is a Schottky FEG, the tip is also coated in zirconium oxide. When heated, this allows the emission of thermally generated electrons. The electron source acts as a cathode. The electrons are accelerated towards the first anode due to the voltage difference between the anode and the cathode. The second anode then focuses the electron beam. The combination of the two anodes acts as an electrostatic lens (the gun lens), causing the ray paths of the electrons emitted from the FEG to crossover. The electrons are then sped up through the accelerator stack. The accelerator stack is a series of discs connected together by resistors. The final plate is grounded and there is a graded drop in potential between each of the plates. As the electrons pass through the stack, they gain energy. When the electrons emerge, they have gained 200 keV of energy (the operating voltage of the TEM). A diagram of a Schottky field emission source, the gun lens (anodes) and the accelerator stack are given in **Figure 2.2**.
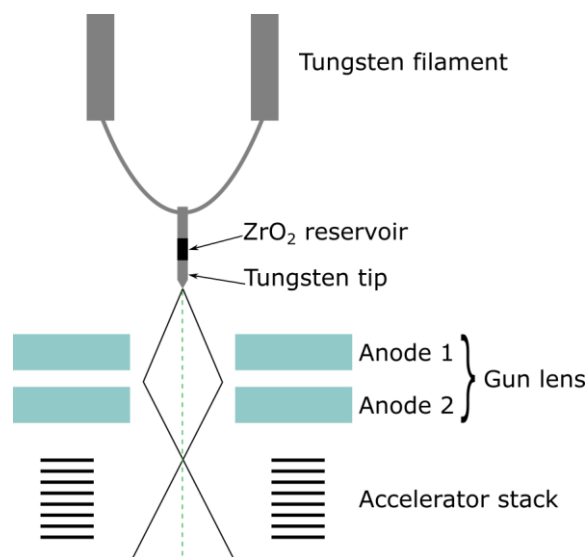
Figure 2.2. Schematic of a Schottky field emission gun. Zirconium oxide coats the tungsten tip. The two anodes work together to act like an electrostatic lens to create a crossover point, this is the gun lens. The electrons are then accelerated through the accelerator stack.

Electrons have wave particle duality; they can act as both particles and waves. The energy E of an electron can be defined both as a particle and as a wave.

Particle:

$$E = m_0 v^2$$ <div align="right">(2.1)</div>

Where:

m_0 = electron mass

v = frequency

Wave:

$$Wave: E = hv$$ <div align="right">(2.2)</div>

Where:

h = Planck's constant

v = frequency

Setting these equations equal to one another and substituting u/λ (velocity/wavelength) for frequency yields the de Broglie equation:[6]

$$\lambda = \frac{h}{m_0 u}$$ <div align="right">(2.3)</div>

Where:

u = velocity

The wavelength of electrons can be calculated using the acceleration voltage in V using the following version of the de Broglie equation:

$$\lambda = \frac{h}{\sqrt{2m_0 e V_a}}$$ <div align="right">(2.4)</div>

Where:

$h = 6.626 * 10^{-34}\ Js$ = Planck's constant

$m_0 = 9.109 * 10^{-31}\ kg$ = mass of an electron

$e = 1.602 * 10^{-19}\ C$ = elementary charge

V_a = acceleration voltage in V

Electrons accelerated by potential of 200 kV have an energy of 200 keV and are travelling at ~70% the speed of light ($2.0845 * 10^8\ m/s$), because of this, a relativistic correction needs to be applied to the de Broglie equation. This results in the following version of the equation:

$$\lambda = \frac{h}{\sqrt{2m_0 eV_a + \dfrac{e^2 V_a{}^2}{c^2}}}$$

Where:

$c = 2.998 * 10^8 \; m/s =$ speed of light

The wavelength of electrons with an energy of 200 keV is 0.025079 Å.

2.1.2 Electromagnetic lenses and apertures

Light microscopy utilises glass lenses to deflect a beam of light. Electrons are blocked by glass, but due to their charged nature, they interact with magnetic fields and as such can be deflected and focused by them. In light microscopy, the focus of the glass lenses is fixed. In contrast, in electron microscopy the focus of the electromagnetic lenses can be changed by varying the current supplied to them. Electromagnetic lenses consist of a solenoid encased within soft iron. A solenoid is a type of electromagnet, comprised of a coil of tightly wound copper wire. When supplied with an electric current, the current flows through the copper wire generating a strong magnetic field which is then concentrated by the soft steel encasing it. The magnetic field is concentrated in the gap between the soft iron pole pieces. This is where the electron beam is deflected as it passes through the lens. A cross-sectional representation of an electromagnetic lens is given in **Figure 2.3**.

By varying the electric current supplied to the lens, the strength of the magnetic field can be varied, allowing the extent to which the electrons are deflected and focused to be carefully controlled. The weaker the lens, the longer the focal length (f_1) and the greater the magnification. The stronger the lens, the shorter the focal length (f_2) and the weaker the magnification, as can be seen in **Figure 2.4**.
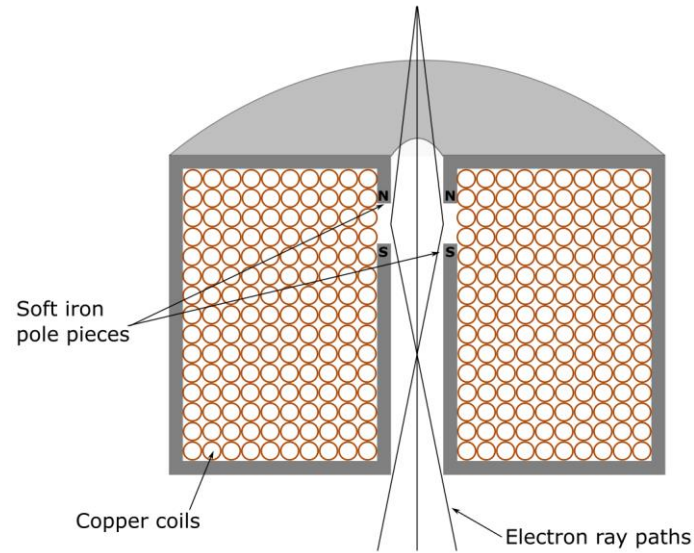
Figure 2.3. Cross-section of an electromagnetic lens, showing how the magnetic field generated deflects the electron beam.

$$M = \frac{d_i}{d_o}$$
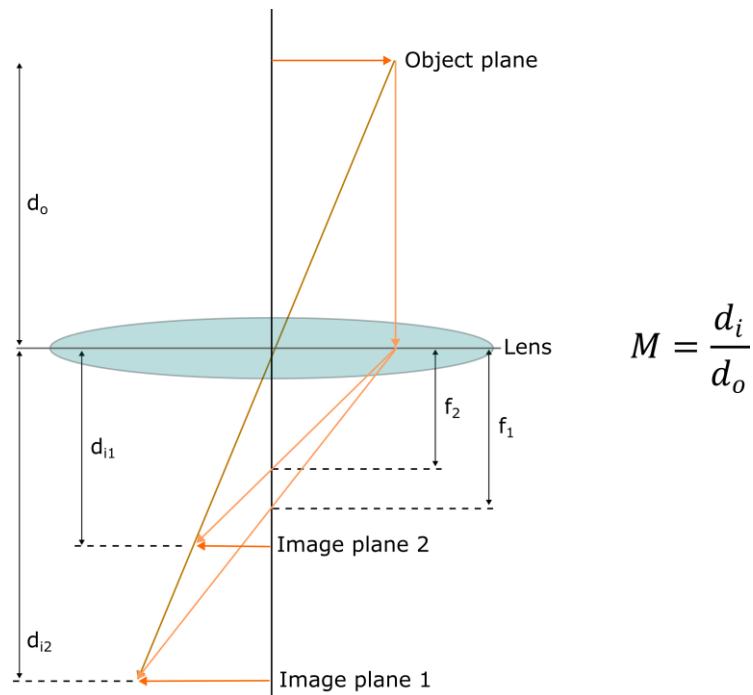
Figure 2.4. Illustration showing how changing the lens strength alters focal distance and magnification of the electron ray path. f = focal length, d_o = distance between lens and object plane, d_i = distance between lens and image plane, M = magnification.

Magnification (M) is calculated using the following equation: $M = \frac{d_i}{d_o}$ *(2.6)*

$Where$:

d_i = distance between lens and image plane

d_o = distance between lens and object plane

A TEM is comprised of a series of these electromagnetic lenses, that each serve a specific function (**Figure 2.1**). The condenser lenses demagnify the beam, reducing the diameter of the beam. The Glacios has a double condenser lens system. The first condenser lens is used to control the spot size and the second condenser lens controls the convergence of the beam on the sample, the diameter of the illuminated area and the centring of the beam. An aperture sits immediately below the C2 lens. The aperture is a hole in a strip of non-magnetic metal that physically blocks fractions of the electron beam from passing through and impacting the sample. The C2 aperture helps control the intensity of illumination on the sample. There are multiple different sized holes in the C2 aperture strip, meaning the size of the opening, and therefore how many electrons are able to pass through it can be varied. Typically, a C2 aperture strip will have aperture sizes of 150, 100, 70 and 50 µm. The Glacios at York has an extended aperture strip, with additional apertures of 30, 10 and 5 µm diameter. A diagram showing how an aperture works is given in **Figure 2.5**. An example illustration of an aperture strip is shown in **Figure 2.6**. The apertures need to be carefully centred to ensure they do not block desired parts of the beam.
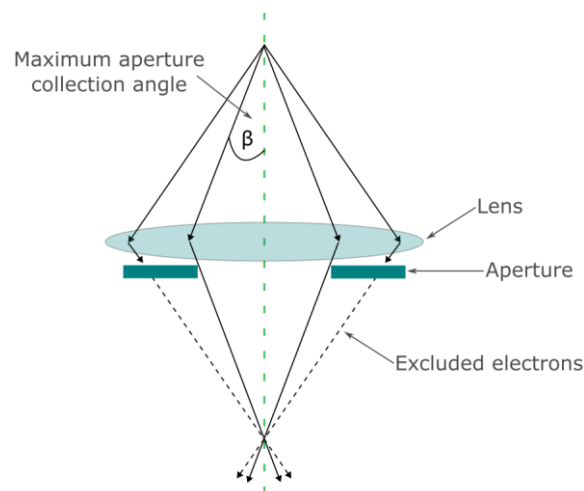
Figure 2.5. Diagram showing how an aperture works. *Electrons that are above the maximum aperture collection angle are blocked from passing through the aperture, these electrons are represented by dotted arrows.*

Figure 2.6. Illustration of an aperture strip with four holes. *The strip is made of a non-magnetic metal and has mechanical holes.*

In addition to the two condenser lenses there is also a mini-condenser lens. The polarity of this lens can be inverted to switch between microprobe and nanoprobe mode. More details on this, and its usefulness for electron diffraction studies will be given in **Section 2.2.3**.

The next lens in the system is the objective lens. The Glacios is equipped with a split pole piece objective lens, meaning there is an upper and lower lens between which the sample sits. The objective lens generates the first intermediate image of the sample and focuses it. An objective aperture can be inserted here. It is not used when collecting electron diffraction data but is used during microscope alignments to ensure the diffraction focus is set so the back focal plane is at focus.

The intermediate lens magnifies the image formed by the objective lens. Varying the power of the intermediate lens determines whether an image or diffraction pattern is observed on the viewing screen. For imaging, the intermediate lens is focused on the initial image formed by the objective lens (in the image plane). For diffraction, the intermediate lens is focused on the back focal plane of the objective lens and a diffraction pattern is observed on the viewing screen. **Figure 2.7** shows schematic ray diagrams highlighting the difference between imaging and diffraction mode.
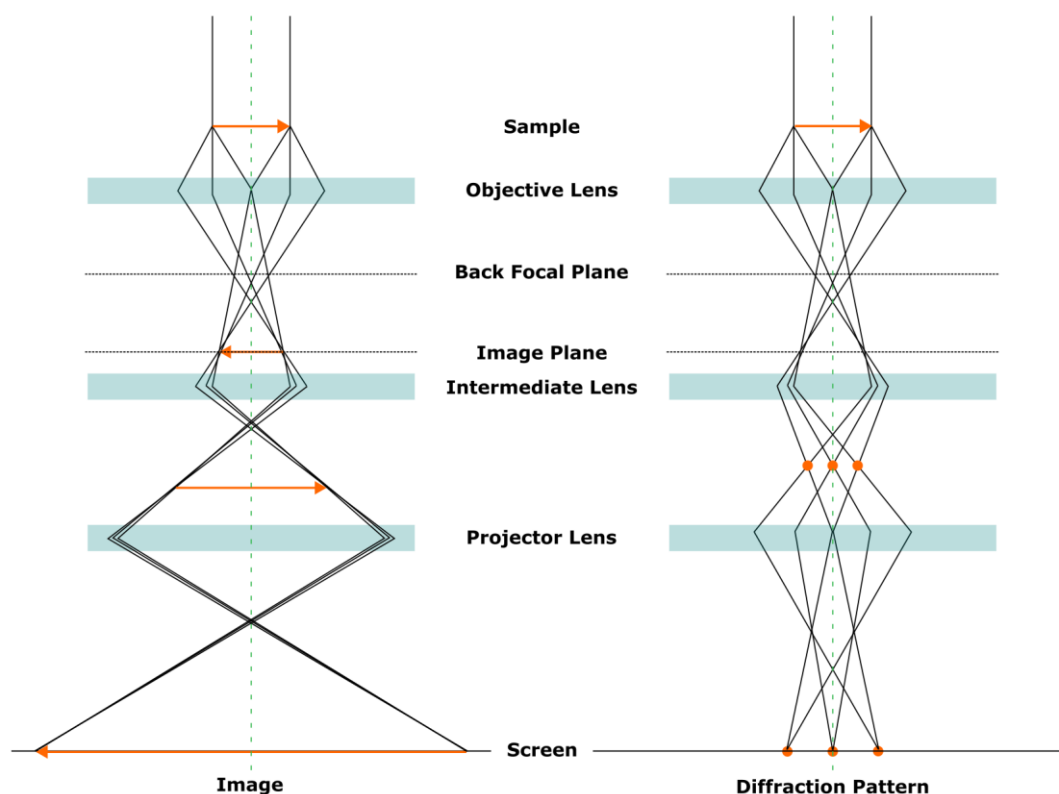
Figure 2.7. Schematic ray diagrams of imaging mode (left) and diffraction mode (right). *The strength of the intermediate lens determines whether an image or diffraction pattern will be observed on the viewing screen.*

The final lenses in a TEM are a series of projector lenses. For simplicity, in figures only a single projector lens is shown. Varying the strength of the projector lenses varies the magnification. Magnification is controlled by both the projector lens and the intermediate lens.

2.1.3 Detectors

The electrons then hit the viewing screen forming an image or diffraction pattern. To capture the image or diffraction pattern, the screen can be lifted, and a detector used instead. A variety of detectors exist, including photographic film, CCDs (charged coupled devices), CMOS detectors (complementary metal-oxide semiconductor), hybrid pixel detectors, and direct electron detectors. The Glacios at York is equipped with a Ceta-D camera (CMOS device), a Falcon-IV (counting direct electron detector) and segmented STEM (scanning transmission electron microscopy) detectors used specifically for STEM applications. The Ceta-D camera is used for electron diffraction data collection.

The Ceta-D is a scintillator coupled CMOS camera, it is highly sensitive and has a short readout time, making it suitable for collecting continuous rotation electron diffraction data. If readout times are long, large portions of reciprocal space are not sampled as the detector is not able to record further data while previous data is being read out. All the while, the sample keeps rotating. See **Chapter 1, Figure 1.4** for a visualisation of this. An illustration of the continuous rotation electron diffraction data collection scheme using a detector with a negligible readout time is shown in **Figure 2.8**.
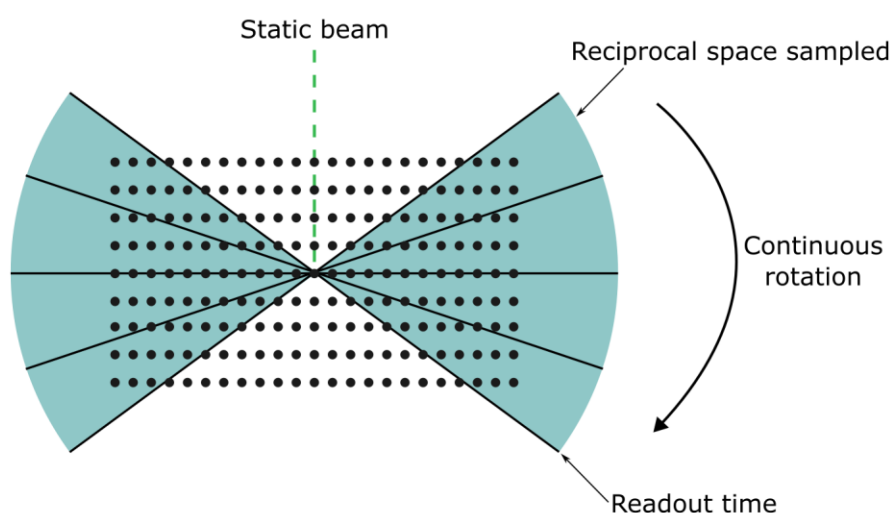
Figure 2.8. Data collection scheme for continuous rotation electron diffraction data collection. *The crystal is continuously rotating while the beam remains static. Diffraction patterns are recorded while the sample is continuously rotating. Each wedge represents a single frame, the wedges are separated by black lines, these represent the readout time of the detector. If the readout time is short, less information is lost during readout.*

In a scintillator coupled CMOS device (henceforth abbreviated to CMOS), the incoming electrons hit a scintillator and are converted into photons. The photons then are transferred to a sensor via a fibre optic plate. The signal is then detected by the sensor. The charge is then converted to a voltage per pixel. This process is illustrated in **Figure 2.9**. In CMOS detectors, each pixel is read out individually. This confers a significant advantage over CCD cameras which are also scintillator-coupled detectors. Whereas in CMOS cameras, the architecture is set up such that each pixel is connected to column wires and whole rows of pixels can be read out simultaneously, in CCDs, the charge is not immediately read out. Instead, it is transferred from pixel to pixel and charge is converted to voltage at an output node. This leads to long readout times, making CCD cameras unsuitable for collecting continuous rotation electron diffraction data. Large wedges of reciprocal space would not be sampled due to dead time when the detector is in readout. A comparison of detector architecture is given in **Figure 2.10**.
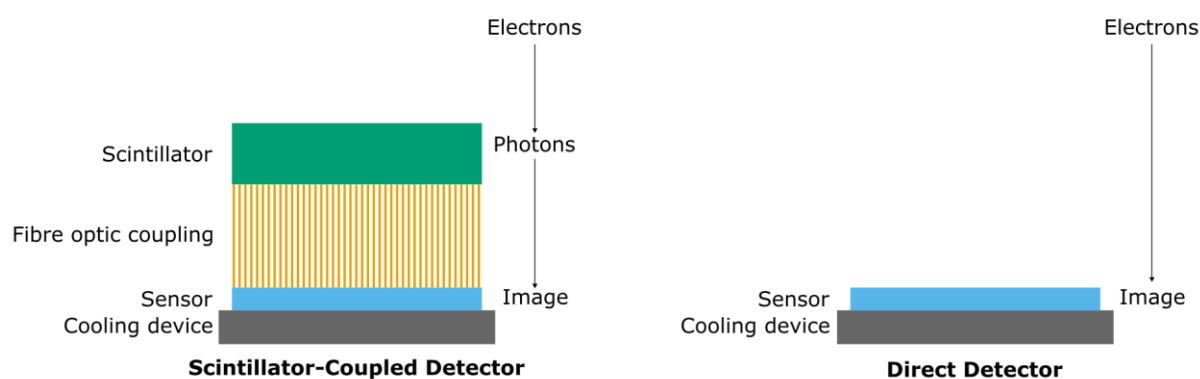
Figure 2.9. Schematic of a scintillator-coupled detector, such as a CCD or CMOS device (left) and a direct electron detector (right). Scintillator based detectors detect electrons indirectly, the electrons hit the scintillator and are converted into photons and transferred to the sensor via fibre optics. This conversion and transport process is inefficient and lowers the detective quantum efficiency of the detector.

A disadvantage of CMOS detectors is that they detect electrons indirectly, electrons are converted into photons and then transferred to the detector via fibre optics. Photon conversion and photon transport are not entirely efficient processes. Direct electron detectors forgo scintillators and fibre optic coupling altogether and instead electrons are detected directly by a radiation hardened sensor (**Figure 2.9**). As there is no signal conversion or transport, these detectors are more efficient and have a higher detective quantum efficiency (DQE). DQE is a measure of how much noise a detector adds to an image, i.e., the worse the DQE of a detector, the more noise will be present in the images and the lower the signal to noise ratio will be. It is a measure of how efficiently a detector is able to detect an electron. DQE is calculated using the following equation:[172]

$$DQE = \frac{SNR^2_{out}}{SNR^2_{in}} \qquad\qquad (2.7)$$

$Where$:

SNR_{out} = signal to noise ratio of the output

SNR_{in} = signal to noise ratio of the input

While conferring an advantage over CMOS detectors in terms of DQE, collecting electron diffraction data on direct electron detectors comes with other difficulties. Primarily, incredibly low fluxes are required when operating in counting mode to allow individual electron events to be distinguished.[173] In counting mode, individual electrons are identified (counted), by the detector and summed over the full exposure. Separating electron events temporally requires that only one electron hits the detector in a given position during a frame. If multiple electrons hit the detector in the same place in rapid succession, they may be counted as a single event. As such, incredibly low fluxes are required.[173] A consequence of this is that the signal to noise ratio becomes very low and it may not be possible to observe diffraction peaks. To combat this, long exposure times are required. This makes data collection a slow process and the stability of the sample stage may become problematic. Direct electron detectors are typically used in counting mode for imaging purposes, where the electrons are randomly distributed over the detector. When collecting electron diffraction data, the electrons are concentrated into Bragg peaks. Even lower fluxes are required to ensure the Bragg peaks do not become saturated. This is particularly challenging for small molecule crystals that diffract strongly. An additional means of reducing the flux is to spread the beam over a large area on the sample and use a selected area aperture to reduce the area from which diffraction is recorded.

Direct electron detectors can also be operated in integrating mode. In integrating mode, electrons hit the detector and charge is accumulated over the course of an exposure. The readout signal from each pixel can then be converted to the number of electrons hitting the pixel using a conversion factor. This requires calibration. Compared to counting mode, integrating mode suffers from a loss in DQE but does not require the same extensive setup or long exposure times to ensure that individual electron events can be counted individually.[174]

While the Glacios is equipped with both a Ceta-D and Falcon-IV detector, the Ceta-D camera was used for electron diffraction data collection in work presented in this thesis, instead of the Falcon-IV direct electron detector. This was because the Ceta-D was significantly less expensive than the Falcon-IV.

Additionally, the Falcon-IV was used for high resolution imaging in cryoEM. While the detector of the Falcon-IV is radiation hardened, hitting it with the direct beam, or even a particularly intense deflected beam could cause a decrease in the DQE of the impacted pixels. This may eventually lead to damage to the detector, and defective or dead pixels. This would negatively affect high resolution imaging work.
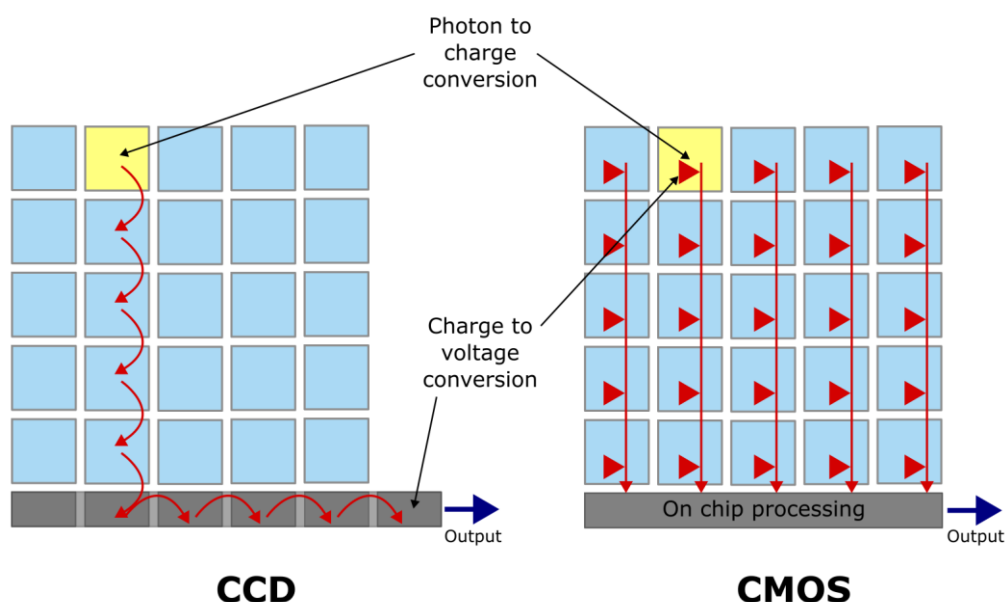
Figure 2.10. The architecture of a CCD detector (left) and a CMOS detector (right). In both devices, the electrons have been previously converted into photons by a scintillator (not pictured). In a CCD device, the photons are then converted to a charge and the charge from each pixel is transferred from pixel to pixel row by row to an output node where the charge to voltage conversion occurs. In a CMOS device, both the photon to charge conversion and the charge to voltage conversion occur in each pixel individually and full rows of pixels are then read out simultaneously. The yellow pixel marks where an electron hits.

Most 3DED studies are performed using CMOS detectors due to their fast readouts, high sensitivity, wide availability, and relative low cost. Data have however also been collected on hybrid pixel detectors[60,63,67,126,127,175] and direct electron detectors[174,176].

2.2 Microscope alignments for 3DED data collection

Exposing crystals to the electron beam in a TEM, exposes them to radiation damage. This damage can accumulate, reducing the crystal's diffraction quality and eventually destroying it. In order to collect 3DED data, the electron flux (the flow of electrons per unit area) should be minimised, while still allowing a sufficient signal to noise ratio such that diffraction peaks can be identified, and electron diffraction patterns can be processed. The TEM can be set up in such a way to minimise how many

electrons are able to pass through the column and impact upon the sample. This will be discussed further here, and the specific set up used to collect data for this thesis will be explained.

2.2.1 Gun lens

By altering the strength of the gun lens, and using a C2 aperture, the amount of electrons incident on the sample can be reduced. Increasing the gun lens causes the first crossover to occur higher in the column, as a result the cone of electrons is wider and more electrons are blocked by the C2 aperture, reducing the electrons in the column. Schematic ray diagrams illustrating this are given in **Figure 2.11**. A 30 µm C2 aperture was used when collecting diffraction data.
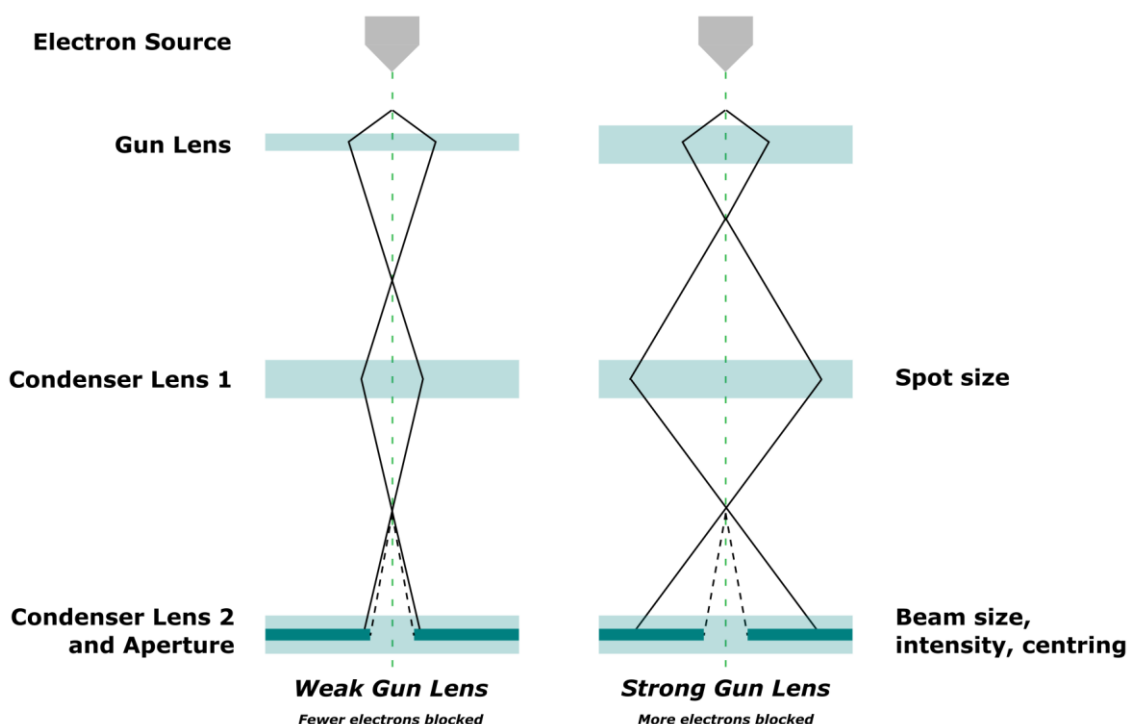
Figure 2.11. Schematic ray diagrams demonstrating weak gun lens (left) and strong gun lens (right). Increasing strength of the gun lens causes the first crossover to occur higher in the column, as a result the cone of electrons is widened, and fewer electrons pass through the condenser lens aperture. The black dashed lines represent the electrons able to pass through the aperture. A higher proportion of the total electrons are able to pass through the aperture when the gun lens is weak.

2.2.2 Spot size

Condenser lens 1 (C1 lens) controls the spot size, i.e., the minimum diameter of the beam incident upon the sample. As with the gun lens, changing the strength of the C1 lens, alters the height at which

crossover occurs and hence how many electrons are able to pass through the 30 μm C2 aperture (**Figure 2.12**). The Glacios is aligned at the highest possible spot size, spot size 11, for 3DED experiments to minimise the electron flux on the sample.
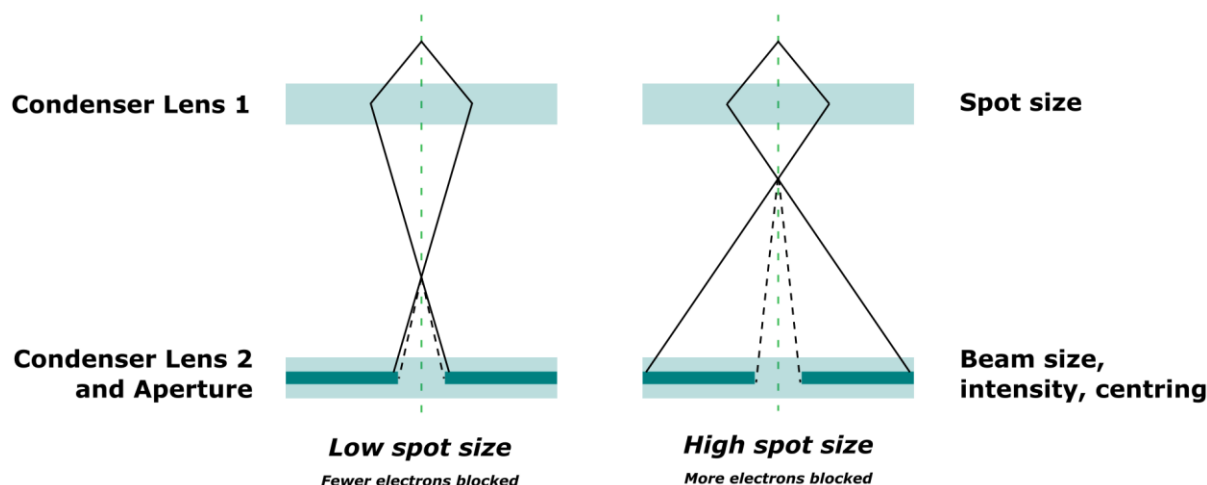
Figure 2.12. Schematic ray diagrams demonstrating low spot size (left) and high spot size (right). *Increasing the strength of the C1 lens (increasing spot size) causes the crossover to be higher, as a result the cone of electrons is widened, and fewer electrons pass through the condenser lens aperture. The black dashed lines represent the electrons able to pass through the aperture. A higher proportion of the total electrons are able to pass through the aperture when the C1 lens is weak (low spot size).*

2.2.3   Microprobe and nanoprobe mode

Electron diffraction data can be collected using multiple collection modes. The collection modes used in this body of work were selected area electron diffraction and nanobeam electron diffraction. In both of these modes, the electron beam is parallel on incident with the sample. All data were collected using nanobeam electron diffraction, with the exception of the σ-alkane and diene complexes in **Chapter 4**, which utilised selected area electron diffraction. The difference between these collection modes will be explained here. Selected area electron diffraction typically employs microprobe mode, generating a large illuminated area at parallel illumination, and a selected area aperture is inserted post sample. Nanobeam electron diffraction uses nanoprobe mode, this results in a smaller illuminated area on the sample compared to microprobe mode. Whether the microscope is operating in microprobe or nanoprobe mode is controlled by a single lens; the mini-condenser lens. The polarity of this lens is reversed to change between the two modes, i.e., the mini condenser lens is turned on in microprobe mode and turned off in nanoprobe mode. Schematic ray diagrams showing the difference between these microscope configurations are shown in **Figure 2.13**.
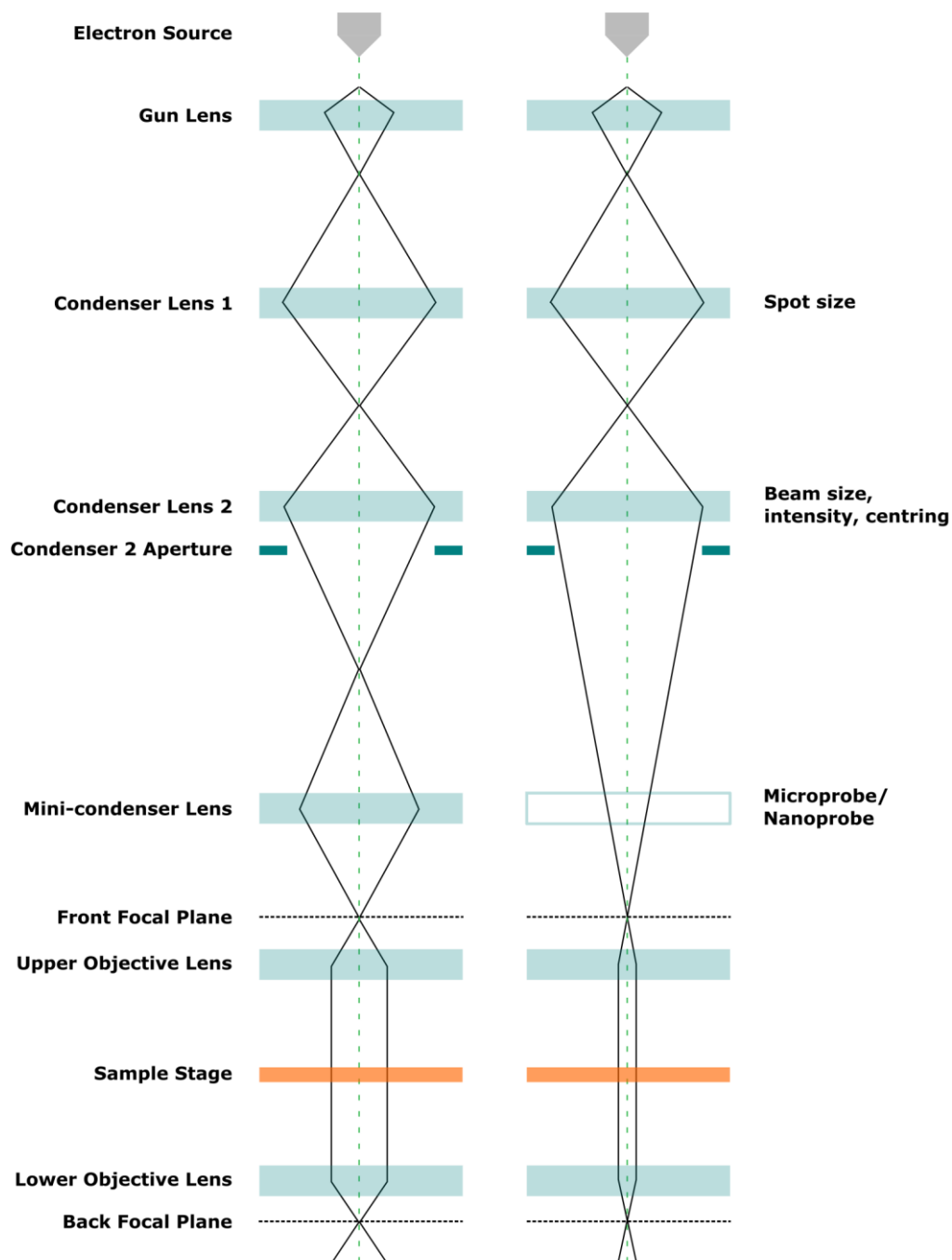
Figure 2.13. Schematic ray diagrams of microprobe mode (left) and nanoprobe mode (right). Microprobe/nanoprobe mode is controlled by the mini-condenser lens. The mini-condenser lens is switched on in microprobe mode (left, indicated by full blue box), and is switched off in nanoprobe mode (right, indicated by empty blue box). This results in a smaller illuminated area on the sample stage using nanoprobe mode.

In selected area electron diffraction, microprobe mode is typically used, and the electron beam needs to be spread over a relatively large area to achieve parallel illumination on the sample. This means a relatively large area is illuminated while diffraction data are recorded. The diameter of the illuminated

area in our selected area electron diffraction was 4 μm (**Chapter 9**). Generally, the target crystal is much smaller than the illuminated area and is suspended on a layer of carbon film. As a result, the signal to noise ratio without a selected area aperture is poor. A selected area aperture can be inserted post sample to reduce the area from which diffraction is recorded. When a selected area aperture is inserted, the overall signal is reduced however, the signal to noise ratio improves as there is no longer (or less of) a contribution from the carbon film. Additionally, insertion of a selected area aperture prevents diffraction being recorded from other diffracting species in the illuminated area that are not the target crystal.

With nanobeam electron diffraction, nanoprobe mode is utilised, the electron beam is spread over a much smaller area to achieve parallel illumination. As such, a selected area aperture is not required. Nanoprobe mode makes the beam smaller, while still having the same current as in microprobe mode. This means that the sample experiences a greater electron flux. This would be unsuitable for collecting electron diffraction data as the target crystals would be exposed to more radiation, causing damage, and rapidly reducing diffraction quality. To combat the higher flux, the strength of the gun lens is increased, causing more electrons to be blocked by the C2 aperture, as explained in **Section 2.2.1**. Increasing the strength of the gun lens from gun lens 4 to gun lens 8 reduces the electrons in the column by approximately half.

Further details on the specific conditions used for data collection are given in the methodology chapter, **Chapter 9, Section 9.2.3**.

3 Introduction to Electron Diffraction and Crystallography

3.1 Crystallography

3.1.1 Crystal symmetry

A crystal is a periodic solid structure comprised of a repeating arrangement of atoms in three dimensions. A unit cell is the smallest and simplest repeating group of atoms within a crystal, from which the entire crystal lattice can be described by translating this unit in all three dimensions. The unit cell is defined by the length of its three axes (a, b, c) and the angles (α, β, γ) between them. In order to describe a crystal structure, information on the contents of the unit cell and the symmetry of the crystal are required. A crystal can be described in terms of its crystal system, Bravais lattice, point group and space group.

By imposing rotational symmetry on the crystal lattice (in addition to the translational symmetry inherent to the unit cell), 7 crystal systems are generated for 3D crystals. These are: triclinic, monoclinic, orthorhombic, tetragonal, trigonal, hexagonal, and cubic. The crystal systems are classified on the basis of the unit cell lengths, angles, and the direction of the symmetry axis. See **Table 3.1**. Combining the 7 crystal systems with lattice centring generates 14 possible lattice types, known as Bravais lattices (**Table 3.2**).

Table 3.1. The 7 crystal systems with their characteristic symmetry and unit cell parameters.

Crystal System	Characteristic Symmetry	Unit-Cell Parameters
Triclinic	1× 1-fold	$a \neq b \neq c$; $\alpha \neq \beta \neq \gamma$
Monoclinic	1× 2-fold	$a \neq b \neq c$; $\alpha = \gamma = 90°$; $\beta \neq 90°$
Orthorhombic	3× 2-fold	$a \neq b \neq c$; $\alpha = \beta = \gamma = 90°$
Tetragonal	1× 4-fold	$a = b \neq c$; $\alpha = \beta = \gamma = 90°$
Trigonal	1× 3-fold	$a = b \neq c$; $\alpha = \beta = 90°$; $\gamma = 120°$ or $a = b = c$; $\alpha = \beta = \gamma \neq 90°$
Hexagonal	1× 6-fold	$a = b \neq c$; $\alpha = \beta = 90°$; $\gamma = 120°$
Cubic	4× 3-fold	$a = b = c$; $\alpha = \beta = \gamma = 90°$

Nº	Crystal System	Lattice Centring	Lattice Symbol
1	Triclinic	P	aP
2	Monoclinic	P	mP
3	Monoclinic	C	mC
4	Orthorhombic	P	oP
5	Orthorhombic	C	oC
6	Orthorhombic	F	oF
7	Orthorhombic	I	oI
8	Tetragonal	P	tP
9	Tetragonal	I	tI
10	Trigonal	R	hR
11	Hexagonal & Trigonal	P	hP
12	Cubic	P	cP
13	Cubic	F	cF
14	Cubic	I	cI

There are only 32 distinct combinations of symmetry operations, these leads to the 32 crystallographic point groups. A point group is a mathematical concept defined by which symmetry operation can be applied to a crystal and leave it unchanged, i.e., without any apparent change to the position of the atoms within a crystal. A symmetry operation is the movement of a molecule that results in the molecule appearing the same as it did prior to the movement. Symmetry operations include identity, rotation, reflection, and inversion. The point groups can be represented by symbols that are comprised of numbers and letters. A point group symbol with a number present has a rotational axis, the number refers to how many folds the rotation axis has (1, 2, 3, 4, or 6). Inversion axes are denoted with the symbol "-". m stands for mirror plane. A point group with a "/" before m, represents a mirror plane that is perpendicular to the main rotation axes. The 32 crystallographic point groups are shown in **Table 3.3**.

Table 3.3. The crystallographic point groups.

Crystal System	32 Crystallographic Point Groups						
Triclinic	1	-1					
Monoclinic	2	m	2/m				
Orthorhombic	222	mm2	mmm				
Tetragonal	4	-4	4/m	422	4mm	-42m	4/mmm
Trigonal	3	-3	32	3m	-3m		
Hexagonal	6	-6	6/m	622	6mm	-62m	6/mmm
Cubic	23	m-3	432	-43m	m-3m		

There are 230 possible space groups. Space group symmetry combines the translation symmetry of the lattice with additional symmetry elements. A symmetry element describes the location at which a symmetry operation is applied, such as a point, axis, or plane. The symmetry elements that exist in crystalline structures are: mirror planes, glide planes, rotation axes, screw axes, inversion centres, and their combinations. For simplicity, a table showing all 230 space groups is not given. If the space group symmetry is known, describing the full contents of the unit cell is unnecessary, as the full contents can be inferred by applying symmetry operators. This reduces the information required to fully characterise the contents of the unit cell to the asymmetric unit (ASU).

3.1.2   Bragg's law

When electrons (or X-rays) of fixed wavelength are incident on a crystalline sample, they can be scattered by the atoms within it. As crystals are comprised of repeating atomic motifs stacked on top of one another, the incident beam can be scattered by the Miller planes of atoms within the crystal lattice. This leads to constructive or destructive interference of the scattered waves (**Figure 3.2**). When Bragg's law, Equation (3.1), is satisfied,[5] constructive interference of the scattered waves from successive planes of atoms occurs (**Figure 3.1**). This leads to an intense diffracted beam being registered by the detector as a Bragg reflection.

$$n\lambda = 2d \sin \theta$$

(3.1)

$Where$:

$n =$ integer number of wavelengths

$\lambda =$ wavelength of the incident beam

$d =$ lattice spacing

$\theta =$ half the scattering angle
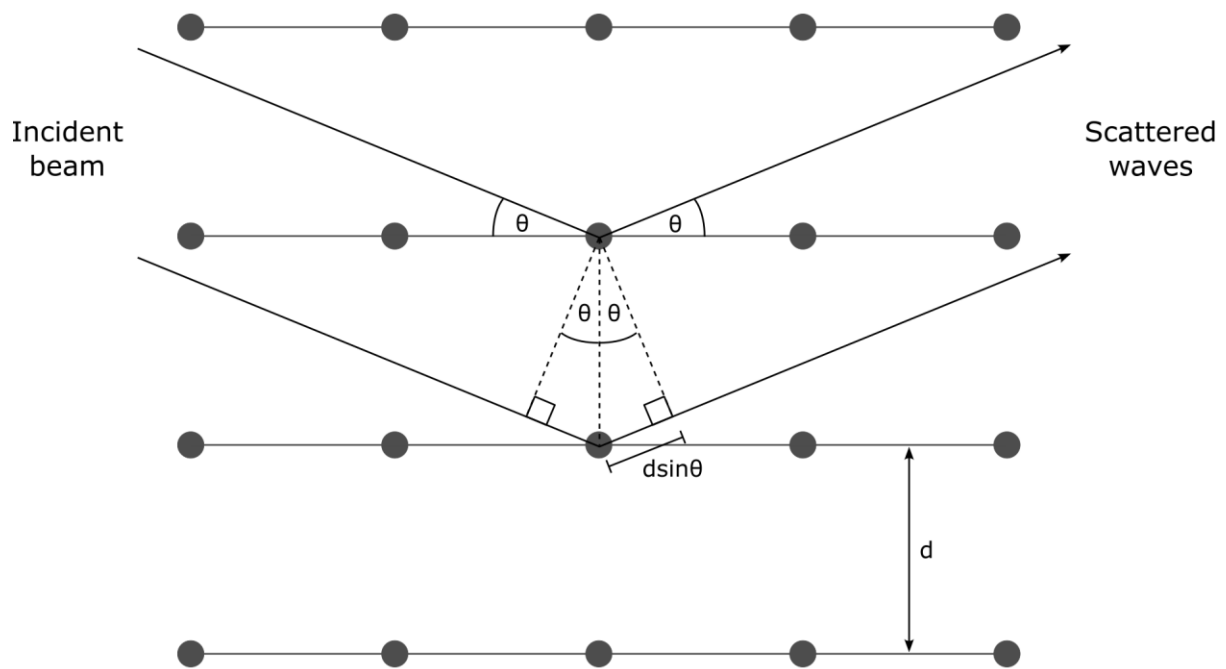
Figure 3.1. Origin of Bragg's law. *Electrons or X-rays are scattered by atoms within the crystal lattice with a scattering angle of 2ϑ. This is the angle between the incident beam and scattered waves. Constructive interference of the scattered waves occurs when the difference in path length between the scattered waves is equal to an integer number of wavelengths. This leads to the derivation of Braggs law: nλ=2d sinϑ.*
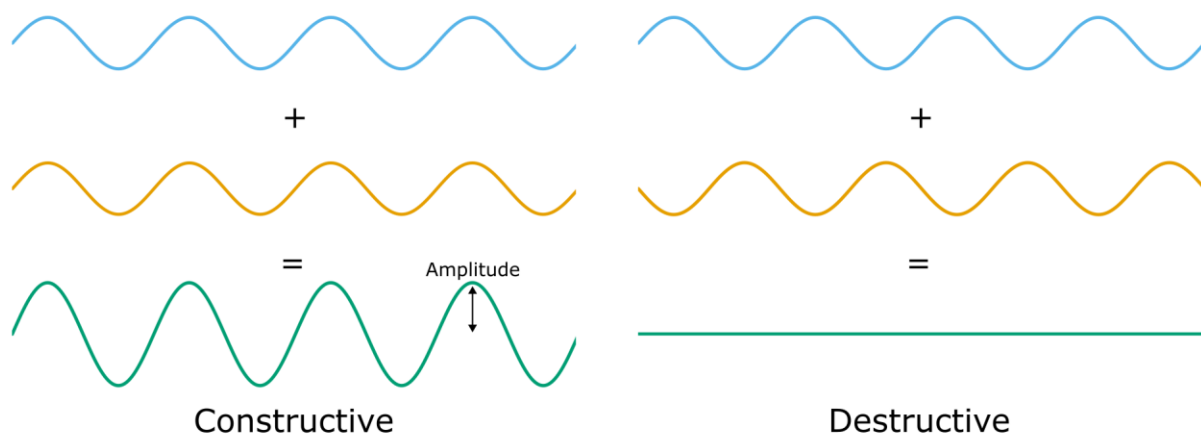
Figure 3.2. Constructive and destructive interference. *In constructive interference (left), the waves are in phase and the amplitudes add together, the resulting wave is the sum of the waves. The amplitude of the wave is indicated by a black arrow. In destructive interference (right), the waves are out of phase and the amplitudes cancel out completely.*

In diffraction experiments, the wavelength of the incident electrons (or X-rays) is known, and the intensity of the scattered waves are measured while the crystal is rotated. When the reciprocal lattice and the Ewald sphere intersect (**see 3.1.3**), this gives rise to a diffraction pattern which can be recorded by a detector. A diffraction pattern is a pattern of regularly spaced spots (reflections) that

results from the constructive interference of scattered waves. A reciprocal lattice is related to the real space lattice of the crystal by the Fourier transform, i.e., reciprocal space is the Fourier transform of real space. As the crystal rotates, different planes of atoms will satisfy the Bragg condition and generate Bragg peaks. Diffraction patterns recorded at different rotations can be combined together to generate a 3D model of reciprocal space.

A diffraction pattern contains information about the intensity of the scattered radiation however, phase information of the diffracted wave is lost. This is known as the phase problem. The phase information needs to be reconstructed in order to determine the structure of the crystal. This will be discussed in **Section 3.3**. Using a kinematical approximation, where electrons or X-rays are scattered elastically only once, the intensity of the diffracted beam is proportional to the structure factor amplitude:

$$|F_{hkl}| \propto \sqrt{I_{hkl}}$$

(3.2)

$Where$:

F_{hkl} = structure factor

I_{hkl} = intensities

The structure factor is a mathematical function that describes both the amplitude and phase of the diffracted wave, scattered by crystal lattice planes with Miller Indices: h, k, l. The structure factors will be explored in more detail in **Section 3.3.2**.

3.1.3   The Ewald sphere

Bragg's law can be represented in reciprocal space using an Ewald sphere construction. The Ewald sphere is a representation in reciprocal space of all the reflections that satisfy Bragg's law. When a reflection lies on the Ewald sphere it meets the Bragg condition and will be excited. The concept of the Ewald sphere was formulated by Paul Peter Ewald.[177] The radius of the Ewald sphere is $1/\lambda$, where λ is equal to the wavelength of radiation used. For simplicity, the Ewald sphere is often represented two-dimensionally as a circle. Bragg's law is satisfied when the incident beam vector $|k_I|$ is equal to the diffracted wave vector $|k_D|$ (**Figure 3.3**). By trigonometry, the reciprocal lattice vector, $1/d_{hkl}$ is equal to $2sin\theta/\lambda$, which can be rearranged to give Bragg's law. As the crystal rotates, different reflections intersect the Ewald sphere and are excited.
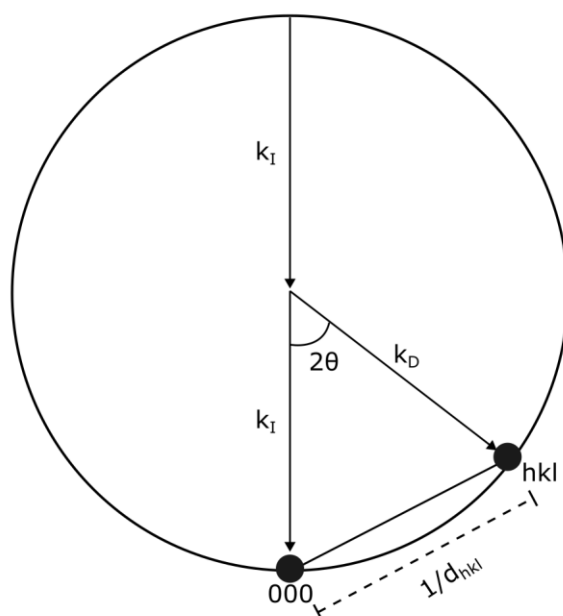
Figure 3.3. The Ewald sphere. *The radius of the sphere is 1/λ. Bragg's law is satisfied when the incident beam vector $|k_I|$ and the diffracted wave vector $|k_D|$ are equal. Bragg's law can be derived by setting the reciprocal lattice vector $1/d_{hkl}$ equal to $2\sin\theta/\lambda$.*

3.2 Electrons versus X-rays

The elucidation of crystal structures is of critical importance in chemistry. X-ray crystallography is the gold standard for structure determination of small molecules. Unfortunately, obtaining crystals of sufficient size and quality for single crystal X-ray diffraction can be prohibitively difficult. For synchrotron sources, the size requirement for crystals is that they need to have a minimum volume of 5x5x5 μm^3.[67] For laboratory sources, the crystal size requirement increases and a minimum crystal side length of at least 50 μm is required.[67] PXRD can be used in characterisation of crystalline powders. This technique has a reduced crystal size requirement, in that crystals of only 10s to 100s of nanometres are required.[43] However, as a structural determination technique, PXRD is limited due to the fact that the diffraction data are compressed into one-dimension. In a crystalline powder, the crystals lay in different orientations. Instead of seeing individual peaks, the reflections from many crystals form a continuous circle. In some instances, these circles are in close proximity and overlap. This is known as peak overlap. Extracting information and intensities from the overlapping peaks is complicated. As such, PXRD is typically used for identification of known samples due to its distinctive "fingerprint" region or in qualitative analysis. An alternate technique that has a low crystal size requirement is small-molecule serial femtosecond crystallography using an X-ray Free-Electron Laser (XFEL). XFELs produce a high-flux X-ray beam with an ultrashort duration. A crystal is hit with the high-

flux beam and a diffraction pattern is recorded before radiation damage occurs. Individual snapshots from many crystals are needed in order to obtain a complete dataset. This technique not only requires a large quantity of sample, which may be prohibitive or impossible to produce, but also access to XFEL facilities which can be particularly expensive and difficult to acquire time on. Additionally, indexing small molecule diffraction patterns from individual still images is non-trivial process.

Electrons provide an alternative means of structure determination from crystals on the nanometre to sub-micrometre size range. Electrons interact strongly with matter, they are negatively charged particles that interact with the electrostatic potential of molecules, i.e., the negatively charged electron clouds and positively charged atomic nuclei (protons). Generating high energy electrons for diffraction experiments does not require specialised large scale facilities such as synchrotrons or XFELs. Electrons can be generated using TEMs. Comparatively, TEMs are easier to access and also have a much lower cost compared to synchrotron sources or XFELs.

3.2.1   Scattering events

3.2.1.1   Radiation damage per elastic scattering event

The size requirement for crystals from X-ray diffraction experiments is determined by radiation damage. X-rays can be scattered either elastically or inelastically. X-ray photons that are elastically scattered give the high resolution information needed to determine the crystal structure. During an elastic scattering event, the energy of the X-ray photon is unchanged, but the X-ray is scattered at an angle of 2θ. Unfortunately, for every useful elastic scattering event that occurs, there are additional inelastic interactions taking place that cause radiation damage. In an inelastic scattering event, the X-ray photon is absorbed, and its energy is deposited in the sample. With 12 keV X-rays (λ = 1.0332 Å), elastic scattering only occurs once in every 20 scattering events, this results in an approximately 200 keV radiation damage per every useful elastic scattering event.[109,178,179] These metrics are based on hydrated protein crystals.

The interaction of electrons with matter is markedly different to X-rays. Elastic scattering of electrons is typically localised on the positively charged nuclei, with a negligible loss in the energy of the electron. Electrons are scattered inelastically by the electron clouds. During an inelastic event, 40 eV are deposited on average, there is a small change in the scattering angle of inelastically scattered electrons, however this is much smaller than the scattering angle of elastically scattered electrons.[180]

With electrons of 200 keV energy (λ = 0.02508 Å), it is expected that elastic scattering should occur once in every 5 scattering events. The collateral damage per useful elastic scattering event is therefore only 200 eV.[178] This is three orders of magnitude less damaging than X-rays. Once again, these figures pertain to protein crystals. As fewer damaging interactions occur with electrons compared to X-rays, and because these interactions deposit less energy into the sample, diffraction data can be collected from much smaller crystals (on the nanometre to sub-micrometre range).

An important caveat here is that although electrons are less damaging than X-rays, radiation damage still occurs. This damage is particularly noticeable the smaller the crystal.[178] Data collection conditions need to be optimised to ensure as much data as possible is collected before diffraction quality reduces due to radiation damage. Another way in which radiation damage is minimised is by maintaining a low temperature (80 K) during data collection.

3.2.1.2   Inelastic and multiple scattering events

When X-rays are inelastically scattered, they are absorbed by the sample and do not reach the detector. This is not the case for inelastically scattered electrons. Inelastically scattered electrons continue to pass through the sample and can be detected. Additionally, as electrons are efficient scatterers, they will likely undergo multiple scattering events as they pass through the crystal. The probability of multiple scattering increases with increasing sample thickness. The electrons can be scattered either elastically or inelastically during multiple scattering events, meaning a single electron could be scattered both elastically and inelastically. Electrons that have been scattered inelastically and then elastically contribute to the radially symmetric ring of diffuse background scattering in diffraction patterns. This negatively impacts the signal to noise ratio of Bragg peaks. Diffuse scattering from a crystal can be seen in **Figure 3.4**. This diffraction pattern comes from a thick organometallic crystal. This diffraction pattern was recorded during early 3DED experiments at York before the data collection conditions had been optimised.
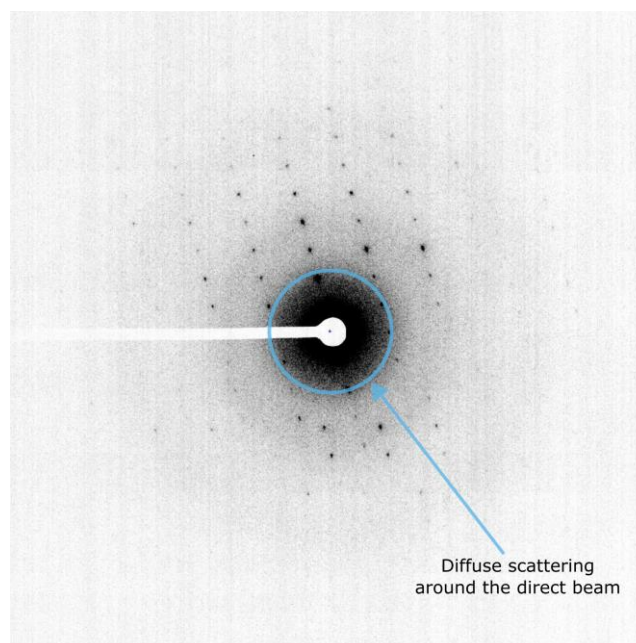
Figure 3.4. A diffraction pattern from an organometallic crystal showing diffuse scattering in addition to Bragg reflections. *This is caused by electrons that have been scattered multiple times, first inelastically and then elastically. The diffuse scattering is centred around the direct beam and is radially symmetric. The additional rings visible are likely due to scattering from the carbon film.*

As electrons that are inelastically scattered lose energy, they can be removed using an energy filter. An energy filter is comprised of a magnetic prism. As electrons of different energy pass through the magnetic field generated by the energy filter, electrons of different energies are accelerated at different rates and are therefore deflected differently. An adjustable slit can be inserted, such that only electrons with a given energy pass through the filter. Electrons that have lost energy during inelastic scattering events can be excluded and prevented from reaching the detector. The Glacios at York is not currently equipped with an energy filter, as such care should be taken to select thin crystals to minimise multiple scattering events.

3.2.1.3   Dynamical scattering

Electrons can also be scattered elastically multiple times; this is known as dynamical diffraction. In X-ray crystallography, kinematical scattering is the norm, where the X-rays are only elastically scatted once. With electrons on the other hand, the electrons can be elastically scattered multiple times as they pass through the sample. The probability of an electron being dynamically scattered is dependent on sample thickness, sample composition, accelerating voltage of the microscope and how the crystal is aligned with the beam (i.e., if the beam is aligned with a zone-axis).[180] The multiply elastically

scattered electrons experience no loss in energy due to these multiple events and the position of the Bragg peaks remains unchanged. However, the intensities of the Bragg peaks are affected. This is due to redistribution of the intensities. When an electron is elastically scattered by an atom, the point at which it was scattered acts as a secondary direct beam position from which further elastic scattering events can occur. This leads to the intensities of Bragg peaks in a diffraction pattern all appearing to be similar to one another. The intensity of weak peaks become more intense, and the strong peaks become less intense.[23,24] This effect is particularly pronounced when the beam is aligned with the zone-axes and many reflections are excited simultaneously.[23,43] As such, the kinematical approximation for the linear relationship between the squared structure factor amplitudes and intensities ($|F_{hkl}| \propto \sqrt{I_{hkl}}$), Equation (3.2) no longer holds true in the presence of dynamical scattering.[126] The intensities of weak reflections are overestimated as a result.[126] Additionally, due to dynamical scattering, reflections that are symmetry forbidden because of screw axes or glide planes can appear in diffraction patterns.[16,28–30] As a result of dynamical diffraction, performing symmetry determination, structure solution and structure refinement can become challenging.[44]

Dynamical theory can be used to perform dynamical refinement of electron diffraction data. This calculates the diffracted intensities, while considering dynamical scattering. Previous dynamical refinement approaches focused on precession-assisted 3DED.[56,181] A protocol for the dynamical refinement of continuous rotation 3DED data now exists.[182] Using dynamical refinement significantly improves results (decreased R_1 values) and can even be used to better locate weak scatterers such as hydrogen atoms and to determine absolute configuration.[182]

For work presented in this thesis, dynamical refinement was not performed, and standard approaches using the kinematical approximation were used instead. This was because procedures for dynamical refinement of continuous rotation 3DED data were still in progress at the time work was carried out,[182] specialised data processing software (PETS2[183] and JANA[184]) were required, and dynamical refinement was computationally expensive. Despite not performing dynamical refinement, it was still possible to determine and refine small molecule structures by selecting thin crystals from which to collect data, thus minimising the effect of dynamical scattering.

3.2.2 The Ewald sphere

Electrons have a much shorter wavelength than X-rays. The wavelength of electrons at 200 keV is 0.02508 Å, compared to X-rays generated from Cu K-α which has a wavelength of 1.5406 Å. As the wavelength of electrons is much shorter, the radius of the Ewald sphere ($1/\lambda$) becomes exceptionally large and appears to be almost flat. **Figure 3.5** shows the difference between the Ewald spheres of Cu K-α X-rays and 200 keV electrons interacting with the same reciprocal lattice. As the Ewald sphere of electrons is so flat, many reflections can be excited at once.
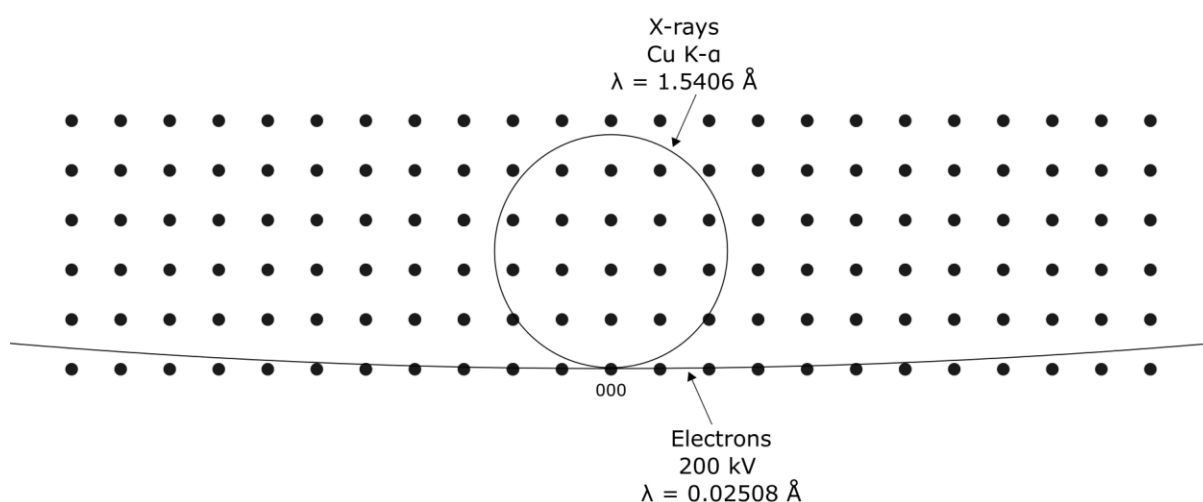
Figure 3.5. The Ewald spheres of 200 keV electrons and Cu K-α X-rays interacting with the same reciprocal lattice. The radius of the Ewald sphere for electrons is over 60 times larger than the radius of the Ewald sphere for X-rays, as such only a small portion of the electron Ewald sphere is shown. For simplicity, the Ewald sphere for electrons and X-rays have different origins, this is so they can both be represented in a single figure.

A consequence of the flatness of the Ewald sphere is that a single electron diffraction pattern can typically only give information on two of the three unit cell dimensions. Information on the reciprocal lattice in the direction of the incident beam is missing, as can be seen in **Figure 3.5**. As such, multiple electron diffraction patterns, collected as the crystal is rotated are required to determine the full unit cell parameters. This is unlike X-ray diffraction patterns, from which all unit cell dimensions can usually be determined from a single pattern. An illustration of a crystal lattice rotating and new reflections meeting the Bragg condition is given in **Figure 3.6**.
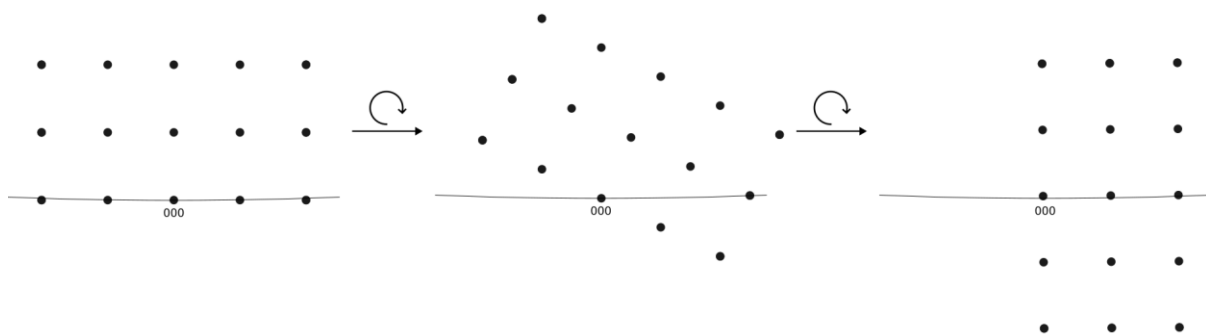
Figure 3.6. Illustration showing a crystal lattice rotating in a static beam. *As the crystal rotates, new reflections intersect the Ewald sphere and are excited.*

3.3   Structure determination

The data processing workflow is described in the Methods Chapter (**Chapter 9**). Data processing generates the unit cell parameters, determines the space group, and integrates and scales the intensity of the reflections. The scaled, unmerged data can then be supplied for structure determination.

3.3.1   Atomic scattering factors

The atomic scattering factor describes the scattering power of an individual atom. It is dependent on the source of radiation used. For X-rays, the scattering factor is a Fourier transform of the electron density of an atom. For electrons, the scattering factor is a Fourier transform of the electrostatic potential of an atom. Electron scattering factors can be calculated from X-ray form factors using the Mott-Bethe formula. Electron atomic scattering factors can be represented by the following equation:[185]

$$f^e(s) = \frac{m_0\,e^2}{8\pi^2\hbar^2}\frac{[Z - f^x(s)]}{s^2}$$

(3.3)

$Where$:

$m_0 =$ mass of electron

$e =$ charge on electron

$\hbar = h/2\pi$

$Z =$ atomic number

$f^x(s) =$ X-ray atomic scattering factor

$s = sin\theta/\lambda$

3.3.2 Structure factor

Each atom has an individual atomic scattering factor. A crystal is made up of various atoms in a periodic arrangement. Each of these atoms can scatter electrons. The structure factor results from all of the scattered waves diffracted by all of the atoms within the unit cell. The structure factor is described as:

$$F(hkl) = \sum_{j=1}^{N} f_j(hkl)\, e^{2\pi i \left(hx_j + ky_j + lz_j\right)} \qquad (3.4)$$

$Where$:

$N =$ number of atoms in the unit cell

$f_j(hkl) =$ atomic scattering factor of the jth atom

$x_j + y_j + z_j =$ fractional coordinates of the jth atom

3.3.3 Electrostatic potential

As aforementioned (**Section 3.1.2**), phase information is lost during diffraction experiments. This is known as the phase problem. In order to reconstruct the electrostatic potential $\varphi(xyz)$ and thus solve the crystal structure, both the structure factor amplitudes $|F(hkl)|$ and the phases $\phi(hkl)$ are required. The amplitudes and phases of all the individual structure factors for all the reflections hkl are required in order to construct the full electrostatic potential map of the crystal. The electrostatic scattering potential $\varphi(xyz)$ of a crystal can be described by a summation of cosine wave functions:[186]

$$\varphi(xyz) = \frac{\lambda}{\sigma\Omega}\left[\sum_{hkl} |F(hkl)|\, cos[2\pi(hx + ky + lz) - \phi(hkl)]\right] \qquad (3.5)$$

$Where$:

$\lambda =$ wavelength of radiation

$\sigma = \frac{2\pi m e \lambda}{h^2} =$ interaction constant

$\Omega =$ unit cell volume

$|F(hkl)| =$ structure factor amplitude

$\phi(hkl) =$ structure factor phase

The structure factor amplitudes are proportional to the intensities of the reflections, Equation (3.2). Unfortunately, the structure factor phases are lost and need to be retrieved through phase retrieval.

3.3.4   Structure determination using SHELXT

To determine the phases, several approaches can be applied. In this body of work, direct methods have been used, specifically the program SHELXT[164] which utilises a dual-space algorithm. SHELXT reads the unit cell, Laue group and expected elemental composition from the supplied .ins file.[164] Command line switches can be applied to aid structure determination. For the organometallic molecules studied in this body of work, the switches `-a` `-y` `-m500` have typically been applied.

`-a` ensures the program tests all space groups in the specified Laue group. `-m500` forces the program to run 500 macrocycles for each dual-space iteration. `-y` is useful for dealing with organometallic compounds, particularly with incomplete data, as it focuses on the CHEM, (chemical figure of merit) rather than R_{weak} in the CFOM (combined figure of merit) calculation.[164] The default CFOM calculation is:

$$CFOM = 0.01CC - XR_{weak} \qquad\qquad (3.6)$$

Where, $X = 1.0$ unless otherwise specified

When `-y` is specified, this calculation is used instead:

$$CFOM = 0.01CC * CHEM \qquad\qquad (3.7)$$

This favours the generation of solutions where peaks in the map are at distances and angles from each other that are chemically feasible for the placement of organic atoms in organic molecules. CHEM is the fraction of peaks at distances $1.1 - 1.8$ Å away from one another whose vectors have defined bond angles between 95 and 135°.[187] It is not helpful for inorganics because these bond lengths and distances are much less constrained.

3.3.4.1   Dual-space recycling

Dual-space methods reconstruct the phases of the structure factors by iteratively modifying the phases in reciprocal space and the electrostatic potential in real space.[164] The starting point can be either random phases or a Patterson superposition minimum function. By default, the Patterson function is the starting point. Two copies of the Patterson function are superimposed upon each other,

displaced by a Patterson vector. This results in a map that can be used as the initial electrostatic potential map.

The Patterson function removes the term containing the phases from the electrostatic potential calculation and the structure factor amplitudes are replaced by their squares. As such, the Patterson function does not show the atomic positions but instead a map of the interatomic vectors, or the positions of the atoms relative to one another. The height of the peaks is proportional to the scattering from the atom. Patterson methods are particularly useful when heavy atoms are present.

The initial electrostatic potential map (Patterson superposition) can then be Fourier transformed to obtain initial phases ϕ_c and structure factors G_c. The structure factors are then modified G_o. The calculated structure factors G_c and the modified observed structure factors G_o are compared and a new electrostatic potential map φ is generated by Fourier transform. A mask is then applied and new phases ϕ_c and structure factors G_c are generated. This process is repeated until the desired number of iterations is reached. A schematic showing how dual-space recycling works is given in **Figure 3.7**
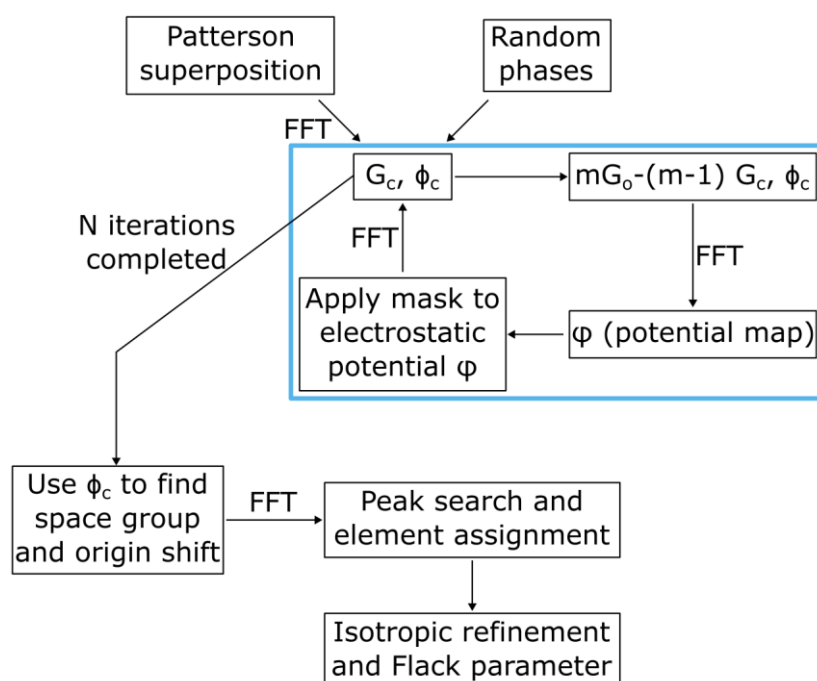
Figure 3.7. Flow chart summarising the SHELXT dual-space structure solution for electron diffraction data.[164] *Dual space recycling is indicated by the blue box. FFT = Fast Fourier Transform, G_c= Calculated structure factors, G_o= modified observed structure factors, ϕ_c= phase of G_c, m=figure of merit. Space group assignment and isotropic refinement are run in parallel. This figure is adapted from Sheldrick 2015.*[164]

3.4 Structure refinement

Structure refinement is a mathematical process by which the differences between the experimental observations and their calculated equivalents are minimised. Specifically, the differences between the observed and calculated structure factors, and the differences between the ideal and real geometry. For small molecule data, geometrical restraints are not always required, unlike in macromolecular crystallography where geometrical restraints are almost always used. This is because there are few atoms in the unit cell of small molecule crystals and thus more observations per atom are made. Geometrical restraints for small molecule data may be required when the resolution of the dataset is limited, or parts of the model are not well defined due to disorder. In these instances, geometrical restraints may be required.

For every atom there are three coordinates to refine (x,y,z) and six atomic displacement parameters. This totals nine parameters to be refined for each atom. An additional parameter is the atom type, this is not refined during refinement. For refinement to be stable, there must be a sufficient data to parameter ratio. The data to parameter ratio should be higher than 7 for a structure containing atoms with Z less than 18,[188] and higher than 8 for structures containing heavy atoms with Z greater than 18.[189] For small molecule crystals that diffract to high resolution (better than 0.8 Å), there is usually surplus data. Constraints and restraints improve the data to parameter ratio. Constraints remove parameters and restraints add to the data.

3.4.1   Atomic scattering factors

Once the structure has been determined, it then needs to be refined. The process of structure refinement ensures the best fit of the model to the data. The first step of structure refinement is to supply the correct atomic scattering factors. Electrons and X-rays interact with matter differently, and therefore X-ray scattering factors are not representative of the interaction between electrons and matter. Eight parameter fits for electron atomic scattering factors from Peng 1999[190] were used in refinement of electron diffraction data in this thesis.

Gaussians can be summed together to make an analytical approximation of the electron atomic scattering factors.[191,192] Eight parameter fits are used as an approximation of the electron atomic

scattering factors $f^e(s)$, see Equation (3.3). Four Gaussians are summed together using the following approximation, where n=4:[190]

$$f^e(s) = \sum_{i=1}^{n} a_i exp(-b_i s^2)$$ (3.8)

$Where$:

$a_i \ and \ b_i$ = fitting parameters

$s = sin\theta/\lambda$

While 10 parameter fits have been tabulated for the electron atomic scattering factors for all neutral atoms,[193] crystallographic software originally designed for X-ray diffraction studies, generally only use 8 parameter fits to represent the scattering factors.

Presently, in our work, only neutral atom scattering factors are applied. However, it is known that electrons interact differently with charged atoms than with non-charged atoms of the same element. At low resolutions, this difference is marked, with cation scattering factors diverging to infinity and anion scattering factors diverging to negative infinity.[194,195] In future, scattering factors of charged ions could be considered but most refinement programmes are currently unable to model this divergence at low resolution. Additionally, atoms are placed individually into the refinement program and formal charges would need to be applied to each atom, which may not be an accurate representation of what is happening within the molecule. A more sensible way of dealing with partial charges is required. This is an exciting potential application of electron diffraction as, in future, it may also be possible to differentiate charge states using this technique.[196]

3.4.2   Anisotropic displacement parameters and restraints

The motion of atoms in small molecules is best described anisotropically, i.e., the thermal motion of each atom is different in all 3 dimensions. The thermal motion of the atoms during scattering and the static disorder of the crystal are described by anisotropic Atomic Displacement Parameters (ADPs). The ADPs are refined for all non-hydrogen atoms. ADP restraints may be used to help obtain a physically sensible model. The ADP restraints commonly applied in this thesis were: DELU, SIMU, ISOR. Each of these and their impact on the ADPs will be described here.

DELU is a rigid bond restraint that is applied to the ADPs along bonded 1,2-directions or 1,3 directions. It restrains the ADPs in the direction of the bond to be equal within an effective standard deviation. The DELU restraint is not often used here as it has been replaced by the enhanced rigid bond restraint, RIGU which generates 3 or 6 restraints as opposed to the 1 or 2 restraints generated by DELU.[197] The RIGU restraint was typically applied to all atoms in a molecule. It is a restraint that limits the relative motion of atoms connected by a rigid bond, so that the motion of the two atoms forming the bond are at right angles to the bond itself. This is a realistic descriptor of atomic motion. SIMU is another ADP restraint that sets U_{ij} components (essentially the ADPs) as equal for atoms that are spatially close. The SIMU restraint is often applied to 5- or 6-membered rings. The ISOR restraint forces the ADPs of specified atoms to become approximately isotropic. This restraint can be particularly helpful to prevent atoms from becoming non-positive-definite (NPD). A two-dimensional representation of how the ADP restraints affect the ADPs is given in **Figure 3.8**.
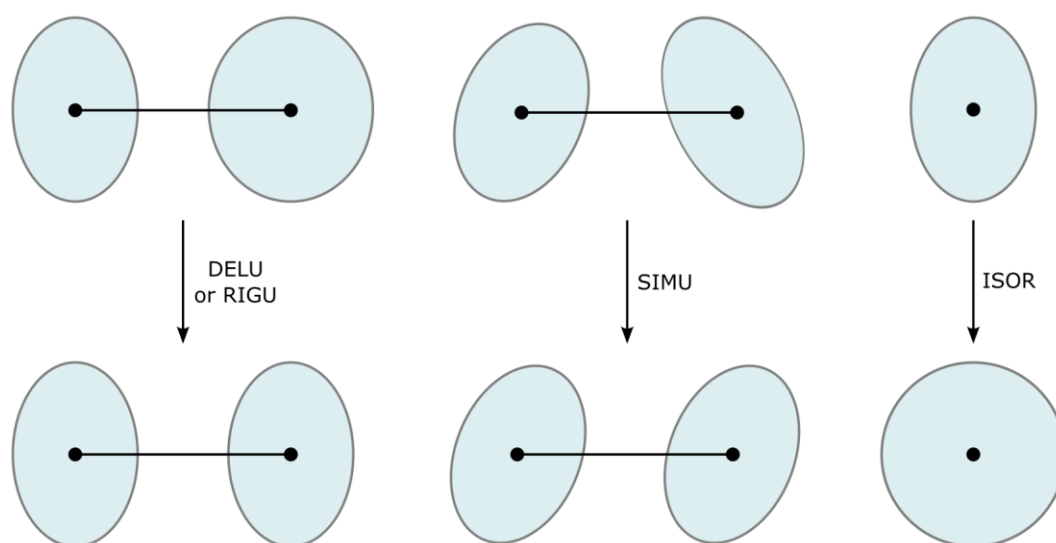
Figure 3.8. A two-dimensional schematic demonstrating how the application of DELU, RIGU, SIMU and ISOR restraints affects the anisotropic atomic displacement parameters. The blue ovals represent the ADPs, the black circles are the mean atomic positions, and the black lines represent bonds between atoms.

3.4.3 Geometric restraints

Additional restraints, which relate to the physical geometry of the model and not the ADPs may be applied if required. These are known as geometric restraints. In this body of work, the only geometric restraint utilised was SADI. SADI is a geometrical restraint which restrains the distance between the first and second named atoms to be equal to the distance between the third and fourth named atoms, and any subsequently named atom pairs. This restraint has been particularly useful when handling

complexes that have fluorous counter ions present, for example the complexes in **Chapter 4** which contain an S-BAr$^F_4$ anion.

3.4.4 Refinement of the extinction parameter

The EXTI instruction was used in refinement of all compounds presented in this thesis. This refines the extinction parameter x where F_C is multiplied by the following expression:

$$k\left[1 + \frac{0.001 * x * F_c^2 * \lambda^3}{sin(2\theta)}\right]^{-\frac{1}{4}} \tag{3.9}$$

Where:

$k = $ overall scale factor

$x = $ scattering factor

$F_c = $ calculated structure factor

$\lambda = $ wavelength

$2\theta = $ scattering angle

EXTI typically refines to large values for electron diffraction data, such that SHELXL will typically generate a warning: (** Warning: unusual EXTI or SWAT parameter **). As EXTI has a λ dependence, and the wavelength for electrons is much smaller than the wavelength of X-rays, this is unsurprising. Refinement of the EXTI parameter stops the ADPs refining to non-physical values by absorbing some of the systematic errors in the measured reflections.

The R$_1$ values for electron diffraction (15-30%)[66,198], are still much larger than those of X-ray diffraction which are typically less than 5%. The reason for this discrepancy is partially due to dynamical effects not being considered. Refinement of the EXTI parameter accounts for this somewhat, but it is not a robust method for doing so as the correction was not designed for this purpose. Dynamical refinement of continuous rotation electron diffraction data is possible,[182] but this is a computationally expensive process that currently requires specialist software, as such dynamical refinement has not been performed in this work.

3.4.5   R-factors and statistics

To evaluate the quality of the structural model, R-factors are used. During refinement, these R-factors should converge to a minimum. The most common statistic reported is R_1, this is often simply referred to as the R-factor. The term R_1 will be used throughout this thesis. The R_1 is a measure of how well the observed structure factors F_{obs} match the calculated structure factors F_{calc}. The structure factor is defined in Equation (3.4). R_1 is defined by the following equation:

$$R_1 = \frac{\sum ||F_{obs}| - |F_{calc}||}{\sum |F_{obs}|}$$

(3.10)

Where:

F_{obs} = observed structure factor

F_{calc} = calculated structure factor

R_1 values are often quoted as a percentage. As mentioned in the previous section, typical R_1 values for electron diffraction data are 15-30%,[66,198] this is much larger than the R_1 values of X-ray diffraction data. R_1 is an unweighted R-factor. R_1 values are typically quoted for all data and also for reflections with intensity greater than $2\sigma(I)$. This removes weak, poorly measured reflections from the calculation.

A weighted R-factor (wR_2) is generally also reported for all data. This considers the uncertainties of each reflection by using a weighting scheme. wR_2 is based on the squared structure factors F^2 and is defined as:

$$wR_2 = \sqrt{\frac{\sum w(|F_{obs}|^2 - |F_{calc}|^2)^2}{\sum w(|F_{obs}|^2)^2}}$$

(3.11)

Where:

w = weighting scheme

Additional measures of structure quality are reported in this thesis and are defined below. The goodness of fit (GooF) is a measure of how well the calculated model fits the observed data, taking into account the number of observed reflections and the number of parameters used in the refinement. SHELXL encourages adjustment of weighting scheme so that the GooF is equal to one. This is because unlike wR₂, the weighting scheme is only in the numerator of the GooF equation. If the value of GooF is significantly less than one, this suggests that sigmas of the measured data have been overestimated. If the value is significantly higher than one, this indicates that aspects of the structure may be missing or unmodelled.

$$GooF = \sqrt{\frac{\sum w(|F_{obs}|^2 - |F_{calc}|^2)^2}{n - p}} \qquad (3.12)$$

$Where$:

n = number of reflections

p = total number of parameters refined

R_{int} is a measure of whether the intensities of symmetry equivalent reflections are in fact equivalent. The value of R_{int} should be low. High values of R_{int} indicate poor quality data or incorrect space group assignment.

$$R_{int} = \frac{\sum ||F_{obs}|^2 - |F_{obs}|^2 (mean)|}{\sum |F_{obs}|^2} \qquad (3.13)$$

The residual potential is a measure of the most positive and most negative peaks in a map of $F_{obs} - F_{calc}, \phi_{calc}$. The largest differences are then reported as the highest peak and deepest hole. These map values are reported in unit of Å^{-2} and can be converted to units of electrostatic potential (e/Å) by multiplication by the value 3.32494.[199] Details on the origin of this conversion factor are described in **Chapter 9, Section 9.5**.

4 Characterisation of a σ-alkane complex via on-grid solid/gas single-crystal to single crystal reactivity

The structure of the diene complex [Rh(Cy$_2$PCH$_2$CH$_2$PCy$_2$)(norbornadiene)][S-BAr$^F_4$], [S-BAr$^F_4$] = [B(3,5-(SF$_5$)$_2$C$_6$H$_3$)$_4$]$^-$ (**Compound 4.1**) and the σ-alkane complex [Rh(Cy$_2$PCH$_2$CH$_2$PCy$_2$)(norbornane)][S-BAr$^F_4$] (**Compound 4.2**) formed from its hydrogenation had been previously determined using single-crystal X-ray diffraction. This however, was particularly challenging as the synthesis of **Compound 4.1** almost always resulted in the formation of microcrystalline material.[200] Additionally, when exposed to hydrogen during the solid/gas single-crystal to single-crystal reaction, the crystals would crack and fragment. This made it particularly difficult to obtain suitably large, diffracting crystals of the σ-alkane complex **Compound 4.2** for single-crystal X-ray diffraction and many crystals had to be screened before the structure was determined. 3DED has previously been used to determine the structures of organometallic materials[157] and it was hoped that this technique could provide a complementary structural solution, establishing electron crystallography as a possible alternative to single-crystal X-ray crystallography when the formation of suitably sized crystals is prohibitory.

4.1 Methods

4.1.1 Sample Preparation

The synthesis of **Compound 4.1** and **Compound 4.2**, grid preparation and hydrogenation reaction were performed by Dr Laurence Doyle, working under the supervision of Professor Andrew Weller at the University of York. Details of the synthesis are provided in our paper, 3DED characterization of a robust cationic σ-alkane complex stabilized by the [B(3,5-(SF$_5$)$_2$C$_6$H$_3$)$_4$]$^-$ anion, via on-grid solid/gas single-crystal to single-crystal reactivity.[200]
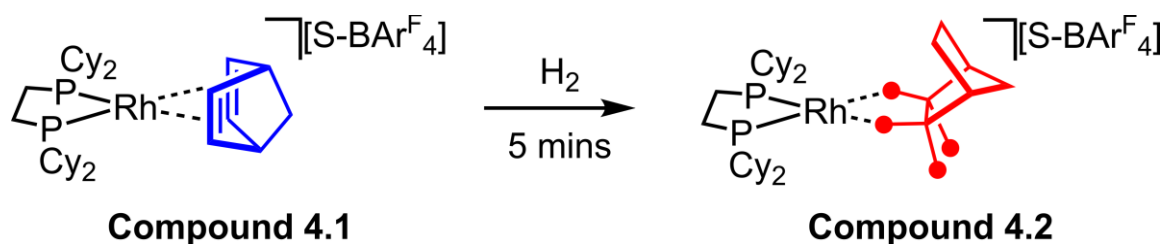
Figure 4.1. Reaction scheme for the single-crystal to single-crystal hydrogenation of the diene complex Compound 4.1 to form σ-alkane complex Compound 4.2. Red circles = hydrogen atoms.

4.1.1.1 Compound 4.1

The diene complex **Compound 4.1** was ground under an argon atmosphere to create a fine microcrystalline powder. The resulting powder was deposited onto pre-clipped Quantifoil Cu R1/4 grids. These grids were then stored in separate glass vials and transported to the microscope under an atmosphere of argon. The individual grids were plunged into liquid nitrogen and transferred to the cassette before loading into the TEM. See **Chapter 9, Section 9.1** for further details on grid preparation.

4.1.1.2 Compound 4.2

The remaining **Compound 4.1** grids were treated with H_2 gas at 1.3 atm pressure for 5 minutes (**Figure 4.1**) to form a σ-alkane complex: **Compound 4.2**. This work was performed by Dr Laurence Doyle. Initial 3DED studies on this material indicated it was particularly air sensitive or that the crystals may have experienced temperature shock and fragmented when plunged into liquid nitrogen. Poorly diffracting crystals were observed on **Compound 4.2** grids that had been transported to the microscope following the same protocol as described above for the diene complex. To remedy this, a new transfer method was developed. Freshly hydrogenated grids were placed into an autogrid box and transported to the microscope under an argon atmosphere. The transfer station was filled with liquid nitrogen (**Figure 4.2**) and the transfer station was allowed to cool to liquid nitrogen temperature creating a protective nitrogen atmosphere in the transfer station. The autogrid box was placed in the cold metal holder under a nitrogen blanket and was allowed to cool conductively to liquid nitrogen temperature. The individual grids were then transferred to the cassette and loaded into the TEM.
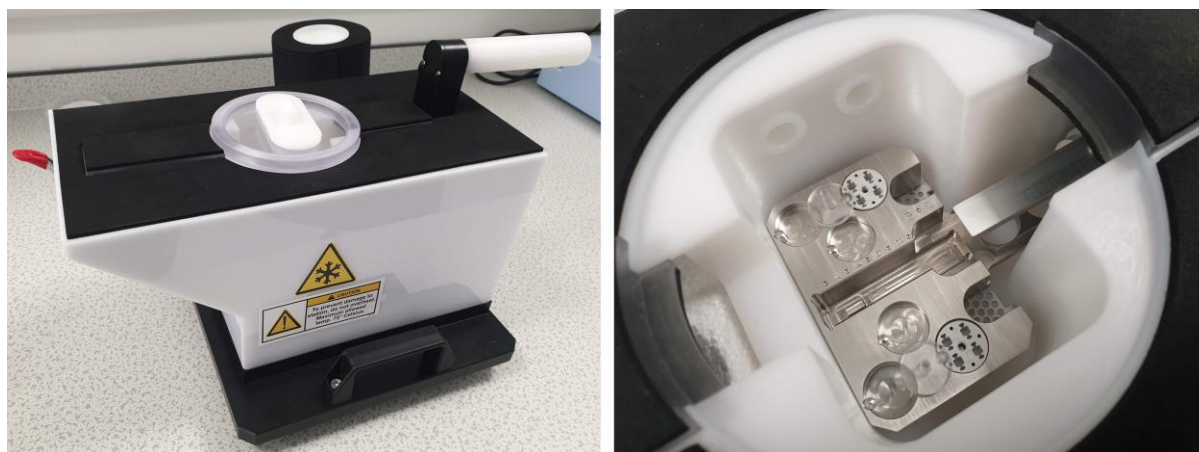
Figure 4.2. The TEM Transfer station. Left: TEM Transfer station right: Inside of transfer station, the white circular autogrid boxes are sat within the metal holder. Note: No liquid nitrogen is present, the transfer station pictured is at room temperature.

4.1.2 Data acquisition

Electron diffraction data were acquired using a Thermo Fisher Glacios microscope operating at a voltage of 200 kV as described in **Chapter 9 Section 9.2**. A Ceta-D camera was used. Data were collected at 80 K. Selected area electron diffraction using microprobe mode was utilised with the following illumination conditions to achieve a low flux of ~0.01 e$^-$ Å^{-2} s^{-1}: gun lens 4, spot size 11, 30 μm C2 aperture. These illumination conditions resulted in a parallel beam of 4 μm diameter. The area from which diffraction was observed was reduced further by the insertion of a 40 μm selected area aperture (1.4 μm on the sample plane). This improved the signal to noise ratio of diffraction events and ensured diffraction was only observed from the target crystal. Further details on the selected area electron diffraction set up are provided in **Chapter 2, Section 2.2.3**. Data were collected while the stage was rotating continuously. Due to the configuration of the Glacios microscope, and to prevent collision with the pole pieces, the maximum allowable tilt angles were ±69°. In practice, the rotation range is further limited as at high tilt angles crystal centring is challenging and other species (other crystals, contaminants, or grid bars) may obstruct the beam. EPU-D was used to collect data in a semi-automated fashion with the following settings: 2x binning, a rotation speed of 0.5°/s and an exposure time of 2 s, resulting in a Δφ of 1°/frame.

A total of 28 datasets were collected from the diene complex, **Compound 4.1**. These datasets typically covered a rotation range of 60-90° with minimum and maximum tilt angles of -45°/+55° respectively. Crystals of the σ-alkane complex, **Compound 4.2**, were found to be much more sensitive to radiation than their diene counterparts, with a visible loss of diffraction quality occurring after only 20-30° of rotation. The sample preparation and data collection protocols for this species were optimised to collect the highest quality data. Over the course of this optimisation, a total of 111 datasets were collected from the σ-alkane complex. The highest quality datasets were recorded in a single 24-hour microscope session from 29 crystals across 2 duplicate grids, which were prepared following the modified sample preparation and loading protocol described in **Section 4.1.1.2**. An example crystal and corresponding diffraction pattern are shown in **Figure 4.3**.
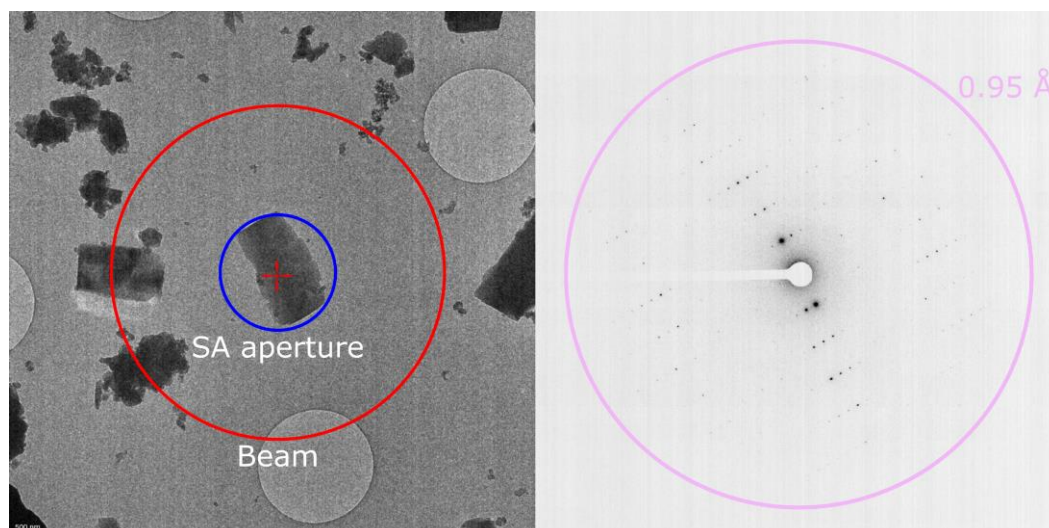
Figure 4.3. Example Compound 4.2 crystal and diffraction pattern. Left: TEM brightfield image of a Compound 4.2 crystal, red circle represents the beam diameter (4 µm), blue circle shows the area from which diffraction was recorded (1.4 µm). Right: Representative electron diffraction pattern, these crystals diffracted to 0.95 Å (pink circle).

4.1.3 Data processing and structure determination

Data were processed using DIALS software.[201] To enable data processing, several parameters needed to be defined. A pedestal value of 64 ADU (analog-to-digital units) was added to each individual pixel value, to reduce issues during background modelling caused by negative pixel values. The detector distance, calibrated from aluminium powder, was set to 958.5 mm. The correct goniometer rotation axis was also specified, for the York Glacios this was 1,0,0 for positive rotation about the horizontal axis.

The data processing workflow is detailed in in **Chapter 9, Section 9.3**. A semi-automatic processing script[202] was used which processed each dataset individually up to the integration stage by running through a standard series of DIALS commands. The integrated datasets were then scaled together, selecting the fewest datasets, which led to the best statistics. Datasets were selected based on primarily on their impact on CC½, R_{merge} and completeness of the data. Further explanation of this selection process is given in **Chapter 9, Section 9.3.6**, The strong reflections from the combined datasets were then filtered for joint refinement of the detector distance and unit cell parameters from each dataset, see **Chapter 9, Section 9.3.7**. The mean refined detector distance for the diene complex **Compound 4.1** was found to be 956.87(22) mm, and the σ-alkane complex **Compound 4.2** was 958.33(24). Both values were within 0.2% of the initial estimate suggesting the camera length

calibration was accurate. The unit cell parameters for each of the combined datasets were then refined by fitting calculated to observed 2θ values.

The structures were then determined *ab initio* using SHELXT[164] as described in **Chapter 3, Section 3.3.4** and **Chapter 9, Section 9.4**. Structure determination was trivial as the combined datasets were of high completeness and quality and both structures contained heavy atoms. Structure refinement was performed with SHELXL[165] using electron scattering factors from Peng[190]. General information on structure refinement is provided in **Chapter 3, Section 3.4**, and information on how the structures within this thesis were refined is given in **Chapter 9, Section 9.5**. The ADPs were refined for all non-hydrogen atoms. Hydrogen atoms were placed using the HFIX function in SHELXL. The internuclear X-H distances were changed to match the idealised distances determined from neutron diffraction data.[203] A riding model was used for hydrogen atom placement. To reflect any uncertainty in the model position, hydrogens attached to C1, C2, C4 and C5 in the σ-alkane complex **Compound 4.2** had their isotropic ADPs set to 5x that of their attached carbon atoms, rather than the default of 1.2x.

The only distance restraints applied were to make the S-F bond distances in the SF_5 groups of the counterion equal. A combination of rigid body restraints was used on different fragments of the structures. The use of SIMU, RIGU and DELU restraints, alongside the use of the EXTI instruction, negated the need for ISOR and XNDP instructions to prevent any atoms becoming non-positive definite in the refinement. Information on the impact of using the geometric and ADP restraints described above is given in **Chapter 3, Section 3.4**.

4.2   Results and Discussion

4.2.1 Compound 4.1

4 datasets from 4 crystals were merged together to give 96.6% complete data to a resolution of 0.95 Å. Crystallographic and refinement data for this complex are presented in **Table 4.1**. Determining the structure with SHELXT was trivial and almost all atoms for the diene complex **Compound 4.1** were placed in the correct positions. However, some atoms were misassigned at this stage. This is a relatively common problem when using SHELXT to assign elements with electron diffraction data. This is due to several factors: poor data quality (compared to X-ray diffraction), use of X-ray scattering factors in SHELXT, and the smaller difference in the electron scattering from different atoms

(compared to X-ray scattering factors).[50] Refinement resulted in a good structural solution (R_1 = 15.7%, $C2/c$ space group), the structure model and electrostatic potential map are shown in **Figure 4.4**. The thermal ellipsoids with a 50% probability are shown in **Figure 4.5**.

Table 4.1. Crystallographic and refinement data for Compound 4.1.

Empirical formula	$C_{57}H_{68}BF_{40}P_2RhS_8$
Formula weight	1945.25
Temperature (K)	80
Crystal system	monoclinic
Space group	$C2/c$
a (Å)	19.603(3)
b (Å)	18.393(3)
c (Å)	20.438(2)
β (°)	92.355(12)
Volume (Å³)	7362.8(18)
Z	4
ρ_{calc} (g/cm³)	1.755
Reflections measured	19560
Independent reflections (with I > 2 σ(I))	4380 (2563)
Resolution (Å)	0.95
Completeness (%)	96.6
Restraints/parameters	585/494
R_{int}	0.2348
R_1 [I > 2 σ(I)]	0.1565
R_1 [all data]	0.2194
wR_2 [all data]	0.3584
GooF	1.718
Residual potential (e/Å)	0.828/-0.632

Figure 4.4. 3DED structure of Compound 4.1. *Fo map contoured at 1.13 e/Å. For clarity, thermal ellipsoids are not shown. Key: black=C, white (small)=H, blue=B, green=F, pink=P, white (large)=Rh, yellow=S. Yellow dashed line represents hydrogen bonding.*
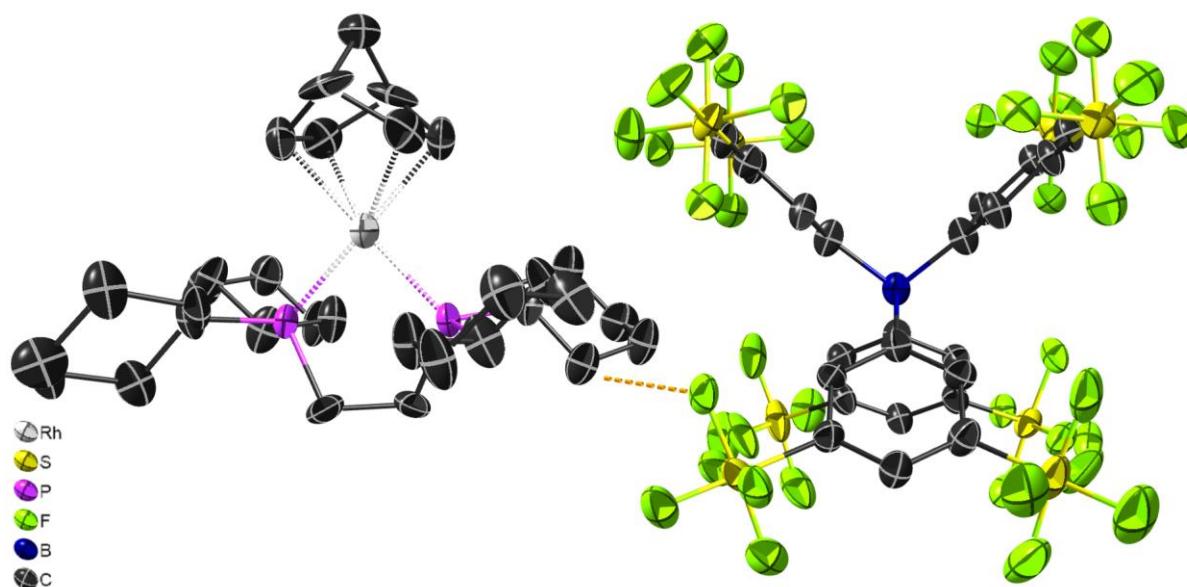
Figure 4.5. 3DED structure of Compound 4.1 with thermal ellipsoids are shown at a probability level of 50%. *For clarity, hydrogen atoms are not shown. Key: black=C, blue=B, green=F, pink=P, white (large)=Rh, yellow=S. Yellow dashed line represents hydrogen bonding.*

The bond distances and bond angles of the 3DED structure of **Compound 4.1** were compared to those of the X-ray structure of the same compound from Doyle *et al.,*[200] see **Table 4.2**. There were no significant differences in the bond distances and angles of the 3DED structure and the reported X-ray structure, with the exception of the C5—C5 bond.[200] 3DED was capable of generating a crystal structure of **Compound 4.1** with very few significant differences in bond distances and bond angles compared to its X-ray counterpart. This shows that the 3DED technique can be used to generate crystal structures with comparable accuracy in bond distances and bond angles to X-ray structures. Further, obtaining a 3DED crystal structure with the same bond distances and bond angles as X-ray structure indicated that the detector distance had been correctly calibrated and the data processing workflow allowed for the determination of correct unit cell parameters.

Table 4.2. Selected bond distances and angles from the reported X-ray structure of Compound 4.1 and the corresponding 3DED structure obtained in this work.
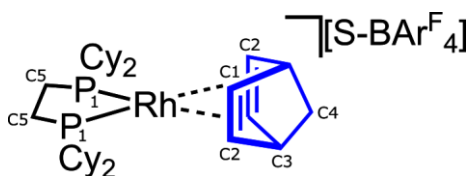
Bond distance (Å)	X-ray Doyle *et al.*[200]	3DED
Rh—P1	2.2892(16)	2.280(7)
Rh—C1	2.211(7)	2.246(15)
Rh—C2	2.224(6)	2.231(15)
C1—C2	1.361(10)	1.393(18)
C1—C3	1.562(10)	1.571(18)
C2—C3	1.566(10)	1.584(19)
C3—C4	1.552(9)	1.609(19)
C5—P1	1.852(7)	1.831(14)
C5—C5	1.508(13)	1.59(2)

Bond angle (°)	X-ray Doyle *et al.*[200]	3DED
P1—Rh—P1	85.25(8)	85.5(3)
C1—Rh—C2	35.7(3)	36.3(5)
C1—Rh—C2	67.1(3)	66.5(5)

4.2.2 Compound 4.2

4.2.2.1 Initial transfer method

The data that were collected from the σ-alkane complex **Compound 4.2**, before the optimised transfer protocol was introduced, could be processed in $P2_1/n$ space group. However, the structure could also be processed in $C2/c$, the same space group as the starting material, this is because the majority of the structure is still related by the inversion centre, the only part of the structure that breaks this symmetry element is the σ-alkane ligand. As the symmetry around the inversion centre should change during hydrogenation, data processing was continued using the $P2_1/n$ space group. More detail on space group determination is given in **Section 4.2.2.3**. 5 datasets were merged together to give a completeness of 99.1% to 0.95 Å. The $P2_1/n$ cell had the following unit cell parameters: a=19.5385 Å, b=18.9606 Å, c=20.3499 Å, α=90°, β=92.391°, γ=90° and reasonable merging statistics (Rmerge=0.286, CC ½=0.994). The unit cell parameters determined for this material were notably different from the ground state diene complex suggesting that a transformation had occurred on hydrogenation.

Structure determination was conducted using SHELXT[164] and it was possible to refine the structure (R_1=0.1612, wR_2=0.3737). However, SHELXT had difficultly placing the carbons in the σ-alkane ligand. Refinement using SHELXL generated an electrostatic potential map that did not clearly indicate the arrangement of carbon atoms. Suggesting that there was significant disorder in this fragment due to sample degradation, meaning it was not possible to resolve the ligand of interest. This could be as a result of air exposure, beam damage or temperature shock. The electrostatic potential maps for this fragment are shown in **Figure 4.6**. It is likely that the potential shown here is a superposition of different, degraded forms of the ligand.
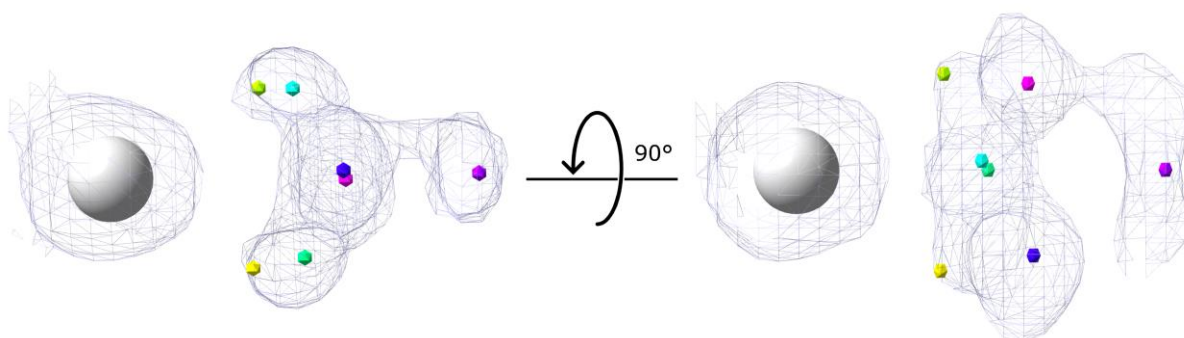
Figure 4.6. Fobs map for the ligand of interest in the initial Compound 4.2 structure. *Right image is rotated ~90° from Left. Q peaks are represented by coloured hexagons, these show the regions of highest electrostatic potential that has not been included in the model. Unfortunately, it was not possible to model the ligand as carbon atoms could not be placed in a chemically sensible manner, without breaking bond length and geometry requirements. Fo map contoured at 1.20 e/Å.*

A limitation of 3DED is that multiple datasets need to be merged together to have sufficiently complete data to enable structure determination. Some crystals may exhibit more disorder than others so even if a particularly well diffracting crystal of **Compound 4.2** was found that exhibited no disorder or degradation at the σ-alkane site, this could be masked by disorder at this site introduced from other datasets.

4.2.2.2   Optimised transfer method

Optimising the transfer process was key to fully determining the structure of the σ-alkane ligand. There was a marked improvement in the diffraction quality of the crystals compared to the previous transfer method. However, these well diffracting crystals were also more beam sensitive and only ~20° of data could be collected before there was a notable drop in diffracting resolution. As a result, it was necessary to merge data from more crystals to achieve a relatively complete dataset. 20° wedges from 9 datasets were merged together to give a completeness of 94.0% to 0.95 Å. Crystallographic and refinement data for this complex are presented in **Table 4.3**. Refinement resulted in a good structural solution (R$_1$ = 16.4%, $P2_1/n$ space group), the structure model and electrostatic potential map are shown in **Figure 4.8**. The thermal ellipsoids with a 50% probability are shown in **Figure 4.9**. It was possible to fully determine the structure of **Compound 4.2** as it was possible to resolve the ligand of interest from the higher quality diffracting crystals (**Figure 4.7**).
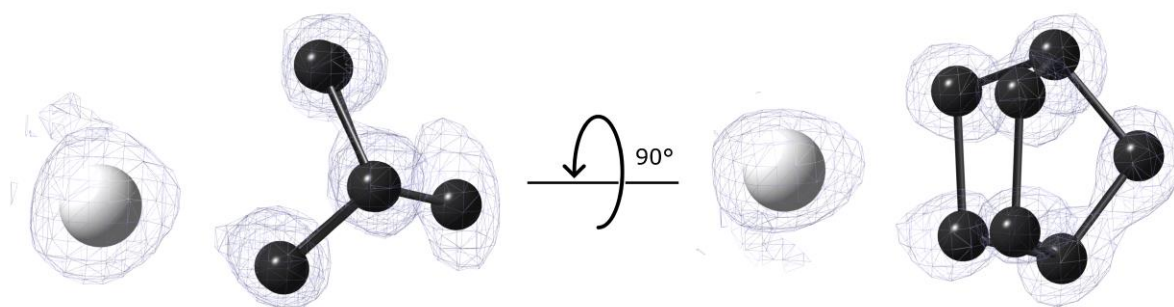
Figure 4.7. Fobs map for the ligand of interest in the optimised Compound 4.2 structure. *Right image is rotated ~90° from Left. Carbon atoms were easily placed by SHELXL, and it was possible to resolve the structure of the ligand. Hydrogen atoms have been removed for clarity. Fo map contoured at 1.83 e/Å. Key: black=C, white=Rh.*

Table 4.3. Crystallographic and refinement data for Compound 4.2.

Empirical formula	$C_{57}H_{72}BF_{40}P_2RhS_8$
Formula weight	1949.29
Temperature (K)	80
Crystal system	monoclinic
Space group	$P2_1/n$
a (Å)	19.5339(11)
b (Å)	19.0160(14)
c (Å)	20.3007(9)
β (°)	91.727(5)
Volume (Å^3)	7537.4(8)
Z	4
ρ_{calc} (g/cm^3)	1.718
Reflections measured	35027
Independent reflections (with I > 2 σ(I))	8652 (4374)
Resolution (Å)	0.95
Completeness (%)	94.0
Restraints/parameters	1476/983
R_{int}	0.1906
R_1 [I > 2 σ(I)]	0.1640
R_1 [all data]	0.2369
wR_2 [all data]	0.3800
GooF	1.672
Residual potential (e/Å)	0.845/-0.768

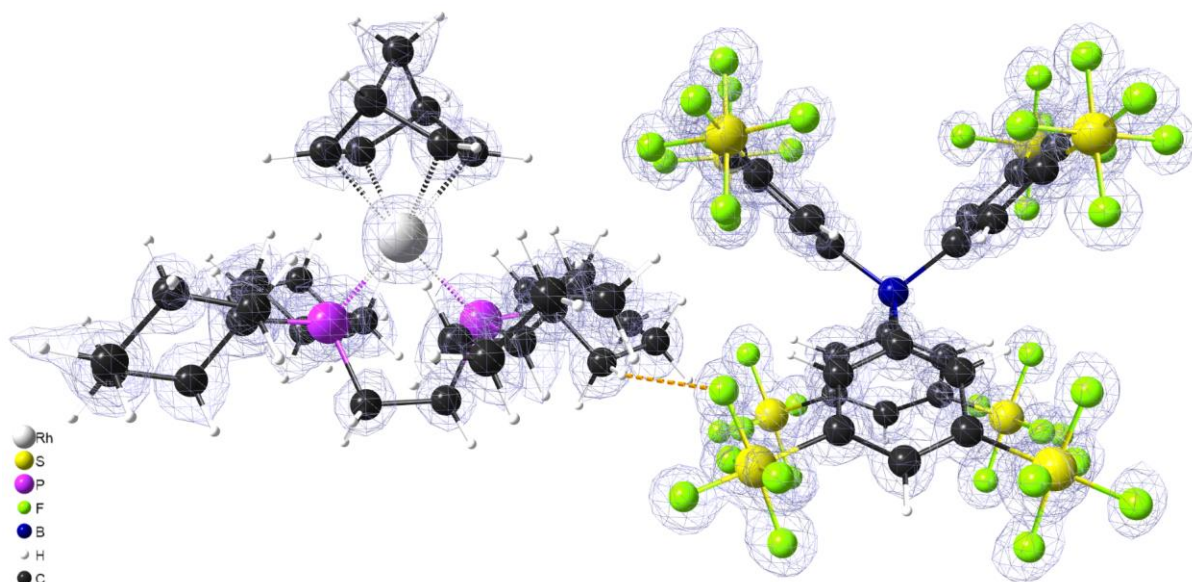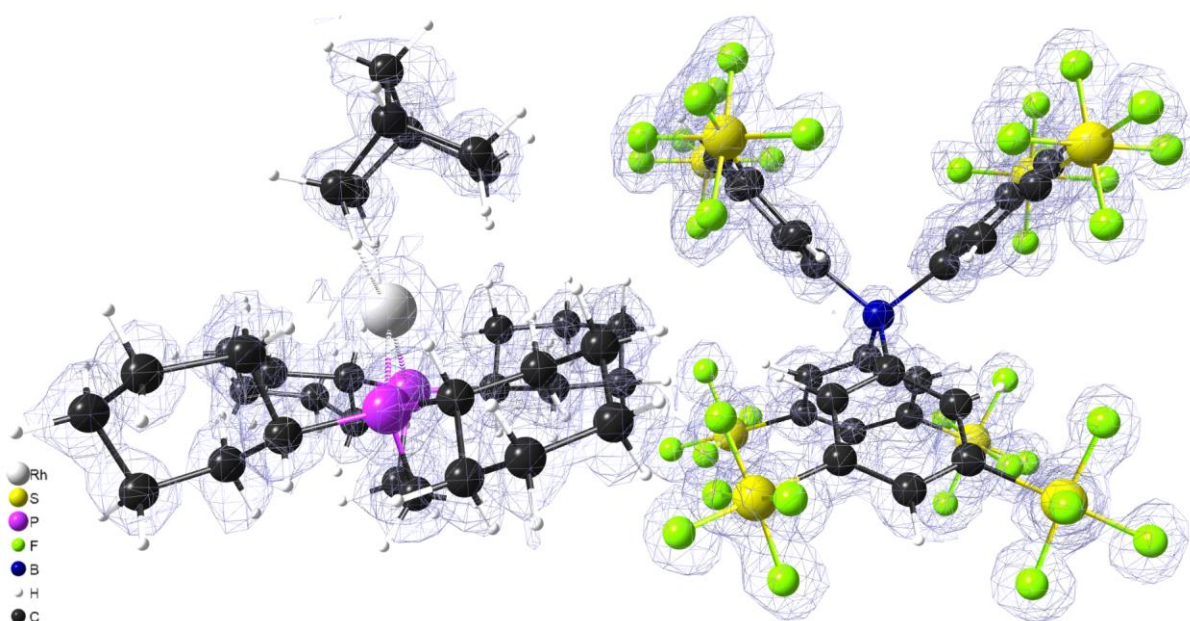**Figure 4.8. 3DED structure of Compound 4.2.** *Fo map contoured at 1.40 e/Å. For clarity, thermal ellipsoids are not shown.*

Key: black=C, white (small)=H, blue=B, green=F, pink=P, white (large)=Rh, yellow=S
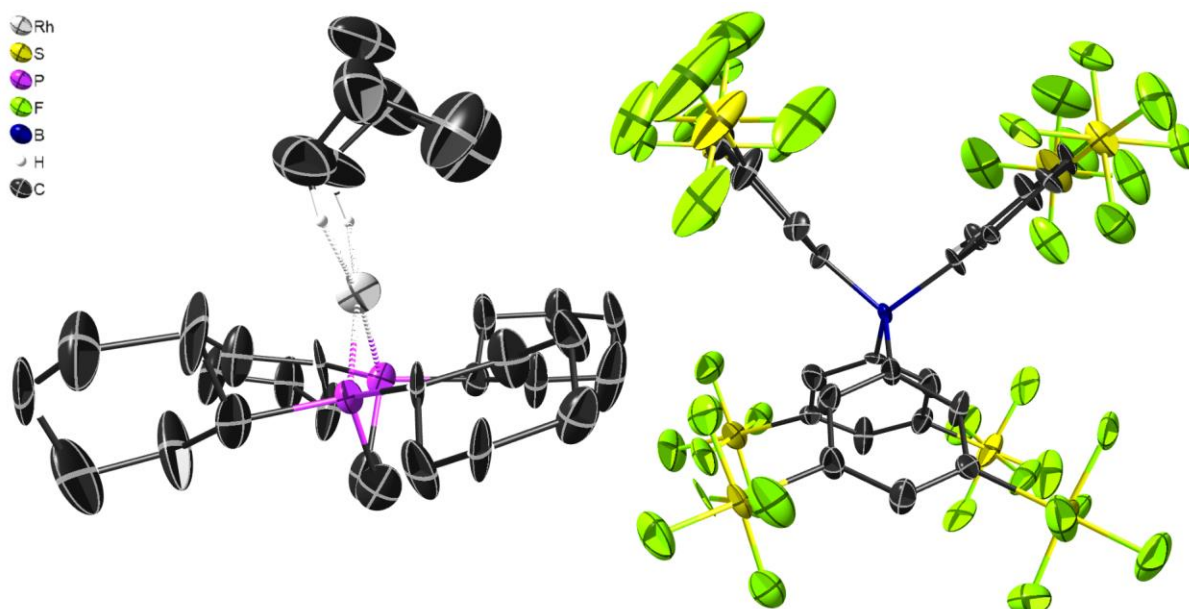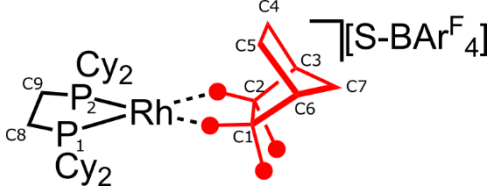
Figure 4.9. 3DED structure of Compound 4.2 with thermal ellipsoids are shown at a probability level of 50%. For clarity, only the hydrogen atoms involved in bonding to the rhodium are shown. Key: black=C, white (small)=H, blue=B, green=F, pink=P, white (large)=Rh, yellow=S

Table 4.4. Selected bond distances and angles from the reported X-ray structure of Compound 4.2 and the corresponding 3DED structure obtained in this work.

Bond distance (Å)	X-ray Doyle *et al.*[200]	3DED
Rh—P1	2.184(2)	2.229(7)
Rh—P2	2.195(2)	2.222(7)
Rh—C1	2.408(10)	2.479(19)
Rh—C2	2.416(11)	2.46(2)
C1—C2	1.597(14)	1.74(2)
C4—C5	1.538(15)	1.67(2)
C8—P1	1.840(10)	1.820(16)
C9—P2	1.842(10)	1.807(16)
C8—C9	1.538(13)	1.572(16)

Bond angle (°)	X-ray Doyle *et al.*[200]	3DED
P1—Rh—P2	85.54(9)	86.0(3)
C1—Rh—C2	38.7(3)	41.3(6)

The bond distances and bond angles of the 3DED structure of **Compound 4.2** were compared to those of the X-ray structure of the same compound from Doyle *et al.,*[200] see **Table 4.4**. Significant differences in the bond distances and bond angles were noted for the σ-alkane ligand. These differences could be as a result of the different methods of hydrogenation used to prepare the crystals for 3DED and SCXRD. Alternatively, as previously mentioned, the 3DED structure is an amalgamation of multiple datasets from multiple crystals. Some crystals may exhibit more disorder or degradation at the σ-alkane site, impacting the overall geometry of the ligand in the combined crystal structure.

4.2.2.3 Space group determination

Reliably determining unit cell parameters is challenging when indexing small wedges of electron diffraction data. Unlike in X-ray crystallography, where a single diffraction pattern typically contains information about all three reciprocal lattice dimensions, with a single electron diffraction pattern it is usually only possible to elucidate two of the three unit cell vectors. This is due to the flatness of the Ewald sphere resulting due to the short wavelength (0.02508 Å at 200 kV) of electrons. Further details on this are provided in **Chapter 3, Section 3.2.2**. Determination of unit cell parameters from electron diffraction data requires the indexing of consecutive frames in a rotation series, typically covering a 15-25° wedge of reciprocal space.[50] Indexing solutions may be unstable when only small wedges of reciprocal space are sampled, as was the case for **Compound 4.2** where only 20° of data could be collected before there was a decrease in diffraction quality and resolution.

An additional challenge for indexing **Compound 4.2** was that the majority of the compound was structurally identical to **Compound 4.1**, with only the ligand changing upon the hydrogenation reaction. During hydrogenation, the symmetry around the inversion centre changed as the diene was hydrogenated. As the inversion symmetry breaks upon reaction, the space group should no longer be $C2/c$ and should instead be $P2_1/n$ (**Figure 4.10**).
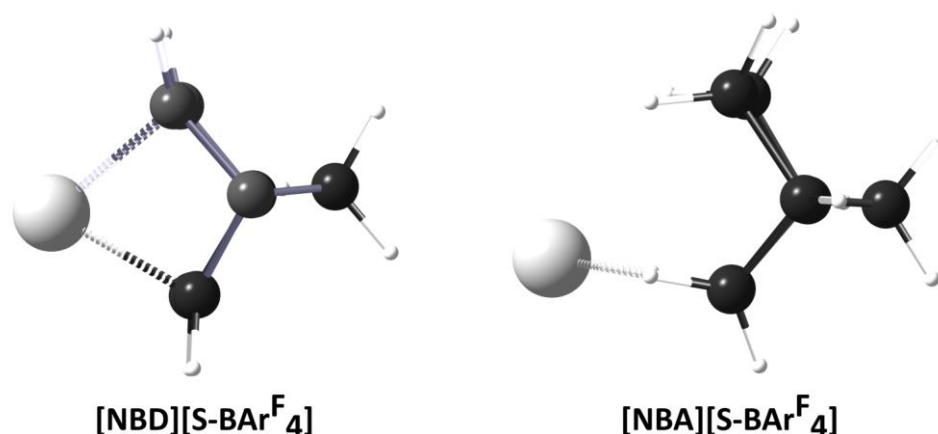
Figure 4.10. Changes to ligand of interest in single-crystal to single-crystal hydrogenation. *Only rhodium centre and ligand shown for clarity. Left:* ***Compound 4.1*** *(before hydrogenation), Right:* ***Compound 4.2*** *(after hydrogenation) atoms in the ligand are no longer symmetry related. Key: black=C, white (small)=H, white (large)=Rh.*

Indexing the **Compound 4.2** datasets proved somewhat challenging. Firstly, the majority of the structure was still related by the inversion centre and only the relatively weakly scattering carbon and hydrogen atoms in the ligand break this. Secondly, only small wedges of reciprocal space could be sampled. This meant it was possible to index the datasets in both $P2_1/n$ and $C2/c$ space groups.

When indexing the data without specifying space group, two indexing solutions were possible. A triclinic cell with unit cell parameters a ≈ b ≈ 13.5 Å, and c ≈ 20.3 Å, which could be reindexed to give a centred monoclinic cell resembling the starting **Compound 4.1** complex, and a second triclinic cell with unit cell parameters a ≈ 19 Å, b ≈ 19.5 Å, and c ≈ 20.3 Å, which could be reindexed to a primitive monoclinic cell (xtal04 and xtal05, **Table 4.5**). The crystals that indexed to the second triclinic cell when processed in $P1$ (xtal04 and xtal05) give a higher percentage indexed spots than the other indexing solutions. Early attempts at manual processing had also shown it was possible to change the indexing solution obtained by changing how many images were used in indexing, or by supplying rough unit cell parameters of the primitive monoclinic cell. By supplying rough unit cell parameters during indexing (`unit_cell=19.5,19,20.5,90,91.5,90`) and specifying the space group ($P2$) it was possible to index all crystals with the primitive monoclinic space group. There was a marked improvement in the percentage of reflections indexed in almost all datasets. With the exception of xtal01, all other datasets now had over 90% of reflections indexed, and over 95% of reflections were indexed for most (**Table 4.6**). Notably, the β angle for xtal05 was now acute, this could be rectified using a simple change of basis operator command; -h,-k,l. Alternatively, `dials.symmetry` can be used in conjunction with the

other datasets and then all datasets can be scaled together and solved with SHELXT[164] to yield a solution with a $P2_1/n$ space group presented in **Section 4.2.2.2**.

Table 4.5. Initial indexing solutions of Compound 4.2 crystals when processed in P1.

Dataset	a (Å)	b (Å)	c (Å)	α (°)	β (°)	γ (°)	Number of spots indexed	Number of spots unindexed	Percentage of spots indexed (%)
xtal01	13.65	13.71	20.29	88.86	88.53	88.90	153	39	79.7
xtal02	13.65	13.72	20.21	88.88	89.03	88.45	351	24	93.6
xtal03	13.42	13.65	20.32	88.60	89.13	88.05	680	88	88.5
xtal04	19.05	19.63	20.30	91.77	90.19	89.62	851	22	97.5
xtal05	19.02	19.35	20.32	91.62	90.03	89.89	724	27	96.4
xtal06	13.62	13.65	20.25	88.45	88.92	88.61	453	37	92.4
xtal07	13.60	13.55	20.31	88.59	88.58	88.08	585	52	91.8
xtal08	13.52	13.61	20.25	88.44	89.22	87.76	467	69	87.1
xtal09	13.62	13.89	20.30	88.50	88.89	88.57	611	96	86.4

Table 4.6. Indexing solutions of Compound 4.2 crystals when processed in P2 with rough unit cell parameter supplied.

Dataset	a (Å)	b (Å)	c (Å)	α (°)	β (°)	γ (°)	Number of spots indexed	Number of spots unindexed	Percentage of spots indexed (%)
xtal01	19.53	19.05	20.29	90	91.88	90	154	38	80.2
xtal02	19.48	19.07	20.20	90	91.10	90	362	13	96.5
xtal03	19.51	19.34	20.32	90	91.69	90	744	24	96.9
xtal04	19.49	19.02	20.27	90	91.41	90	851	22	97.5
xtal05	19.44	19.02	20.31	90	88.35	90	724	27	96.4
xtal06	19.52	19.14	20.28	90	91.91	90	473	17	96.5
xtal07	19.50	18.83	20.31	90	91.93	90	612	25	96.1
xtal08	19.58	18.99	20.27	90	91.78	90	494	42	92.2
xtal09	19.53	19.01	20.29	90	91.56	90	664	43	93.9

4.3   Conclusions

3DED has been successfully used to characterise the structure of a challenging to isolate, air-sensitive σ-alkane complex without structural decomposition. The compounds studied here had already been fully characterised by single-crystal X-ray diffraction, however 3DED provided a complementary solution. This sets the precedent for the study of other materials generated by single-crystal to single-

crystal reactions where obtaining an X-ray structure is not possible due to small crystal size and reduction in diffraction quality on reaction.

Optimisation of sample preparation and microscope transfer allowed the structure of the σ-alkane ligand to be fully resolved. Additionally, direct feedback on beam damage from the data collection allowed the data collection strategy to be adapted on the fly to ensure the highest quality data was obtained. This required reducing the angular range at which datasets were collected to 20°.

For **Compound 4.1**, the 3DED structure and X-ray structure had the same bond distances and bond angles, with one exception. This showed that the 3DED technique could be used to generate crystal structures with comparable accuracy in bond distances and bond angles to X-ray structures. Unfortunately, the 3DED structure of **Compound 4.2** showed significant differences in bond geometry compared to the X-ray structure. **Compound 4.2** contained a weakly binding ligand of interest that was prone to degradation, either as a result of air exposure, beam damage or temperature shock. Merging multiple datasets from multiple crystals together, in cases where binding is particularly weak or the sample is prone to degradation, may result in less reliable structure solution.

5   Characterisation of gold (III) porphyrin complexes using powder X-ray diffraction to pre-screen for crystallinity

A requirement for electron diffraction is that the sample must contain suitably thin diffracting material. The individual crystals should have a thickness no greater than 540 nm, when collecting data with 200 keV electrons.[204] This is to allow the electron beam to pass through the crystal without prohibitive amounts of inelastic scattering.[204] As such, it is typically not possible to visualise whether a sample contains suitably sized crystals in advance, via light microscopy. The maximum resolution of an idealised optical microscope is 200 nm, due to the wavelength of light. It is therefore difficult to determine whether a sample will contain crystalline material of suitable thickness, without screening in a TEM. While the process for recording diffraction data on a TEM is fast, once diffracting material of suitable thickness is found, finding well diffracting, thin crystals can take several hours, particularly for poor or challenging samples. Frustratingly, despite lengthy TEM screening, sometimes no diffraction is observed. PXRD experiments may provide an indicator of sample crystallinity prior to screening and data collection on a TEM. The inclusion of a pre-screening step to test for sample crystallinity would enable a more efficient use of valuable microscope time and resources.

Previous attempts to solve the structures of a series of gold (III) porphyrin complexes using single-crystal X-ray diffraction, had been unsuccessful. This was due to difficulty in obtaining large crystals. Additionally, any diffraction patterns observed when a home X-ray source was used, contained weak, smeared reflections, characteristic of a structure in which layer slipping had occurred. Electron diffraction could provide an alternative means of studying such complexes, when SCXRD does not yield a structure.

5.1   Methods

5.1.1   Sample Preparation

The porphyrin samples were prepared by Alice Jane McEllin, of Professor Duncan Bruce's group at the University of York and received as a dry powder for PXRD and 3DED analysis. The details of the synthesis are provided in Alice Jane McEllin's PhD thesis.[205] The structures of the di-substituted zinc porphyrin (**Compound 5.1**) and tetra-substituted zinc porphyrin (**Compound 5.2**) are given in **Figure 5.1**. The gold (III) complex units used to substitute the porphyrins utilised n-butoxy-chains (OC_4H_9).

Zinc was subsequently removed from the porphyrins to give free base porphyrins (**Compound 5.3** and **Compound 5.4**) shown in **Figure 5.2**.
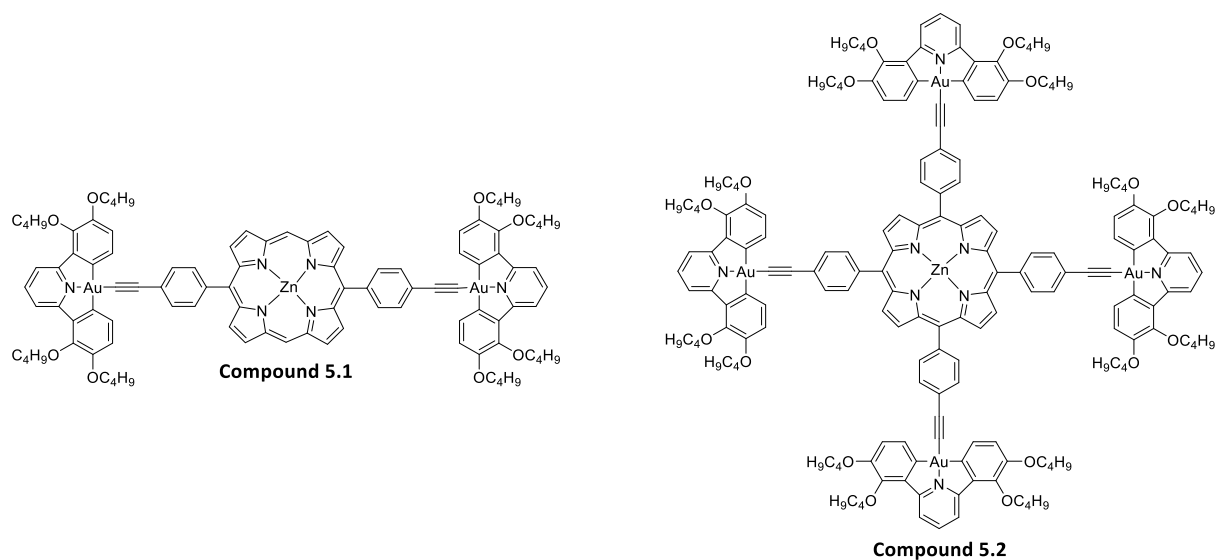
Figure 5.1. Structures of the di- and tetra-substituted zinc porphyrin complexes.
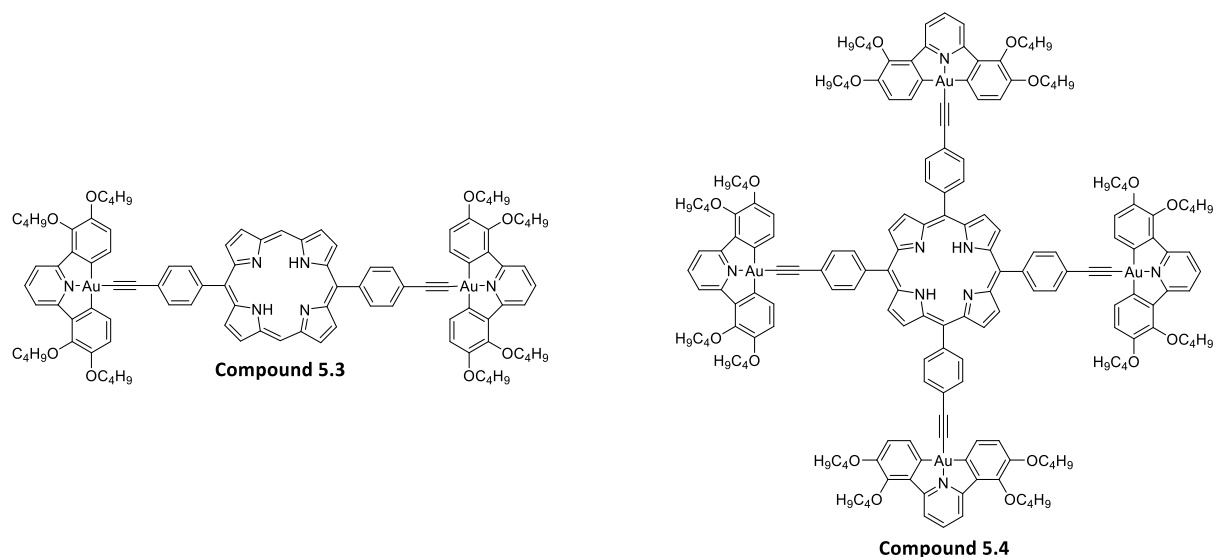
Figure 5.2. Structures of the di- and tetra-substituted free base porphyrin complexes.

5.1.2   Powder X-ray diffraction screening

The porphyrin samples were finely ground using a mortar and pestle, and a small amount (~1 micro-spatula tip) of each sample was deposited on a PXRD sample holder. PXRD data were collected at room temperature using a Panalytical Aeris powder X-ray diffractometer equipped with a 600 W copper source and a PIXcel1D-Medipix3 detector. The instrument was operated in reflectance mode with the

sample on a silicon single crystal low background plate. A scan range of 5-45°was used. **Figure 5.3** shows an example gold porphyrin sample deposited on the sample holder.
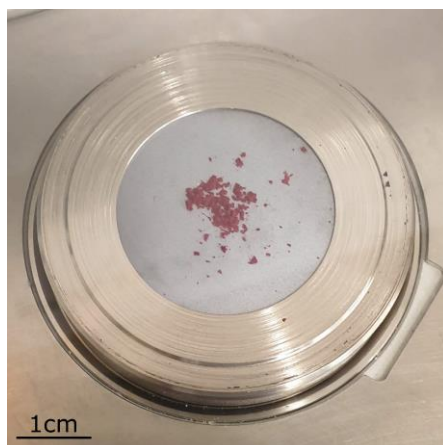
Figure 5.3. A PXRD sample holder with an example gold porphyrin sample.

The powder patterns were examined visually for an indication of crystallinity. PXRD provides information on the crystallinity of the bulk material. If a powder pattern contains numerous, strong, sharp peaks, this shows the bulk material is crystalline. From this, it may be expected that suitably thin diffracting crystals are already present in the bulk material, or that they may be formed upon further sample grinding. Alternatively, if a powder pattern from a sample contains no peaks, this suggests that no crystalline material is present in the bulk material, and that the sample is amorphous. It is possible that crystalline material could be present in trace amounts below the detection limit of the diffractometer. For such samples, finding diffracting material using a TEM is technically possible, if trace amounts of crystalline diffracting material are indeed present. However, searching for diffracting material in a sample where the bulk material is amorphous would likely be an arduous and time-consuming process that would likely not be successful. Instead of inefficiently using valuable microscope time, efforts could be redirected to optimising sample preparation or recrystallisation of the sample.

In the middle of these extremes, samples that produce powder patterns with weak, broad, or few peaks may warrant investigation by 3DED, with the understanding that screening for well diffracting, single crystals may be difficult or unsuccessful. With weak, broad, or scarce peaks, there is an indication of some crystallinity in the bulk material but that some form of disorder exists. In such circumstances, it should be carefully considered whether pursuing 3DED analysis is worthwhile or if sample optimisation is required

5.1.3 Single crystal X-ray

By altering the crystallisation conditions,[205] it was possible to obtain needle-like crystals of **Compound 5.1**, from which X-ray data could be collected. Details of the changes to crystallisation conditions are provided in Alice Jane McEllin's PhD thesis.[205] However, the quality of the single crystals still proved to be poor for SCXRD, resulting in weak, streaked reflections. While it was possible to determine the structure from this data, the SCXRD structure had very large and elongated ADPs for all atoms. A comparison of the SCXRD and 3DED structures for **Compound 5.1** could be made. However, it is important to note that crystals suitable for each method were formed via different crystallisation methods, which may result in different crystal packing. It was not possible to obtain SCXRD structures of any of the other compounds (**Compound 5.2 – 5.4**), due to difficulty in growing sufficiently large crystals, even with the alternate crystallisation method.

SCXRD data collection and structure refinement were performed by Theo Tanner as described in Alice Jane McEllin's PhD thesis.[205] Data were collected at 110 K using an Oxford Diffraction SuperNova dual-source X-ray diffractometer with Cu Kα radiation (λ=1.54184 Å). An EOS CCD camera was used. Crystal cooling was achieved using an Oxford Instruments CryoJet. CrysAlisPro[206] was used for diffractometer control, data collection and initial unit cell determination, frame integration and unit-cell refinement. OLEX2[207] was used for overall structure solution and refinement. Within OLEX2, structure solution was achieved using SHELXS[69] and refinement was performed using SHELXL[165].

The crystal diffracted poorly with streaked reflections. This led to very poor, elongated ADPs of all atoms. The ADPs for all atoms were restrained to be approximately isotropic with particularly hard restraints for 2 carbon atoms which were bonded to the gold. These carbon atoms are highlighted in **Figure 5.4**. The two phenyl rings bonding to the gold were constrained to be regular hexagons with C-C bond lengths of 1.39 angstroms. The two gold-carbon bond lengths were restrained to be equal. The bridging C_6H_4 unit was disordered and modelled in two positions with refined occupancies of 0.56:0.44(2).
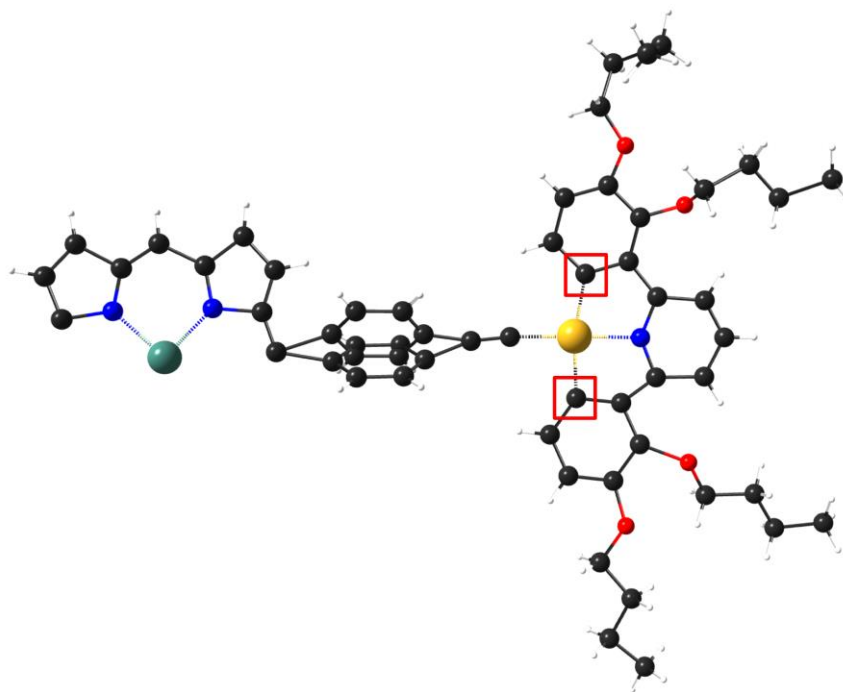
Figure 5.4. SCXRD structure of Compound 5.1 showing the carbon atoms to which hard restraints have been applied. *For clarity, the thermal ellipsoids are not shown. The bridging C_6H_4 unit was disordered and modelled in two positions with refined occupancies of 0.56:0.44(2). Symmetry equivalent atoms have been removed for clarity. Atom Key: black=C, white=H, yellow=Au, blue=N, red=O, green=Zn*

5.1.4 Electron diffraction data acquisition

The gold porphyrin samples were ground to a fine powder between two microscope slides and deposited onto pre-clipped Quantifoil Cu R1/4 grids. The grids were cooled to liquid nitrogen temperature, transferred to the cassette, and loaded into the TEM. See **Chapter 9, Section 9.1** for further details on grid preparation. The individual grids were screened for diffracting material using a Thermo Fisher Glacios microscope operating at a voltage of 200 kV and temperature of 80 K, as described in **Chapter 9, Section 9.2**. Data were collected using nanobeam electron diffraction with the following illumination conditions: gun lens 8, spot size 11, 30 μm C2 aperture. These illumination conditions resulted in a parallel beam with a diameter of 1.05 μm. This resulted in a flux of ~0.07 e⁻ Å⁻² s⁻¹. Further details of the nanobeam electron diffraction set up are provided in **Chapter 2, Section 2.2.3**. An example crystal from **Compound 5.1** and corresponding diffraction pattern are shown in **Figure 5.5**. The detector used for both screening and data collection was a Ceta-D. Data were collected while the stage was rotating continuously. EPU-D was used to collect data in a semi-automated fashion with the following settings: 2x binning, a rotation speed of 1.333°/s and an exposure time of 0.75 s. This resulted in a Δφ of 1°/frame.

Figure 5.5. Example Compound 5.1 crystal and diffraction pattern. *Left: TEM brightfield image of **Compound 5.1** crystal, red circle represents the beam diameter (1.05 μm). Right: Representative electron diffraction pattern, with resolution rings. Outer resolution ring is 0.83 Å.*

Typically, each sample was allocated 1 hour of screening time. During this time, if no data are collected, ~40-50 targets can be screened by taking single test diffraction images of each target. If no, or only poor, diffraction was observed during this period, the next sample was loaded.

5.1.5 Electron diffraction data processing and structure determination

Datasets were processed using DIALS software.[201] To enable data processing, several parameters needed to be defined. A pedestal value of 64 ADU was added to each individual pixel value. The detector distance, calibrated from aluminium powder, was set to 958.5 mm. The correct goniometer rotation axis was also specified, 1,0,0 for rotation about the horizontal axis in a positive direction. This is further detailed in **Chapter 9, Section 9.3.1**.

A script was used to run through a series of DIALS commands to process the individual datasets.[202] This improved the speed and reproducibility of data processing. The script had no intelligence or decision making capabilities and required manual data input and examination of the output by researchers. Integrated datasets with the same space group and unit cell parameters were then scaled together. This was a manual process where the results of scaling were carefully analysed and full datasets, or frames from datasets, were removed to achieve the best solution. The selection process

for scaling multiple datasets is described in **Chapter 9, Section 9.3.6**. Datasets selection was based on improvements in the overall completeness of the data without compromising CC½ or R_{merge}.

For **Compound 5.1**, 6 datasets from 6 crystals were combined to give 94.8% complete data to 0.83 Å resolution. For **Compound 5.3**, 5 datasets from 5 crystals could be combined resulting in 91.7% complete data to 0.83 Å resolution. The strong reflections from the combined datasets were then filtered for joint refinement of the detector distance and unit cell parameters from each dataset. The unit cell parameters for each of the combined datasets were then refined by fitting calculated to observed 2θ values. This allowed estimation of the estimated standard deviations on the 'best' cell parameters for the combined datasets, see **Chapter 9, Section 9.3.7**.

The structures were then determined *ab initio* using SHELXT.[164] Further details on structure determination are given in **Chapter 3, Section 3.3.4** and **Chapter 9, Section 9.4**. Structure refinement was performed with SHELXL[165] using electron scattering factors from Peng.[190] General information on structure refinement is provided in **Chapter 3, Section 3.4**, and information on how the structures within this thesis were refined is given in **Chapter 9, Section 9.5**. Anisotropic ADPs were refined for all non-hydrogen atoms and all hydrogen atoms were geometrically placed using the idealised internuclear X-H distances used in refinement of structures against neutron diffraction data with SHELXL.[203] A riding model was used for hydrogen atom placement. The recommended SHELXL weighting schemes were used in refinement.

ADP restraints were applied in refinement, which, together with refinement of the extinction parameter (EXTI), enabled anisotropic refinement of all non-hydrogen atoms without using XNPD instructions to prevent ADPs of some atoms becoming non-positive definite. For refinement of both **Compound 5.1** and **Compound 5.3**, RIGU restraints were applied to all non-hydrogen atoms. For both compounds, ISOR restraints were applied to particular atoms to prevent them having unacceptably anisotropic ADPs. The atoms which have had the ISOR restraint (`ISOR 0.005 0.01`) applied are shown in **Figure 5.6**. The use of geometric restraints was not required for either structure and the bridging C_6H_4 unit was not disordered. Further information and explanation of the ADP restraints used are given in **Chapter 3, Section 3.4**.

Compound 5.1   **Compound 5.3**
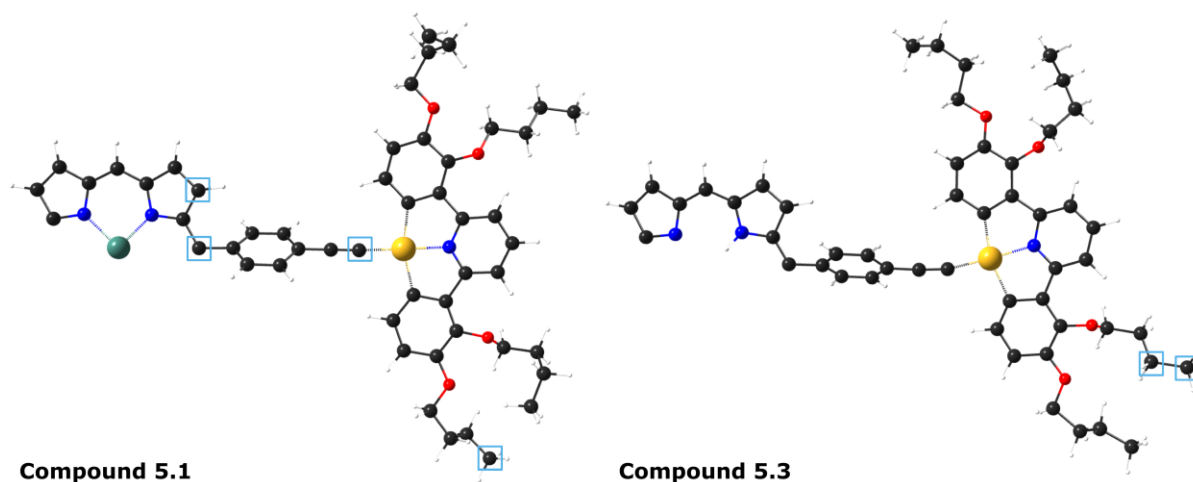
Figure 5.6. 3DED structure of Compound 5.1 and 5.3 showing which atoms have ISOR restraints applied during refinement. Left: Compound 5.1. Right: Compound 5.3. For clarity, thermal ellipsoids are not shown. The blue boxes around the carbon atoms represent atoms to which the ISOR restraint (ISOR 0.005 0.01) has been applied. Symmetry equivalent atoms have been removed for clarity. Atom Key: black=C, white=H, yellow=Au, blue=N, red=O, green=Zn

5.2 Results and Discussion

5.2.1 Powder X-ray diffraction

The PXRD patterns for each of the gold porphyrin complexes are shown in **Figure 5.7**. Notably, the presence, or absence, of zinc did not appear to have an impact on crystallinity. Conversely, the level of substitution appeared to have a marked effect. The powder patterns for the di-substituted species (**Compound 5.1** and **Compound 5.3**) both showed numerous clear, sharp diffraction peaks, a strong indicator of crystallinity, while the tetra-substituted species (**Compound 5.2** and **Compound 5.4**) only showed a few weak, broad peaks at low scattering angles. This suggests that the bulk material of **Compound 5.2** and **Compound 5.4** was largely amorphous.

Assuming the hypothesis from **Section 5.1.2** holds true, **Compound 5.1** and **Compound 5.3** are promising targets for analysis via electron diffraction, while **Compound 5.2** and **Compound 5.4** will likely not be suitable candidates for 3DED and will require further optimisation of crystallisation.
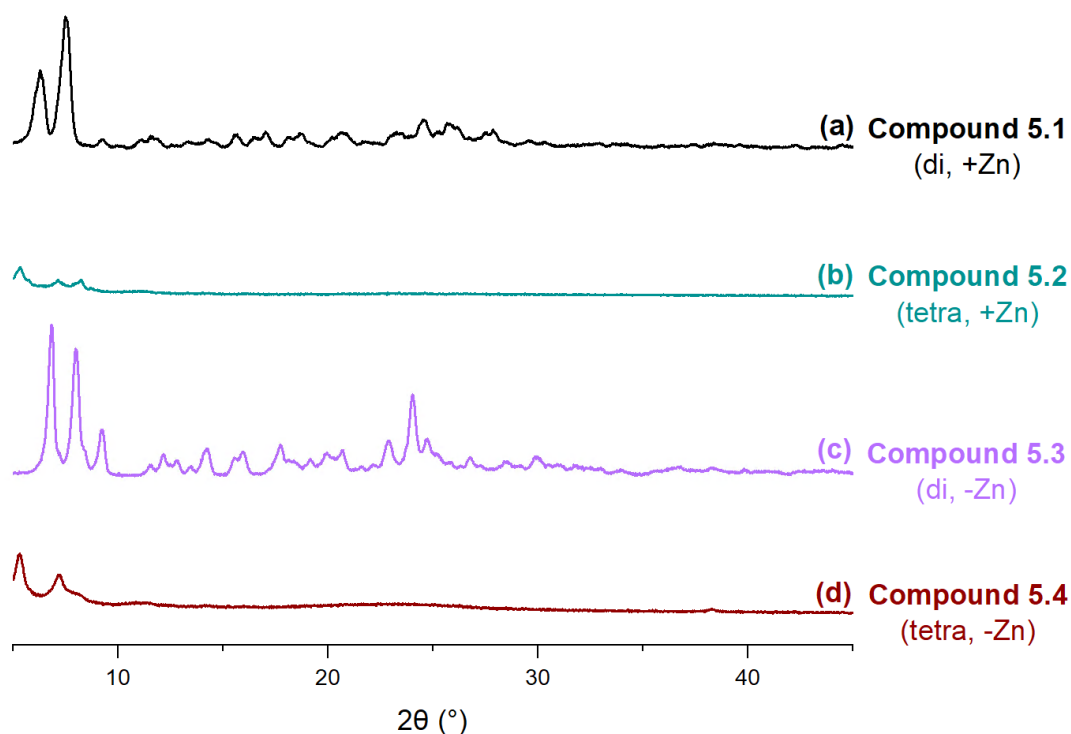
Figure 5.7. PXRD patterns of the gold porphyrin complexes. Where (a) is the powder pattern of Compound 5.1, (b) of Compound 5.2, (c) of Compound 5.3 and (d) of Compound 5.4.

5.2.2 Single crystal X-ray diffraction

The structure of **Compound 5.1** was determined using SCXRD. Data were collected from a single crystal resulting in data completeness of 99.9%. Only a 0.95 Å resolution was attained. Refinement resulted in a poor structural solution for X-ray diffraction data (R_1=12.3%, $P2_1/c$ space group). The structure model with thermal ellipsoids at 50% probability is given in **Figure 5.8**. The crystallographic and refinement data are provided in **Table 5.1**.

The quality of the single crystals of **Compound 5.1** proved to be poor for SCXRD. The diffraction observed was weak and smeared, characteristic of a structure in which layer slipping has occurred. The ADPs were particularly large and elongated, as can be seen in **Figure 5.8**. The phenyl groups (C_6H_4 linkers) were disordered and were modelled across two positions. The alkyne groups appear to be distorted from linearity (C-C-Au and C-C-C bond angles were 174° and 163°/166° respectively (see **Table 5.4**), accounting for the two potential carbon positions in the phenyl group). However, it is believed that this is an artefact of the poor data quality. The zinc porphyrin core was planar, with the gold complexes being almost coplanar to the porphyrin core (~5 -7°).

89
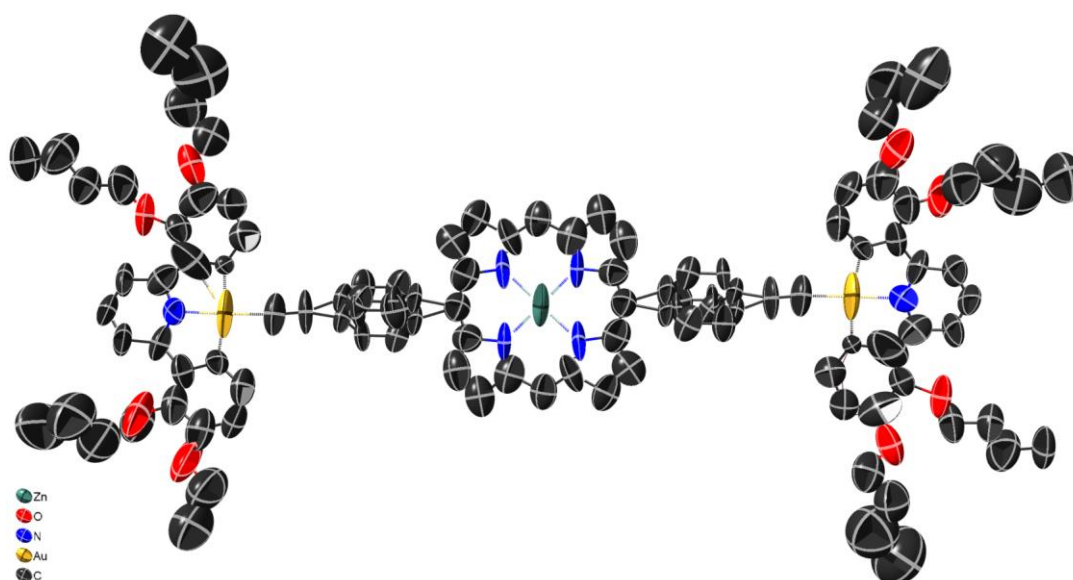
Figure 5.8. SCXRD structure of Compound 5.1. *Thermal ellipsoids are shown at a probability level of 50%. For clarity, hydrogen atoms are not displayed. The bridging C_6H_4 unit was disordered and modelled in two positions with refined occupancies of 0.56:0.44(2). Atom Key: black=C, yellow=Au, blue=N, red=O, green=Zn*

Table 5.1. SCXRD crystallographic and refinement data for Compound 5.1.

Empirical formula	$C_{102}H_{104}Au_2N_6O_8Zn$
Formula weight	2001.21
Temperature (K)	110
Crystal system	monoclinic
Space group	$P2_1/c$
a (Å)	11.6257(13)
b (Å)	27.837(8)
c (Å)	13.3257(10)
β (°)	99.291(10)
Volume (Å^3)	4255.9(14)
Z	2
ρ_{calc} (g/cm^3)	1.562
Reflections measured	12339
Independent reflections (with I > 2 σ(I))	5182 (2182)
Resolution (Å)	0.95
Completeness (%)	99.9
Restraints/parameters	402/528
R_{int}	0.0839
R_1 [I > 2 σ(I)]	0.1228
R_1 [all data]	0.2173
wR_2 [all data]	0.4004
GooF	1.088
Residual potential(e/Å)	1.747/-1.422

5.2.3 Electron diffraction sample screening

During sample screening, it was found that the di-substituted complexes (**Compound 5.1** and **Compound 5.3**) contained numerous well diffracting crystals that were easy to find and abundant on the grid (**Figure 5.9 (a) and (c)**). It was possible to collect electron diffraction data from these species and determine their structures. Conversely, sample screening for **Compound 5.2** and **Compound 5.4**, the tetra-substituted species, proved less successful. Although a few targets of these samples did produce diffraction patterns, finding diffracting material was challenging and time consuming as most of the targets were amorphous, i.e., they did not produce diffraction patterns.

When diffraction patterns were observed from **Compound 5.2** and **Compound 5.4**, the resolution was substantially lower than for the di-substituted complexes (~2.49 Å compared to ~0.8 Å). The reflections observed for the tetra-substituted complexes was streaked (**Figure 5.9 (b) and (d)**). This is consistent with a planar structure in which layer slipping has occurred. This may be as a result of the high degree of planarity of the tetra-substituted complexes. Some disorder may be introduced due to dislocations or slipping of the stacked, large planar molecules. Stacked, planar molecules may be prone to shear. Grinding the samples between two microscope slides to generate suitably thin material may have exacerbated this, introducing more disorder. However, it was not possible to grow crystals of **Compound 5.2** and **Compound 5.4** that were large enough and of sufficient quality for structure determination via SCXRD suggesting this disorder was intrinsic to the complexes and not as a result of sample grinding. The tetra-substituted complexes are large, planar molecules with a high number of n-butoxy-chains in the gold complexes, that likely impede crystal packing.

(a)

Compound 5.1
(di, +Zn)

(b)

Compound 5.2
(tetra, +Zn)

(c)

Compound 5.3
(di, -Zn)

(d)

Compound 5.4
(tetra, -Zn)
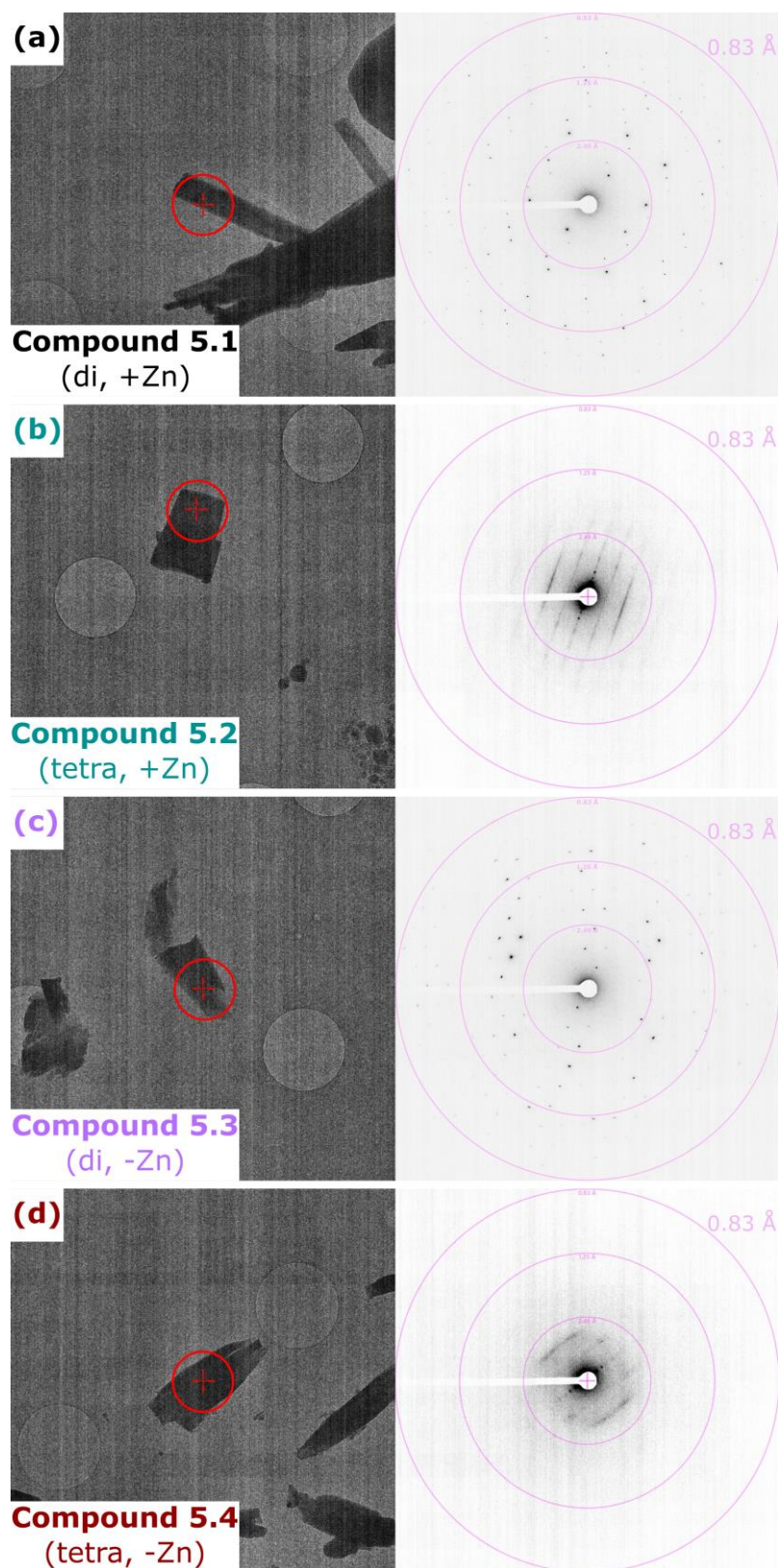
*Figure 5.9. Representative crystals and diffraction test images from each of the gold porphyrin samples. Left: TEM brightfield image of a crystal, red circle represents the beam diameter (1.05 µm). Right: Representative diffraction test image, outer resolution ring is 0.83 Å. Where (a) is a crystal and test image from **Compound 5.1**, (b) from **Compound 5.2**, (c) from **Compound 5.3** and (d) from **Compound 5.4**.*

5.2.4 Electron diffraction structures of di-substituted gold porphyrin complexes

For **Compound 5.1**, 6 datasets from 6 crystals were combined to give 94.8% complete data to 0.83 Å resolution. Crystallographic and refinement data for **Compound 5.1** are presented in **Table 5.2**. Refinement resulted in a good structural solution (R$_1$=17.6%, $P\bar{1}$ space group), the structure model is shown in **Figure 5.10**. The structure model of the ASU with the electrostatic potential map is presented in **Figure 5.11**. The zinc porphyrin core was planar, and the gold complexes were almost coplanar with the porphyrin core (2.41°). Distortion of the alkyne group from linearity was observed about the triple bond. With C-C-Au and C-C-C bond angles measuring 176.9° and 176.2° respectively. This was however consistent with the linker starting material, suggesting there was little change in linker structure on binding to the porphyrin.[205] A table of selected bond distances and bond angles for the 3DED structure of **Compound 5.1** is presented in **Table 5.4**.

Table 5.2. Electron diffraction crystallographic and refinement data for Compound 5.1.

Empirical formula	$C_{102}H_{104}Au_2N_6O_8Zn$
Formula weight	2001.21
Temperature (K)	80
Crystal system	Triclinic
Space group	$P\bar{1}$
a (Å)	10.3836(12)
b (Å)	14.4055(8)
c (Å)	16.6489(9)
α (°)	114.396(4)
β (°)	90.968(7)
γ (°)	110.053(6)
Volume (Å^3)	2093.6(3)
Z	1
ρ_{calc} (g/cm^3)	1.587
Reflections measured	34782
Independent reflections (with I > 2 σ(I))	8025 (6411)
Resolution (Å)	0.83
Completeness (%)	94.8
Restraints/parameters	508/543
R$_{int}$	0.1419
R$_1$ [I > 2 σ(I)]	0.1763
R$_1$ [all data]	0.1996
wR$_2$ [all data]	0.4078
GooF	1.239
Residual potential (e/Å)	1.220/-0.884
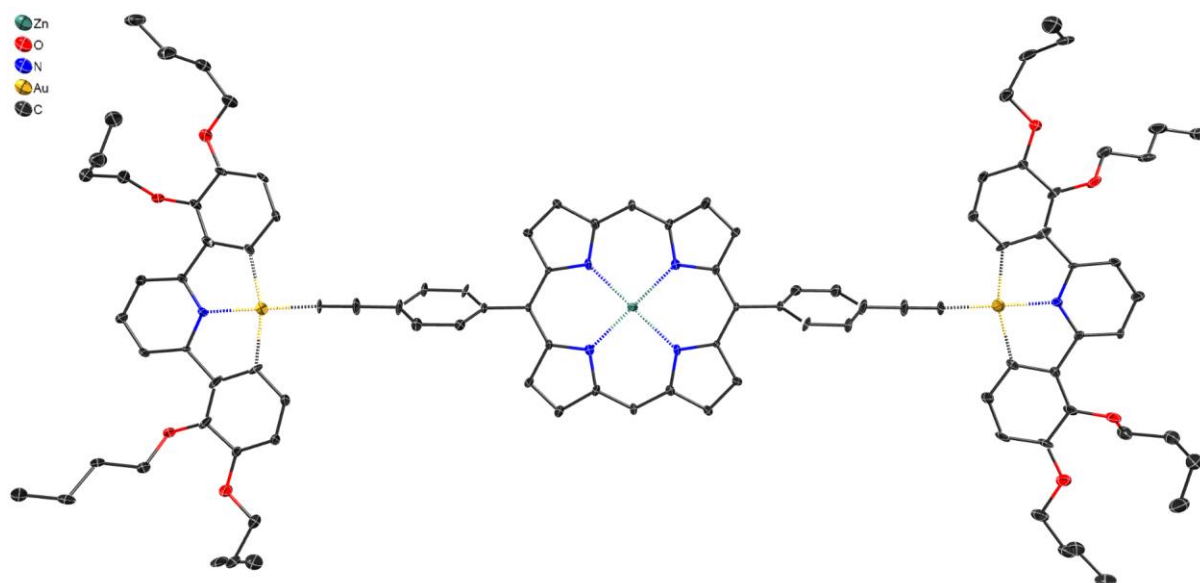
Figure 5.10. 3DED structure of Compound 5.1. *Thermal ellipsoids are shown at a probability level of 50%. For clarity, hydrogen atoms are not displayed. Atom Key: black=C, yellow=Au, blue=N, red=O, green=Zn.*
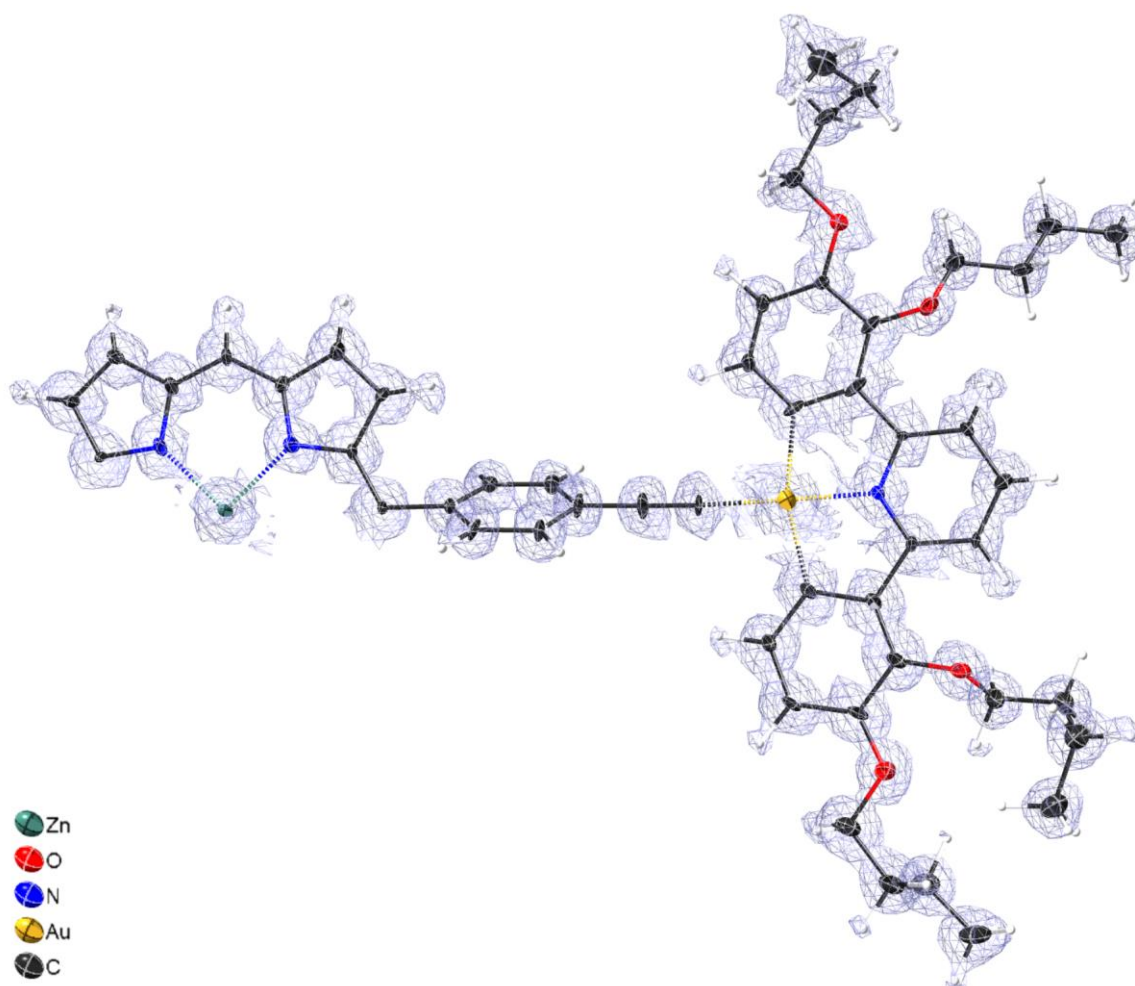
Figure 5.11. 3DED structure of Compound 5.1. Fo map contoured at 1.20 e/Å. *Thermal ellipsoids are shown at a probability level of 50%. Atom Key: black=C, yellow=Au, blue=N, red=O, green=Zn, white=H. For clarity, only the ASU is shown.*

For **Compound 5.3**, 5 datasets from 5 crystals could be combined resulting in 91.7% complete data to 0.83 Å resolution. Crystallographic and refinement data for this **Compound 5.3** are presented in **Table 5.3**. Refinement resulted in a good structural solution (R₁=17.2%, $P\bar{1}$ space group), the structure model is shown in **Figure 5.12**. The structure model of the ASU with the electrostatic potential map is presented in **Figure 5.13**. The zinc porphyrin core was slightly distorted from planarity by a singular pyrrole. The gold complexes were almost coplanar with the porphyrin core (9.87°). Distortion of the alkyne group from linearity was observed about the triple bond. With C-C-Au and C-C-C bond angles measuring 167.2° and 175.6° respectively. This was a strong distortion from linearity. A table of selected bond distances and bond angles for the 3DED structure of **Compound 5.3** is presented in **Table 5.4**.

Table 5.3. Crystallographic and refinement data for Compound 5.3.

|	
Empirical formula	$C_{102}H_{106}Au_2N_6O_8$
Formula weight	1937.86
Temperature (K)	80
Crystal system	Triclinic
Space group	$P\bar{1}$
a (Å)	12.1045(6)
b (Å)	14.7327(17)
c (Å)	15.1904(11)
α (°)	115.601(6)
β (°)	93.921(6)
γ (°)	113.621(6)
Volume (Å³)	2140.5(3)
Z	1
ρ_{calc} (g/cm³)	1.503
Reflections measured	26561
Independent reflections (with I > 2 σ(I))	7196 (5631)
Resolution (Å)	0.83
Completeness (%)	91.7
Restraints/parameters	475/537
Rint	0.1237
R_1 [I > 2 σ(I)]	0.1722
R_1 [all data]	0.1971
wR_2 [all data]	0.4169
GooF	1.026
Residual potential (e/Å)	1.277/-0.791
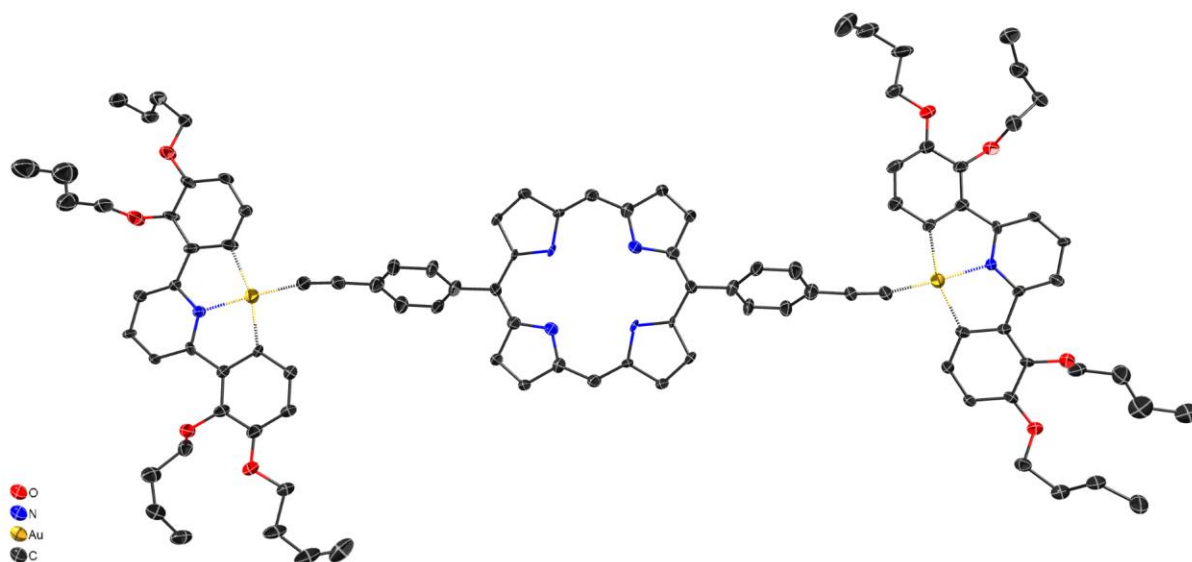
Figure 5.12. 3DED structure of Compound 5.3. *Thermal ellipsoids are shown at a probability level of 50%. For clarity, hydrogen atoms are not displayed. Atom Key: black=C, yellow=Au, blue=N, red=O.*
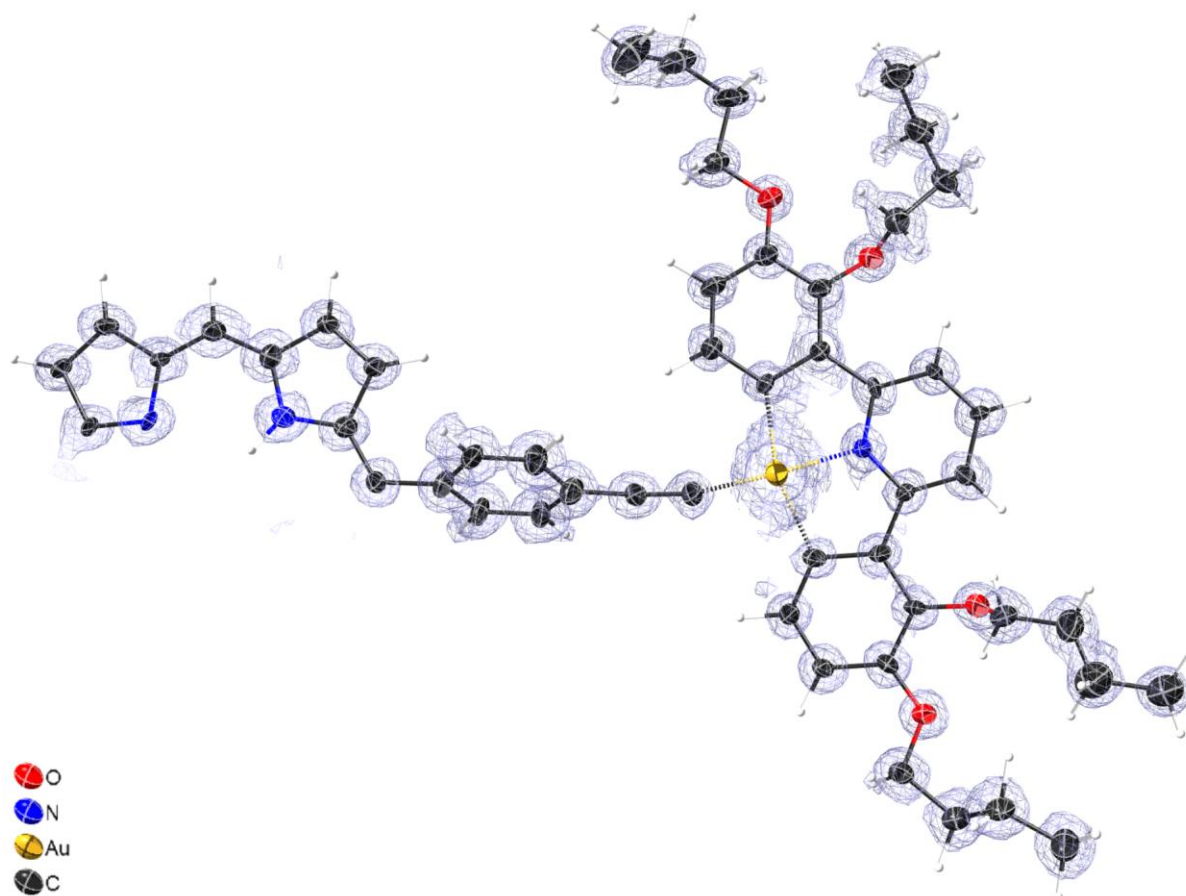
Figure 5.13. 3DED structure of Compound 5.3. Fo map contoured at 1.13 e/Å. *Thermal ellipsoids are shown at a probability level of 50%. Atom Key: black=C, yellow=Au, blue=N, red=O white=H. For clarity, only the ASU is shown.*

Table 5.4. Selected bond distances and angles from the X-ray and 3DED structures of Compound 5.1 and the 3DED structure of Compound 5.3.
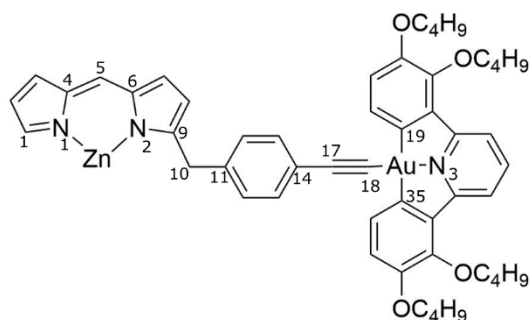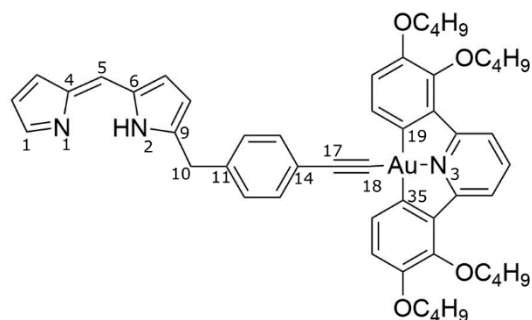
Compound 5.1   Compound 5.3

Bond distance (Å)	Compound 5.1 X-ray	Compound 5.1 3DED	Compound 5.3 3DED
Zn—N1	2.06(3)	2.085(9)	—
Zn—N2	2.03(3)	2.052(9)	—
N1—C4	1.31(4)	1.385(14)	1.379(12)
C4—C5	1.32(4)	1.392(13)	1.370(13)
C5—C6	1.51(5)	1.412(13)	1.401(14)
C6—N2	1.30(4)	1.381(14)	1.360(14)
N2—C9	1.46(4)	1.376(12)	1.377(14)
C9—C10	1.28(4)	1.433(14)	1.385(14)
C10—C1	1.33(5)	1.421(13)	1.441(13)
C10—C11*	1.71(4) 1.74(4)	1.491(12)	1.494(14)
C14—C17*	1.52(4) 1.46(4)	1.421(13)	1.421(15)
C17—C18	1.21(4)	1.240(13)	1.259(15)
C18—Au	1.98(3)	1.953(9)	1.936(11)
Au—N3	2.04(2)	1.997(8)	2.009(9)
Au—C19	1.951(15)	2.033(11)	2.021(10)
Au—C35	1.910(14)	2.055(10)	2.061(11)

Bond angle (°)	Compound 5.1 X-ray	Compound 5.1 3DED	Compound 5.3 3DED
N1—Zn—N2	88.7(12) 91.3(12)	88.6(4) 91.4(4)	—
C14—C17—C18*	163(4) 166(5)	176.2(13)	175.6(13)
C17—C18—Au	174(4)	176.9(10)	167.2(10)

Two conformations are modelled in the X-ray structure due to disorder of the phenyl group linkers, as such two numbers are reported for the X-ray bond distances and angles.

5.2.5   Comparison of X-ray and electron diffraction experiments

5.2.5.1   Compound 5.1

In the SCXRD studies, a single crystal of **Compound 5.1** gave a structure with a monoclinic unit cell in a $P2_1/c$ space group, with unit cell parameters: a=11.6257 Å, b=27.837 Å, c=13.3257 Å, α=90°, β=99.291°, γ=90°. However, the quality of the crystal proved to be poor. The diffraction from the crystal was weak and smeared, yielding a structure with very large and elongated ADPs. By comparison, the structure obtained from 3DED was of higher quality and had smaller ADPs.

In the 3DED studies, a total of 14 datasets were collected from 14 crystals of **Compound 5.1**. The final structure resulted from the combination of 6 of these datasets to give a triclinic unit cell in a $P\bar{1}$ space group. The unit cell parameters of this structure were: a=10.3836 Å, b=14.4055 Å, c=16.6489 Å, α=114.396°, β=90.968°, γ=110.053°. Of the 14 datasets collected, 11 indexed to give this solution. It was not possible to reindex these datasets to obtain a solution with $P2$ symmetry. This suggests that the crystals studied in SCXRD experiments and electron diffraction experiments had different crystal packing. This is not entirely surprising as the crystals were formed via different crystallisation methods. The crystals suitable for SCXRD were grown via slow diffusion, whereas the microcrystals suitable for electron diffraction were formed much more rapidly. While the packing of these structures is similar, the slow diffusion crystallisation method may have allowed the molecules to pack more efficiently, however as the crystals grew larger, disorder was introduced due to the planarity and size of the molecules, reducing the diffraction quality.

The remaining 3 datasets collected by electron diffraction could be indexed to give a solution that appeared to be similar to the SCXRD structure. The data indexed in a $P2$ space group with approximate unit cell parameters: a=11.7 Å, b=28.2, c=13.4 Å, α=90°, β=99°, γ=90°. Unfortunately, like the crystal from the SCXRD experiment, the diffraction from these crystals was poor and characterised by low resolution, smeared reflections. Due to the poor quality, low resolution, and low completeness of the data, structure determination from these datasets was not possible. This does however suggest that multiple crystal forms were present in the sample.
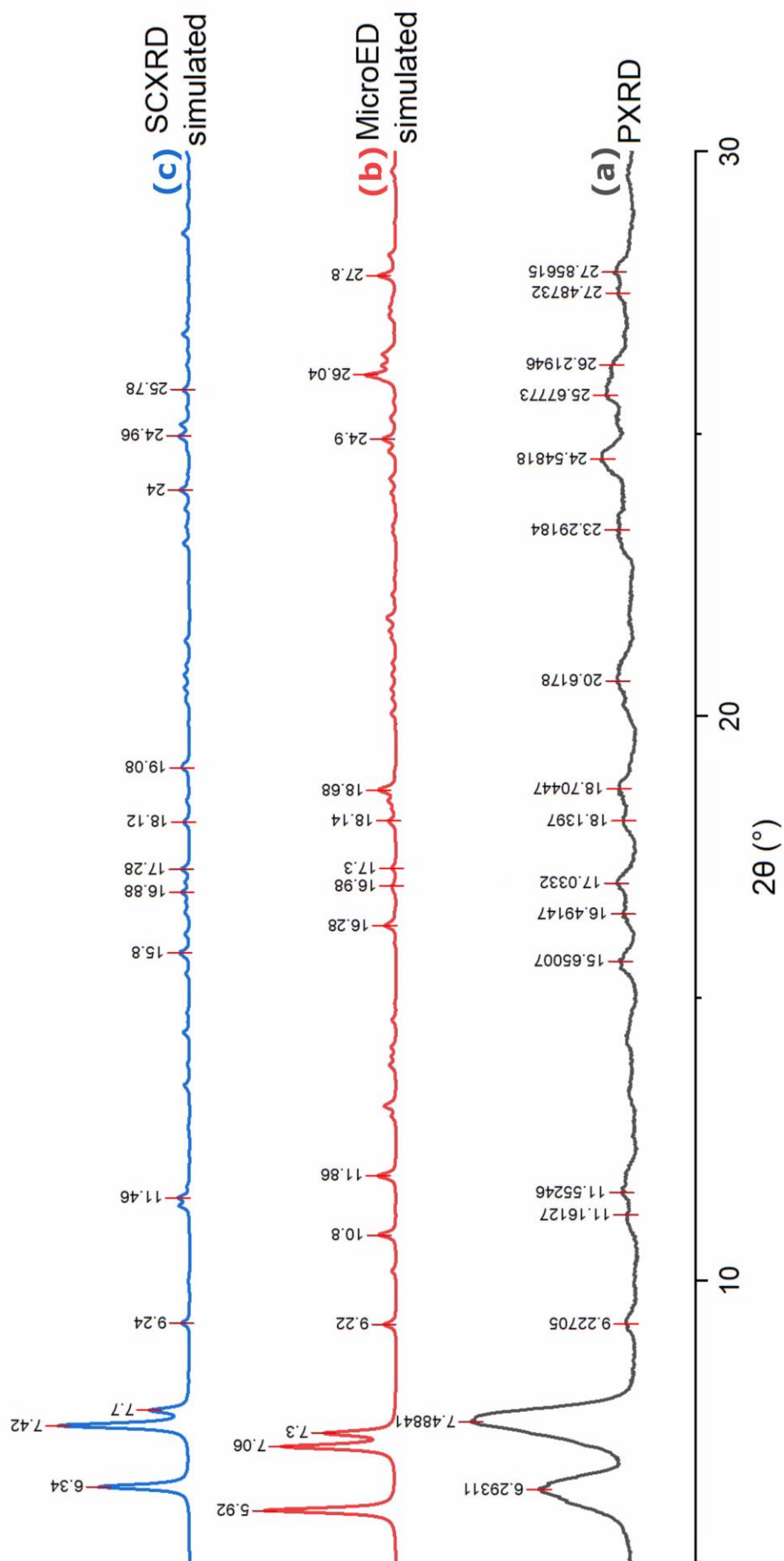
Figure 5.14. Comparison of simulated and actual PXRD diffraction patterns of Compound 5.1. *Where (a) is the PXRD pattern of the bulk material, (b) is the simulated 3DED pattern of **Compound 5.1**, and (c) is the simulated SCXRD pattern of **Compound 5.1**. Notably, the sample used in (c) was formed via a different crystallisation method to those used in (a) and (b).*

Powder patterns were simulated for the SCXRD and 3DED structures of **Compound 5.1**. These simulated patterns were then compared with the actual PXRD data from the sample of the material later used in 3DED studies. The simulated and actual PXRD patterns for **Compound 5.1** are shown in **Figure 5.14**. It should be noted that data were collected at different temperatures for each of the diffraction methods. PXRD data were recorded at room temperature, 3DED data at 80 K, and SCXRD data at 110 K. Another point of consideration is that the peak positions for the simulated 3DED powder pattern may be affected by inaccuracies in the calibration of the detector distance. Detector distance and unit cell parameters are intrinsically linked. The simulated peak positions for 3DED data result from the best estimate of the average unit cell parameters from multiple crystals. As such, the unit cell parameters may not be a reflection of a single crystal.

The simulated powder patterns for SCXRD and 3DED data appear to be similar. Each having three peaks of similar intensity and distribution in the 5.92° − 7.7° 2θ region. In the PXRD powder pattern, there are only 2 peaks present in this region, however peak broadening is observed. While the peak maxima (6.29° and 7.49°) and peak intensities more closely match the peak maxima of the SCXRD data (6.34° and 7.42°) than the 3DED data (5.92° and 7.06°), the broadness of the peaks does encompass the 2θ region in which the 3DED peaks lie. The remainder of the peaks are of lower intensity. However, in the PXRD pattern, peaks are present in the region of 25.5° to 26.5° and 27.3° and 28.2° that appear to correspond, albeit at a slight offset with peaks in the 3DED pattern at 26.04° and 27.8°. These peaks are not present in the simulated SCXRD pattern.

The PXRD pre-screening of **Compound 5.1** confirmed that the sample contained crystalline material. While peak broadening made it difficult to directly compare and match the simulated and actual peak positions in the powder patterns, a visual comparison indicates that the $P2_1/c$ crystal form determined by SCXRD is likely the bulk component in the sample. Additionally, it appears that the $P\overline{1}$ crystal form determined by 3DED may also be present and detectable in the bulk material by PXRD. In 3DED experiments, the best diffracting crystals found were those with a $P\overline{1}$ space group. 11 of the 14 datasets collected indexed to give this crystal form. An additional 3 crystals were found that indexed to give a solution with similar parameters as the structure determined by SCXRD. Despite being a bulk component in the material as identified by PXRD, the $P2_1/c$ crystal form was less prevalent on the scale of 3DED data collection.

5.2.5.2 Compound 5.3
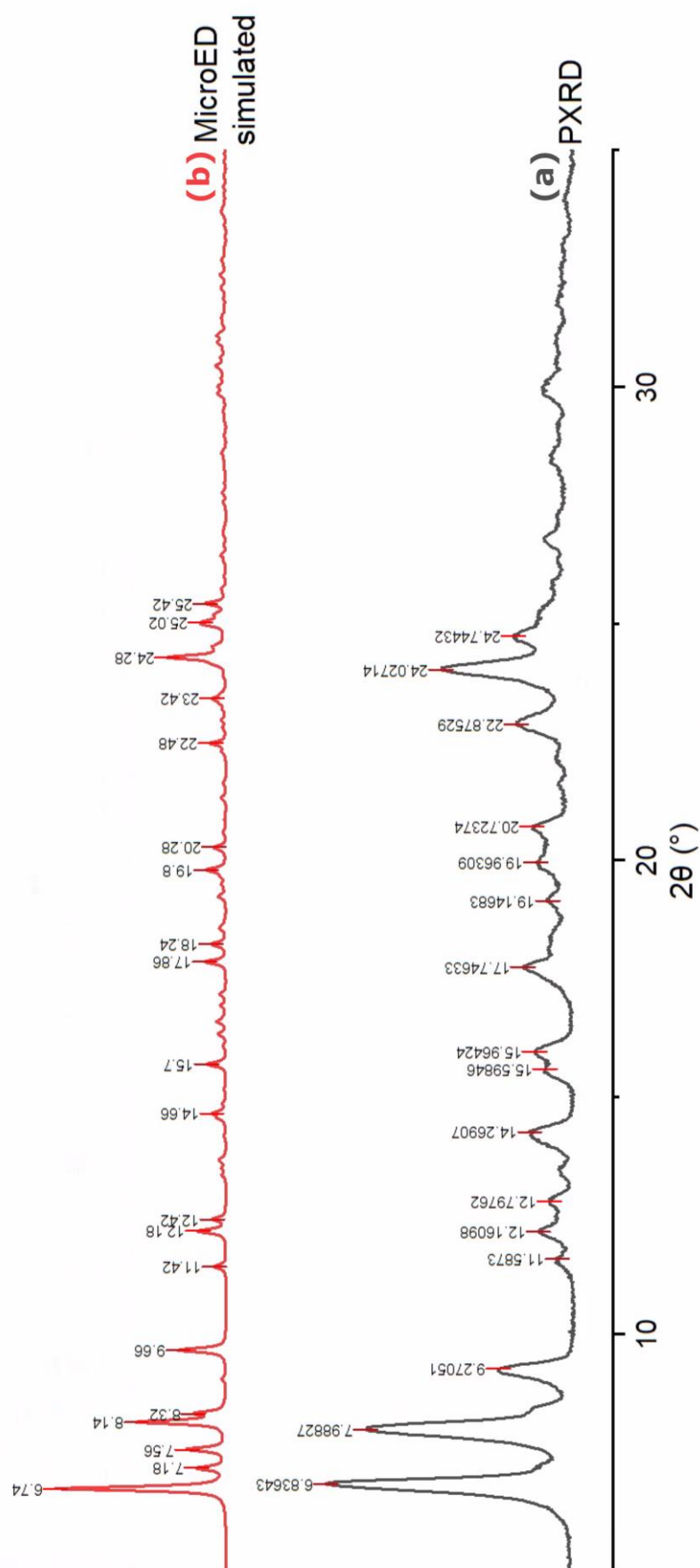
Figure 5.15. Comparison of simulated and actual PXRD diffraction patterns of Compound 5.3. Where (a) is the PXRD pattern of the bulk material and (b) is the simulated 3DED pattern of Compound 5.3.

A powder pattern was simulated from the 3DED structure of **Compound 5.3**. This simulated pattern was then compared with the actual PXRD pattern of the bulk sample of **Compound 5.3**. The simulated and actual diffraction patterns are presented in **Figure 5.15**.

The PXRD experiment performed on **Compound 5.3** indicated that the sample contained crystalline material. This was confirmed during the 3DED studies. A total of 6 datasets were collected from 6 different crystals present on the grid. All datasets indexed to give the same solution. 5 of the 6 datasets were merged to give the final solution in a $P\bar{1}$ space group.

The simulated and actual powder patterns do show similarities. The peak positions of the largest peaks (6.74° and 8.14°) in the 3DED pattern are similar to those in the PXRD patten (6.84° and 7.99°). The broadness of the peaks in the PXRD pattern may have led to the intermediate peaks (7.18° and 7.56°) being obscured by the baseline. Additionally, there are similarities in the peaks located in the region of 11.3° and 13.0° in both patterns, as well as peaks in the 24.0° to 25.5° areas. Conversely, there are peaks present in the PXRD patterns that are absent from the simulated pattern. Notably the peaks with maxima at 2θ angles of 14.27°, 15.60°, 15.96°, and 22.88°. This may suggest that an alternate crystal form or impurity is present in the bulk material. No alternate crystal forms were observed during electron diffraction data collection, however only a small number of datasets (6) were collected from this sample, so alternate crystal forms or impurities may have been missed.

This raises an interesting discussion point. When screening samples, researchers aim to target crystals that produce high quality diffraction patterns. Once well diffracting crystals have been found, researchers then search for targets with similar attributes, such as size, thickness, morphology, and edge sharpness, in the hopes of collecting further data. In the case of **Compound 5.1**, needle-like crystals were found to produce the best quality diffraction patterns, as such needle-like crystals were subsequently targeted in preference to other morphologies from which no or poor diffraction patterns were previously observed. This may introduce a selection bias, and other diffracting crystal forms may be missed, as such the data collected in 3DED experiments may not be representative of the bulk material.

5.3   Conclusions

Structure determination of two di-substituted gold porphyrin complexes (**Compound 5.1** and **Compound 5.3**) using electron diffraction was successful. It was possible to grow crystals of **Compound 5.1** of sufficient size for characterisation via SCXRD, however the quality of the crystals proved to be poor, resulting in a poor SCXRD structure with particularly elongated ADPs. It was not possible to grow crystals of **Compound 5.3** suitable for SCXRD. It was not possible to determine the structures of the tetra-substituted gold porphyrin complexes (**Compound 5.2** and **Compound 5.4**) via SCXRD or 3DED. This is likely due to the nature of the complexes. The tetra-substituted gold porphyrin complexes are large planar complexes with a high number of n-butoxy-chains, that likely impede crystal packing. Using 3DED, it was possible to determine the structure of **Compound 5.1** to a higher quality than that which could be achieved using SCXRD. Additionally, it was possible to determine the structure of **Compound 5.3** using 3DED when the quality and size of the crystals proved insufficient for SCXRD.

PXRD provided a valuable insight into the crystallinity of the samples prior to screening and data collection on a TEM. The PXRD studies showed that samples of the di-substituted complexes (**Compound 5.1** and **Compound 5.3**) were crystalline, this was confirmed when well diffracting crystals were found in 3DED experiments, and the structures of **Compound 5.1** and **Compound 5.3** could be determined via electron diffraction studies. Conversely, the PXRD patterns showed that samples of the tetra-substituted complexes (**Compound 5.2** and **Compound 5.4**) were not crystalline. During 3DED experiments, only poorly diffracting material was observed, and it was not possible to solve these structures. These results suggest that PXRD can be used as a valuable pre-screening tool for electron diffraction to indicate crystallinity before microscope screening. This enables a more efficient and effective use of valuable microscope time and researcher resources. PXRD is a fast and effective test for crystallinity when sufficient quantity of sample is available.

In some cases, it may be possible to find trace amounts of well diffracting material via electron diffraction even if PXRD studies indicate the bulk sample crystallinity is poor. Unfortunately, finding diffracting material in a sample that is largely comprised of amorphous material will likely be a difficult and time consuming process that may not result in success.

PXRD is the study of bulk material, whereas electron diffraction utilises individual, tiny crystals. As such, the crystals studied in 3DED experiments may not be representative of the bulk material. This may be further exacerbated by human bias introduced during target selection. If particular morphologies are favoured when selecting crystals, other crystal forms may be missed. However, selecting targets with similar attributes to well diffracting crystals that have been previously found, may be the most efficient way to collect data and achieve structures with high completeness. It is important to note, that in this study, the samples provided for 3DED experiments had gone through an attempted recrystallisation step, rather than being freshly synthesised. The aim of the experiment was to determine whether structural determination could be performed on these materials using 3DED. As such, an extensive search for alternate crystal forms or impurities was not performed once structures had been determined. As such, it would not be a valuable use of researcher time to continue to screen targets with unfavourable morphologies similar to those which had not produced diffraction patterns during the sample screening.

This could be a case of interest for future automation, in instances where the sample contains multiple species or crystal forms that need to be identified, for instance, in an as synthesised sample where further purification and crystallisation have not been performed. **Chapter 7** provides an example of such a case. Target selection could be performed in an automated fashion, and data would be collected from all targets, in an attempt to identify as many crystal forms as possible. This would, however, likely lead to many poor quality, unusable datasets being collected. This automated approach could be performed by collecting a single diffraction image from each crystal in a method known as serial electron diffraction (SerialED) as developed by Stephan Smeets *et al.*[208,209] The downside of the SerialED approach is that indexing individual electron diffraction patterns can be particularly difficult as all three unit cell dimensions cannot usually be determined from a single diffraction image due to the flatness of the Ewald sphere, see **Chapter 3, Section 3.2.2** for further details. This difficulty would be exacerbated if multiple crystal forms or impurities were present. Alternatively, data could be collected via a serial rotation electron diffraction (SerialRED) as developed by Wang *et al*.[210] SerialRED has been successfully used to identify multiple phases of a polycrystalline material.[211] This is a high throughput method and confers an advantage over the SerialED approach as indexing rotation electron diffraction data is easier than indexing single diffraction images.

6 Characterisation of a series of manganese complexes of relevance to catalysis

A series of manganese complexes and their precursor ligand were studied by electron diffraction. Only a scarce quantity of each sample was available for 3DED analysis (<1 mg). Due to the minimal quantities, no PXRD pre-screening, or sample grinding were performed prior to TEM screening and data collection. Additionally, the small size of the crystals precluded their characterisation by in-house, SCXRD, as such, analysis by 3DED was the only way to provide structural information. The six previously uncharacterised samples provided a valuable test set, allowing the throughput and efficiency of our electron diffraction workflow (See **Chapter 9**) on the York Glacios to be examined. The samples were allocated two days of microscope time, all data were collected over the course of two 12-hour sessions. Preliminary data processing and structure solution were performed concurrently to data collection. This ensured whether structure determination was possible for each sample and verified whether the sample was the expected complex. On the fly data processing also gave an indication of when sufficient data had been collected from an individual sample to achieve a high completeness merged dataset for each structure. The target completeness for combined datasets from each individual compound was ~90-95%. Once this was achieved, the next compound could be loaded, enabling efficient use of microscope time by avoiding collection of tens of unnecessary datasets.

6.1 Methods

6.1.1 Sample Preparation

The manganese complexes, and precursor ligand shown in **Figure 6.1** were prepared by Thomas Burden, of Professor Ian Fairlamb's group at the University of York. While the synthesis of these complexes is beyond the scope of this thesis, as the primary focus is their characterisation by electron diffraction, details can be found in Thomas Burden's Thesis.[212]

Pre-clipped Quantifoil Cu R2/4 grids were placed directly in individual vials containing samples of **Compounds 6.1 – 6.6**. The vials were gently shaken to allow sample transfer. The grids were cooled to liquid nitrogen temperature, transferred to the cassette, and loaded into the TEM. See **Chapter 9, Section 9.1** for further details on grid preparation. For **Compound 6.4,** initial screening indicated that there had been insufficient transfer of sample to the grid, as the grid was sparsely populated with

sample. However, diffraction from the few targets that were present and of suitable thickness indicated that the sample was crystalline. On visual inspection of this sample in the vial, it appeared to have formed larger aggregates (<1mm in diameter), whereas the other samples were fine powders. The size and thickness of the aggregates were prohibitively large for study by electron diffraction. Additionally, the large size of the aggregates likely inhibited sample transfer. To remedy this, the sample was gently crushed in the vial using a micro-spatula. Once crushed, a second grid with this sample was prepared as described above. This improved the transfer of sample to grid, as such more targets of suitable thickness were present on the grid. Brightfield, low magnification images of the first and second grids prepared of **Compound 6.4** are shown in **Figure 6.2**, highlighting the improved sample transfer. This simple optimisation would have been impossible without feedback from preliminary screening using the TEM to observe the extent of sample transfer.
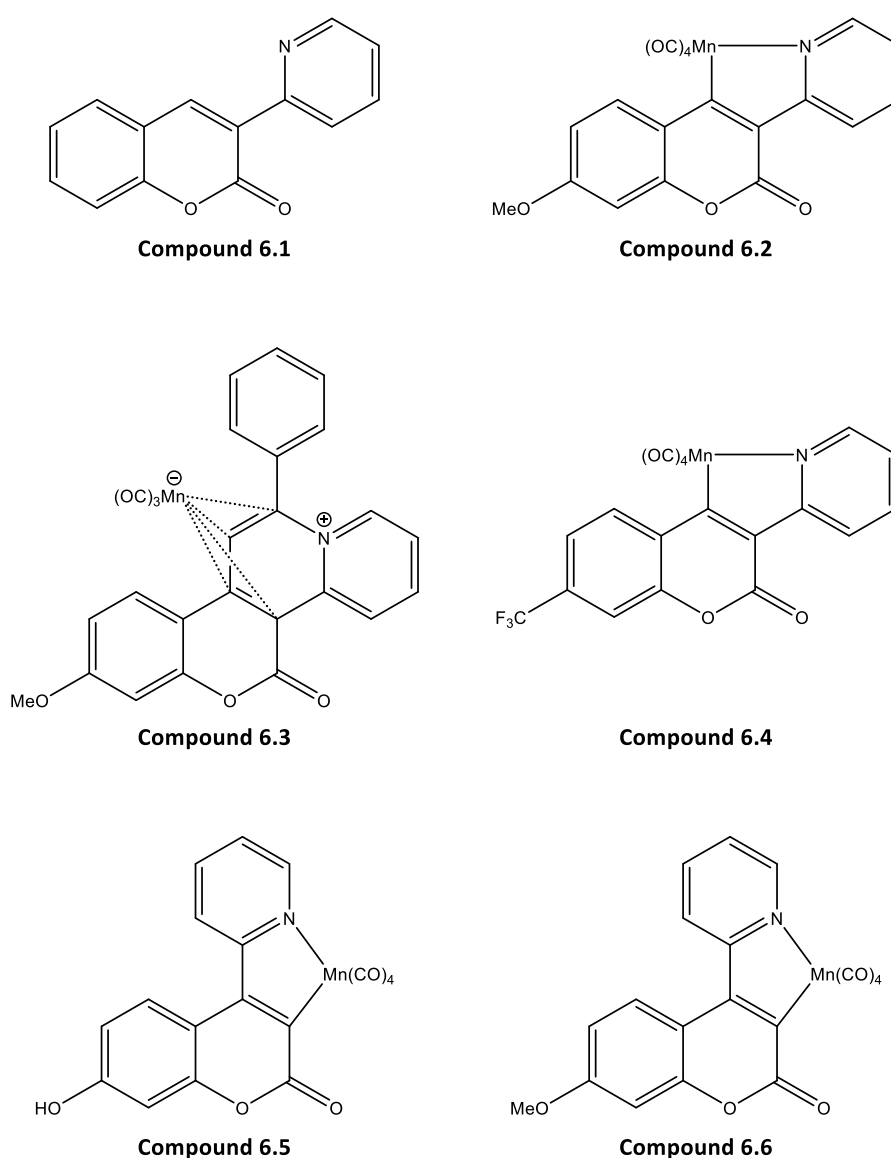
Figure 6.1. Structures of the ligand and manganese complexes (Compounds 6.1 – 6.6).
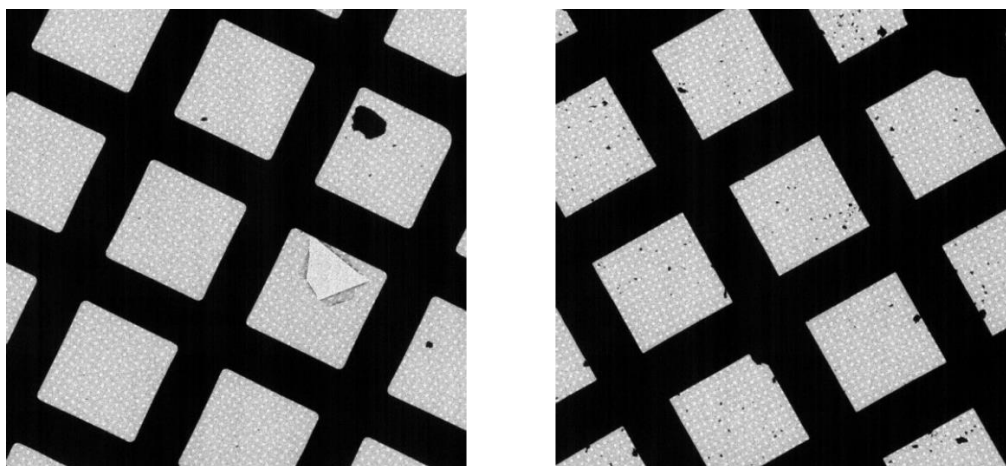
Figure 6.2. TEM brightfield low magnification images of grids containing Compound 6.4. Left: first grid prepared from unground sample, the grid is sparsely populated, with a few large materials that are too thick to study by electron diffraction. Right: second grid prepared after sample grinding, the grid is better populated and contains numerous targets of suitable size for electron diffraction.

6.1.2   Data acquisition

Electron diffraction data were acquired using a Thermo Fisher Glacios microscope operating at a voltage of 200 kV using a Ceta-D camera, as described in **Chapter 9, Section 9.2**. Data were collected at 80 K. Nanobeam electron diffraction with the following illumination conditions was used to achieve a low flux of ~0.07 e$^-$ Å^{-2} s^{-1}: gun lens 8, spot size 11, 30 µm C2 aperture. The illumination conditions resulted in parallel beam with a diameter of 1.05 µm. Please see **Chapter 2, Section 2.2.3** for further details. EPU-D was used to collect data in a semi-automated fashion with the following settings: 2x binning, a rotation speed of 1.333°/s and an exposure time of 0.75 s, resulting in a $\Delta\varphi$ of 1°/frame. A representation of the beam diameter on the sample and an example electron diffraction pattern from **Compound 6.1** are shown in **Figure 6.3**.

Notably, in the top right-hand corner of brightfield image in **Figure 6.3**, the edge of a curled piece of carbon film is visible. This is more clearly shown in a lower magnification brightfield image of the same area (**Figure 6.4**). Collecting datasets from crystals on film that has been damaged and as a result, has curled, or from crystals which overhang broken film, can significantly increase the overall data completeness.[213] This is especially important when crystals lie on the grid in a preferred orientation and therefore data completeness is not improved by collecting data from additional crystals on unbroken film. Crystals on damaged film are often in completely different orientations to those on flat, unbroken film. Despite this being excellent for collecting data from different wedges of reciprocal

space, it can be particularly challenging to centre such crystals at eucentric height, as such it may only be possible to collect small wedges of data from them.
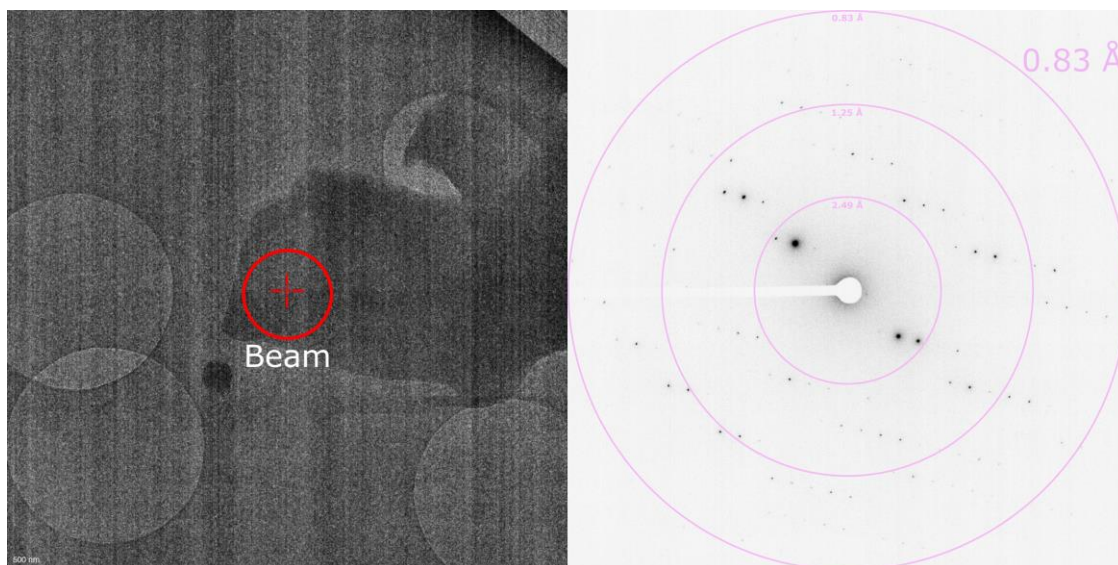
Figure 6.3. Example Compound 6.1 crystal and diffraction pattern. *Left: TEM brightfield image of **Compound 6.1** crystal, red circle represents the beam diameter (1.05 μm). Right: Representative electron diffraction pattern, with resolution rings. Outer resolution ring is 0.83 Å.*
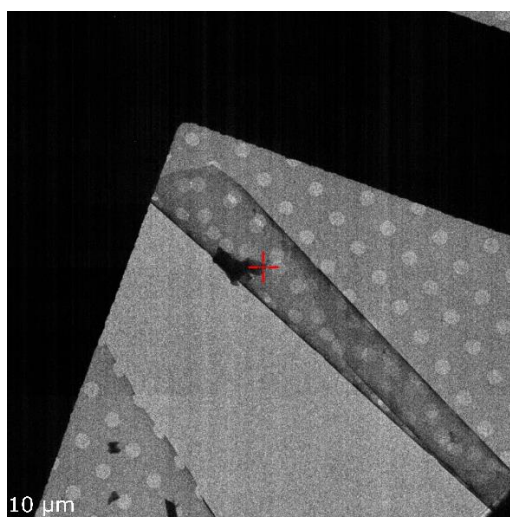
Figure 6.4. Low magnification brightfield image of a grid square with curled film. *On the curled film there are crystals of **Compound 6.1**. The red cross is centred on the same crystal as seen above in **Figure 6.3**. Note, the image is flipped compared to **Figure 6.3**, this is as a result of changes to the projector lens system when changing magnification from SA mode to low mag mode. Details of the projector lens system are given in **Chapter 2, Section 2.1.2**.*

6.1.3   Data processing and structure determination

Data processing was performed using DIALS software.[201] Full details of the data processing workflow are presented in **Chapter 9, Section 9.3**. For each of the datasets, a pedestal of 64 ADU was added to each pixel value. The detector distance of 958.5 mm, as calibrated by aluminium powder was specified, as was the goniometer rotation axis of 1,0,0, for rotation of the goniometer in a positive direction around the horizontal axis. Explanation of these terms and why they needed to be specified is given in **Chapter 9, Section 9.3.1**.

The semi-automatic processing script[202] processed each dataset individually up to the integration stage by running through a standard series of DIALS commands. This required input datasets to be manually added. Once all datasets for a compound had been integrated, the results were manually inspected and datasets with the same space group and unit cell parameters could be scaled together. To achieve the best solution, the results of scaling were carefully analysed and entire datasets, or frames from a dataset could be removed. Dataset selection was based on maximising completeness, while negating a detrimental impact on $CC\frac{1}{2}$ or R_{merge}. The selection process and terms $\Delta CC\frac{1}{2}$ and R_{merge} are described in **Chapter 9, Section 9.3.6**.

For **Compound 6.1**, 5 datasets from 5 crystals were combined to give a completeness of 92.5% to 0.83 Å resolution. For **Compound 6.2**, a single dataset from 1 crystal gave a completeness of 93.1% to 0.83 Å resolution. For **Compound 6.3**, 3 datasets from 3 crystals were combined to give a completeness of 86.6% to 0.83 Å resolution. For **Compound 6.4**, 5 datasets from 5 crystals were combined to give a completeness of 99.9% to 0.83 Å resolution. For **Compound 6.6**, 5 datasets from 5 crystals were merged together to give a completeness of 91.7% to 0.83 Å resolution. Unfortunately, for **Compound 6.5**, no diffracting material was observed during sample screening and as such no datasets could be collected from this material.

The strong reflections from the combined datasets were then filtered for joint refinement of detector distance and unit cell parameters for each dataset. The unit cell parameters for each of the combined datasets were then refined by fitting calculated to observed 2θ values. This allows estimation of the estimated standard deviations (ESDs) on the 'best' cell parameters for the combined datasets, see **Chapter 9, Section 9.3.7** for more details.

Structure determination was performed *ab initio* using SHELXT.[164] General information on structure determination by direct methods using SHELXT is presented in **Chapter 3, Section 3.3.4** and information on how structures within this thesis were phased is given in **Chapter 9, Section 9.4**. The command line switches `-a -y -m500` were applied when phasing data for **Compounds 6.1 – 6.4 and Compound 6.6**.

Structure refinement was performed using SHELXL[165] using electron scattering factors from Peng.[190] General information on structure refinement is provided in **Chapter 3, Section 3.4**, and information on how the structures within this thesis were refined is given in **Chapter 9, Section 9.5**. For all compounds, anisotropic ADPs were refined for all non-hydrogen atoms and all hydrogen atoms were geometrically placed using a riding hydrogen model at the idealised internuclear X-H distances used in refinement of structures against neutron diffraction data with SHELXL.[203]

For **Compound 6.1** and **Compound 6.2**, no restraints were applied during refinement. Refinement of the EXTI parameter alone was sufficient to prevent any atoms from becoming non-positive definite. For the other compounds, ADP restraints were applied in refinement, which together with the refinement of EXTI prevented atoms from becoming non-positive definite without resorting to the use of XNPD or ISOR instructions. For **Compound 6.3** and **Compound 6.4**, RIGU restraints were applied. **Compound 6.6** was refined using a combination of RIGU and SIMU restraints. The use of geometric restraints was not required for any of the structures. Further information on the ADP restraints applied is provided in **Chapter 3, Section 3.4**.

For all compounds presented below, the default weighting scheme was used, as opposed to the recommended SHELXL weighting scheme. The reasoning for this will be explained in further detail in **Section 6.2.7**.

6.2   Results and Discussion

6.2.1   Compound 6.1

For **Compound 6.1**, 5 datasets from 5 crystals were combined to give a completeness of 92.5% to 0.83 Å resolution. Crystallographic and refinement data for this compound are given in **Table 6.1**. Refinement resulted in a good structural solution (R_1 = 13.3%, $Pbca$ space group). The structure model with thermal ellipsoids from the anisotropic refinement and electrostatic potential map are shown in **Figure 6.5**. Structure determination for this compound was trivial. No restraints were applied during structure refinement. A refinement of the EXTI parameter was performed to account for some of the deficiencies of kinematical refinement against electron diffraction data.

Table 6.1. Crystallographic and refinement data for Compound 6.1.

Empirical formula	$C_{14}H_9NO_2$
Formula weight	223.22
Temperature (K)	80
Crystal system	orthorhombic
Space group	$Pbca$
a (Å)	7.0778(2)
b (Å)	13.7315(8)
c (Å)	21.3139(11)
Volume (Å^3)	2071.47(17)
Z	8
ρ_{calc} (g/cm^3)	1.432
Reflections measured	25596
Independent reflections (with I > 2 σ(I))	2219 (1649)
Resolution (Å)	0.83
Completeness (%)	92.5
Restraints/parameters	0/155
R_{int}	0.1939
R_1 [I > 2 σ(I)]	0.1338
R_1 [all data]	0.1601
wR_2 [all data]	0.3268
GooF	1.952
Residual potential (e/Å)	0.539/-0.645

Figure 6.5. 3DED structure of Compound 6.1. *Fo map contoured at 1.76 e/Å. Thermal ellipsoids are shown at a probability level of 50%. Atom key: black=C, white=H, blue=N, O=red.*

6.2.2   Compound 6.2

For **Compound 6.2**, a single dataset from a single crystal gave a completeness of 93.1% to 0.83 Å resolution. Crystallographic and refinement data for this compound are presented in **Table 6.2**. Refinement gave a good structural solution (R_1 = 14.4, $Pbca$ space group). The structure model with thermal ellipsoids and electrostatic potential map are shown in **Figure 6.6**. As with **Compound 6.1**, structure determination with SHELXT was trivial and no restraints were applied during refinement of this structure. A refinement of the EXTI parameter was performed.

Table 6.2. Crystallographic and refinement data for Compound 6.2.

Empirical formula	$C_{19}H_{10}MnNO_7$
Formula weight	419.22
Temperature (K)	80
Crystal system	orthorhombic
Space group	$Pbca$
a (Å)	17.1134(9)
b (Å)	7.2889(4)
c (Å)	27.560(2)
Volume (Å^3)	3437.8(4)
Z	8
ρ_{calc} (g/cm^3)	1.620
Reflections measured	12732
Independent reflections (with I > 2 σ(I))	3012 (1862)
Resolution (Å)	0.83
Completeness (%)	93.1
Restraints/parameters	0/255
R_{int}	0.1628
R_1 [I > 2 σ(I)]	0.1441
R_1 [all data]	0.1877
wR_2 [all data]	0.3323
GooF	1.640
Residual potential (e/Å)	0.652/-0.565
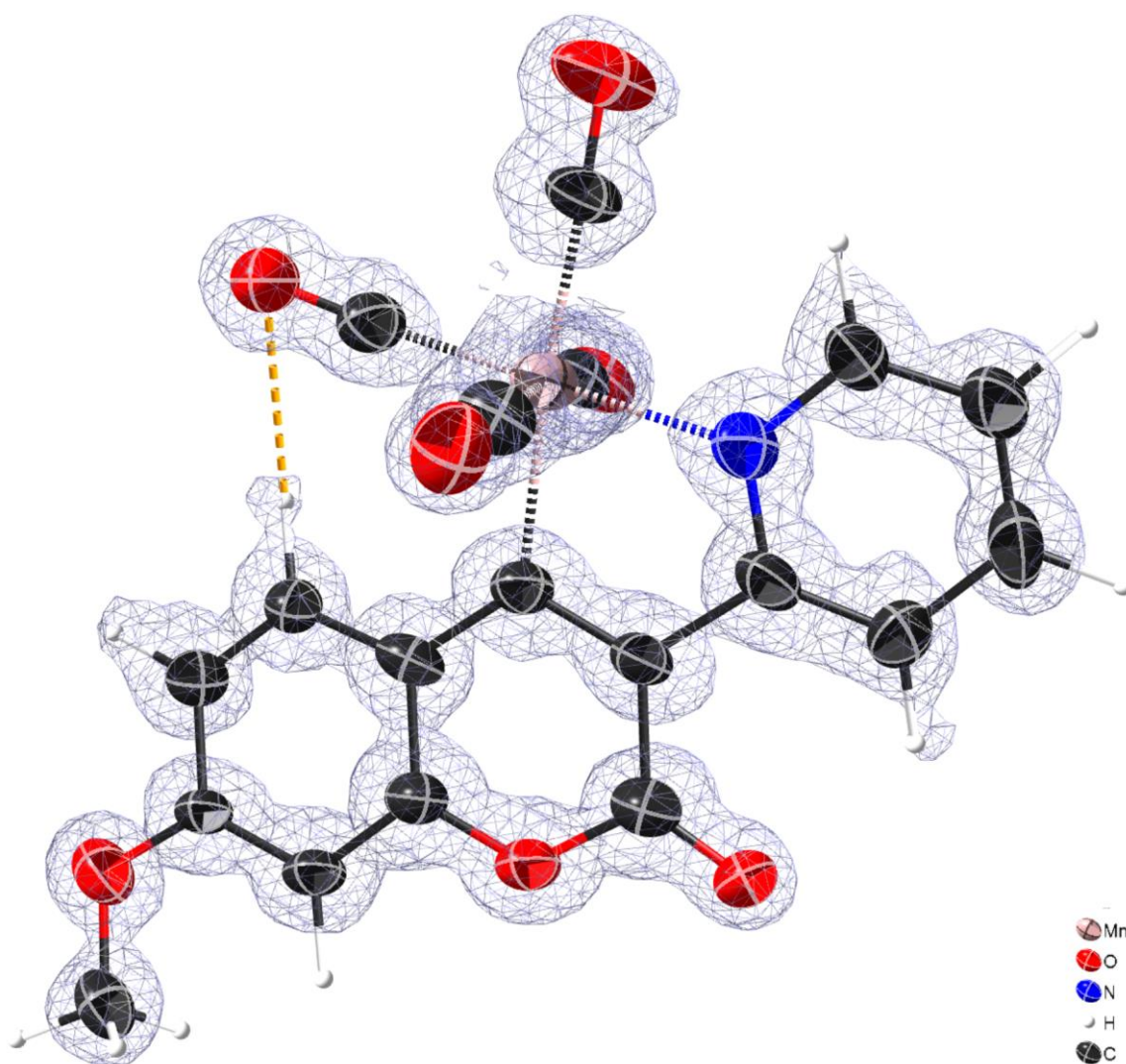
Figure 6.6. 3DED structure of Compound 6.2. Fo map contoured at 1.60 e/Å. Thermal ellipsoids are shown at a probability level of 50%. Atom Key: black=C, white=H, blue=N, O=red, Mn=pink. Yellow dashed line represents hydrogen bonding.

6.2.3   Compound 6.3

For **Compound 6.3**, 3 datasets from 3 crystals were combined to give a completeness of 86.6% to 0.83 Å resolution. Crystallographic and refinement data are shown in **Table 6.3**. Refinement resulted in a good structural solution (R_1 = 16.1, $P2_1/n$ space group), with 2 molecules present in the asymmetric unit (ASU). The 2 molecules are shown separately in the same orientation in **Figure 6.7**. The structure model with thermal ellipsoids and electrostatic potential map are shown in **Figure 6.8**. Structure determination with SHELXT was trivial. RIGU restraints were applied to the ADPs of all non-hydrogen atoms and the EXTI parameter was refined.

Table 6.3. Crystallographic and refinement data for Compound 6.3.

Empirical formula	$C_{26}H_{16}MnNO_6$
Formula weight	493.34
Temperature (K)	80
Crystal system	monoclinic
Space group	$P2_1/n$
a (Å)	16.1523(5)
b (Å)	13.7390(5)
c (Å)	20.648(3)
β (°)	104.036(5)
Volume (Å^3)	4445.3(6)
Z	8
ρ_{calc} (g/cm^3)	1.474
Reflections measured	54390
Independent reflections (with I > 2 σ(I))	8160 (5793)
Resolution (Å)	0.83
Completeness (%)	86.6
Restraints/parameters	660/616
R_{int}	0.1383
R_1 [I > 2 σ(I)]	0.1611
R_1 [all data]	0.1909
wR_2 [all data]	0.3631
GooF	2.139
Residual potential (e/Å)	1.303/-1.034
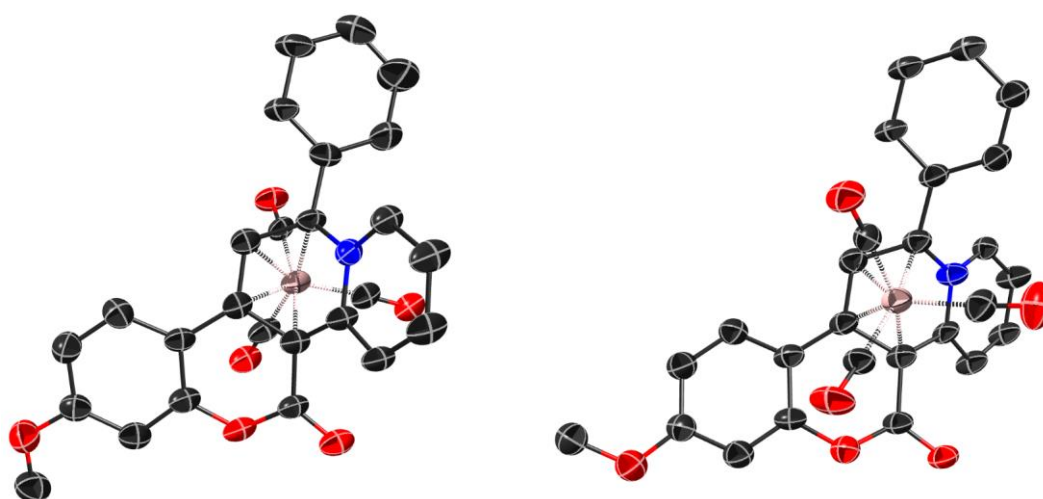
Figure 6.7. 3DED structure of Compound 6.3 with the 2 molecules in the asymmetric unit displayed separately, in the same orientation. *The coumarin ligand is displayed mostly in plane. In the lefthand molecule, the manganese and carbonyl groups point into the plane and the nitrogen containing ring points out of the plane. In the righthand molecule, the manganese and carbonyl groups point out of the plane and the nitrogen containing ring points into the plane. For clarity, hydrogens are not displayed. Thermal ellipsoids are shown at a probability level of 50%. Atom Key: black=C, blue=N, O=red, Mn=pink.*
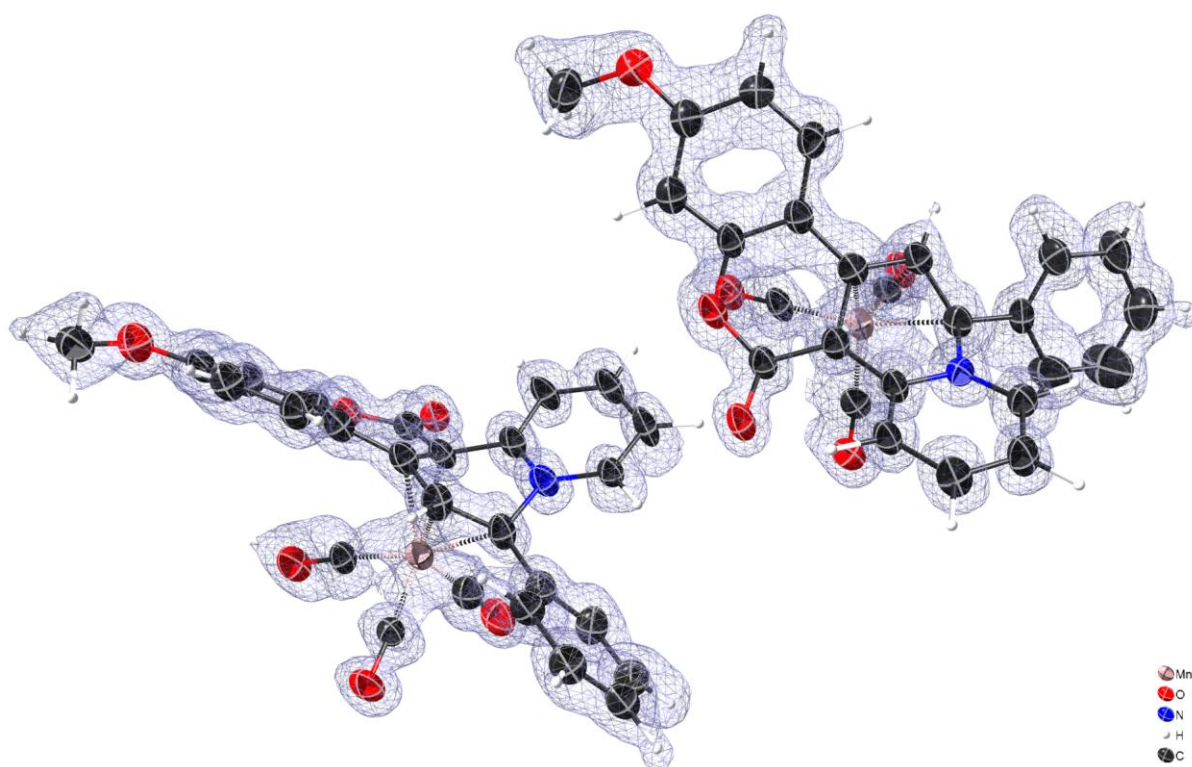
Figure 6.8. 3DED structure of Compound 6.3. *Fo map contoured at 1.73 e/Å. Thermal ellipsoids are shown at a probability level of 50%. Atom Key: black=C, white=H, blue=N, O=red, Mn=pink.*

The 3DED study of **Compound 6.3** confirmed that the manganese coordinated to the ligand via the carbon atoms in the nitrogen containing ring. This arrangement is shown in **Figure 6.1**, and is observed in the subsequent figures, **Figure 6.7** and **Figure 6.8**.

6.2.4   Compound 6.4

For **Compound 6.4**, 5 datasets from 5 crystals were combined to give a completeness of 99.9% to 0.83 Å resolution. The crystallographic and refinement data are shown in **Table 6.4**. Refinement yielded a good structural solution (R_1 = 17.5, $P\bar{1}$ space group). There were 2 molecules present in the ASU. The 2 molecules are shown separately in the same orientation in **Figure 6.9**. The structure model with thermal ellipsoids and electrostatic potential map are presented in **Figure 6.10**. As with previous compounds in this chapter, structure determination with SHELXT was trivial. RIGU restraints were applied to the ADPs of all non-hydrogen atoms and the EXTI parameter was refined to account for ignoring the dynamical contribution to scattering during refinement.

Table 6.4. Crystallographic and refinement data for Compound 6.4.

Empirical formula	$C_{19}H_7F_3MnNO_6$
Formula weight	457.20
Temperature (K)	80
Crystal system	triclinic
Space group	$P\bar{1}$
a (Å)	11.7401(10)
b (Å)	11.9216(14)
c (Å)	14.2162(9)
α (°)	103.081(8)
β (°)	112.798(6)
γ (°)	91.078(9)
Volume (Å^3)	1774.1(3)
Z	4
ρ_{calc} (g/cm^3)	1.712
Reflections measured	30719
Independent reflections (with I > 2 σ(I))	7934 (5415)
Resolution (Å)	0.83
Completeness (%)	99.9
Restraints/parameters	540/542
R_{int}	0.1646
R_1 [I > 2 σ(I)]	0.1749
R_1 [all data]	0.2129
wR_2 [all data]	0.3987
GooF	2.197
Residual potential (e/Å)	0.961/-0.811
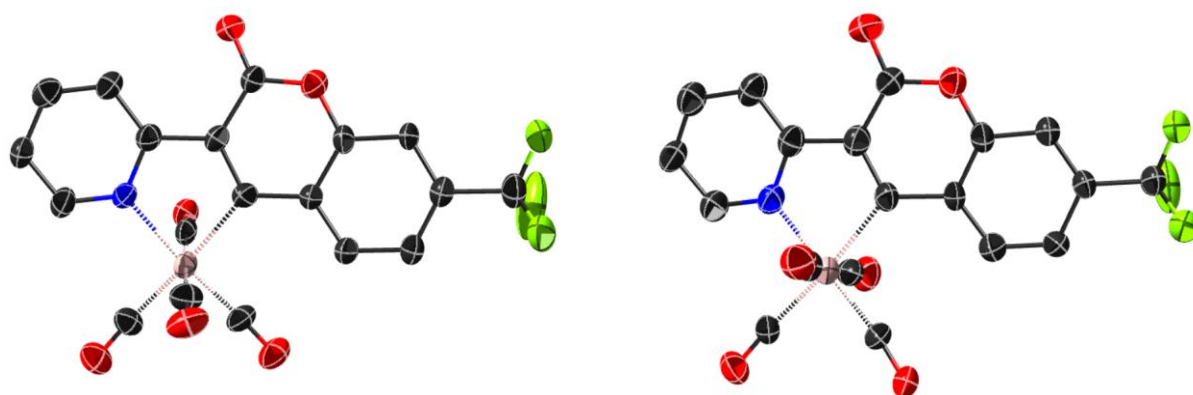
Figure 6.9. 3DED structure of Compound 6.4 with the 2 molecules in the asymmetric unit displayed separately, in the same orientation. *The coumarin ligand is displayed in plane. For clarity, hydrogens are not displayed. Thermal ellipsoids are shown at a probability level of 50%. Atom Key: black=C, blue=N, O=red, F=green, Mn=pink.*
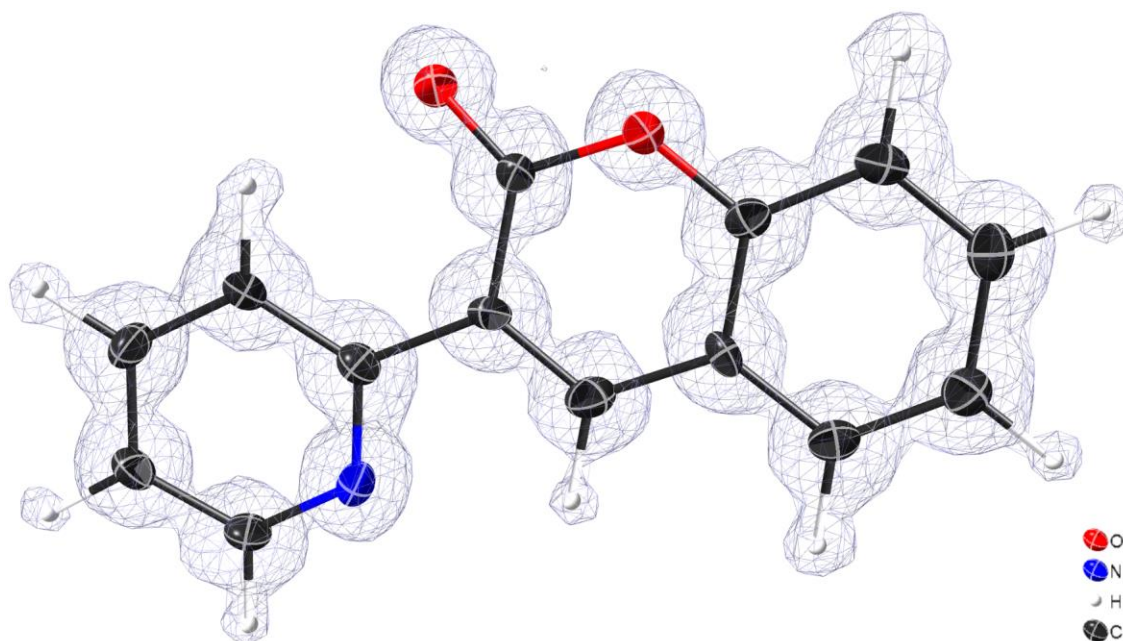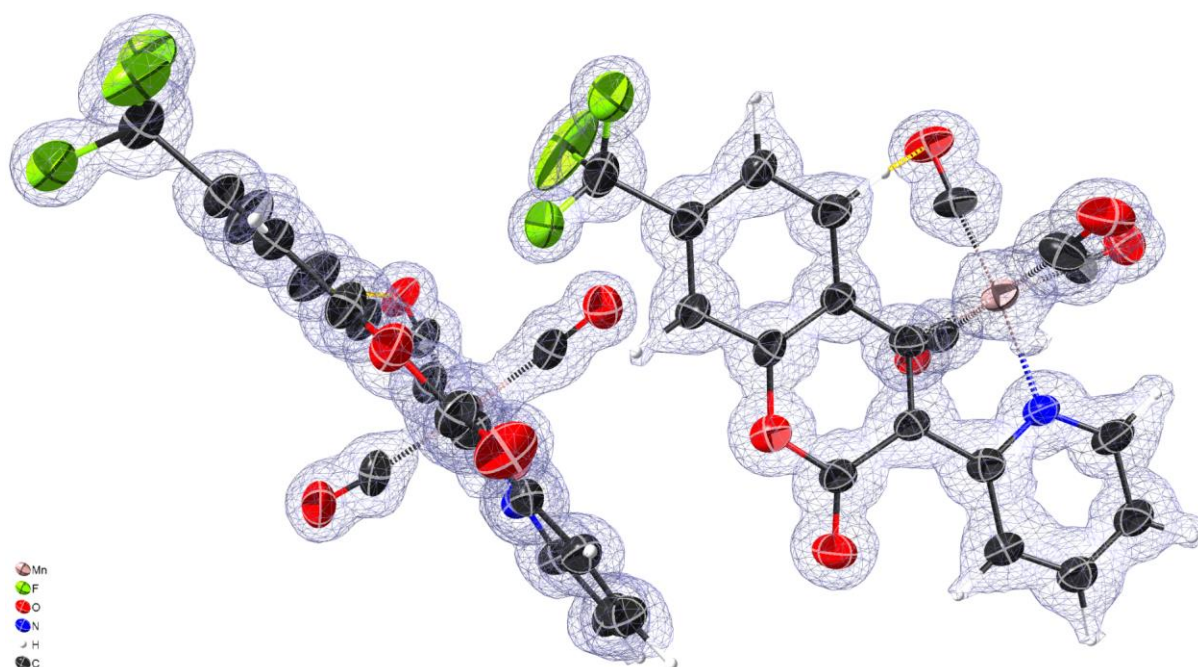
Atom Key:
- Mn
- F
- O
- N
- H
- C

Figure 6.10. 3DED structure of Compound 6.4. Fo map contoured at 1.13 e/Å. Thermal ellipsoids are shown at a probability level of 50%. Atom Key: black=C, white=H, blue=N, O=red, F=green, Mn=pink. Yellow dashed line represents hydrogen bonding.

6.2.5   Compound 6.5

It was not possible to determine the structure of **Compound 6.5** using 3DED. This was because no diffracting material was found during sample screening, despite the grid being well populated with material and containing targets of suitable thickness. An example atlas image of the grid on which **Compound 6.5** was deposited is shown in **Figure 6.11**.
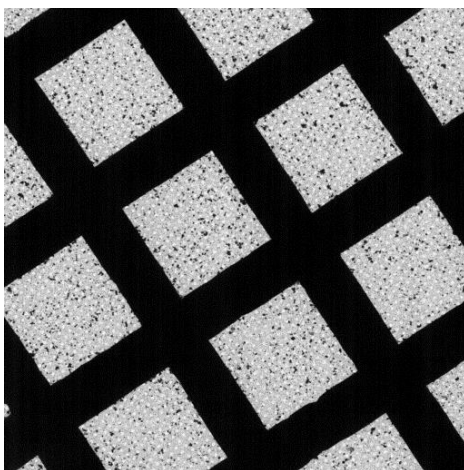
Figure 6.11. TEM brightfield low magnification image of a grid containing Compound 6.5. No diffracting material was found on this grid

6.2.6 Compound 6.6

For **Compound 6.6**, 5 datasets from 5 crystals were merged together to give a completeness of 91.7% to 0.83 Å resolution. The crystallographic and refinement data are provided in **Table 6.5**. Refinement yielded a good structural solution (R$_1$ = 15.7, $P2_1/c$ space group). The structure model for **Compound 6.6** with thermal ellipsoids and electrostatic potential map is presented in **Figure 6.12**. Determining the structure with SHELXT was trivial. During refinement, a global RIGU restraint was applied, alongside a SIMU restraint pertaining to the carbon and nitrogen atoms present in the aromatic ring with a nitrogen hetero atom. A refinement of the EXTI parameter was also performed.

Table 6.5. Crystallographic and refinement data for Compound 6.6.

|	
Empirical formula	$C_{19}H_{10}MnNO_7$
Formula weight	419.22
Temperature (K)	80
Crystal system	monoclinic
Space group	$P2_1/c$
a (Å)	13.4331(8)
b (Å)	10.3241(3)
c (Å)	14.0700(4)
β (°)	117.209(4)
Volume (Å^3)	1735.37(14)
Z	4
ρ_{calc} (g/cm^3)	1.605
Reflections measured	25824
Independent reflections (with I > 2 σ(I))	3298 (2724)
Resolution (Å)	0.83
Completeness (%)	91.7
Restraints/parameters	285/255
R$_{int}$	0.1777
R$_1$ [I > 2 σ(I)]	0.1568
R$_1$ [all data]	0.1788
wR$_2$ [all data]	0.3778
GooF	2.465
Residual potential (e/Å)	0.884/-0.731
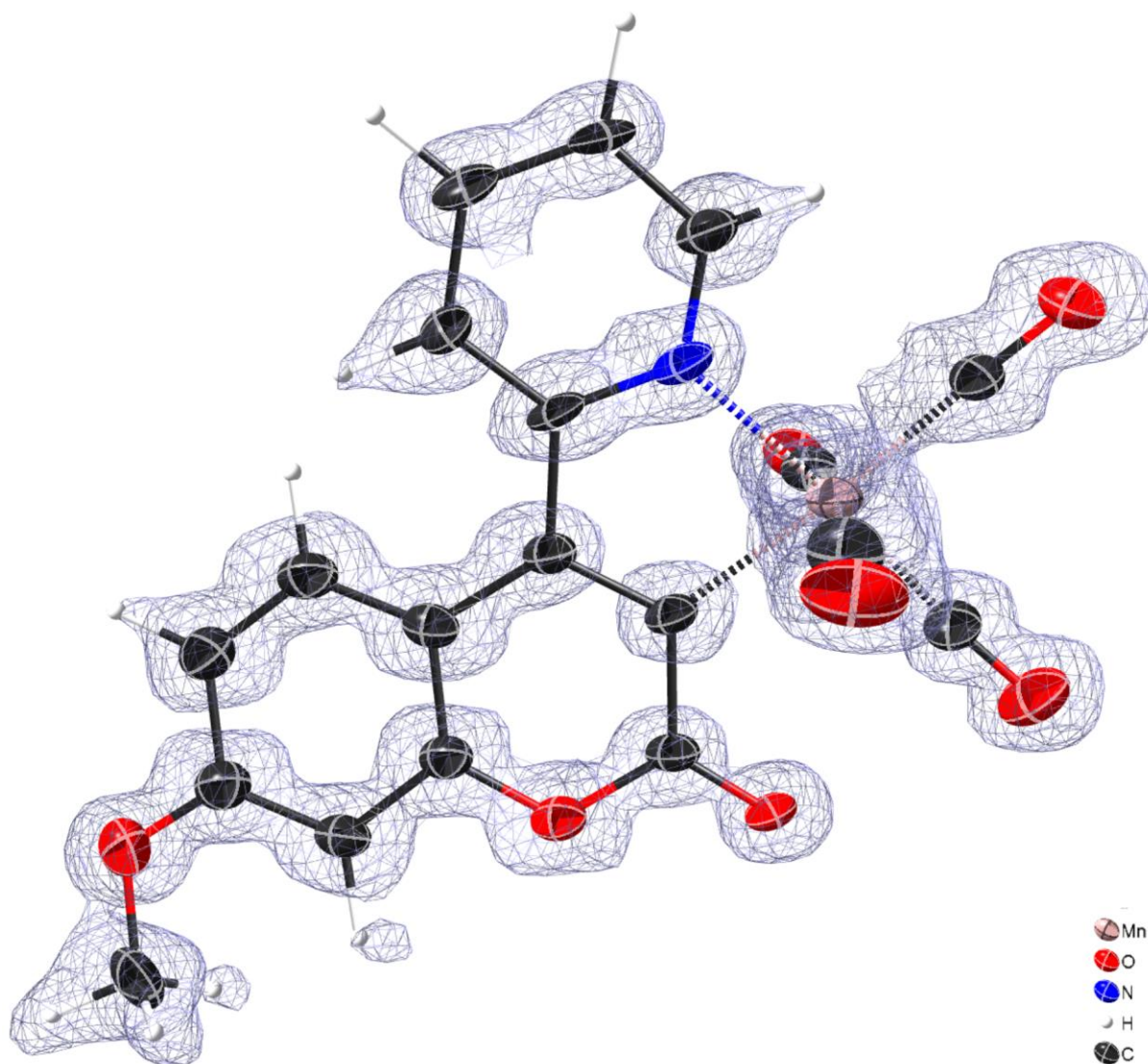
Figure 6.12. 3DED structure of Compound 6.6. *Fo map contoured at 1.43 e/Å. Thermal ellipsoids are shown at a probability level of 50%. Atom Key: black=C, white=H, blue=N, O=red, Mn=pink.*

Selected bond distances and bond angles for all the 3DED structures presented in this chapter are given in **Table 6.6**. No X-ray data for these complexes were available. Notably, the C3—C4 bond of **Compound 6.3** is elongated compared to the other complexes. This is likely as a result of the coordination of the manganese ligand to the nitrogen containing ring at four of the carbon positions, including C3 and C4. Additionally in **Compound 6.3**, the C7—C8 bond is significantly elongated compared to the corresponding bond of the free ligand, **Compound 6.1**. This could be as a result of the electron donating OMe group attached to the C7 position in **Compound 6.3**. However, **Compound 6.2** and **Compound 6.4** are also substituted with an OMe group at the C7 position and the bond is not significantly elongated in these structures.

Table 6.6. Selected bond distances and angles for the 3DED structures of Compounds 6.1 – 6.4 and Compound 6.6.

Compound 6.1

Compound 6.2: R=OMe
Compound 6.4: R=CF$_3$

Compound 6.3
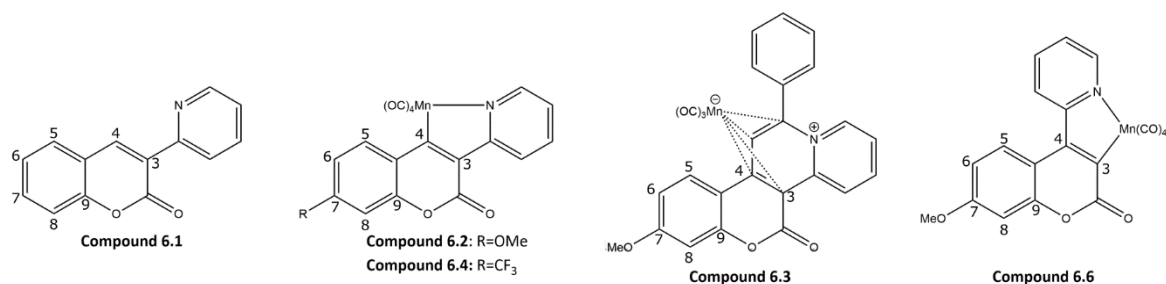
Compound 6.6

Bond distance (Å)	Compound 6.1	Compound 6.2	Compound 6.3	Compound 6.4	Compound 6.6
C3—C4	1.356(7)	1.396(11)	1.475(10) 1.489(11)	1.373(9) 1.379(10)	1.395(11)
C5—C6	1.396(6)	1.353(10)	1.380(14) 1.379(13)	1.417(10) 1.377(11)	1.404(14)
C8—C9	1.416(6)	1.399(10)	1.420(13) 1.372(12)	1.412(9) 1.416(10)	1.422(12)
C6—C7	1.414(7)	1.412(10)	1.413(9) 1.408(8)	1.394(10) 1.427(11)	1.423(10)
C7—C8	1.384(6)	1.396(11)	1.458(13) 1.424(13)	1.388(10) 1.396(10)	1.401(13)

Bond angle (°)	Compound 6.1	Compound 6.2	Compound 6.3	Compound 6.4	Compound 6.6
C5—C6—C7	119.4(4)	121.0(9)	119.2(9) 121.9(9)	118.4(7) 117.9(8)	120.9(8)
C7—C7—C8	118.5(5)	119.2(7)	121.7(8) 117.1(7)	118.2(6) 120.3(7)	117.1(8)
C7—C8—C9	121.4(4)	118.9(7)	115.8(6) 120.3(6)	122.1(7) 119.6(7)	121.1(6)

*There are two molecules in the ASU of **Compound 6.3** and **Compound 6.4**, as such the bond distances and bond angles for both molecules are reported.*

6.2.7 Weighting Scheme

For refinement of the above structures (**Sections 6.2.1 to 6.2.6**), the weighting scheme was not optimised, and the default weight in SHELXL (WGHT 0.1) was used. Typically, SHELXL recommends a weighting scheme. The GooF is a measure of how well the data calculated from the model fits the data observed. The GooF value should be close to unity (1). For all compounds presented here, when using the default weighting scheme, the GooF values were not close to unity. With the best GooF value being 1.64 for **Compound 6.2**, and the worst of 2.465 for **Compound 6.6**. The formula used to calculate GooF (Equation (3.12)) and further details on GooF are presented in **Chapter 3, Section 3.4.5**.

GooF values that are much higher than 1, indicate that aspects of the structure may be unmodelled. In the case of electron diffraction data refined assuming kinematic scattering, the contribution from dynamical scattering is ignored. In an attempt to account for some of this discrepancy, the EXTI parameter is refined. This can compensate for some of the deficiencies in refinement due to the dynamical effects not being considered. Electrons can scatter elastically multiple times as they pass through a crystal; they experience no loss in energy during these events. As a result, the position of the Bragg peaks remains unchanged while the intensities of the Bragg peaks are redistributed. See **Chapter 3, Section 3.2.1**. This leads to the intensity of weak peaks becoming systematically stronger, and the strong peaks becoming systematically weaker.[23,24] EXTI has a dependence on $sin(2\theta)$, as such EXTI refinement weights reflections differently depending on their intensity, as low resolution reflections are typically stronger than high resolution reflections. See **Chapter 3, Section 3.4.4**. This is similar to what an empirical dynamical scattering correction[24] would achieve, where the transfer of intensity due to dynamical scattering would be addressed properly. Full dynamical refinement would be preferable[182] instead of compensating for the dynamical effects using refinement of the EXTI parameter, however this was beyond the scope of this work.

The structures of **Compounds 6.1 – 6.4 and Compound 6.6** were refined again using the weighting scheme suggested by SHELXL. All other variables in the refinement were kept the same. Only the weighting scheme was changed, and a single round of refinement (10 least squares refinement cycles) was performed. The results of refinement with the default and recommended weighting schemes are presented below in **Table 6.7**. As expected, when utilising the SHELXL recommended weighting scheme, the GooF values for all structures become closer to unity. For all compounds, the R_1 values decreased, an apparent improvement, while the wR_2 values increase compared to refinement with the default weighting scheme.

While using the SHELXL recommended weighting scheme does improve the R_1 values and GooF for all structures. It was decided that the default weight would be used instead here. By utilising the SHELXL weighting scheme, the GooF for almost any dataset can be made close to unity, making GooF an essentially meaningless measure of data and model quality. It would be beneficial to have a standardised means of reporting the GooF values on deposited electron diffraction structures so that the values can be comparative and meaningful. The models refined with SHELXL weight optimisation are not necessarily better refined than the models refined without weight optimisation. For X-ray data, where it can generally be reasonably assumed that the data have been reliably recorded, if GooF is

still much higher than 1 following weight optimisation, this provides a strong suggestion that the model is deficient. For electron data, treated kinematically, this assumption does not hold true as the data contain systematic errors.

Table 6.7. Comparative table showing the refinement data for Compounds 6.1 – 6.4 and Compound 6.6 when the default weighting scheme and SHELXL recommended weighting scheme are utilised.

	Compound 6.1		Compound 6.2		Compound 6.3		Compound 6.4		Compound 6.6	
	Default	SHELXL	Default	SHELXL	Default	SHELXL	Default	SHELXL	Default	SHELXL
R_1 [I > 2 σ(I)]	0.1338	0.1317	0.1441	0.1422	0.1611	0.158	0.1749	0.1721	0.1568	0.1555
R_1 [all data]	0.1601	0.1581	0.1877	0.1844	0.1909	0.187	0.2129	0.2088	0.1788	0.1771
wR_2 [all data]	0.3268	0.3391	0.3323	0.3851	0.3631	0.3963	0.3987	0.4426	0.3778	0.3995
GooF	1.952	1.21	1.64	1.077	2.139	1.183	2.197	1.134	2.465	1.296
Residual density ($e^-/Å$)	0.539/ -0.645	0.492/ -0.648	0.652/ -0.565	0.638/ -0.562	1.303/ -1.034	1.317/ -1.001	0.961/ -0.811	0.964/ -0.788	0.884/ -0.731	0.861/ -0.738

6.3 Conclusions

Compounds 6.1 – 6.6 provided an excellent test set to allow the throughput and efficiency of our workflow to be investigated. Data were collected over the course of two 12-hour sessions. During this time, the structures of five of the six compounds were successfully determined, to a high resolution (0.83 Å) and high completeness (>90%). With the exception of **Compound 6.3** which only reached a completeness of 86.6%. Data collection and data processing were performed concurrently. This allowed the microscope time to be utilised efficiently, minimising wasted time as further datasets were not collected once the structure had been determined and achieved a high completeness. Performing collection and processing simultaneously also allowed for rapid feedback on the as synthesised samples and allowed us to answer the following questions. Was diffracting material present? Was data collected from the compound that was expected? Or was other material present on the grid? This can occur when impurities or contaminants were present. In some instances, it was possible to determine the structure from a single crystal, even the first crystal that was collected, as was the case for **Compound 6.4**. Although this resulted in low completeness, it was possible to solve the structure in SHELXT. The final structure of **Compound 6.4** came from data collected from a total of 5 crystals, as this yielded a solution with higher completeness. On the other hand, although multiple

datasets were collected for **Compound 6.2**, the final solution came only from the penultimate crystal from which data were collected.

A key advantage of using 3DED to study these compounds is that further workup or recrystallisation were not required, as would be necessary for in-house single crystal X-ray diffraction. Only scarce quantities of sample were available (<1 mg), and this was sufficient to successfully characterise the structures of the samples, as synthesised, that contained crystalline material. If microscope time is available, rapid characterisation of samples containing crystalline material is possible without additional, time consuming, experimental steps required to grow crystals of sufficient size or quality for X-ray diffraction.

3DED allowed for the unambiguous assignment of the manganese coordination position in **Compound 6.3**. 3DED proved essential in confirming the coordination of the metal to the ligand in a complex where multiple coordination positions were possible.

Compounds 6.1 – 6.6 (excluding **Compound 6.5**), all diffracted to high resolution and were radiation hard, i.e., the diffraction quality did not reduce over the course of the data collection. For well diffracting crystals, our workflow was effective and provided an efficient means of collecting data and determining structures. The workflow established for data collection at York is not a limiting factor in electron diffraction data collection, rather the limitation is sample quality itself. If diffraction from a target crystal is not observed, this is a reflection of the poor quality, non-crystalline nature of the sample. It would be better, and more efficient to optimise the sample preparation process, rather than use the TEM to continue to search for diffracting material from a poor sample.

The workflow is a manual process that requires researcher input during screening, selecting, and centring the crystals. In future, the workflow could be further optimised by automating these steps. However, automation would likely not confer an advantage in these circumstances. The aim of these experiments was to characterise the as synthesised samples and provide rapid feedback to the chemists by determining their structure and verifying the expected complexes had been formed. The researcher was able to centre a target crystal and rapidly assess whether it produced a high quality diffraction pattern in the test image, and whether it warranted full data collection. With an automated

system, there would need to be accurate auto-targeting and robust auto-eucentric procedures, tailored to crystal data collection. Even with this in place, the automated system would still likely collect many low quality datasets from crystals that produce poor diffraction patterns, as is seen in single particle cryoEM where automated data collection has become routine.[214] With manual data collection, the researcher is able to assess diffraction quality, meaning the datasets collected are likely to be good, usable datasets. Additionally, the researcher is able to determine when sufficient data has been collected and the structure can be determined to high resolution and completeness. The researcher can then stop collecting further datasets and load the next sample, maximising the efficiency of precious microscope time, whereas an automated system could go on collecting further datasets unnecessarily unless a sophisticated feedback mechanism was in place. Without researcher input and concurrent data collection and data processing, it may not be possible to rapidly determine the structures and verify the expected compound has been made. An automated system could continue to collect data unnecessarily. For instance, if the expected structure could be solved to a high completeness from the first crystal or, if the wrong material had been produced or the reaction were not successful, the automated system could collect many datasets from an impurity or starting material. This could take many hours and would waste microscope time. Screening samples and collecting data manually is more convenient in these circumstances and allows for rapid feedback.[214]

7 Characterisation of materials derived directly from reaction mixtures

Isolating products from a reaction mixture and subsequently crystallising them can be a particularly challenging, if not impossible process, especially if crystals large enough for SCXRD are required. For synchrotron sources, the size requirement for crystals is to have a minimum volume of 5x5x5 μm^3.[67] For laboratory sources, the crystal size requirement increases and a minimum crystal side length of at least 50 μm is required.[67]

The reaction mechanism for the transformation of a linear palladium species to a cyclic palladium species was studied by 3DED. This reaction had previously been studied by SCXRD; however, characterisation of the starting materials, impurities, and products had taken over 2 years to achieve. Separation and crystallisation of the desired product proved challenging. Additionally, the full reaction mechanism was unknown, and the generation of various side products was possible.

It was hoped that by placing TEM grids directly into the reaction vessel containing dry material, it would be possible to find crystalline material and characterise the different species present via 3DED, with the ultimate goal being to characterise the desired product species while negating additional purification and recrystallisation steps. 3DED allows for the rapid determination of crystal structures when diffracting material is present. It can be used to provide chemists with direct feedback on the success of a reaction and identify what crystalline species are present in the reaction mixture.

7.1 Methods

7.1.1 Sample Preparation

Freshly synthesised, as prepared samples of the reaction mixtures containing palladium species were provided by Neda Jeddi of Professor Ian Fairlamb's group at the University of York. Details of the synthesis are provided in Neda Jeddi's PhD thesis.[215] The samples provided had not undergone any purification or crystallisation attempts. The aim of the reaction was to generate cyclic palladium cluster complexes via the transformation of linear Pd_3 cluster complexes. Two samples were provided, these were attempts to synthesise the same cyclic palladium species. The differentiating factor between the samples was the counter ion used. **Reaction 7.1** utilised a triflate ($CF_3SO_3^-$) counterion, henceforth abbreviated to OTf, while **Reaction 7.2** utilised a tetrafluoroborate (BF_4^-) counterion. The

reaction schemes are presented in **Figure 7.1**. Further details on the synthesis are provided in Neda Jeddi's PhD thesis.[215]
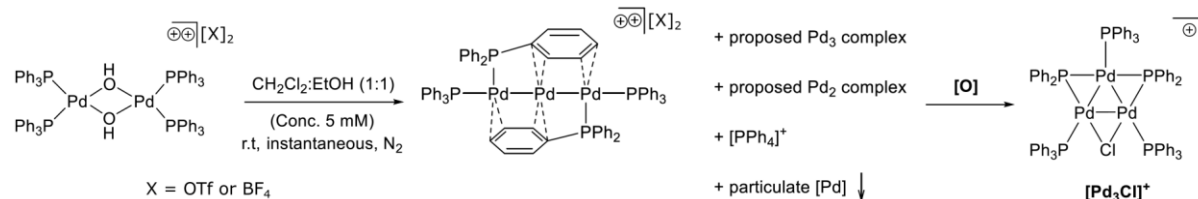
Figure 7.1. Reaction scheme for the formation of cyclic palladium clusters. *The reaction to generate the linear palladium cluster leads to the formation of unknown species whose characterisation has not yet been possible. The reaction mixture containing the linear Pd$_3$ cluster was exposed to adventitious air over a few days. This resulted in the complete consumption of the intermediates and generated the cyclic Pd$_3$Cl cluster in addition to colloidal Pd.*

Solvent was removed from the samples to generate a powder. Grids were then placed directly into the reaction vessels with the dry powder, in a glove box under an argon atmosphere. The grids were transferred to separate glass vials and transported to the microscope under an atmosphere of argon. The individual grids were plunged into liquid nitrogen and transferred to the cassette before loading into the TEM. **Chapter 9, Section 9.1** contains further details on grid preparation. In total, 6 grids were prepared and loaded into the TEM, 2 of these contained samples of **Reaction 7.1** and the remaining 4 were of **Reaction 7.2**.

The aim of the 3DED experiments were to identify and characterise any diffracting species present on the grids, whether this be the starting material, product, side product or impurities.

7.1.2   Data acquisition

The individual grids containing samples from **Reaction 7.1** and **7.2** were screened for diffracting material using a Thermo Fisher Glacios microscope operating at a voltage of 200 kV and temperature of 80 K, as described in **Chapter 9, Section 9.2**. Electron diffraction data were acquired with nanobeam electron diffraction using the following illumination conditions: gun lens 8, spot size 11, 30 μm C2 aperture. This resulted in a beam with a diameter of 1.05 μm and a flux of ~0.07 e$^-$ Å^{-2} s^{-1}. EPU-D was used to collect data in a semi-automated fashion with the following settings: 2x binning, a rotation speed of 1.333°/s and an exposure time of 0.75 s, resulting in a Δφ of 1°/frame. A representation of the beam diameter on the sample and an example electron diffraction pattern from **Compound 7.1a**

are shown in **Figure 7.2**. The thickness of the crystal is prohibitively large in places, as can be observed by the opaque, black colour. This indicates no electrons can penetrate. However, the edge of the crystal is much thinner and appears to be grey in colour. Data were collected from the edge of the crystal, the area from which data were collected is highlighted by a red circle.
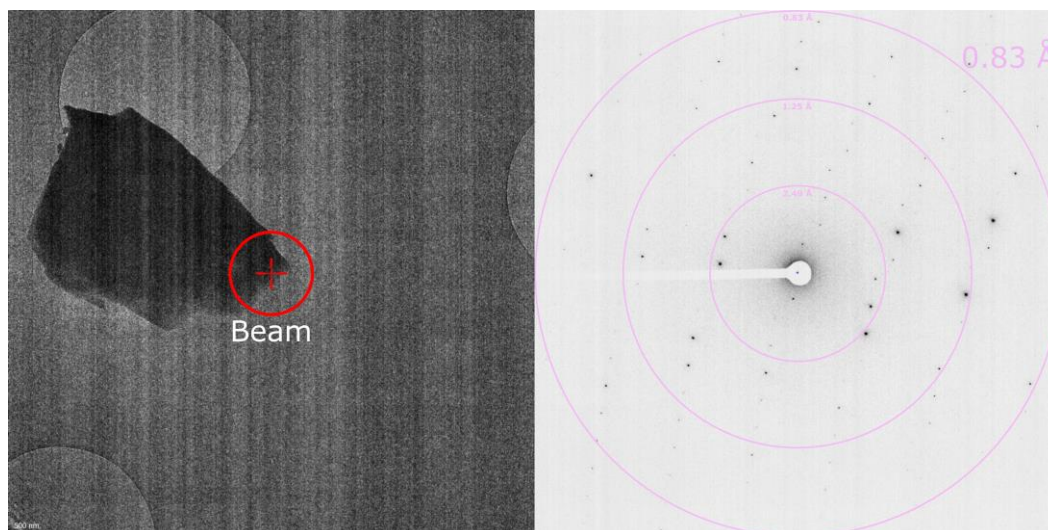
*Figure 7.2. Example Compound 7.1a crystal and diffraction pattern. Left: TEM brightfield image of **Compound 7.1a** crystal, red circle represents the beam diameter (1.05 µm). Right: Representative electron diffraction pattern, with resolution rings. Outer resolution ring is 0.83 Å.*

7.1.3 Data processing and structure determination

Data processing was performed using DIALS software.[201] For full details of the data processing workflow, see **Chapter 9, Section 9.3**. To enable data processing, a pedestal of 64 ADU was added to each pixel value, the detector distance was specified to be 958.5 mm, and the goniometer rotation axis was set to 1,0,0, for rotation of the goniometer in a positive direction around the horizontal axis. Further details on importing the data are provided in **Chapter 9, Section 9.3.1**.

A semi-automatic processing script[202] was used to process the individual datasets up to integration. The script utilised a standard series of DIALS commands to achieve this. The individual datasets were then inspected. The unit cell parameters were examined to determine whether they matched any of the known products, starting materials or impurities expected in this reaction scheme. Datasets with the same space group and unit cell parameters were scaled together. Datasets were removed or added as required to obtain the best solution. This was achieved by examining the impact on completeness, CC½, and R_{merge} as datasets were removed. This procedure is described in more detail in **Chapter 9, Section 9.3.6**.

The strong reflections from the combined datasets were then filtered for joint refinement of detector distance and unit cell parameters for the individual datasets. The unit cell parameters for each of the combined datasets were then refined by fitting calculated to observed 2θ values. This allowed estimation of the estimated standard deviations on the 'best' cell parameters for the combined datasets, see **Chapter 9, Section 9.3.7**.

SHELXT[164] was used to determine the structures. This utilises direct methods. See **Chapter 3, Section 3.3.4** for general information on *ab initio* structure determination, and **Chapter 9, Section 9.4** for more specific details on how the structures in this body of work were determined. The command line switches `-a` – `y` `-m500` were used. SHELXL[165] was used for structure refinement. Instead of the default X-ray scattering factors, the electron scattering factors from Peng[190] were applied. Further details on structure refinement are provided in **Chapter 3, Section 3.4**, for general information, and **Chapter 9, Section 9.5** for refinement of structures in this thesis. For all compounds in this chapter, the default weighting scheme was used, as opposed to the recommended SHELXL weighting scheme. The reasons behind this are described in **Chapter 6, Section 6.2.7**.

7.2   Results and Discussion

Finding diffracting material on these grids proved difficult. Over the course of a 13 hour screening and data collection period, only 17 datasets were collected. 10 datasets came from samples of **Reaction 7.1** across two grids, and 7 datasets came from samples of **Reaction 7.2** across 3 grids. The final grid containing **Reaction 7.2** was bent and broken, and as such was not used.

7.2.1   Reaction 7.1 - Triflate counterion

7.2.1.1   Compound 7.1a

A total of 10 datasets were collected from the sample of **Reaction 7.1**. Of these, 9 datasets indexed to yield the same solution with a $P\bar{1}$ space group and approximate unit cell parameters: a=9.5 Å, b=12.8 Å, c=14.8 Å, α=80.8°, β=80.8°, γ=72.7°. The structure of this material (**Compound 7.1a**) could be determined. **Compound 7.1a** was found to be the linear starting material, $[Pd_3(PPh_3)_4][OTf]_2$. For the final solution, a total of 5 datasets from 5 crystals were merged to give a completeness of 98.0% to 0.83 Å. Crystallographic and refinement data for **Compound 7.1a** are presented in **Table 7.1**.

Refinement resulted in a good structural solution (R_1=17.6%, $P\bar{1}$ space group). No restraints were used during refinement. The structure model is shown in **Figure 7.3**. The structure model of the ASU with the electrostatic potential map is presented in **Figure 7.4**. The crystal packing of **Compound 7.1a** is displayed in **Figure 7.5**.

It was not possible to determine the structure of the crystal from the single dataset that did not index to give the above solution. This was due to the low resolution and low completeness of the data.

Table 7.1. Crystallographic and refinement data for Compound 7.1a.

Empirical formula	$C_{74}H_{60}P_4Pd_3S_2F_6O_6$
Formula weight	1666.42
Temperature (K)	80
Crystal system	Triclinic
Space group	$P\bar{1}$
a (Å)	9.4953(6)
b (Å)	12.7863(7)
c (Å)	14.7518(8)
α (°)	80.844(6)
β (°)	80.819(6)
γ (°)	72.713(5)
Volume (Å^3)	1676.30(18)
Z	1
ρ_{calc} (g/cm^3)	1.651
Reflections measured	25015
Independent reflections (with I > 2 σ(I))	6036 (4822)
Resolution (Å)	0.83
Completeness (%)	98.0
Restraints/parameters	0/431
R_{int}	0.1730
R_1 [I > 2 σ(I)]	0.1756
R_1 [all data]	0.1991
wR_2 [all data]	0.3892
GooF	2.327
Residual potential (e/Å)	1.001/-1.011

Figure 7.3. 3DED structure of Compound 7.1a. Thermal ellipsoids are shown at a probability level of 50%. For clarity, hydrogen atoms are not displayed. Atom Key: black=C, yellow=S, green=f, red=O, purple=P, white=Pd.

Figure 7.4. 3DED structure of Compound 7.1a. Fo map contoured at 1.23 e/Å. Thermal ellipsoids are shown at a probability level of 50%. For clarity, only the ASU is shown. Atom Key: black=C, yellow=S, green=f, red=O, purple=P, large white=Pd, small white=H.
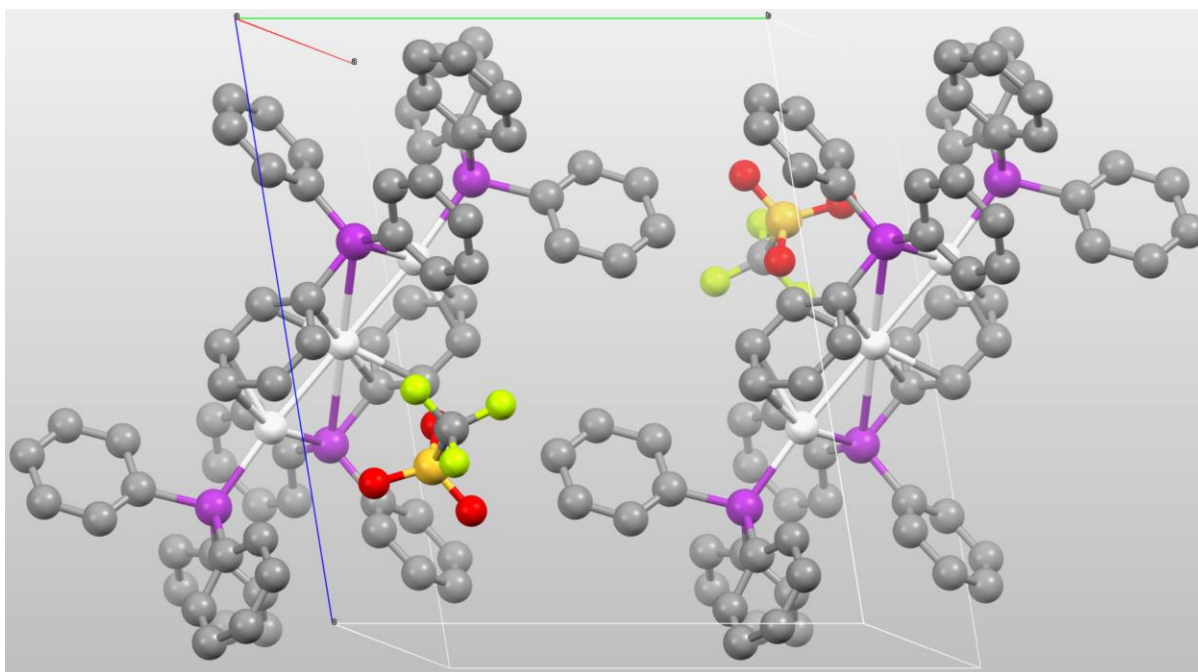
Figure 7.5. Packing of Compound 7.1a as viewed along the a* crystallographic axis. *For clarity, hydrogen atoms are not displayed, and depth cueing is enabled. Atom Key: grey=C, yellow=S, green=f, red=O, purple=P, white=Pd.*

7.2.2   Reaction 7.2 – Tetrafluoroborate counterion

A total of 7 datasets were collected from the sample of **Reaction 7.2** across 3 grids. These yielded a total of 4 different indexing solutions. It was not possible to determine the structures of all of these materials. This was primarily due to poor data quality or low completeness. The resolution to which the crystals diffracted, or the nature of the diffraction (e.g. streaked/smeared) proved prohibitory to structure determination. Additionally, two of the indexing solutions could not be matched to the unit cell parameters of the expected structures (starting material, impurity, or product) that were previously determined using SCXRD.

7.2.2.1   [PPh$_4$]BF$_4$ impurity

A single dataset from 1 crystal yielded a solution in an $I\bar{4}$ space group with unit cell parameters: a=b=12.0079 Å, b=6.8886Å, α=β=γ=90°. The single crystal gave a completeness of 85.4% to a resolution of 0.83 Å. These unit cell parameters were used to search the Cambridge Structural Database (CSD) and were found to match previously identified [PPh$_4$] species. Including a [PPh$_4$]BF$_4$ species (Database identifier: KOVBIJ).[216]

It was possible to determine the 3DED structure of the single crystal ($I\bar{4}$ space group). The single crystal was indeed found to be a [PPh$_4$]BF$_4$ impurity. The structure model of the [PPh$_4$]BF$_4$ impurity is given in **Figure 7.6**. Refinement of this structure was not performed. This was due to the identity of the species, being a known impurity, and as such not a species of interest, as starting materials or products would be.
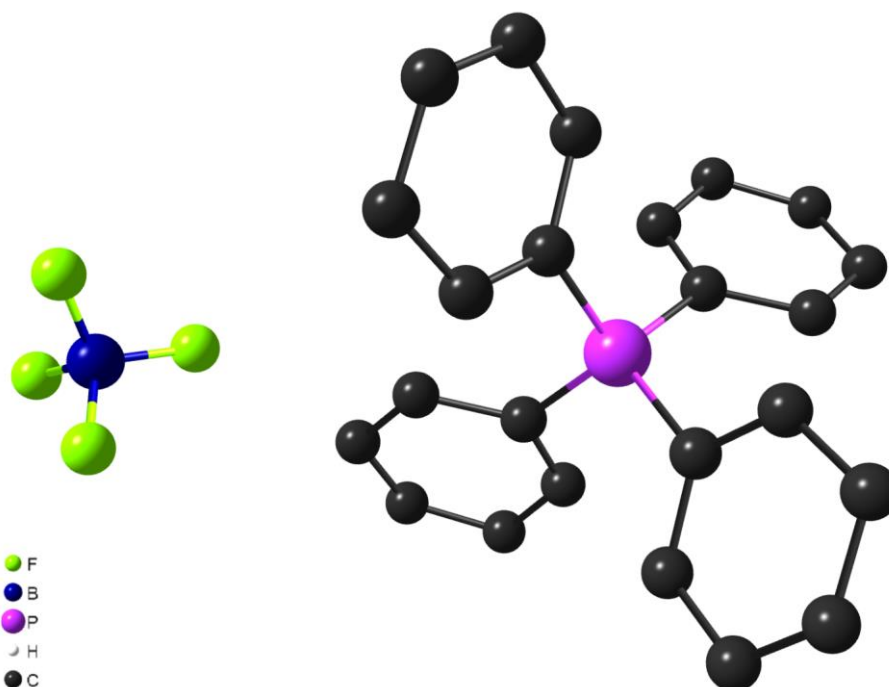
Figure 7.6. 3DED structure of [PPh$_4$]BF$_4$ impurity. *Thermal ellipsoids are not shown as refinement of this structure was not performed. Hydrogen atoms are not displayed. Atom Key: black=C, purple=P, blue=B, green=F.*

7.2.2.2 Streaky diffraction

Several needle-like crystals were found from the sample of **Reaction 7.2**. These are usually promising targets for 3DED data collection. Unfortunately, these crystals, despite diffracting to high resolution of 0.83 Å, yielded streaky, smeared diffraction. As such, structure determination was not possible. Additionally, the spacing between the diffraction planes suggested a unit cell with the shortest parameter of ~3.45 Å. This is much shorter than would be expected for the starting material or product which would contain multiple palladium atoms and bulky ligands. A brightfield image of one of these needle-like crystal and a diffraction pattern from it are provided in **Figure 7.7**.
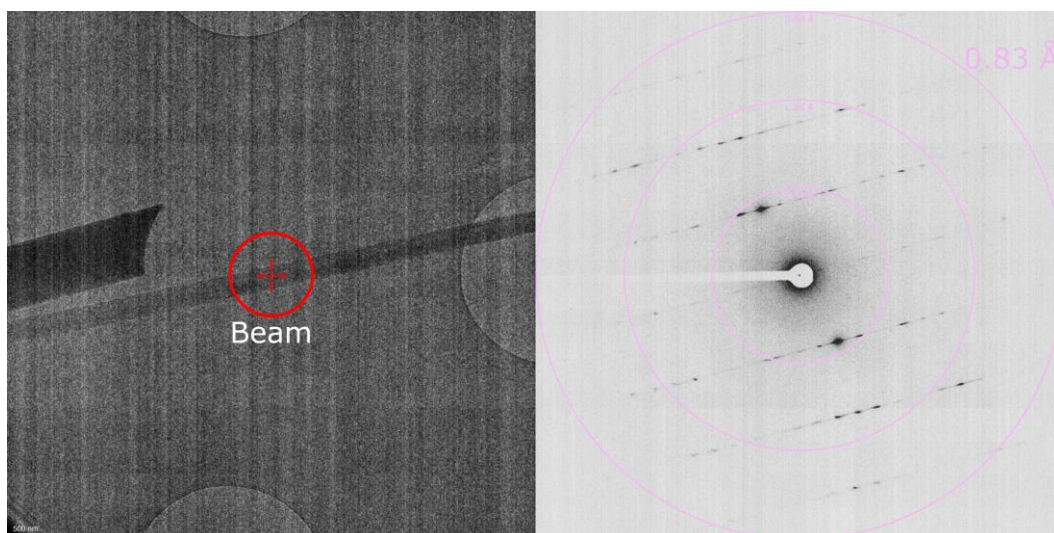
Figure 7.7. Example needle-like crystal and diffraction pattern from sample of Reaction 7.2. Left: TEM brightfield image of needle-like crystal, red circle represents the beam diameter (1.05 µm). Right: Representative electron diffraction pattern, with resolution rings. Outer resolution ring is 0.83 Å.

7.2.2.3 Compound 7.2a

A single crystal was found that yielded a solution with an $R\overline{3}$ space group and unit cell parameters of a=b=40.05 Å, c=14.19 Å, α=β=90°, γ=120°. The structure of this crystal (**Compound 7.2a**) could be determined. **Compound 7.2a** was found to be the linear starting material, $[Pd_3(PPh_3)_4][BF_4]_2$. Unfortunately, it was not possible to resolve the BF_4 counterions in the structure due to their disorder. Additionally, it was not possible to resolve any solvent ions that may have been present.

The structure of the linear starting material, $[Pd_3(PPh_3)_4][BF_4]_2$, had previously been determined using SCXRD, however the previously determined structure crystallised with triclinic symmetry in a $P\overline{1}$ space group, with markedly different unit cell parameters: a=12.41 Å, b=12.62 Å, c=14.41 Å, α=95.15°, β=103.28°, γ=110.47°. The SCXRD structure could not be transformed to yield a solution with trigonal symmetry, suggesting the structures were indeed different.

The 3DED solution for **Compound 7.2a** came from a single crystal. The data completeness was 96.2% to a resolution of 1.2 Å. Despite the relatively low resolution, structural solution was possible (R_1=21.9%, $R\overline{3}$ space group). Crystallographic and refinement data are presented in **Table 7.2**. During refinement, RIGU restraints were applied to all non-hydrogen atoms and SIMU restraints were applied

to all phenyl rings. The structure model is given in **Figure 7.8**. The structure model of the ASU with the electrostatic potential map is displayed in **Figure 7.9**.

Table 7.2. Crystallographic and refinement data for Compound 7.2a.

Empirical formula (ASU)	$C_{36}H_{30}P_2Pd_{1.50}$
Formula weight (ASU)	684.14
Temperature (K)	80
Crystal system	Trigonal
Space group	$R\bar{3}$
a (Å)	40.052(3)
c (Å)	14.1941(14)
Volume (Å^3)	19719(3)
Z	18
ρ_{calc} (g/cm^3)	1.037
Reflections measured	7193
Independent reflections (with I > 2 σ(I))	2560 (1249)
Resolution (Å)	1.2
Completeness (%)	96.2
Restraints/parameters	567/359
R_{int}	0.2180
R_1 [I > 2 σ(I)]	0.2191
R_1 [all data]	0.3013
wR_2 [all data]	0.4935
GooF	2.198
Residual potential (e/Å)	1.473/-0.685

The 3DED structure of **Compound 7.2a** showed an intriguing arrangement. **Compound 7.2a** crystallised in such a way that was unlike the previously determined SCXRD structure of the linear starting material, $[Pd_3(PPh_3)_4][BF_4]_2$. Additionally, the crystal packing was unlike that observed in the 3DED structure of **Compound 7.1a**, which, like the SCXRD structure, crystallised in a $P\bar{1}$ space group despite having a different counter ion. See **Figure 7.5**.

The structure of **Compound 7.2a** was comprised of 11 clusters of $[Pd_3(PPh_3)_4]^{2+}$ in a hexagonal arrangement forming two pores, with one clusters connecting both pores. The pore structure is shown in **Figure 7.10**. Unfortunately, it was not possible to resolve the structure of the solvent or counterions. This was likely due to their disorder. As such it was not possible to determine the contents of the pores.
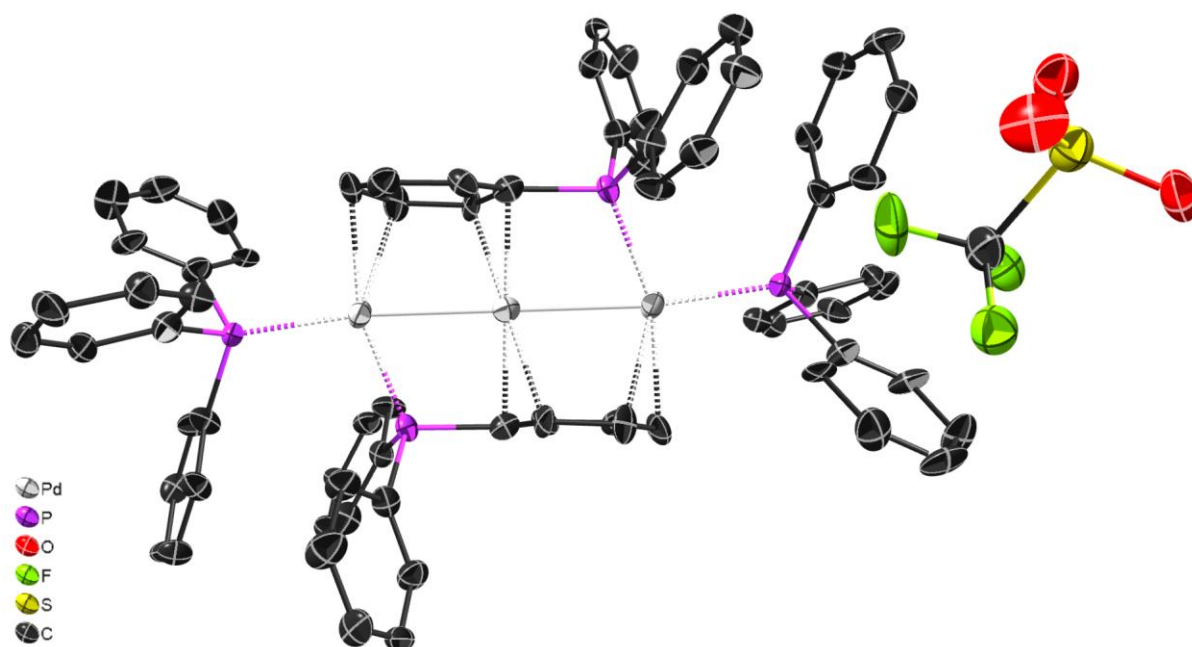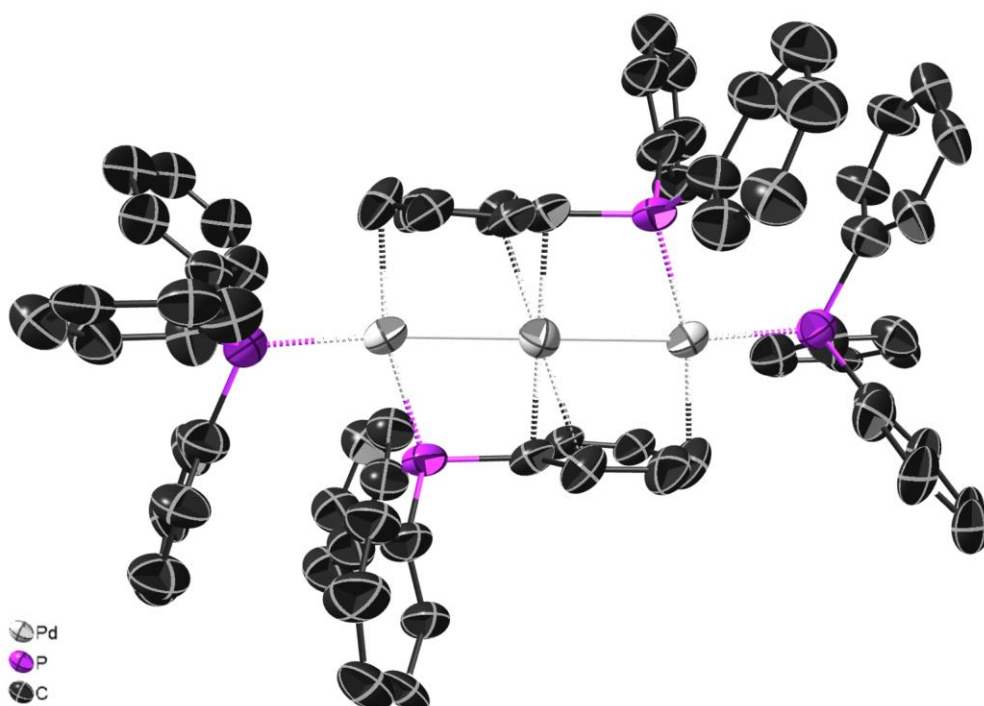
Figure 7.8. 3DED structure of Compound 7.2a. *Thermal ellipsoids are shown at a probability level of 50%. For clarity, hydrogen atoms are not displayed. Atom Key: black=C, purple=P, white=Pd. It was not possible to model the anions due to their disorder.*
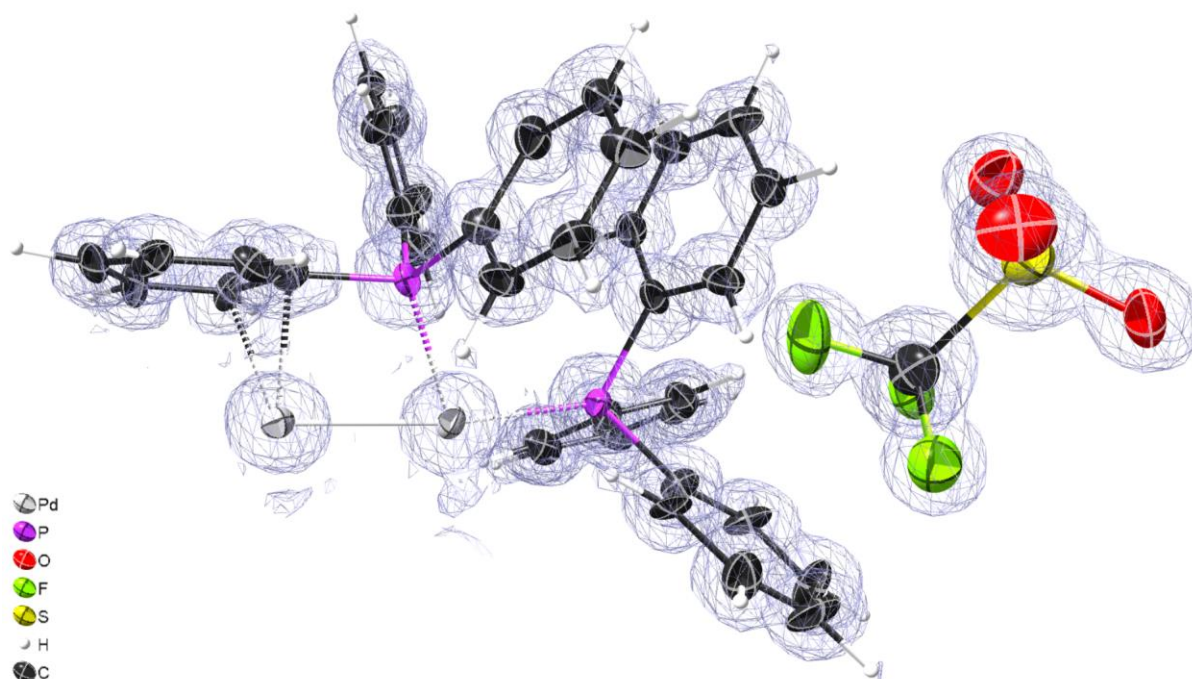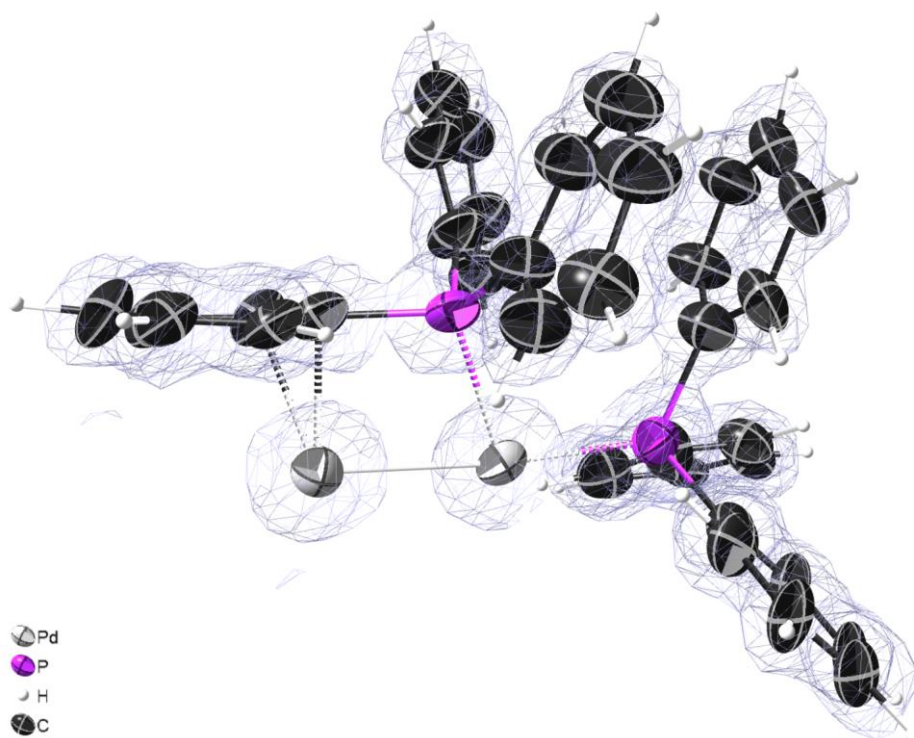

Figure 7.9. 3DED structure of Compound 7.2a. Fo map contoured at 0.964 e/Å. *Thermal ellipsoids are shown at a probability level of 50%. For clarity, only the ASU is shown. Atom Key: black=C, purple=P, large white=Pd, small white=H.*
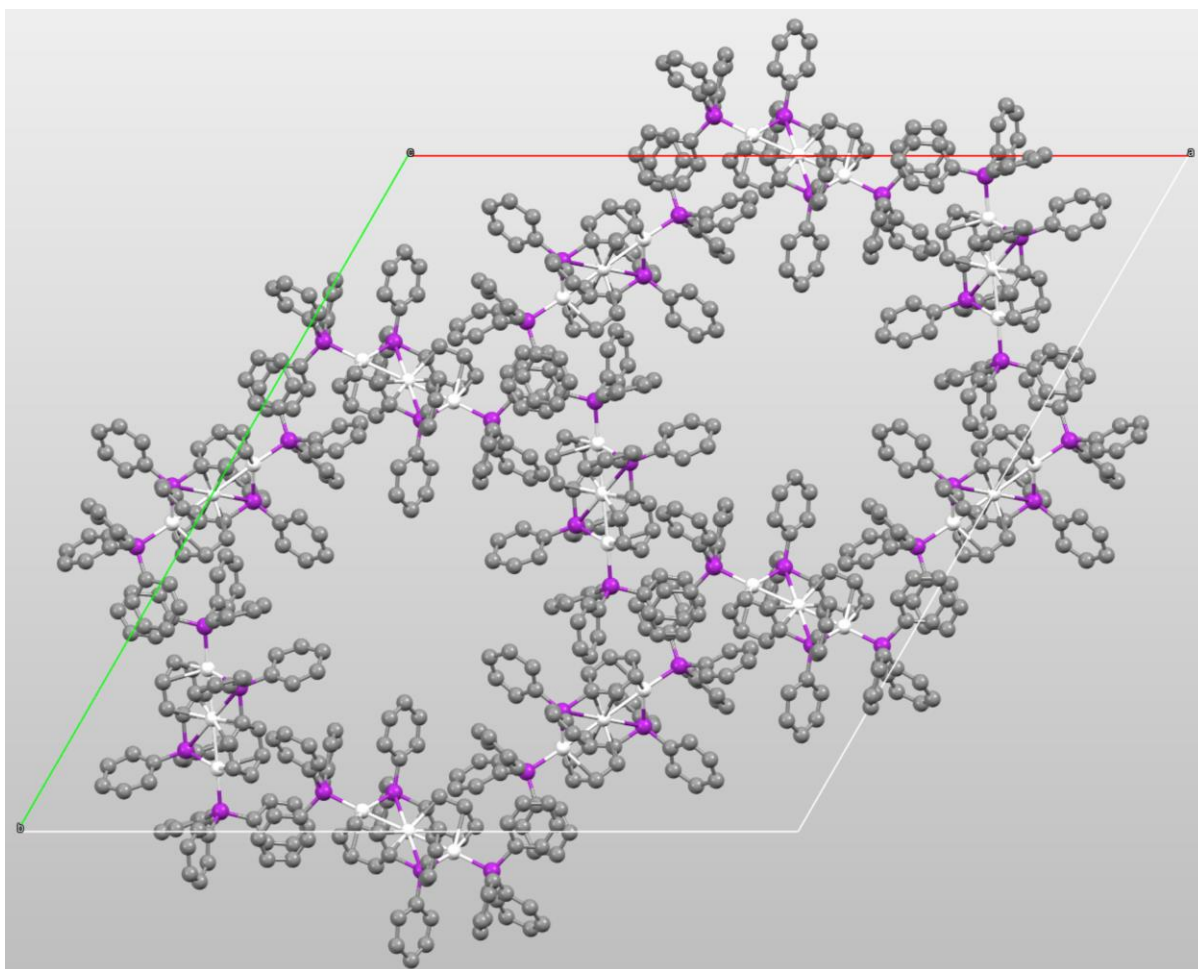
Figure 7.10. Packing of Compound 7.2a as viewed along the c crystallographic axis. *The molecules arrange to form a hexagonal structure comprised of 11 [Pd$_3$(PPh$_3$)$_4$]$^{2+}$ clusters forming two pores. For clarity, hydrogen atoms are not displayed. Atom Key: grey=C, purple=P, white=Pd.*

7.2.3 Comparison of 3DED structures with existing X-ray structures

The 3DED structures of **Compound 7.1a** and **Compound 7.2a** showed no significant differences in the Pd—Pd, Pd—P, and Pd—C bond distances compared to the [Pd$_3$(PPh$_3$)$_4$][OTF]$_2$ and [Pd$_3$(PPh$_3$)$_4$][BF$_4$]$_2$ structures previously reported by Fairlamb *et al.*[217] and Sharp *et al.*[218] respectively. A comparative table detailing selected bond distances and bond angles for the X-ray and 3DED structures of the [Pd$_3$(PPh$_3$)$_4$]$^{2+}$ salts is given in **Table 7.3**.

Table 7.3. Selected bond distances and angles from reported X-ray structures of the [Pd₃(PPh₃)₄]²⁺ salts and the corresponding 3DED structures obtained in this work.
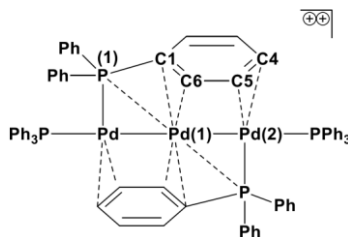
Bond distance (Å)	$[Pd_3(PPh_3)_4][OTf]_2$ (Fairlamb *et al.*[217])	$[Pd_3(PPh_3)_4][BF_4]_2$ (Sharp *et al.*[218])	**Compound 7.1a**	**Compound 7.2a**
Pd1—P1	2.857(9)	2.875(1)	2.866(5)	2.907(17)
Pd1—Pd2	2.631(8)	2.659(4)	2.679(2)	2.654(8)
Pd1—C1	2.192(4)	2.183(4)	2.208(9)	2.16(3)
PD2—C4	2.299(4)	2.287(4)	2.310(10)	2.23(3)
Pd2—C5	2.387(6)	2.396(5)	2.383(11)	2.47(4)
Pd1—C6	2.265(4)	2.318(5)	2.266(9)	2.44(3)

Bond angle (°)	$[Pd_3(PPh_3)_4][OTf]_2$ (Fairlamb *et al.*[217])	$[Pd_3(PPh_3)_4][BF_4]_2$ (Sharp *et al.*[218])	**Compound 7.1a**	**Compound 7.2a**
P1—Pd1—Pd2	48.165(9)	47.89(2)	48.31(10)	48.7(4)
Pd1—Pd2—P2	175.268(12)	172.27(3)	172.73(13)	173.7(5)

7.3   Conclusions

It was possible to determine the structures of samples directly from their reaction mixtures for **Reaction 7.1** and **7.2** without further purification or recrystallisation. Structure determination of the starting materials from each of the reactions was successful, alongside a [PPh₄]BF₄ impurity from **Reaction 7.2**. A novel crystal form of the salt [Pd₃(PPh₃)₄][BF₄]₂ was identified (**Compound 7.2a**) from a single crystal.

The discovery of the single crystal of the linear starting material, [Pd₃(PPh₃)₄][BF₄]₂, which crystallised in the novel trigonal arrangement, highlights the power of 3DED to find previously unknown and unexpected crystal forms. Akin to finding a needle in a haystack. The advantage of 3DED is that it allows for structure determination on such a small scale. Data can be easily collected from crystals of only a few hundred nanometres in diameter; crystals that are too small to study by conventional SCXRD methods. It is possible that crystals such as these may have a limit on how large they can grow, so obtaining crystals large enough to study by SCXRD may prove difficult, if not impossible. Attempts

to yield sufficiently large crystals of these novel species would likely be difficult and involve convoluted purification and recrystallisation steps. Additionally, these tiny crystals found by 3DED may not make up the bulk of the material, so they may not be detectable by methods such as PXRD. 3DED may be the only means by which discovery of these crystal forms is possible.

Finding novel crystal forms such as these could also provide mechanistic insight into the reaction taking place. Formation of the 11 membered [$Pd_3(PPh_3)_4$] clusters may be a key step in the reaction process. Conversely, formation of these clusters may hinder the reaction by resulting in the formation of palladium nanoparticles. Formation of these particles may use up starting material and prevent the reaction from progressing to the desired product. Knowledge of the mechanism would help inform experimental design, potentially leading to improved reaction conditions and higher product yields.

While it was unfortunately only possible to determine the structures of the starting materials and impurities, instead of the products, the 3DED studies were able to find a previously unknown crystal form. Additionally, the reaction process studied was the culmination of over 2 years of work reliant on structure determination by SCXRD. Using 3DED it was possible to determine structures directly from the reaction mixture without additional lengthy or complicated recrystallisation steps, in a single day. 3DED could be utilised as a helpful tool for chemists to obtain immediate feedback on the success of a reaction and which species are present in reaction mixtures. This may give a more representative overview of what materials are present in a sample, and which species spontaneously crystallise.

As aforementioned in **Chapter 5, Section 5.3**, an automated serial data collection approach[208–210] would likely be useful in cases such as these, where the sample contains multiple species or different crystal forms.[211] In the cases of samples from **Reaction 7.1** and **7.2**, the sample quality was a limiting factor. Over the course of a 13 hour screening and data collection period, only 17 datasets were collected, despite the screening of hundreds of crystals. An overnight, automated data collection may be able to collect further datasets and potentially allow for the discovery of further rare crystal forms. However, if the target crystals do not produce diffraction patterns or only diffract poorly this may not be a valuable use of microscope time and resources, or researcher time during data analysis.

8   Conclusions and future perspectives

The initial aim of this PhD project was to participate in implementing 3D electron diffraction as a technique at the University of York. At this time, no dedicated instrumentation for the 3DED technique was available, and it hadn't yet been implemented in the UK for routine structure determination. At the start of the project, it was unknown whether 3DED data collection from small molecule organic and organometallic compounds would be possible on the instrumentation available. Once it had been established that data collection from well-studied test compounds was possible, studies of small molecule organometallic species using 3DED commenced. The project experienced a significant acceleration with the installation and commissioning of the Thermo Fisher Scientific Glacios microscope in April 2021.

The secondary aim of this project was to establish a data collection and processing workflow for 3D electron diffraction data based on the instrumentation available at the University of York i.e., a Thermo Fisher Scientific Glacios microscope equipped with a Ceta-D camera. This workflow is presented in full in **Chapter 9**. The workflow includes an optional PXRD pre-screening step, where the crystallinity of a sample is assessed prior to insertion into the microscope. The PXRD pre-screening step proved to be a valuable indicator of crystallinity, as seen in **Chapter 5**, where 3DED was used to attempt to characterise a series of bulky planar porphyrin species that proved difficult to crystallise and could not be studied by SCXRD. The PXRD pre-screening was able to determine which porphyrin samples contained crystalline material, and which did not. These results were reflected in the 3DED experiments where well-diffracting crystals were only found in the samples shown to be crystalline by PXRD. As such, PXRD was demonstrated to be a fast and effective test for crystallinity and it should be used when sufficient quantity of sample is available, to enable efficient and effective use of valuable microscope time and researcher resources.

The data collection and processing workflow was validated by successfully collecting 3DED data from a range of organometallic (and some organic) small molecule compounds, some of which have been presented in **Chapters 4-7** of this thesis, or released as publications.[219] The throughput and efficiency of the workflow were tested using a series of manganese complexes and their precursor organic ligand, see **Chapter 6**. A total of six compounds were investigated over the course of two 12 hour sessions. Only a scarce quantity of each of these samples were available (<1 mg) and as such PXRD pre-screening was not performed. However, the initial screening and crystal targeting steps of the

workflow were able to quickly confirm whether the grids contained well distributed, crystalline material of suitable thickness for 3DED data collection. During the two sessions, the structures of five of the six compounds were successfully determined, to a high resolution (0.83 Å) based on highly complete (typically >90%) datasets.

Exploration of the limitations of 3DED in determining the structures of small molecule organometallic compounds was the next aim. A range of organometallic compounds, synthesised in the chemistry laboratories, were studied and the primary limitation to structure determination was found to be the sample itself. If well diffracting material was present, it was possible to consistently collect data to a resolution better than 0.83 Å and achieve a high data completeness by collecting and merging data from multiple crystals. The caveats to this were entirely dependent on the sample. If no crystalline material was found, and the sample was deemed to be amorphous, diffraction patterns could not be obtained and the structure could not be solved by 3DED, as was the case for **Compounds 5.2, 5.4, and 6.5** in this thesis. A base requirement for 3DED is the presence of crystalline material. 3DED data cannot be collected from amorphous materials. If the sample was found to be beam sensitive, with diffraction quality reducing over the course of the data collection, the conditions were adapted to allow for the collection of the highest quality data possible. The σ-alkane complex in **Chapter 4** provides an excellent example of such adaptations. In which, the adaptations implemented made it possible to fully characterise the structure of the σ-alkane complex, including the weakly binding ligand of interest.

Full reciprocal space sampling from each crystal was typically not possible, as such data from multiple crystals were typically merged together to obtain a dataset with high completeness. This was due to the tilt angle limitation imposed by both the microscope configuration and prevention of the occlusion of the target crystal by other species on the grid, or grid bars. As datasets can be collected from multiple crystals and merged together this typically doesn't create a problem in itself, However, in instances of rare crystal forms, where only one or very few crystals of this type are found on the grid, this could become problematic. An example of a rare crystal form discovery is presented in **Chapter 7**. Fortunately, in this case, the molecules in the rare single crystal that was found had crystallised in a trigonal arrangement. Thanks to the high symmetry of this crystal, it was possible to obtain a high completeness dataset (96.2% to 1.2 Å resolution) and determine the crystal structure.

Traditional TEM grids are comprised of a flat carbon film supported by metal grid bars. This is not the optimal sample support for 3DED data collection. Due to the flatness of the film, crystals were often found to lie in preferred orientations. Additionally, the metal grid bars were opaque to electrons, reducing the rotation range from which diffraction data could be collected from a crystal. To maximise data completeness, strategies were implemented to collect data from crystals in unusual orientations on traditional TEM grids. An example of such a strategy was to intentionally yet carefully damage the film after crystal deposition.[213] This could be achieved with delicate contact from a small paintbrush.[213] The aim of this was to break the film so that data could be collected from crystals overhanging the broken film or from crystals positioned on curled pieces of broken film. Despite challenges in centring these crystals at eucentric height, data collection from such crystals often improved data completeness. An example of this is given in **Chapter 6**. Alternative sample supports better suited to 3DED are being developed. Wennmacher *et al*. proposed a sample support comprised of ~100 nm diameter nylon fibres deposited on lacey carbon grids.[213] The resulting grids were comprised of a "chaotic network" of nylon fibres atop lacey carbon creating holes of various sizes. The deposition of nylon fibres could be controlled such that the holes and the crystals were of comparable size. The aim of this was for the crystals to become entangled in the nylon fibre network and lay in random orientations.[213] While this was successful, increased sensitivity to the beam was noted compared to conventional grids. Additionally, the sample support was still comprised of a metal mesh impenetrable to electrons.[213] Future efforts could be focused to creating an idealised sample support for 3DED without opaque areas, although with the limitation of current hardware, this could prove challenging.

While structure determination of small molecule organometallic compounds was shown to be routine for the well diffracting crystals studied, the resulting structures had significantly larger R_1 values than those typical of X-ray structures. The R_1 values for electron diffraction data typically lie in the 15-30% range while those from X-ray diffraction data are generally <5%.[66,198] The range of R_1 values for reflections with intensity greater than $2\sigma(I)$ for compounds studied in this thesis was 13.4-21.9%. The reason for the elevated R_1 values can be partially attributed to the dynamical effects not being considered. All data in this thesis were refined assuming the kinematical approximation. As a result, the calculated structure factor amplitudes ($|F_{hkl}|$) are likely to be systematically inaccurate.[126] As such, the elevated R_1 values for electron diffraction structures do not necessarily represent inaccurate atomic models.

The discrepancy in R_1 values can be somewhat reduced by performing dynamical refinement. These approaches utilise dynamical diffraction theory to calculate the intensities.[51,52,182,183] To completely model experimental electron diffraction intensities requires extensive knowledge of the crystal shape, orientation, mosaicity, bending and defects.[182] Knowledge of the crystal to this level is not typically possible, and even if it were, the expense of the computation of this calculation would be substantial. To enable calculation of the dynamical intensities, without extortionate computational cost, assumptions need to be made. It is assumed that the crystal is a perfect block shape with no mosaicity.[182] Despite dynamical refinement significantly reducing R_1 values, it is not yet routinely utilised. This is in part due to the computational expense of such calculations, and the requirement for specific software to perform the calculations. [183,184] An important consideration about dynamical refinement is that it involves treating the data differently compared to kinematical refinement. Due to the orientation dependence, symmetry equivalent reflections cannot be merged, making it difficult to draw direct comparisons to kinematically refined electron diffraction data. This raises the question of whether improvements in R_1 values are entirely due to accounting for dynamical effects or whether they arise as the result of the different treatment of the data. While dynamical refinement was not performed for the compounds presented in this thesis, it was still possible to obtain accurate atomic models.

One of the challenges encountered during structure determination and refinement was the inaccuracy of atom assignment. Currently, SHELXT[164] utilises X-ray scattering factors when determining electron diffraction structures. This often leads to the misassignment of atoms in initial structure models. If there is some knowledge of the expected structure of the compound in question, either from predictions based on knowledge of the reaction mechanism or from other analytical techniques (e.g. NMR studies or mass spectrometry), these misassignments can be corrected. During structure refinement, electron scattering factors are applied,[190] another issue arises here due to the small difference between electron scattering factors for atoms of different elements. The electron scattering factors for carbon, nitrogen and oxygen atoms are markedly similar.[190] This can make it difficult to discern whether atom assignment is correct. This difficulty can be observed in the difference map (the map of $F_{obs} - F_{calc}, \phi_{calc}$). For X-ray data, when an atom is misassigned a peak is observed in the difference map, for electrons this peak can be non-existent with atoms incorrectly assigned. As such, unambiguous atom assignment, particularly for compounds containing carbon, nitrogen, and oxygen atoms, may not be possible from electron diffraction data alone.[50,153,220] Atom assignment may be inferred from knowledge of the wider structure. For instance, SHELXT misassigned some of the carbon and oxygen atoms in the n-butoxy-chains of the porphyrin complexes in **Chapter**

5. No peaks were present in the difference map for these atoms however, some hydrogen positions were observable. In such cases, model building can be facilitated by prior knowledge about geometrical parameters (bond lengths and angles) of expected hydrogen atoms attached to carbon and oxygen.

Despite the challenges outlined above, it was possible to complete the final aim of this PhD project and characterise small molecule organometallic compounds whose structures could not be determined using SCXRD. This was vital in establishing whether 3DED was a technique that could be used routinely to aid synthetic chemists in determining structures of compounds synthesised and provide rapid verification that the expected complexes had been formed. The first indication, from this project, that 3DED could be used to study complexes precluded from characterisation by SCXRD was the study of the σ-alkane complex formed via a single-crystal to single-crystal hydrogenation presented in **Chapter 4**.[200] The hydrogenation reaction caused the crystals to crack and fragment, forming microcrystalline material largely unsuitable for study via SCXRD. While it was eventually possible to determine the structure of the σ-alkane complex (**Compound 4.2**) via SCXRD, this was a difficult and frustrating process that required the screening of many crystals until a suitable candidate, of sufficient size and diffraction quality was found. 3DED provided an attractive alternate means of structure determination. Following optimisation of the sample preparation and data collection protocols, 3DED was able to provide a high quality, complementary crystal structure.

Following this success, a series of four bulky planar porphyrin species were studied in **Chapter 5.** Crystallisation of these materials was particularly challenging and as such only one of the porphyrin complexes, **Compound 5.1,** had been characterised by SCXRD. To obtain this SCXRD structure, an alternate crystallisation method from that used to produce suitable 3DED crystals was required. However, the SCXRD structure was of poor quality with very large and elongated ADPs for all atoms. 3DED was used to determine the structure of **Compound 5.1** to a higher quality than that which could be achieved using SCXRD. The structure attained with 3DED had crystallised in a different arrangement to that of the SCXRD structure. This is not entirely surprising as different crystallisation methods were used. Interestingly, alternate crystal forms could be observed via 3DED. Overall, this chapter demonstrates the superior power of 3DED over SCXRD, allowing the derivation of accurate structural information from tiny crystals.

In **Chapter 7**, the discovery of a rare crystal form of a palladium species is presented. A single crystal was found where the complex had crystallised in a novel arrangement with trigonal symmetry. This crystal form had not previously been encountered and as such had been studied by no other means. 3DED can be advantageous in discovering novel crystal forms undetectable by other analytical methods, highlighting the power of the 3DED technique.

3DED has been extensively used to study small molecule organometallic compounds.[157,158,200,219] This is becoming increasingly routine as more researchers begin to explore this technique. The work presented in this thesis shows that 3DED can be used to characterise a range of small molecule organometallic compounds, some of which were difficult or impossible to study using SCXRD. 3DED can be used in complement to X-ray crystallography and in some instances surpass what is attainable with SCXRD. Limitations to structure determination using 3DED were found to be primarily dependent on sample quality, although other issues such as the inability to unambiguously assign atoms,[50,153,220] and difficulty fully sampling reciprocal space arose. 3DED structures refined assuming a kinematical approximation have larger R_1 values than those typical of X-ray structures.[66,198] Improvement in R_1 values is observed when a dynamical model is used during refinement,[182] however dynamical refinement is not yet routinely implemented.

Despite much pessimism in the past, the future of the field of 3D electron crystallography looks promising, and the technique continues to draw more and more interest from synthetic chemists.[170,171,221–223] Advances in hardware, and the creation of specialised hardware specifically designed to collect 3DED data should help to alleviate some of the current challenges associated with data collection and help elevate the technique further.[224] The first commercialised dedicated electron diffractometers, the ELDICO ED-1[225,226] from ELDICO Scientific AG, and the XtaLAB Synergy-ED[227,228] from a Rigaku and JEOL collaboration, are now available. Methodological advances, including further development of dynamical refinement approaches, may also help to improve electron diffraction structures and bridge the current statistical gap between electron and X-ray structures. As dynamical refinement becomes more accessible and routine, R_1 values for electron diffraction data should become more comparable to their X-ray counterparts.[182] Depositing raw, unprocessed datasets alongside refined structures is critical, as it not only increases transparency in the field, but will also empower method developers to use those datasets when establishing and validating new protocols and software.[229,230]

An intriguing area of future development lies in the automation of the 3DED technique. However, the usefulness of automation will depend entirely on the question to which 3DED is being applied to solve. Currently, our workflow requires manual input from researchers during screening, selecting, and centring the crystals, then assessing whether diffraction quality warrants data collection. The initial steps (screening, selecting, and centring) have potential to be automated, as has been done with software such as SerialED[208,209] and SerialRED[210] (see **Chapter 5** for further details), however this would require accurate auto-targeting and robust auto-eucentric procedures specifically designed for data collection from crystals. Assessment of diffraction quality may be more difficult to automate, an automated system would likely collect many low quality datasets from crystals that produce poor quality diffraction patterns. A similar trade off occurs for single particle cryoEM where automated data collection has become routine.[214]

In cases where rapid verification that the expected complexes have been formed and data collection is stopped once sufficient data has been collected, such that the structure can be determined to high resolution and completeness (see **Chapter 5 and Chapter 6**), automation would likely not be beneficial. The manual approach allows the researcher to stop collecting further datasets once the structure has been satisfactorily determined. This maximises the efficiency of precious microscope time. An automated system on the other hand, could go on collecting further datasets unnecessarily unless a sophisticated feedback mechanism was in place. Conversely, an automated system could be extremely useful when assessing polycrystalline materials or samples that contain multiple species.[79,211] The automated system could be used to select and collect data from many targets without human bias. Although many of these datasets may not contain high quality diffraction, the automated system could be used to identify as many different crystal forms as possible. This could have significant implications for the pharmaceutical industry, where polymorph screening is essential as different polymorphs of the same species can have vastly different properties. This can affect the efficacy and safety of a pharmaceutical agent. Pharmaceutical agents are often available as microcrystalline powders. An automated 3DED approach could be used to assess the safety of a drug by identifying whether any harmful, crystalline polymorphs or impurities are present. These may not be detectable by other methods. It has been suggested that it is even conceivable that 3DED structures of drugs will be required before they can be given FDA (U.S. Food and Drug Administration) approval.[79,231] More significant implications of 3DED for the pharmaceutical industry may lie in intellectual property, whereby pharmaceutical companies could test competitor's products to determine whether traces of patent protected APIs are present.

9 Methodology

All electron diffraction data presented in this thesis were collected in house on a Thermo Fisher Scientific Glacios microscope equipped with a Ceta-D camera. This chapter will detail how data were collected and processed. The schematic in **Figure 9.1** gives an overview of this process, further information on the individual stages of this workflow will be given throughout this chapter.
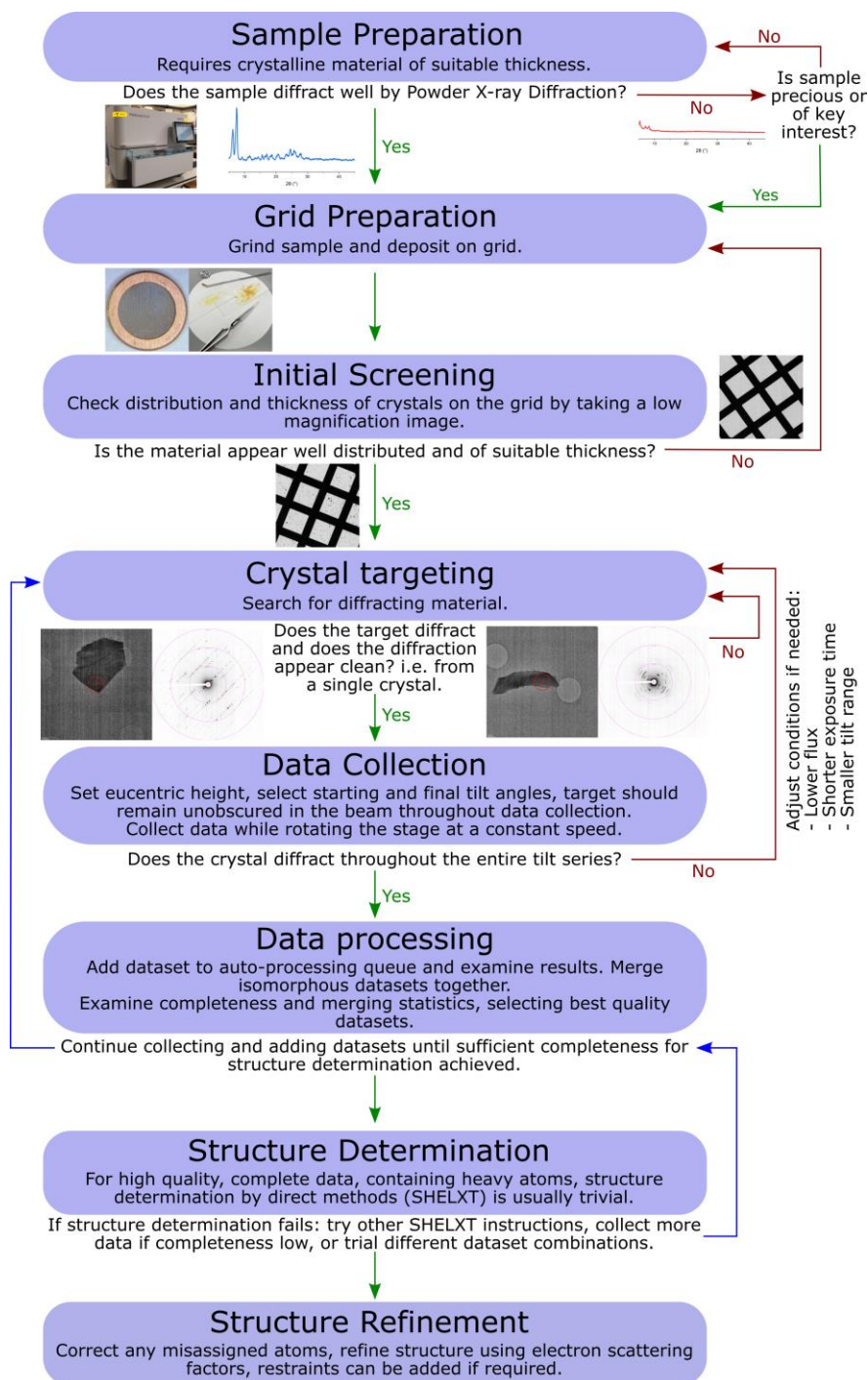
Figure 9.1. A schematic showing the electron diffraction data collection and processing workflow utilised in this thesis.

9.1 Specimen preparation for 3DED experiments

9.1.1 Sample Preparation

Sample and grid preparation for dry, non-air sensitive, small molecule organometallic powders is a relatively trivial process. The key sample requirements are that the sample must be crystalline and thin enough to allow the incident electron beam to pass through, without prohibitive amounts of inelastic scattering[204]. Crystals should have a thickness of less than a few hundred nanometres, or as suggested by Martynowycz *et al.*,[204] be less than twice the inelastic mean free path (MFP) length. Equating to a maximum crystal thickness of 540 nm at 200 kV (MFP=270 nm).[204] It is worth noting this calculation is likely to be dependent on crystal composition and is based on protein crystals which have much larger unit cells than small molecule crystals and contain solvent channels. Unfortunately, it is not possible to quantitatively determine the thickness of crystals using a TEM prior to data collection. This is because the crystals would be destroyed by radiation damage in the process of tilting and reconstruction by tomography, so subsequent data collection would not be possible. Crystal thickness is qualitatively assessed by examining differences in grey scale levels on brightfield TEM images. To minimise microscope screening time and ensure efficient use of resources, PXRD experiments can be used to assess sample crystallinity prior to insertion into the microscope.[149] **See Chapter 5**. To produce crystals of a suitable thickness, small molecule organometallic crystalline powders often require grinding.[76] This can be achieved using a mortar and pestle or grinding between two microscope slides.

Adaptations can be made to the specimen preparation process as required for samples that are particularly air sensitive or difficult to handle. An example of such an adaptation is given in **Chapter 4**.

9.1.2 Grid preparation

The ground sample is then transferred to a pre-clipped TEM grid. This is typically done by placing a pre-clipped grid into a vial containing the sample and gently flicking the vial to coat the grid in sample or, by placing a grid directly on top of the ground sample on a slide or in a mortar and pestle. Excess powder is removed to ensure the grid is not oversaturated with sample. The grid is then cooled to liquid nitrogen temperature ready for insertion into the TEM. This process is shown in the schematic in **Figure 9.2**.

Grind sample   Transfer to grid   Remove excess   Cool to liquid N$_2$ temperature
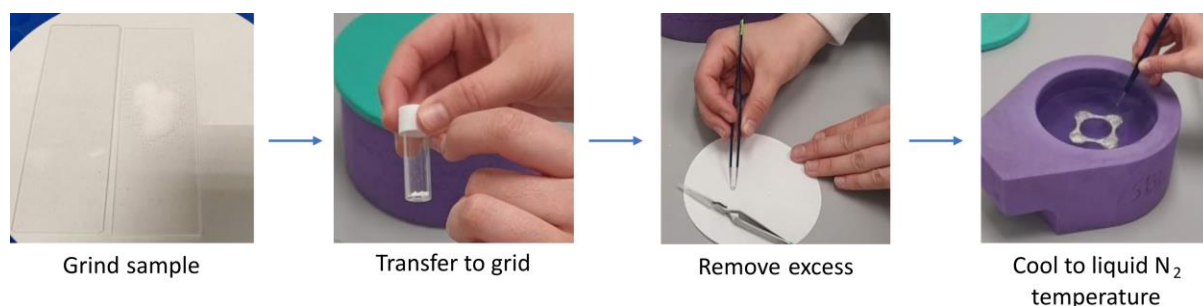
Figure 9.2. Specimen preparation for small molecule organometallic powder samples. The sample is crushed to obtain crystals of a suitable thickness, transferred to a pre-clipped TEM grid (typically by direct application or by transfer to a vial). The excess powder is removed by turning the grid several times on a piece of filter paper. The grid is then cooled to liquid nitrogen temperature ahead of insertion into the TEM.

In order to study samples in a TEM, the samples need to be deposited onto a support medium compatible with the microscope, a TEM grid. A TEM grid is comprised of a fine metal mesh, typically copper, overlain with a carbon film. The grids are 3.05 mm in diameter. In this work, Quantifoil R1/4 200 mesh copper grids and R2/4 200 mesh copper grids were used. The carbon film of these grids is punctuated with a regular pattern of holes. R1/4 means that the carbon film has holes of 1 μm diameter separated by a distance of 4 μm. In R2/4 grids, the 2 μm diameter holes are separated by film with a distance of 4 μm. Mesh refers to the number of grid squares per inch. Common grids have meshes of 200, 300 and 400 grid squares per inch. It was decided that 200 mesh grids were most suited to 3DED as the larger grid squares allow for the sample stage to be tilted to a greater extent than the 300 or 400 mesh grids before the beam becomes blocked by a grid bar. A Quantifoil 200 mesh grid is shown in **Figure 9.3**. The grid has been visualised from both the film side and the grid side by light microscopy.
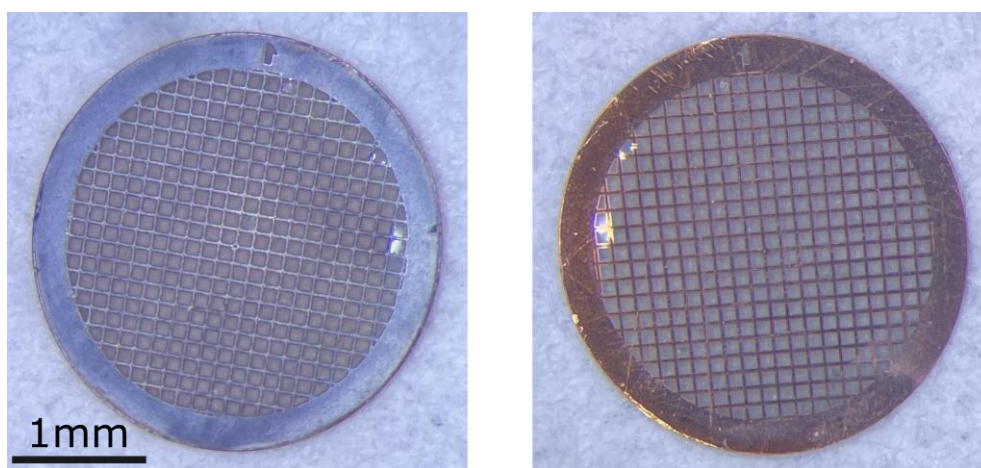
Figure 9.3. A Quantifoil 200 mesh grid visualised by light microscopy. Left: Film side - side of grid with carbon film overlain. Right: Grid side - side of grid with copper mesh only. A 1 mm scale bar is shown.

The Glacios at York utilises autoloader technology, as such, the TEM grids need to be clipped to form an "autogrid" prior to insertion into the microscope. Typically, for cryoEM experiments with aqueous samples, the grids are clipped after the sample has been loaded and the grids have been vitrified in liquid ethane. For these 3DED experiments, dry powders were used. As the powders did not require vitrification, the grids were clipped prior to sample loading. In the process of clipping, a grid is inserted into a clip ring film side down. The grid is secured in place using a C-clip. This forms an assembled autogrid. Images of an assembled autogrid are shown in **Figure 9.4**.
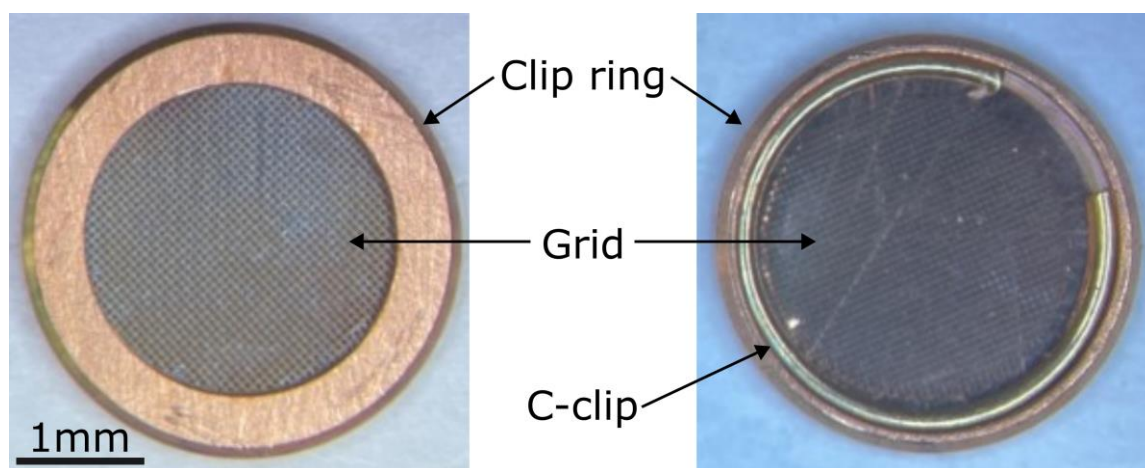
Figure 9.4. An assembled autogrid visualised by light microscopy. Left: Top of an autogrid, the grid has been placed in the clip ring film side down. Right: bottom of an autogrid, the C-clip securing the grid in the clip ring can be seen. A 1 mm scale bar is shown

Pre-clipping increases the rigidity of the grids, which are flimsy and easily broken or damaged, making it easier to load the grids with sample. A disadvantage of pre-clipping is that the clip ring does not sit flush with the grid, it creates a lip around the edge of the grid. As such, the powdered sample may become trapped at the edge of the C clip and not be dispersed on the grid itself.

9.2   Microscope screening and data acquisition

All data in this thesis were acquired using a Thermo Fisher Scientific Glacios microscope equipped with a Ceta-D camera. Data were collected using the Thermo Fisher Scientific software, EPU-D. Data were typically collected using nanobeam electron diffraction. Microscope alignments were performed prior to screening and data collection. Further details on the microscope configuration for data collection are given in **Section 9.2.3**.

9.2.1 Initial screening

Once loaded into the microscope, a low magnification overview image of the grid is taken. In EPU-D, this image is referred to as an atlas. Individual images of areas of the grid (tiles) are taken at 155x magnification and the software then stitches these together to create an image of the entire grid (atlas). The atlas created is not an exact representation of the grid as the image stitching is often imperfect. However, it is a useful tool for grid navigation and quickly assessing the distribution and thickness of samples.

In order to collect electron diffraction data, crystalline material of ~<500 nm thick needs to be present.[204] Additionally, the individual crystals need to be separated from other material on the grid, and at a sufficient distance from the grid bars. This ensures that the target crystal can be isolated throughout the full course of a rotation data collection, with no additional material obstructing the beam. Examining the atlas image allows for a rapid assessment of whether the grid is likely to be suitable for 3DED data collection. Examples of unsuitable grids are those with a very scarce distribution of sample (**Figure 9.5(a)**), grids containing material that is too thick to allow the electron beam to penetrate (**Figure 9.5(b)**) or grids where the majority of the film is damaged (**Figure 9.5(c)**). An example of a grid with well distributed, small targets is shown in **Figure 9.5(d)**. If grids are found to be unsuitable at this stage, further grids can be prepared. For instance, samples which contain overly thick material can be further ground before application to a new grid.
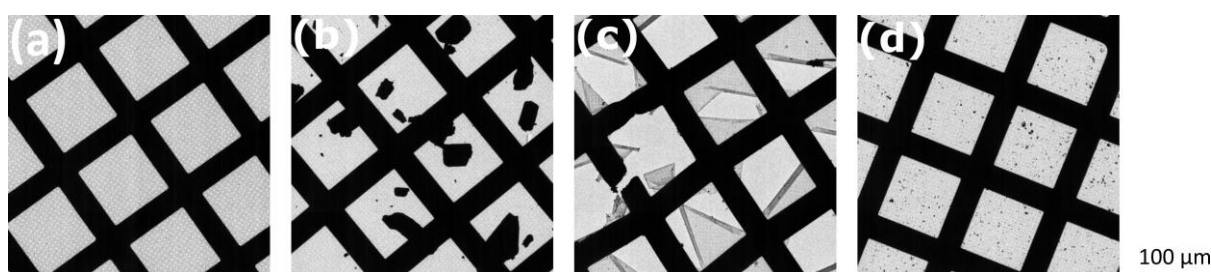
Figure 9.5. Example tiles from atlas images showing potential issues with grids that can be identified during initial screening. (a)-(d) are TEM brightfield images, a 100 µm scale bar is shown. (a) shows a grid that is very sparsely populated with sample. (b) shows a grid containing crystalline material that is too thick for electron diffraction. The crystals are large and appear completely black, as such, no transmission is recorded from these areas on the detector. (c) shows a damaged grid with lots of areas of vacuum due to broken film. (d) is a grid with ideal sample distribution and size. There are lots of small, grey targets that are well distributed on the grid.

9.2.2 Crystal targeting and centring

Crystals can only be visualised and centred using the electron beam. This means that they are accumulating radiation damage whenever they are exposed to the beam, potentially reducing diffraction quality. Exposure to the beam should be minimised prior to data collection to reduce damage. However, crystalline targets need to be identified and these must then be centred in order to collect electron diffraction data. Using EPU-D, this is achieved by taking a short exposure brightfield image of the centred target crystal. The red cross on the TEM brightfield images in **Figure 9.6** indicates where the centre of the field of view is. During setup, the beam is aligned with the centre of the field of view. The red circle visualised in the TEM brightfield images represents the beam diameter. This does not appear on EPU-D and has been added post data collection. A test diffraction image is then taken using the same lens conditions and exposure time that will be used during data collection. The stage remains stationary for this test image. The test image is used to determine whether a diffraction pattern is observed from the target and whether this is of sufficient quality to warrant a full data collection. Examples from a well diffracting crystal and a poorly diffracting crystal are shown in **Figure 9.6(a)** and **Figure 9.6(b)** respectively. In **(a)** sharp spots are observed that follow a repeating pattern of even spacing, and only one orientation of spots is observed indicating these originate from a single lattice. The resolution of this diffraction test image is better than 0.83 Å. In contrast, diffraction observed from the crystal in **(b)** is much poorer. The spots are streaked and smeared rather than sharp, indicating that they originate from multiple different lattices. The resolution is also lower indicating poor quality diffraction. Data would not be collected from crystals such as this.

If high, or reasonable quality diffraction patterns are observed. The crystal is then centred at eucentric height. This is the height at which the stage axis intersects the optic axis at the specific point, such that when the sample is placed there, it is at focus when the objective lens current is optimal. This can be performed automatically in EPU-D using the auto eucentric function which utilises the stage tilt method. The stage is moved to progressively higher tilt angles, fluctuating between positive and negative tilt angles, and brightfield images of the crystal are taken. EPU-D then attempts to correlate the images and adjusts the Z height in an attempt to ensure the target crystal remains centred at tilt angles ±30°. A higher magnification than suggested in the EPU-D manual was used to ensure that Z height was more accurate and that the crystal remained centred throughout data collection. Z height will need to be adjusted manually in cases where auto eucentric fails, care should be taken to minimise exposure to the beam during this process. Auto eucentric may fail for numerous reasons, including when the target crystal is in close proximity to the grid bars or other crystals, if the target is oddly

shaped, or if the film is bent or broken. Often the auto eucentric function fails due to low signal, when the cross-correlation fails to produce a single clear peak. If the target crystals are particularly sensitive to damage from the electron beam, Z height adjustments should be performed on an alternative area of the grid, close to the target crystal. This ensures that data are collected while the target is at (or at least close to) eucentric height but precludes the target from exposure to unnecessary radiation prior to data collection.
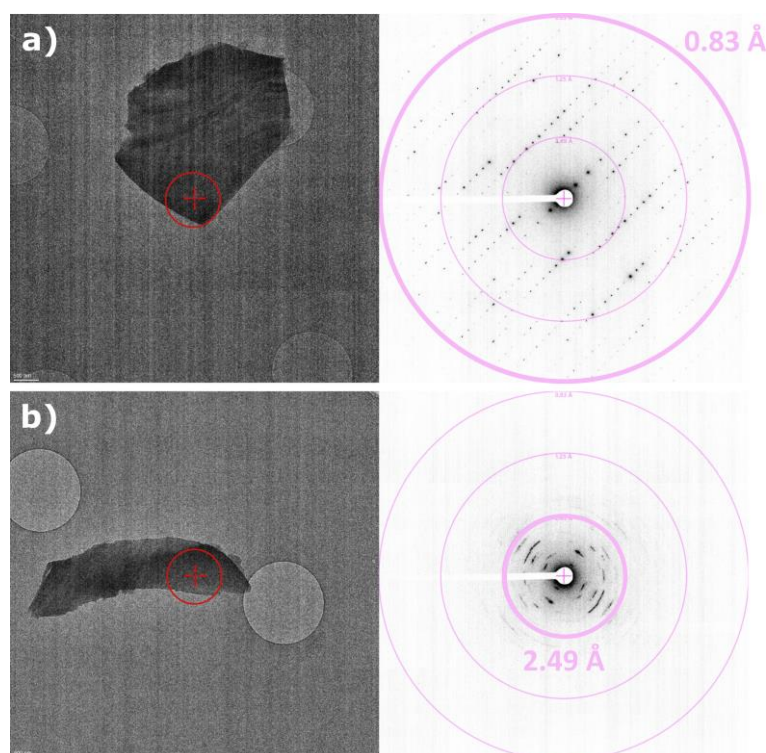
Figure 9.6. TEM brightfield images and example diffraction patterns from a) a well diffracting crystal, and b) a poorly diffracting crystal. *The red circle on the brightfield images represents the size of the beam used during data collection. The pink circles on the diffraction patterns indicate resolution.*

Once the target crystal is at eucentric height, an additional brightfield image of the target should be taken with no stage tilt to ensure the crystal remains in the centre of the screen and will be illuminated during data collection. Images should also be taken at the start and final tilt angles to ensure the crystal remains centred and will not be obscured by other material on the grid or by the grid bars themselves. The maximum allowable tilt angles were ±69° to avoid collision with the pole pieces, account for backlash correction, and allow the stage to accelerate to a constant speed prior to the start of data collection. Practically, data cannot typically be collected from this full range as the target does not remain isolated and centred in the beam. Data were typically recorded between ±45°. The rotation range varies for each target and should be adjusted accordingly. Once this has been checked, data collection can commence.

153

Finding, centring, and testing target crystals for diffraction is currently a manual process in this workflow. This is a stage of the process that has potential to be automated.[210,232] At the time of our data collection sessions, it was possible to perform a batch data collection using EPU-D. However, this still required the manual finding of targets, taking test shots and centring of crystals. This is the most time consuming stage of data acquisition and once complete, performing the data collection only takes a couple of additional minutes. Therefore, it was sensible to collect data immediately rather than adding targets to a queue. Additionally, when using batch mode, all datasets were collected between the same tilt angles and customisation of the starting and final tilt angles for each crystal was not possible.

9.2.3   Data collection

All data were recorded at 80K with the microscope operating at 200 kV. For all datasets 2x binning was applied, rolling shutter was used, and noise reduction mode was enabled. Binning refers to the process by which signals from neighbouring pixels are combined together. As each pixel has its own readout element, the signals are combined through software after readout. This leads to a faster readout time and reduces the file size so datasets can be exported and processed more rapidly, and less space is required for dataset storage. The sacrifice of binning is that spatial resolution is reduced. 2x binning provides a compromise that makes data collection more rapid and accessible without inhibiting data processing due to reduced image resolution. With 2x binning, a total of 4 pixels (2x2) are combined together to make one pixel (**Figure 9.7**). On the Ceta-D detector, there are 4096x4096 unbinned pixels (16.78 megapixels), with 2x binning applied the number of pixels reduces to 2048x2048 (4.19 megapixels). Rolling shutter refers to the fact that the pixels are read out line by line. Noise reduction mode means that detector readout is recorded twice, once with signal and once after the signal has been reset. The readout when there is no signal is subtracted from the total signal to give the actual signal. This helps to reduce noise compared to the Ceta-D's predecessor, the Ceta.

No binning
4 pixels
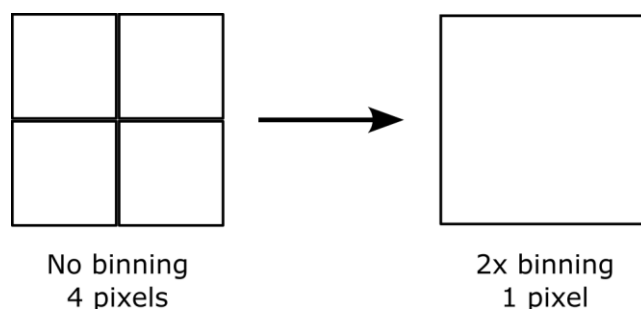
2x binning
1 pixel

Figure 9.7. Schematic representing 2x binning.

Further details on specific data collection conditions for each compound are provided in the relevant chapters. The majority of datasets were collected using nanobeam electron diffraction, with the exception of the complexes in **Chapter 4**, for which selected area electron diffraction was used instead. The difference between these collection modes is explained in **Chapter 2, Section 2.2.3**.

The conditions for the selected area electron diffraction set up were as follows; gun lens 4, spot size 11, 30 µm C2 aperture, 40 µm selected area aperture. This resulted in a flux of ~0.01 e$^-$ Å^{-2} s^{-1}, an illuminated area of 4 µm and a sample plane area of 1.4 µm from which diffraction was recorded. An illustration of the resulting beam conditions for this setup is shown in a brightfield TEM image in **Figure 9.8(a)**. The typical exposure time under such conditions was 2s.

The conditions for the nanobeam electron diffraction set up were as follows; gun lens 8, spot size 11, 30 µm C2 aperture. This resulted in a flux of ~0.07 e$^-$ Å^{-2} s^{-1} and an illuminated area of 1.05 µm. This flux is still relatively high compared to the selected area electron diffraction set up. To counter the higher flux, a shorter exposure time of 0.75 s was utilised. A TEM brightfield image is given in **Figure 9.8(b)** which shows the size of the resulting illuminated area in nanobeam electron diffraction.
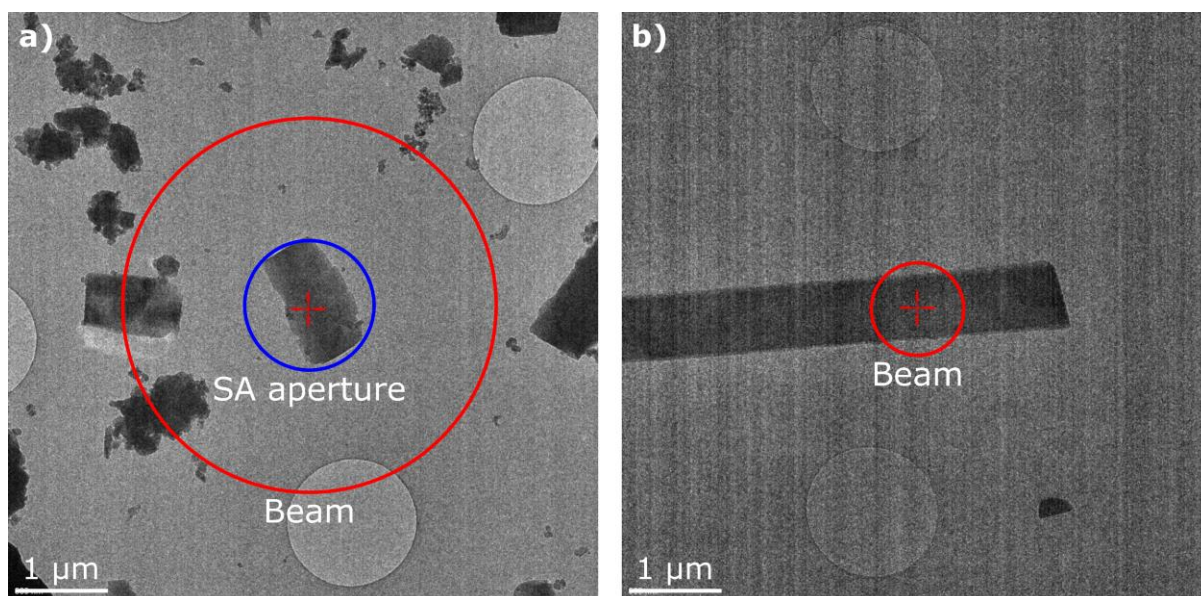
Figure 9.8. TEM brightfield images illustrating the illuminated areas for a) selected area electron diffraction mode and b) nanobeam electron diffraction mode. The beam diameters are indicated by the red circle and are ~4 µm and 1.05 µm for a) and b) respectively. Image a) also depicts a blue circle of 1.4 µm diameter. This is the area from which diffraction data are collected when the 40 µm selected area aperture is inserted.

Data were collected while the stage rotated at a constant speed between the starting and final tilt angles specified above in **Section 9.2.2**. During data collection the crystal should remained centred and illuminated by the beam and the crystal should diffract throughout the full data collection. In some instances, diffraction may not be recorded over the full rotation range. This may be because the crystal was no longer centred in the beam, or could be as a result of radiation destroying the crystallinity of the lattice. The first step to rectifying this problem was to determine whether the crystal remained centred by taking brightfield images from the tilt angle where diffraction was no longer observed. If the crystal remains centred but diffraction does not continue, this indicates substantial radiation damage has occured. For crystals that are particularly radiation sensitive, data collection conditions may need to be adapted to allow for collection of high quality data. This can be achieved in a number of ways. Firstly, the exposure time for each image can be shortened, as long as each exposure still allows sufficient signal to noise ratio. Secondly, the rotation range can be reduced so only data before significant reduction in data quality are collected. This method was utilised in the collection of data from the beam sensitive σ-alkane complex in **Chapter 4**.

9.3 Data processing

Data were processed with DIALS[201] using a semi-automatic processing script, `process_datasets.py`, authored by Dr Huw Jenkins.[202] All datasets were processed using the same, standard sequence of DIALS commands. The script simply allowed the data to be processed more reproducibly and rapidly, but manual data input and subsequent examination of data processing was required. The script reads a JSON file where options for processing and the image paths for the datasets were specified. A template `datasets.json` file is given below (**Figure 9.9**). The script processes the datasets individually up to the integration stage and organises the output by grid and crystal number. Once all datasets have been integrated, their outputs can be manually inspected and datasets with the same space group and unit cell parameters can be scaled together.

Further details on the individual stages of data processing are given in the following sections.

```
{"parameters":{
        "sample":"Compound_Name",
        "spacegroup":"P1",
        "njobs":2,
        "nproc":4,
        "import":"distance=958.5  goniometer.axes=1,0,0 panel.pedestal=-64",
        "generate_mask":"untrusted.circle='1031 1023 50' untrusted.polygon='0 1010 600 1010 976 1004 988 998
986 1044 978 1041 650 1051 0 1051'",
        "search_beam":true,
        "find_spots":"d_min=0.8",
        "index":"detector.fix=distance",
        "refine":"detector.fix=distance",
        "integrate":""
        },
 "datasets":[
        {"template":"Compound_Name_xtal1/Compound_Name_xtal1_####.mrc", "image_range":null, "grid":1, "xtal":1},
        {"template":"Compound_Name_xtal99/Compound_Name_xtal99_####.mrc", "image_range":null, "grid":1, "xtal":99}
                ]
}
```

Figure 9.9. Template input file for auto-processing script.

9.3.1   Importing

The images collected were in MRC format, this format is native supported in dxtbx from DIALS-3.5 onwards [233]. As such, DIALS can read the metadata in the headers of the MRC files to obtain most of the information needed to process the datasets. However, key parameters need to be specified in order to give DIALS the correct information about the detector setup. One of these parameters is the detector distance. The detector distance displayed in EPU-D may not be correctly calibrated and as such must be determined using an aluminium powder standard. The detector distance and unit cell parameters are intrinsically linked so it is important that the detector distance is well calibrated. An additional parameter that requires specification is the goniometer rotation axes, for the York Glacios this is 1,0,0 when the stage is rotated in a positive direction.

As a result of an unspecified correction the Ceta-D camera applies, and due to the noisy nature of the detector, the images recorded contain pixels of negative intensity value. These pixels still contain valuable information, but negative pixel values can cause problems during profile fitting in integration. This happens because background modelling for profile fitting fails when there are too many pixels of negative value in the background of a reflection. This means that weak, high resolution spots can be excluded from integration. To prevent the systematic loss of weak, high resolution reflections, an offset (pedestal) is applied to all pixel values to artificially inflate the intensity of all pixels, reducing the number of negative pixels. The behaviour of our detector has been observed and is relatively consistent. A dataset was collected on the Ceta-D camera with the screen inserted, no beam and no sample present. 0.5 s exposures were taken with 2x binning to observe detector behaviour and negative pixel values. The intensities of the individual pixel values were then plotted against the count for each frame, a representative frame from this series is shown in **Figure 9.10**. The resulting graph

shows a curve of intensity values, centred around zero, extending visibly to around ±50. For a perfectly noiseless detector, one would expect to see all pixels with a value of 0 as there is no electron beam incident on the detector. A pedestal value of 64 ADU was added to each individual pixel value. This value was chosen as it encompassed the majority of negative pixel values while excluding further negative outliers that were likely anomalous, as such some negative pixels would still be present in the images.
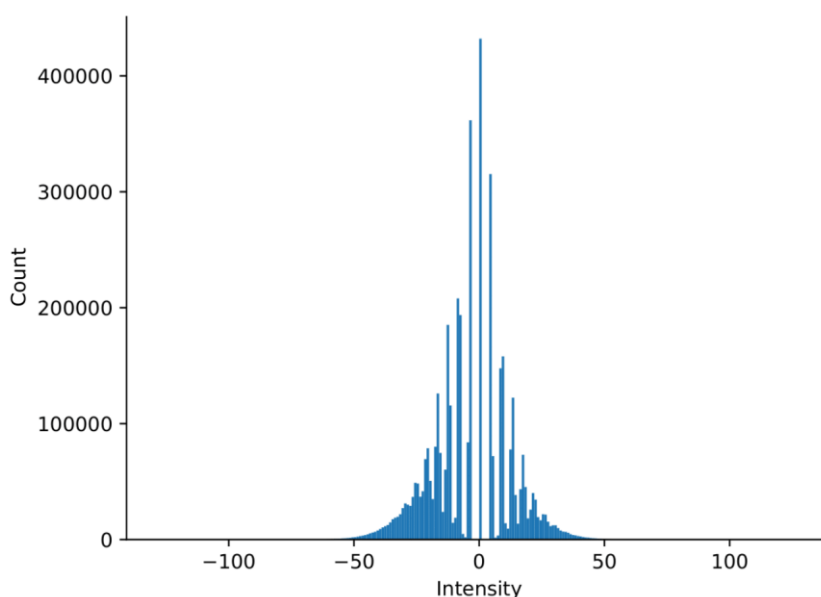
Figure 9.10. A graph showing individual pixel intensity against pixel count for a representative frame of a series of 0.5 s exposures recorded on the Ceta-D detector with no beam and 2x binning.

A mask was then generated to cover the beam stop, preventing DIALS from finding spots in the area blocked by the beam stop. The beam stop was used for all data collections in this thesis and had a fixed position, after the lenses, as such the mask did not need to be changed for different camera lengths. A mask was applied to all images using the following command:

```
dials.generate_mask imported.expt untrusted.circle=1031,1023,50
untrusted.polygon=0,1010,600,1010,976,1004,988,998,986,1044,978,1041,650,1051,
0,1051
```

9.3.2 Spot finding

The next step is spot finding. Due to the low flux used when collecting electron diffraction data, the intensity of the Bragg peaks can be weak. This means it is often possible for DIALS and other processing programs to detect background noise as spots in addition to finding spots corresponding to the lattice points. Spot finding parameters should be carefully checked and adjusted to ensure that spots are being identified correctly. Typically, for data collected in this thesis, only d_min (high resolution limit) was changed. This was altered depending on how well crystals diffracted, or on the resolution limit at the edge of the detector.

Prior to data collection, the direct beam was manually aligned with the centre of the detector using the aluminium standard as a guide. As this was a manual alignment, it was prone to user error and the beam may not have been perfectly centred. Additionally, the beam may move somewhat (by a few pixels or less) between datasets when the lens configuration changes between the various imaging modes and diffraction mode. When a beam stop is present, DIALS can use the results of spot finding to search for a better beam centre.[234] The function: `"search_beam":true`, was used to account for the potential variation in direct beam position. If no beam stop is present, the beam can be tracked directly.

9.3.3 Indexing

The spots were then indexed in P1 symmetry to find the lattice parameters of the triclinic unit cell. The detector distance, and τ_2 and τ_3 rotations of the detector were fixed using: `detector.fix=distance`. This stabilises the refinement of diffraction geometry, preventing the detector distance, and subsequently the unit cell distances, refining to unreasonable and incorrect values. It is essential that the detector distance is carefully and accurately calibrated as a result of this. No other parameters were specified during indexing.

The aim of indexing is to obtain a unit cell whose predicted reflections match the observed reflections. This can be checked visually using dials.image_viewer. Additionally, the log file contains information on how well the geometry model fits the observed spots (RMSD_X (fast axis) , RMSD_Y (slow axis) and RMSD_Z (tilt angle direction)) and the percentage of spots indexed. Generally, the lower the RMSDs

and the higher the percentage of spots indexed, the better the solution. If these statistics are poor, it may indicate that the correct indexing solution has not been reached.

9.3.4 Refinement

Although a refinement was performed during indexing, further refinement is required to ensure the best fit of predicted spots to the observed data as possible. The refinement stage is split into two parts. First a scan-static refinement is performed, followed by a scan-varying refinement. The detector distance and τ_2 and τ_3 angles are once again fixed to prevent refinement of detector distance and unit cell lengths to unfeasible values.

The scan static refinement refines a static unit cell for the entire dataset. This refinement step focuses on refinement of the orientation of the beam and detector. As the name suggests, scan varying refinement allows parameters (excluding detector distance and τ_2 and τ_3 angles) to change over the course of the dataset. This is valuable because it allows the unit cell parameters to change over the course of the dataset, improving the ratio of predicted to observed reflections as the dataset progresses. During data collection, as the crystal is being exposed to the electron beam, the unit cell lengths will expand as the crystal accumulates radiation damage.

9.3.5 Integration

Default parameters were used for integration. Integration is the process by which the intensity of the spots is measured. To accomplish this, the background noise must be calculated and removed from the contribution to intensity for each spot, this is particularly important for noisy data with weak reflections. DIALS utilises both profile and summation fitting. For strong reflections, the contribution from the background is very small and as such is obscured by the reflection itself. For these spots, summation integration is the best measurement of intensity. Whereby the pixel values of pixels contributing to the spot are simply added together. For weak reflections, summation is not a good estimate of spot intensity as the contribution from the background is greater. A better measure of intensity can be achieved using profile fitting. Profile fitting generates a predicted Gaussian[235] shape of the reflections from strong, well measured spots. This distribution can then be fitted to the raw data for weak reflections, greatly improving the intensity measurement.

9.3.6   Scaling multiple datasets

A single reflection will be measured multiple times, either during the course of a single data collection, via symmetry related reflections, or the same reflection may be measured from multiple different crystals. However, the intensity values of different measurements of the same single reflection will be different. This is due to experimental effects, primarily radiation damage. As the dataset progresses and the crystal is exposed to the electron beam, it accumulates radiation damage, reducing the intensity of high resolution spots. Merging multiple measurements of the same reflection together allows for the best estimate of the intensity of the reflection. Scaling attempts to accomplish this by determining a scale factor that can be applied to each reflection from a smoothly varying function (a scale model) that is dependent on rotation.

Until now, all datasets have been processed individually. After integration, the processed datasets are inspected manually, and datasets with the same space group and unit cell parameters can be scaled together. An additional step can be included here to search for compatible higher symmetry space groups using dials.symmetry. Often, the datasets have already been processed manually during data collection to ensure enough data has been collected to solve the structure with sufficient completeness, so there is already an indication of whether the high symmetry space group leads to a solvable structure.

The symmetrised datasets can then be scaled using dials.scale with the following parameters specified: `intensity_choice=profile physical.absorption_correction=false min_Ih=1`. The high resolution limit (d_min) is also specified. This is typically set at the same limit used in spot finding but may be adjusted depending on the quality of the scaling statistics. The intensity choice was set to include profile fitted reflections only, due to a bug in the dials.scale code where the weighted combination of profile and summation reflections was incorrect. This has now been rectified so the intensity choice no longer needs to be specified. The physical absorption correction was set to false, as this model applies to X-ray absorption. Additionally, this correction has a 2θ dependence and as the scattering angles for electron diffraction data are much smaller than X-ray scattering angles, the correction term is tiny and meaningless for electron diffraction data. In future, this correction may be automatically removed when processing electron diffraction data in DIALS. When optimising the error model, DIALS uses reflections with expected intensities above a set threshold (`min_Ih=25` by default). By setting `min_Ih=1`, more reflections are used in error model refinement. This is necessary because

for small molecule compounds with low symmetry and small unit cells, there are few reflections that are symmetry equivalent. The cut off is set to a low value to ensure as many reflections as possible are used in error modelling to ensure the best possible σ(I) estimates.

The scaling step in our workflow is currently a manual process. With the results being carefully analysed and individual datasets or frames being removed to achieve the best solution. Datasets are selected that improve the overall completeness of the data without sacrificing ΔCC½ or R$_{merge}$. R$_{merge}$ is defined by the following equation, where $\langle I(hkl) \rangle$ is the average of the symmetry related observations of the same unique reflection.[236]

$$R_{merge} = \frac{\sum_{hkl} \sum_j \left| I_j(hkl) - \langle I(hkl) \rangle \right|}{\sum_{hkl} \sum_j I_j(hkl)} \qquad (9.1)$$

CC½ is typically calculated by dividing the unmerged data into two parts. The two parts each contain half of the measurements of the unique reflections. The intensities of the unique reflections are randomly assigned to each half, and the correlation coefficient between the average intensities in each half is then calculated to give CC½.[237] CC½ can be calculated in a different way such that the intensities of the unique reflections are not randomly assigned to each half.[238] This method was utilised by DIALS, as random assignment of the reflections would add an additional factor that would cause CC½ to change when recalculating CC½ when datasets are added or removed. The quality of the data can be assessed as datasets are added and removed by calculating the change in CC½ (ΔCC½). ΔCC½ is defined by the following equation:[238]

$$\Delta CC_{1/2-i} = CC_{1/2-i} - CC_{1/2(overall)} \qquad (9.2)$$

$Where$:

$\Delta CC_{1/2-i} =$ the change in correction coefficient when dataset i is excluded

$CC_{1/2-i} = CC_{1/2}$ when dataset i is excluded

$CC_{1/2(overall)} =$ the average $CC_{1/2}$ when all datasets are included

If $\Delta CC_{1/2-i}$ is positive, dataset i improves the overall $CC_{1/2}$. If $\Delta CC_{1/2-i}$ is negative, dataset i has a detrimental impact on the overall $CC_{1/2}$. The dataset that results in the most negative $\Delta CC_{1/2-i}$ can be removed and the data can then be rescaled.

Datasets that do not add to overall completeness and negatively impact $\Delta CC_{1/2}$ and R_{merge} are usually removed. The `dials.scale.html` file is particularly helpful for deciding which frames or datasets to remove, as it includes a graph which plots scale and R_{merge} against each of the individual datasets and their frames, so it is easy to visualise which frames lead to poor statistics and should be removed.

Further data can be collected if the completeness or quality of the combined datasets is low. Once satisfied, data can be exported to SHELX hkl format to establish if structure determination is possible and results in a feasible structure. It is often valuable to do this before performing a joint refinement.

9.3.7 Joint refinement

Detector distance and unit cell parameters are intrinsically linked. Until this point, detector distance was fixed to prevent refinement to unfeasible values. Joint refinement attempts to allow detector distance and unit cell lengths to stably refine simultaneously, in the hopes of obtaining a best estimate at an average unit cell that best describes the data. This process also generates errors for the unit cell parameters that are meaningful. The errors don't reflect variance in the cell parameters themselves but how well the refinement converges based on the input data. If a new dataset was compared with the results of joint refinement, the cell parameters for the new dataset would likely be outside of these expected errors. Uncertainty in cell parameters affects uncertainty in bond lengths. These errors are more important in small molecule crystallography than in macromolecular crystallography (MX), in MX restraints are applied to the bond lengths, this isn't typically the case for small molecule crystallography.

To perform a joint refinement, the scaled reflections are first filtered to ensure only reflections in the final dataset are included:

```
dials.filter_reflections scaled.refl flag_expression="scaled&integrated_prf"
```

The filtered reflections are then used in a scan-static refinement for all the datasets, the τ_2 and τ_3 angles remain fixed:

```
dials.refine scaled.expt filtered.refl output.experiments=joint_refined.expt
output.reflections=joint_refined.refl detector.fix_list=Tau2,Tau3
scan_varying=false
```

After this refinement, the detector distance and unit cell parameters should be checked to ensure they have not refined to unreasonable values. This can be achieved using the `dials.show` commands below. If the detector distance changes dramatically (more than a few mm difference between datasets and calibrated detector distance) a limit may need to be applied to the maximum number of iterations allowed for refinement. Examining the refinement steps in the LOG file can aid with this. The number of iterations after which the RMSDs stop converging can be observed.

```
dials.show joint_refined.expt | grep distance

dials.show joint_refined.expt | grep Unit
```

A 2θ refinement can then be performed. During a 2θ refinement, the 2θ values for each reflection are calculated and compared to the observed 2θ values. The difference between the observed and calculated values was then minimised. Dependence on crystal orientation was removed. 2θ refinement yields a refined unit cell with optimised unit cell parameters.

```
dials.two_theta_refine joint_refined.expt joint_refined.refl
```

The data are then rescaled, specifying the new unit cell parameters with `best_unit_cell`. The data are rescaled because changes to the unit cell parameters may cause slight changes in resolution, this may have an impact on the nominal resolution cut off (e.g., changing from 0.83 Å to 0.829 Å). Once the data had been rescaled, it was ready for export to SHELX format. Further details on joint refinement, and a tutorial including troubleshooting advice for when refinements do not converge can be found on Github.[239] For work presented in this thesis, all joint refinements converged naturally or with a limit to the maximum number of iterations.

9.3.8 Export

The scaled, unmerged data are then converted into a SHELX hkl format, ready for structure determination:

```
dials.export scaled.* format=shelx shelx.hklout=Compound_Name.hkl shelx.ins=
Compound_Name.ins
```

9.4 Structure determination

In order to determine the structure of the compound, information about the amplitude and phase of the structure factors are required. The amplitude of the structure factor is directly related to the intensity of a given reflection, but the phase information is lost in diffraction experiments. This is known as the crystallographic phase problem. The phases must be experimentally determined. SHELXT[164] was used to perform structure determination, this utilises a dual-space algorithm to determine the phases. This process is described in **Chapter 3, Section 3.3.4**.

The .ins file generated during export is edited to contain information about the elemental composition of the compound (SFAC), UNIT is set to 0, and HKLF 4 command is used. The unit cell parameters and electron wavelength are automatically supplied. It is important to ensure the correct wavelength for electrons is used, in this case 0.02508 Å for electrons at 200 kV. Structural determination can then be performed using SHELXT[164]. When phasing data from our organometallic molecules, the command line switches -a -y -m500 were typically applied. The function of these switches is described in **Chapter 3, Section 3.3.4**.

If successful, SHELXT will generate an initial structure model. This structure model should then be visualised and checked to ensure it makes chemical sense and that SHELXT hasn't generated a non-sensical solution. This visualisation can be performed using software such as Coot[240]. If a reasonable structure is suggested, i.e. atoms in a sensible arrangement, the structure is then ready for structural refinement using SHELXL[165], after modifying the .ins file. This will be explained in the following section.

9.5   Structure refinement

All structures were refined using SHELXL[165]. SHELXLE[166] is a useful programme for simultaneously editing .ins files, performing refinement using SHELXL, and visualising the structural model. Refinement is essential to ensure the best possible fit of the data to the model. By default, as SHELXL is typically used for X-ray data, the SFAC command applies the neutral atom X-ray scattering factors from the International Tables for Crystallography, Volume C.[241] As electrons and X-rays interact differently with matter, eight parameter fits for electron atomic scattering factors from Peng 1999[190] were used instead. These were manually added to the .ins file for each element present. Using electron scattering factors over the default X-ray scattering factors drastically improves the resulting R_1 values (**See Chapter 3, Section 3.4**). The SFAC command is now split over multiple lines for each individual element, care should be taken to ensure that the elements are listed in the same order as before and the UNIT command should be updated to reflect the number of atoms of each element in the unit cell.

The anisotropic ADPs were refined for all non-hydrogen atoms. Hydrogen atoms were then geometrically placed at the idealised internuclear X-H distances used in refinement of structures against neutron diffraction data in SHELXL.[203] Neutron diffraction distances were used as opposed to X-ray distances as the X-ray X-H bond lengths are shorter than those of neutron or electron bond lengths. This is because X-rays are scattered by the electron cloud, located on the X-H bond, whereas neutrons are scattered by the H nuclei themselves. Electrons are scattered by both electrons as well as the protons in the nuclei, so neutron X-H bond distances are a more representative reflection of electron X-H bond distances. A riding model was used for hydrogen atom placement. This means that the hydrogen atoms ride their parent atoms, i.e., the hydrogen atom and its parent atom have the same coordinate shifts. This is particularly useful as it allows the hydrogen atoms to be easily added without requiring extensive, additional parameters.

Restraints may be required to obtain a chemically sensible model. The most commonly applied restraint in this work is the extended rigid body restraint, RIGU. Additional restraints were also applied where needed, these included: DELU, SIMU, ISOR and SADI. These restraints are described in **Chapter 3, Section 3.4**. These restraints, together with refinement of an extinction parameter (EXTI instruction), typically enable anisotropic refinement of all non-hydrogen atoms without resorting to

XNPD instructions to prevent ADPs of some atoms becoming non-positive definite. The EXTI instruction was used in refinement of all compounds presented in this thesis.

For electron crystallography, the scattering amplitude has a unit of Å. As such, the map units become Å/ Å^3, simplifying to Å^{-2}. Map values, Å^{-2}, were converted to units of electrostatic potential, e/Å.[199] This was achieved by using a conversion factor of 47.87801 Å^{2}V from International Tables for Crystallography (2006) Volume C Section 4.3.1.7,[242] followed by a conversion factor of 1V = 0.069446154 e/Å. The conversion factor is based on recommended values from CODATA 2018.[243] Overall, the map values generated by SHELXL were multiplied by a value of 3.32494.

List of Abbreviations

3DED	Three-dimensional electron Diffraction
ADP	Atomic Displacement Parameters
ADT	Automated Diffraction Tomography
ADU	Analog-to-Digital Units
API	Active Pharmaceutical Ingredients
ASU	Asymmetric Unit
C1	Condenser 1
C2	Condenser 2
CC½	Correlation Coefficient between the average intensities in two sets of intensities
CCD	Charged Coupled Device
CFOM	Combined Figure of Merit
CHEM	Chemical Figure of Merit
CMOS	Complementary Metal-Oxide Semiconductor and Scintillator Coupled CMOS Device
cRED	Continuous Rotation Electron Diffraction
cryoEM	Cryogenic Electron Microscopy
CODATA	Committee on Data of the International Science Council
DIALS	Diffraction Integration for Advanced Light Sources – Processing software
DQE	Detective Quantum Efficiency
EPU-D	Electron diffraction acquisition software from Thermo Fisher Scientific
FDA	U.S. Food and Drug Administration
FEG	Field Emission Gun
FEI	Field Electron and Ion Company
FFT	Fast Fourier Transform
FIB	Focused Ion Beam
IEDT	Integrated electron diffraction tomography
JANA	A crystallographic computing software
JSON	File format - JavaScript Object Notation
$MBBF_4$	Methylene Blue Derivative
MFP	Mean Free Path
microED	microcrystal Electron Diffraction
MOF	Metal Organic Framework
MRC	File format common in electron microscopy
MX	Macromolecular Crystallography

NMR	Nuclear Magnetic Resonance
NPD	Non-Positive-Definite
OLEX2	A crystallographic package for small molecule crystallography
PDB	Protein Databank
PED	Precession Electron Diffraction
PEDT	Precession-assisted Electron Diffraction Tomography
PETS2	Process Electron Tilt Series, version 2 - Computer program for processing a series of diffraction images
PXRD	Powder X-ray Diffraction
RED	Rotation Electron Diffraction
RMSD	Root Mean Square Deviation
$[\text{S-BAr}^F_4]$	$[B(3,5\text{-}(SF_5)_2C_6H_3)_4]^-$
SCXRD	Single-Crystal X-ray Diffraction
SHELX	A crystallographic software package
SHELXL	A program for the refinement of crystal structures from diffraction data
SHELXLE	Graphical user interface for SHELXL
SHELXS	A structure solution program designed for the solution of 'small moiety' structures
SHELXT	A structure solution program
SNR	Signal to Noise Ratio
STEM	Scanning Transmission Electron Microscopy
TEM	Transmission Electron Microscope
XDS	A crystallographic software package
X-FEG	Extreme Field Emission Gun
XFEL	X-ray Free-Electron Laser

References

1   C. Davisson and L. H. Germer, Diffraction of Electrons by a Crystal of Nickel, *Phys. Rev.*, 1927, **30**, 705–740.

2   C. Davisson and L. H. Germer, The Scattering of Electrons by a Single Crystal of Nickel, *Nature*, 1927, **119**, 558–560.

3   G. P. Thomson and A. Reid, Diffraction of Cathode Rays by a Thin Film, *Nature*, 1927, **119**, 890–890.

4   R. K. Gehrenbeck, Electron diffraction: fifty years ago, *Phys. Today*, 1978, **31**, 34–41.

5   W. H. Bragg and W. L. Bragg, The reflection of X-rays by crystals, *Proc. R. Soc. Lond. A*, 1913, **88**, 428–438.

6   L. De Broglie, XXXV. A Tentative Theory of Light Quanta, *Philos. Mag. Lett.*, 2006, **86**, 411–423.

7   G. P. Thomson, The Diffraction of Cathode Rays by Thin Films of Platinum, *Nature*, 1927, **120**, 802–802.

8   G. P. Thomson, Experiments on the diffraction of cathode rays, *Proc. R. Soc. Lond. A*, 1928, **117**, 600–609.

9   W. C. Bigelow, Early Days of Electron Diffraction, *Micros. Today*, 2012, **20**, 38–44.

10   W. E. Laschkarew and I. D. Usyskin, Die Bestimmung der Lage der Wasserstofffionen im NH4Cl-Kristallgitter durch Elektronenbeugung, *Zeitschrift für Physik*, 1933, **85**, 618–630.

11   R. Rigamonti, La Struttura Della Catena Paraffinica Studiata Mediante i Raggi Di Elettroni, *Gazz. Chim. Ital.*, 1936, **66**, 174–182.

12   A. Charlesby, G. I. Finch and H. Wilman, The diffraction of electrons by anthracene, *Proc. Phys. Soc. London*, 1939, **51**, 479–528.

13   Z. G. Pinsker, *Electron Diffraction*, Butterworths Scientific Publications, 1953.

14   Z. G. Pinsker and L. B. Leder, in *Advances in Electronics and Electron Physics*, eds. L. Marton and C. Marton, Academic Press, 1959, vol. 11, pp. 355–412.

15   B. K. Vainshtein, *Structure Analysis by Electron Diffraction*, Pergamin Press Ltd: Oxford, 1964.

16   J. M. Cowley, Crystal structure determination by electron diffraction, *Prog. Mater Sci.*, 1968, **13**, 267–321.

17   J. M. Cowley, Structure analysis of single crystals by electron diffraction. I. Techniques, *Acta Crystallogr.*, 1953, **6**, 516–521.

18   J. M. Cowley, Structure analysis of single crystals by electron diffraction. II. Disordered boric acid structure, *Acta Crystallogr.*, 1953, **6**, 522–529.

19   G. Honjo and K. Shimaoka, Determination of hydrogen position in cubic ice by electron diffraction, *Acta Crystallogr.*, 1957, **10**, 710–711.

20   J. M. Cowley and A. F. Moodie, The scattering of electrons by atoms and crystals. II. The effects of finite source size, *Acta Crystallogr.*, 1959, **12**, 353–359.

21   J. M. Cowley and A. F. Moodie, The scattering of electrons by atoms and crystals. III. Single-crystal diffraction patterns, *Acta Crystallogr.*, 1959, **12**, 360–367.

22   S. Kuwabara, Accurate Determination of Hydrogen Positions in NH4Cl by Electron Diffraction, *J. Phys. Soc. Jpn.*, 1959, **14**, 1205–1216.

23   T. E. Weirich, X. Zou, R. Ramlau, A. Simon, G. L. Cascarano, C. Giacovazzo and S. Hovmöller, Structures of nanometre-size crystals determined from selected-area electron diffraction data, *Acta Crystallogr. A*, 2000, **56**, 29–35.

24   M. T. B. Clabbers, T. Gruene, E. van Genderen and J. P. Abrahams, Reducing dynamical electron scattering reveals hydrogen atoms, *Acta Crystallogr A Found Adv*, 2019, **75**, 82–93.

25   S. Miyake and R. Uyeda, An exception to Friedel's law in electron diffraction, *Acta Crystallogr.*, 1950, **3**, 314–314.

26   P. Goodman and G. Lehmpfuhl, Observation of the breakdown of Friedel's law in electron diffraction and symmetry determination from zero-layer interactions, *Acta Crystallogr. A*, 1968, **24**, 339–347.

27 R. M. Glaeser and T. A. Ceska, High-voltage electron diffraction from bacteriorhodopsin (purple membrane) is measurably dynamical, *Acta Crystallogr. A*, 1989, **45 (Pt 9)**, 620–628.

28 R. D. Heidenreich, Theory of the 'Forbidden' (222) Electron Reflection in the Diamond Structure, *Phys. Rev.*, 1950, **77**, 271–283.

29 J. M. Cowley, A. L. G. Rees and J. A. Spink, Secondary Elastic Scattering in Electron Diffraction, *Proc. Phys. Soc. A*, 1951, **64**, 609.

30 Y. Liao, Practical Electron Microscopy and Database - An Online Book, https://www.globalsino.com/EM/, (accessed 19 September 2023).

31 H. Lipson and W. Cochran, *Determination of Crystal Structures (Crystalline State)*, Cornell University Press, Ithaca, New York, 1966.

32 D. L. Dorset and H. A. Hauptman, Direct phase determination for quasi-kinematical electron diffraction intensity data from organic microcrystals, *Ultramicroscopy*, 1976, **1**, 195–201.

33 D. L. Dorset, Is electron crystallography possible? The direct determination of organic crystal structures, *Ultramicroscopy*, 1991, **38**, 23–40.

34 D. L. Dorset, Electron diffraction structure analysis of diketopiperazine – a direct phase determination, *Acta Crystallogr. A*, 1991, **47**, 510–515.

35 D. L. Dorset, Automated phase determination in electron crystallography: thermotropic phases of thiourea, *Ultramicroscopy*, 1992, **45**, 357–364.

36 D. L. Dorset, Direct phasing in electron crystallography: determination of layer silicate structures, *Ultramicroscopy*, 1992, **45**, 5–14.

37 D. L. Dorset and M. P. McCourt, Automated structure analysis in electron crystallography: phase determination with the tangent formula and least-squares refinement, *Acta Crystallogr. A*, 1994, **50**, 287–292.

38 D. L. Dorset, Electron crystallography, *Acta Crystallogr. B*, 1996, **52 (Pt 5)**, 753–769.

39 D. L. Dorset, Direct methods and refinement in electron and X-ray crystallography – diketopiperazine revisited, *Zeitschrift für Kristallographie*, 2010, **225**, 86–93.

40 T. E. Weirich, R. Ramlau, A. Simon, S. Hovmöller and X. Zou, A crystal structure determined with 0.02 Å accuracy by electron microscopy, *Nature*, 1996, **382**, 144–146.

41 S. Hovmöller, X. Zou and T. E. Weirich, in *Advances in Imaging and Electron Physics*, eds. P. W. Hawkes, P. G. Merli, G. Calestani and M. Vittori-Antisari, Elsevier, 2002, vol. 123, pp. 257–289.

42 X. Zou, S. Hovmöller and P. Oleynikov, *Electron crystallography*, Oxford University Press, New York, 2011.

43 M. Gemmi, E. Mugnaioli, T. E. Gorelik, U. Kolb, L. Palatinus, P. Boullay, S. Hovmöller and J. P. Abrahams, 3D Electron Diffraction: The Nanocrystallography Revolution, *ACS Cent Sci*, 2019, **5**, 1315–1329.

44 M. Gemmi and A. E. Lanza, 3D electron diffraction techniques, *Acta Crystallogr B Struct Sci Cryst Eng Mater*, 2019, **75**, 495–504.

45 R. Vincent and P. A. Midgley, Double conical beam-rocking system for measurement of integrated electron diffraction intensities, *Ultramicroscopy*, 1994, **53**, 271–282.

46 P. A. Midgley and A. S. Eggeman, Precession electron diffraction - a topical review, *IUCrJ*, 2015, **2**, 126–136.

47 U. Kolb, T. Gorelik, C. Kübel, M. T. Otten and D. Hubert, Towards automated diffraction tomography: part I--data acquisition, *Ultramicroscopy*, 2007, **107**, 507–513.

48 U. Kolb, T. Gorelik and M. T. Otten, Towards automated diffraction tomography. Part II--Cell parameter determination, *Ultramicroscopy*, 2008, **108**, 763–772.

49 E. Mugnaioli, T. Gorelik and U. Kolb, 'Ab initio' structure solution from electron diffraction data obtained by a combination of automated diffraction tomography and precession technique, *Ultramicroscopy*, 2009, **109**, 758–765.

50 A. Saha, S. S. Nia and J. A. Rodríguez, Electron Diffraction of 3D Molecular Crystals, *Chem. Rev.*, 2022, **122**, 13883–13914.

51 L. Palatinus, C. A. Corrêa, G. Steciuk, D. Jacob, P. Roussel, P. Boullay, M. Klementová, M. Gemmi, J. Kopeček, M. C. Domeneghetti, F. Cámara and V. Petříček, Structure refinement using precession electron diffraction tomography and dynamical diffraction: tests on experimental data, *Acta Crystallogr B Struct Sci Cryst Eng Mater*, 2015, **71**, 740–751.

52 L. Palatinus, V. Petříček and C. A. Corrêa, Structure refinement using precession electron diffraction tomography and dynamical diffraction: theory and implementation, *Acta Crystallogr A Found Adv*, 2015, **71**, 235–244.

53 M. Colmont, L. Palatinus, M. Huvé, H. Kabbour, S. Saitzek, N. Djelal and P. Roussel, On the Use of Dynamical Diffraction Theory To Refine Crystal Structure from Electron Diffraction Data: Application to KLa5O5(VO4)2, a Material with Promising Luminescent Properties, *Inorg. Chem.*, 2016, **55**, 2252–2260.

54 M. Gemmi, M. Merlini, L. Palatinus, P. Fumagalli and M. Hanfland, Electron diffraction determination of 11.5 Å and HySo structures: Candidate water carriers to the Upper Mantle, *Am. Mineral.*, 2016, **101**, 2645–2654.

55 E. Mugnaioli, M. Gemmi, M. Merlini and M. Gregorkiewitz, (Na,□)5[MnO2]13 nanorods: a new tunnel structure for electrode materials determined ab initio and refined through a combination of electron and synchrotron diffraction data, *Acta Crystallogr B Struct Sci Cryst Eng Mater*, 2016, **72**, 893–903.

56 L. Palatinus, P. Brázda, P. Boullay, O. Perez, M. Klementová, S. Petit, V. Eigner, M. Zaarour and S. Mintova, Hydrogen positions in single nanocrystals revealed by electron diffraction, *Science*, 2017, **355**, 166–169.

57 C. S. Own, A. K. Subramanian and L. D. Marks, Quantitative analyses of precession diffraction data for a large cell oxide, *Microscopy and Microanalysis*, 2004, **10**, 96–104.

58 D. Zhang, P. Oleynikov, S. Hovmöller and X. Zou, Collecting 3D electron diffraction data by the rotation method, *Zeitschrift für Kristallographie*, 2010, **225**, 94–102.

59 W. Wan, J. Sun, J. Su, S. Hovmöller and X. Zou, Three-dimensional rotation electron diffraction: software RED for automated data collection and data processing, *J. Appl. Crystallogr.*, 2013, **46**, 1863–1873.

60 I. Nederlof, E. van Genderen, Y. W. Li and J. P. Abrahams, A Medipix quantum area detector allows rotation electron diffraction data collection from submicrometre three-dimensional protein crystals, *Acta Crystallogr. D Biol. Crystallogr.*, 2013, **69**, 1223–1230.

61 B. L. Nannenga, D. Shi, J. Hattne, F. E. Reyes and T. Gonen, Structure of catalase determined by MicroED, *Elife*, 2014, **3**, e03600.

62 U. W. Arndt and A. J. Wonacott, *The Rotation method in crystallography: data collection from macromolecular crystals*, North-Holland Publishing Company, Amsterdam, 1977.

63 E. van Genderen, M. T. B. Clabbers, P. P. Das, A. Stewart, I. Nederlof, K. C. Barentsen, Q. Portillo, N. S. Pannu, S. Nicolopoulos, T. Gruene and J. P. Abrahams, Ab initio structure determination of nanocrystals of organic pharmaceutical compounds by electron diffraction at room temperature using a Timepix quantum area direct electron detector, *Acta Crystallogr A Found Adv*, 2016, **72**, 236–242.

64 M. Gemmi, M. G. I. La Placa, A. S. Galanis, E. F. Rauch and S. Nicolopoulos, Fast electron diffraction tomography, *J. Appl. Crystallogr.*, 2015, **48**, 718–727.

65 Y. Wang, S. Takki, O. Cheung, H. Xu, W. Wan, L. Öhrström and A. K. Inge, Elucidation of the elusive structure and formula of the active pharmaceutical ingredient bismuth subgallate by continuous rotation electron diffraction, *Chem. Commun.*, 2017, **53**, 7018–7021.

66 Y. Wang, T. Yang, H. Xu, X. Zou and W. Wan, On the quality of the continuous rotation electron diffraction data for accurate atomic structure determination of inorganic compounds, *J. Appl. Crystallogr.*, 2018, **51**, 1094–1101.

67 T. Gruene, J. T. C. Wennmacher, C. Zaubitzer, J. J. Holstein, J. Heidler, A. Fecteau-Lefebvre, S. De Carlo, E. Müller, K. N. Goldie, I. Regeni, T. Li, G. Santiso-Quinones, G. Steinfeld, S. Handschin, E. van Genderen, J. A. van Bokhoven, G. H. Clever and R. Pantelic, Rapid Structure Determination

of Microcrystalline Molecular Compounds Using Electron Diffraction, *Angew. Chem. Int. Ed Engl.*, 2018, **57**, 16313–16317.

68   L. Palatinus and G. Chapuis, SUPERFLIP – a computer program for the solution of crystal structures by charge flipping in arbitrary dimensions, *J. Appl. Crystallogr.*, 2007, **40**, 786–790.

69   G. M. Sheldrick, A short history of SHELX, *Acta Crystallogr. A*, 2008, **64**, 112–122.

70   M. C. Burla, R. Caliandro, B. Carrozzini, G. L. Cascarano, C. Cuocci, C. Giacovazzo, M. Mallamo, A. Mazzone and G. Polidori, Crystal structure determination and refinement via SIR2014, *J. Appl. Crystallogr.*, 2015, **48**, 306–309.

71   T. G. G. Battye, L. Kontogiannis, O. Johnson, H. R. Powell and A. G. W. Leslie, iMOSFLM: a new graphical interface for diffraction-image processing with MOSFLM, *Acta Crystallogr. D Biol. Crystallogr.*, 2011, **67**, 271–281.

72   G. Winter, J. Beilsten-Edmands, N. Devenish, M. Gerstel, R. J. Gildea, D. McDonagh, E. Pascal, D. G. Waterman, B. H. Williams and G. Evans, DIALS as a toolkit, *Protein Sci.*, 2022, **31**, 232–250.

73   M. T. B. Clabbers, T. Gruene, J. M. Parkhurst, J. P. Abrahams and D. G. Waterman, Electron diffraction data processing with DIALS, *Acta Crystallogr D Struct Biol*, 2018, **74**, 506–518.

74   W. Kabsch, XDS, *Acta Crystallogr. D Biol. Crystallogr.*, 2010, **66**, 125–132.

75   C.-T. Zee, A. Saha, M. R. Sawaya and J. A. Rodriguez, in *cryoEM: Methods and Protocols*, eds. T. Gonen and B. L. Nannenga, Springer US, New York, NY, 2021, pp. 329–348.

76   C. G. Jones, M. W. Martynowycz, J. Hattne, T. J. Fulton, B. M. Stoltz, J. A. Rodriguez, H. M. Nelson and T. Gonen, The CryoEM Method MicroED as a Powerful Tool for Small Molecule Structure Determination, *ACS Cent Sci*, 2018, **4**, 1587–1592.

77   E. T. Broadhurst, H. Xu, M. T. B. Clabbers, M. Lightowler, F. Nudelman, X. Zou and S. Parsons, Polymorph evolution during crystal growth studied by 3D electron diffraction, *IUCrJ*, 2020, **7**, 5–9.

78   S. Li, M. Lightowler, X. Ou, S. Huang, Y. Jiang, X. Li, X. Zou, H. Xu and M. Lu, Direct structure determination of vemurafenib polymorphism from compact spherulites using 3D electron diffraction, *Commun Chem*, 2023, **6**, 18.

79   G. Bu, E. Danelius, L. H. E. Wieske and T. Gonen, Polymorphic Structure Determination of the Macrocyclic Drug Paritaprevir by MicroED, *Adv Biol (Weinh)*, 2024, e2300570.

80   M. Lightowler, S. Li, X. Ou, J. Cho, B. Liu, A. Li, G. Hofer, J. Xu, T. Yang, X. Zou, M. Lu and H. Xu, Phase Identification and Discovery of an Elusive Polymorph of Drug-Polymer Inclusion Complex Using Automated 3D Electron Diffraction, *Angew. Chem. Int. Ed Engl.*, 2024, e202317695.

81   Z. Huang, M. Ge, F. Carraro, C. Doonan, P. Falcaro and X. Zou, Can 3D electron diffraction provide accurate atomic structures of metal-organic frameworks?, *Faraday Discuss.*, 2021, **225**, 118–132.

82   Z. Huang, E. S. Grape, J. Li, A. K. Inge and X. Zou, 3D electron diffraction as an important technique for structure elucidation of metal-organic frameworks and covalent organic frameworks, *Coord. Chem. Rev.*, 2021, **427**, 213583.

83   H. Furukawa, K. E. Cordova, M. O'Keeffe and O. M. Yaghi, The chemistry and applications of metal-organic frameworks, *Science*, 2013, **341**, 1230444.

84   J.-R. Li, J. Sculley and H.-C. Zhou, Metal-organic frameworks for separations, *Chem. Rev.*, 2012, **112**, 869–932.

85   Y. Cui, B. Li, H. He, W. Zhou, B. Chen and G. Qian, Metal-Organic Frameworks as Platforms for Functional Materials, *Acc. Chem. Res.*, 2016, **49**, 483–493.

86   J. Duan, W. Jin and S. Kitagawa, Water-resistant porous coordination polymers for gas separation, *Coord. Chem. Rev.*, 2017, **332**, 48–74.

87   N. S. Bobbitt, M. L. Mendonca, A. J. Howarth, T. Islamoglu, J. T. Hupp, O. K. Farha and R. Q. Snurr, Metal-organic frameworks for the removal of toxic industrial chemicals and chemical warfare agents, *Chem. Soc. Rev.*, 2017, **46**, 3357–3385.

88   C. Doonan, R. Riccò, K. Liang, D. Bradshaw and P. Falcaro, Metal-Organic Frameworks at the Biointerface: Synthetic Strategies and Applications, *Acc. Chem. Res.*, 2017, **50**, 1423–1432.

89 P. Horcajada, R. Gref, T. Baati, P. K. Allan, G. Maurin, P. Couvreur, G. Férey, R. E. Morris and C. Serre, Metal-organic frameworks in biomedicine, *Chem. Rev.*, 2012, **112**, 1232–1268.

90 D. Denysenko, M. Grzywa, M. Tonigold, B. Streppel, I. Krkljus, M. Hirscher, E. Mugnaioli, U. Kolb, J. Hanss and D. Volkmer, Elucidating gating effects for hydrogen sorption in MFU-4-type triazolate-based metal-organic frameworks featuring different pore sizes, *Chemistry*, 2011, **17**, 1837–1848.

91 M. Feyand, E. Mugnaioli, F. Vermoortele, B. Bueken, J. M. Dieterich, T. Reimer, U. Kolb, D. de Vos and N. Stock, Automated diffraction tomography for the structure elucidation of twinned, sub-micrometer crystals of a highly porous, catalytically active bismuth metal-organic framework, *Angew. Chem. Int. Ed Engl.*, 2012, **51**, 10373–10376.

92 Q. Yao, A. Bermejo Gómez, J. Su, V. Pascanu, Y. Yun, H. Zheng, H. Chen, L. Liu, H. N. Abdelhamid, B. Martín-Matute and X. Zou, Series of Highly Stable Isoreticular Lanthanide Metal–Organic Frameworks with Expanding Pore Size and Tunable Luminescent Properties, *Chem. Mater.*, 2015, **27**, 5332–5339.

93 S. Dai, W. Gao, S. Zhang, G. W. Graham and X. Pan, Transmission electron microscopy with atomic resolution under atmospheric pressures, *MRS Communications*, 2017, **7**, 798–812.

94 T. Rhauderwiek, H. Zhao, P. Hirschle, M. Döblinger, B. Bueken, H. Reinsch, D. De Vos, S. Wuttke, U. Kolb and N. Stock, Highly stable and porous porphyrin-based zirconium and hafnium phosphonates - electron crystallography as an important tool for structure elucidation, *Chem. Sci.*, 2018, **9**, 5467–5478.

95 S. Yuan, J.-S. Qin, H.-Q. Xu, J. Su, D. Rossi, Y. Chen, L. Zhang, C. Lollar, Q. Wang, H.-L. Jiang, D. H. Son, H. Xu, Z. Huang, X. Zou and H.-C. Zhou, [Ti8Zr2O12(COO)16] Cluster: An Ideal Inorganic Building Unit for Photoactive Metal-Organic Frameworks, *ACS Cent Sci*, 2018, **4**, 105–111.

96 B. Wang, T. Rhauderwiek, A. K. Inge, H. Xu, T. Yang, Z. Huang, N. Stock and X. Zou, A Porous Cobalt Tetraphosphonate Metal-Organic Framework: Accurate Structure and Guest Molecule Location Determined by Continuous-Rotation Electron Diffraction, *Chemistry*, 2018, **24**, 17429–17433.

97 S. Leubner, H. Zhao, N. Van Velthoven, M. Henrion, H. Reinsch, D. E. De Vos, U. Kolb and N. Stock, Expanding the Variety of Zirconium-based Inorganic Building Units for Metal-Organic Frameworks, *Angew. Chem. Int. Ed Engl.*, 2019, **58**, 10995–11000.

98 D. Lenzen, J. Zhao, S.-J. Ernst, M. Wahiduzzaman, A. Ken Inge, D. Fröhlich, H. Xu, H.-J. Bart, C. Janiak, S. Henninger, G. Maurin, X. Zou and N. Stock, A metal-organic framework for efficient water-based ultra-low-temperature-driven cooling, *Nat. Commun.*, 2019, **10**, 3025.

99 S. Smolders, T. Willhammar, A. Krajnc, K. Sentosun, M. T. Wharmby, K. A. Lomachenko, S. Bals, G. Mali, M. B. J. Roeffaers, D. E. De Vos and B. Bueken, A Titanium(IV)-Based Metal-Organic Framework Featuring Defect-Rich Ti-O Sheets as an Oxidative Desulfurization Catalyst, *Angew. Chem. Int. Ed Engl.*, 2019, **58**, 9160–9165.

100 E. S. Grape, H. Xu, O. Cheung, M. Calmels, J. Zhao, C. Dejoie, D. M. Proserpio, X. Zou and A. K. Inge, Breathing Metal–Organic Framework Based on Flexible Inorganic Building Units, *Cryst. Growth Des.*, 2020, **20**, 320–329.

101 F. Carraro, M. de J. Velásquez-Hernández, E. Astria, W. Liang, L. Twight, C. Parise, M. Ge, Z. Huang, R. Ricco, X. Zou, L. Villanova, C. O. Kappe, C. Doonan and P. Falcaro, Phase dependent encapsulation and release profile of ZIF-based biocomposites, *Chem. Sci.*, 2020, **11**, 3397–3404.

102 T. Rabe, H. Pewe, H. Reinsch, T. Willhammar, E. Svensson Grape and N. Stock, Influence of the substitution pattern of four naphthalenedicarboxylic acids on the structures and properties of group 13 metal-organic frameworks and coordination polymers, *Dalton Trans.*, 2020, **49**, 4861–4868.

103 P. Rönfeldt, H. Reinsch, E. Svensson Grape, A. K. Inge, H. Terraschke and N. Stock, Water-based synthesis and properties of a scandium 1,4-naphthalenedicarboxylate, *Z. Anorg. Allg. Chem.*, 2020, **646**, 1373–1379.

104 F. M. Amombo Noa, E. Svensson Grape, S. M. Brülls, O. Cheung, P. Malmberg, A. K. Inge, C. J. McKenzie, J. Mårtensson and L. Öhrström, Metal-Organic Frameworks with Hexakis(4-carboxyphenyl)benzene: Extensions to Reticular Chemistry and Introducing Foldable Nets, *J. Am. Chem. Soc.*, 2020, **142**, 9471–9481.

105 T. C. Terwilliger, D. Stuart and S. Yokoyama, Lessons from structural genomics, *Annu. Rev. Biophys.*, 2009, **38**, 371–383.

106 J. R. Luft, J. R. Wolfley and E. H. Snell, What's in a drop? Correlating observations and outcomes to guide macromolecular crystallization experiments, *Cryst. Growth Des.*, 2011, **11**, 651–663.

107 E. P. Carpenter, K. Beis, A. D. Cameron and S. Iwata, Overcoming the challenges of membrane protein crystallography, *Curr. Opin. Struct. Biol.*, 2008, **18**, 581–586.

108 M. Caffrey, Membrane protein crystallization, *J. Struct. Biol.*, 2003, **142**, 108–132.

109 C. Nave and M. A. Hill, Will reduced radiation damage occur with very small crystals?, *J. Synchrotron Radiat.*, 2005, **12**, 299–303.

110 J. M. Holton and K. A. Frankel, The minimum crystal size needed for a complete diffraction data set, *Acta Crystallogr. D Biol. Crystallogr.*, 2010, **66**, 393–408.

111 R. Sanishvili, D. W. Yoder, S. B. Pothineni, G. Rosenbaum, S. Xu, S. Vogt, S. Stepanov, O. A. Makarov, S. Corcoran, R. Benn, V. Nagarajan, J. L. Smith and R. F. Fischetti, Radiation damage in protein crystals is reduced with a micron-sized X-ray beam, *Proc. Natl. Acad. Sci. U. S. A.*, 2011, **108**, 6127–6132.

112 G. Calero, A. E. Cohen, J. R. Luft, J. Newman and E. H. Snell, Identifying, studying and making good use of macromolecular crystals, *Acta Crystallogr. Sect. F Struct. Biol. Cryst. Commun.*, 2014, **70**, 993–1008.

113 H. P. Stevenson, A. M. Makhov, M. Calero, A. L. Edwards, O. B. Zeldin, I. I. Mathews, G. Lin, C. O. Barnes, H. Santamaria, T. M. Ross, S. M. Soltis, C. Khosla, V. Nagarajan, J. F. Conway, A. E. Cohen and G. Calero, Use of transmission electron microscopy to identify nanocrystals of challenging protein targets, *Proc. Natl. Acad. Sci. U. S. A.*, 2014, **111**, 8470–8475.

114 H. P. Stevenson, G. Lin, C. O. Barnes, I. Sutkeviciute, T. Krzysiak, S. C. Weiss, S. Reynolds, Y. Wu, V. Nagarajan, A. M. Makhov, R. Lawrence, E. Lamm, L. Clark, T. J. Gardella, B. G. Hogue, C. M. Ogata, J. Ahn, A. M. Gronenborn, J. F. Conway, J. P. Vilardaga, A. E. Cohen and G. Calero, Transmission electron microscopy for the evaluation and optimization of crystal growth, *Acta Crystallogr D Struct Biol*, 2016, **72**, 603–615.

115 S. Cusack, H. Belrhali, A. Bram, M. Burghammer, A. Perrakis and C. Riekel, Small is beautiful: protein micro-crystallography, *Nat. Struct. Biol.*, 1998, **5**, 634–637.

116 M. J. de la Cruz, J. Hattne, D. Shi, P. Seidler, J. Rodriguez, F. E. Reyes, M. R. Sawaya, D. Cascio, S. C. Weiss, S. K. Kim, C. S. Hinck, A. P. Hinck, G. Calero, D. Eisenberg and T. Gonen, Atomic-resolution structures from fragmented protein crystals with the cryoEM method MicroED, *Nat. Methods*, 2017, **14**, 399–402.

117 A. M. Wolff, I. D. Young, R. G. Sierra, A. S. Brewster, M. W. Martynowycz, E. Nango, M. Sugahara, T. Nakane, K. Ito, A. Aquila, A. Bhowmick, J. T. Biel, S. Carbajo, A. E. Cohen, S. Cortez, A. Gonzalez, T. Hino, D. Im, J. D. Koralek, M. Kubo, T. S. Lazarou, T. Nomura, S. Owada, A. J. Samelson, T. Tanaka, R. Tanaka, E. M. Thompson, H. van den Bedem, R. A. Woldeyes, F. Yumoto, W. Zhao, K. Tono, S. Boutet, S. Iwata, T. Gonen, N. K. Sauter, J. S. Fraser and M. C. Thompson, Comparing serial X-ray crystallography and microcrystal electron diffraction (MicroED) as methods for routine structure determination from small macromolecular crystals, *IUCrJ*, 2020, **7**, 306–323.

118 J. Hattne, D. Shi, M. J. de la Cruz, F. E. Reyes and T. Gonen, Modeling truncated pixel values of faint reflections in MicroED images, *J. Appl. Crystallogr.*, 2016, **49**, 1029–1034.

119 J. Hattne, D. Shi, C. Glynn, C.-T. Zee, M. Gallagher-Jones, M. W. Martynowycz, J. A. Rodriguez and T. Gonen, Analysis of Global and Site-Specific Radiation Damage in Cryo-EM, *Structure*, 2018, **26**, 759-766.e4.

120 M. W. Martynowycz, W. Zhao, J. Hattne, G. J. Jensen and T. Gonen, Collection of Continuous Rotation MicroED Data from Ion Beam-Milled Crystals of Any Size, *Structure*, 2019, **27**, 545-548.e2.

121 L. S. Richards, C. Millán, J. Miao, M. W. Martynowycz, M. R. Sawaya, T. Gonen, R. J. Borges, I. Usón and J. A. Rodriguez, Fragment-based determination of a proteinase K structure from MicroED data using ARCIMBOLDO_SHREDDER, *Acta Crystallogr D Struct Biol*, 2020, **76**, 703–712.

122 L. Zhu, G. Bu, L. Jing, D. Shi, M.-Y. Lee, T. Gonen, W. Liu and B. L. Nannenga, Structure Determination from Lipidic Cubic Phase Embedded Microcrystals by MicroED, *Structure*, 2020, **28**, 1149-1159.e4.

123 E. V. Beale, D. G. Waterman, C. Hecksel, J. van Rooyen, J. B. Gilchrist, J. M. Parkhurst, F. de Haas, B. Buijsse, G. Evans and P. Zhang, A Workflow for Protein Structure Determination From Thin Crystal Lamella by Micro-Electron Diffraction, *Front Mol Biosci*, 2020, **7**, 179.

124 D. Shi, B. L. Nannenga, M. G. Iadanza and T. Gonen, Three-dimensional electron crystallography of protein microcrystals, *Elife*, 2013, **2**, e01345.

125 B. L. Nannenga, D. Shi, A. G. W. Leslie and T. Gonen, High-resolution structure determination by continuous-rotation data collection in MicroED, *Nat. Methods*, 2014, **11**, 927–930.

126 M. T. B. Clabbers, E. van Genderen, W. Wan, E. L. Wiegers, T. Gruene and J. P. Abrahams, Protein structure determination by electron diffraction using a single three-dimensional nanocrystal, *Acta Crystallogr D Struct Biol*, 2017, **73**, 738–748.

127 H. Xu, H. Lebrette, T. Yang, V. Srinivas, S. Hovmöller, M. Högbom and X. Zou, A Rare Lysozyme Crystal Form Solved Using Highly Redundant Multiple Electron Diffraction Datasets from Micron-Sized Crystals, *Structure*, 2018, **26**, 667-675.e3.

128 H. M. E. Duyvesteyn, A. Kotecha, H. M. Ginn, C. W. Hecksel, E. V. Beale, F. de Haas, G. Evans, P. Zhang, W. Chiu and D. I. Stuart, Machining protein microcrystals for structure determination by electron diffraction, *Proc. Natl. Acad. Sci. U. S. A.*, 2018, **115**, 9569–9573.

129 A. Lanza, E. Margheritis, E. Mugnaioli, V. Cappello, G. Garau and M. Gemmi, Nanobeam precession-assisted 3D electron diffraction reveals a new polymorph of hen egg-white lysozyme, *IUCrJ*, 2019, **6**, 178–188.

130 R. Bücker, P. Hogan-Lamarre, P. Mehrabi, E. C. Schulz, L. A. Bultema, Y. Gevorkov, W. Brehm, O. Yefanov, D. Oberthür, G. H. Kassier and R. J. Dwayne Miller, Serial protein crystallography in an electron microscope, *Nat. Commun.*, 2020, **11**, 996.

131 K. Yonekura and S. Maki-Yonekura, Refinement of cryo-EM structures using scattering factors of charged atoms, *J. Appl. Crystallogr.*, 2016, **49**, 1517–1523.

132 K. Yonekura, T. Ishikawa and S. Maki-Yonekura, A new cryo-EM system for electron 3D crystallography by eEFD, *J. Struct. Biol.*, 2019, **206**, 243–253.

133 K. Takaba, S. Maki-Yonekura, S. Inoue, T. Hasegawa and K. Yonekura, Protein and Organic-Molecular Crystallography With 300kV Electrons on a Direct Electron Detector, *Front Mol Biosci*, 2020, **7**, 612226.

134 H. Xu, H. Lebrette, M. T. B. Clabbers, J. Zhao, J. J. Griese, X. Zou and M. Högbom, Solving a new R2lox protein structure by microcrystal electron diffraction, *Sci Adv*, 2019, **5**, eaax4621.

135 J. D. Bernal and D. Crowfoot, X-Ray Photographs of Crystalline Pepsin, *Nature*, 1934, **133**, 794–795.

136 R. Henderson and P. N. Unwin, Three-dimensional model of purple membrane obtained by electron microscopy, *Nature*, 1975, **257**, 28–32.

137 J. Dubochet and A. W. McDowall, Vitrification of pure water for electron microscopy, *J. Microsc.*, 1981, **124**, 3–4.

138 J. Dubochet, J. Lepault, R. Freeman, J. A. Berriman and J.-C. Homo, Electron microscopy of frozen water and aqueous solutions, *J. Microsc.*, 1982, **128**, 219–237.

139 J. Dubochet, M. Adrian, J. J. Chang, J. C. Homo, J. Lepault, A. W. McDowall and P. Schultz, Cryo-electron microscopy of vitrified specimens, *Q. Rev. Biophys.*, 1988, **21**, 129–228.

140 C. V. Iancu, W. F. Tivol, J. B. Schooler, D. P. Dias, G. P. Henderson, G. E. Murphy, E. R. Wright, Z. Li, Z. Yu, A. Briegel, L. Gan, Y. He and G. J. Jensen, Electron cryotomography sample preparation using the Vitrobot, *Nat. Protoc.*, 2006, **1**, 2813–2819.

141 X. Li, S. Zhang, J. Zhang and F. Sun, In situ protein micro-crystal fabrication by cryo-FIB for electron diffraction, *Biophys Rep*, 2018, **4**, 339–347.

142 M. W. Martynowycz, W. Zhao, J. Hattne, G. J. Jensen and T. Gonen, Qualitative Analyses of Polishing and Precoating FIB Milled Crystals for MicroED, *Structure*, 2019, **27**, 1594-1600.e2.

143 V. Polovinkin, K. Khakurel, M. Babiak, B. Angelov, B. Schneider, J. Dohnalek, J. Andreasson and J. Hajdu, Demonstration of electron diffraction from membrane protein crystals grown in a lipidic mesophase after lamella preparation by focused ion beam milling at cryogenic temperatures, *J. Appl. Crystallogr.*, 2020, **53**, 1416–1424.

144 H. Zhou, Z. Luo and X. Li, Using focus ion beam to prepare crystal lamella for electron diffraction, *J. Struct. Biol.*, 2019, **205**, 59–64.

145 M. W. Martynowycz and T. Gonen, Protocol for the use of focused ion-beam milling to prepare crystalline lamellae for microcrystal electron diffraction (MicroED), *STAR Protoc*, 2021, **2**, 100686.

146 C. Guzmán-Afonso, Y.-L. Hong, H. Colaux, H. Iijima, A. Saitow, T. Fukumura, Y. Aoyama, S. Motoki, T. Oikawa, T. Yamazaki, K. Yonekura and Y. Nishiyama, Understanding hydrogen-bonding structures of molecular crystals via electron and NMR nanocrystallography, *Nat. Commun.*, 2019, **10**, 3537.

147 G. R. Woollam, P. P. Das, E. Mugnaioli, I. Andrusenko, A. S. Galanis, J. van de Streek, S. Nicolopoulos, M. Gemmi and T. Wagner, Structural analysis of metastable pharmaceutical loratadine form II, by 3D electron diffraction and DFT+D energy minimisation, *CrystEngComm*, 2020, **22**, 7490–7499.

148 V. Hamilton, I. Andrusenko, J. Potticary, C. Hall, R. Stenner, E. Mugnaioli, A. E. Lanza, M. Gemmi and S. R. Hall, Racemic Conglomerate Formation via Crystallization of Metaxalone from Volatile Deep Eutectic Solvents, *Cryst. Growth Des.*, 2020, **20**, 4731–4739.

149 J. F. Bruhn, G. Scapin, A. Cheng, B. Q. Mercado, D. G. Waterman, T. Ganesh, S. Dallakyan, B. N. Read, T. Nieusma, K. W. Lucier, M. L. Mayer, N. J. Chiang, N. Poweleit, P. T. McGilvray, T. S. Wilson, M. Mashore, C. Hennessy, S. Thomson, B. Wang, C. S. Potter and B. Carragher, Small Molecule Microcrystal Electron Diffraction for the Pharmaceutical Industry-Lessons Learned From Examining Over Fifty Samples, *Front Mol Biosci*, 2021, **8**, 648603.

150 S. Sekharan, X. Liu, Z. Yang, X. Liu, L. Deng, S. Ruan, Y. Abramov, G. Sun, S. Li, T. Zhou, B. Shi, Q. Zeng, Q. Zeng, C. Chang, Y. Jin and X. Shi, Selecting a stable solid form of remdesivir using microcrystal electron diffraction and crystal structure prediction, *RSC Adv.*, 2021, **11**, 17408–17412.

151 M. Lightowler, S. Li, X. Ou, X. Zou, M. Lu and H. Xu, Indomethacin Polymorph δ Revealed To Be Two Plastically Bendable Crystal Forms by 3D Electron Diffraction: Correcting a 47-Year-Old Misunderstanding, *Angew. Chem. Int. Ed Engl.*, 2022, **61**, e202114985.

152 I. Andrusenko, V. Hamilton, E. Mugnaioli, A. Lanza, C. Hall, J. Potticary, S. R. Hall and M. Gemmi, The Crystal Structure of Orthocetamol Solved by 3D Electron Diffraction, *Angew. Chem. Int. Ed Engl.*, 2019, **58**, 10919–10922.

153 L. J. Kim, M. Xue, X. Li, Z. Xu, E. Paulson, B. Mercado, H. M. Nelson and S. B. Herzon, Structure Revision of the Lomaiviticins, *J. Am. Chem. Soc.*, 2021, **143**, 6578–6585.

154 K. Kato, K. Takaba, S. Maki-Yonekura, N. Mitoma, Y. Nakanishi, T. Nishihara, T. Hatakeyama, T. Kawada, Y. Hijikata, J. Pirillo, L. T. Scott, K. Yonekura, Y. Segawa and K. Itami, Double-Helix Supramolecular Nanofibers Assembled from Negatively Curved Nanographenes, *J. Am. Chem. Soc.*, 2021, **143**, 5465–5469.

155 A. E. Samkian, G. R. Kiel, C. G. Jones, H. M. Bergman, J. Oktawiec, H. M. Nelson and T. D. Tilley, Elucidation of Diverse Solid-State Packing in a Family of Electron-Deficient Expanded Helicenes

via Microcrystal Electron Diffraction (MicroED), *Angew. Chem. Int. Ed Engl.*, 2021, **60**, 2493–2499.

156 M. Ueda, T. Aoki, T. Akiyama, T. Nakamuro, K. Yamashita, H. Yanagisawa, O. Nureki, M. Kikkawa, E. Nakamura, T. Aida and Y. Itoh, Alternating Heterochiral Supramolecular Copolymerization, *J. Am. Chem. Soc.*, 2021, **143**, 5121–5126.

157 C. G. Jones, M. Asay, L. J. Kim, J. F. Kleinsasser, A. Saha, T. J. Fulton, K. R. Berkley, D. Cascio, A. G. Malyutin, M. P. Conley, B. M. Stoltz, V. Lavallo, J. A. Rodríguez and H. M. Nelson, Characterization of Reactive Organometallic Species via MicroED, *ACS Cent Sci*, 2019, **5**, 1507–1513.

158 T. E. Gorelik, S. Habermehl, A. A. Shubin, T. Gruene, K. Yoshida, P. Oleynikov, U. Kaiser and M. U. Schmidt, Crystal structure of copper perchlorophthalo-cyanine analysed by 3D electron diffraction, *Acta Crystallographica Section B: Structural Science, Crystal Engineering and Materials*, 2021, **77**, 662–675.

159 M. Dick, N. S. Sarai, M. W. Martynowycz, T. Gonen and F. H. Arnold, Tailoring Tryptophan Synthase TrpB for Selective Quaternary Carbon Bond Formation, *J. Am. Chem. Soc.*, 2019, **141**, 19817–19822.

160 A. M. Levine, G. Bu, S. Biswas, E. H. R. Tsai, A. B. Braunschweig and B. L. Nannenga, Crystal structure and orientation of organic semiconductor thin films by microcrystal electron diffraction and grazing-incidence wide-angle X-ray scattering, *Chem. Commun.* , 2020, **56**, 4204–4207.

161 H. Lu, T. Nakamuro, K. Yamashita, H. Yanagisawa, O. Nureki, M. Kikkawa, H. Gao, J. Tian, R. Shang and E. Nakamura, B/N-Doped p-Arylenevinylene Chromophores: Synthesis, Properties, and Microcrystal Electron Crystallographic Study, *J. Am. Chem. Soc.*, 2020, **142**, 18990–18996.

162 H. Hamada, T. Nakamuro, K. Yamashita, H. Yanagisawa, O. Nureki, M. Kikkawa, K. Harano, R. Shang and E. Nakamura, Spiro-Conjugated Carbon/Heteroatom-Bridged p-Phenylenevinylenes: Synthesis, Properties, and Microcrystal Electron Crystallographic Analysis of Racemic Solid Solutions, *Bull. Chem. Soc. Jpn.*, 2020, **93**, 776–782.

163 O. Ghashghaei, M. Pedrola, F. Seghetti, V. V. Martin, R. Zavarce, M. Babiak, J. Novacek, F. Hartung, K. M. Rolfes, T. Haarmann-Stemmann and R. Lavilla, Extended Multicomponent Reactions with Indole Aldehydes: Access to Unprecedented Polyheterocyclic Scaffolds, Ligands of the Aryl Hydrocarbon Receptor, *Angew. Chem. Int. Ed Engl.*, 2021, **60**, 2603–2608.

164 G. M. Sheldrick, SHELXT - integrated space-group and crystal-structure determination, *Acta Crystallogr. Sect A*, 2015, **71**, 3–8.

165 G. M. Sheldrick, Crystal structure refinement with SHELXL, *Acta Crystallogr. Sect. C*, 2015, **71**, 3–8.

166 C. B. Hübschle, G. M. Sheldrick and B. Dittrich, ShelXle: a Qt graphical user interface for SHELXL, *J. Appl. Crystallogr.*, 2011, **44**, 1281–1284.

167 B. Kautzner, P. C. Wailes and H. Weigold, Hydrides of bis(cyclopentadienyl)zirconium, *J. Chem. Soc. Dalton Trans.*, 1969, 1105a–1105a.

168 P. C. Wailes and H. Weigold, Hydrido complexes of zirconium I. Preparation, *J. Organomet. Chem.*, 1970, **24**, 405–411.

169 T. Takahashi, N. Suzuki, N. Jayasuriya and P. Wipf, *Encyclopedia of Reagents for Organic Synthesis*, 2006.

170 M. Warren, 'Why didn't we think to do this earlier?' Chemists thrilled by speedy atomic structures, *Nature*, 2018, **563**, 16–17.

171 D. Lowe, Small Molecule Structures: A New World, https://www.science.org/content/blog-post/small-molecule-structures-new-world, (accessed 22 March 2024).

172 G. McMullan, S. Chen, R. Henderson and A. R. Faruqi, Detective quantum efficiency of electron area detectors in electron microscopy, *Ultramicroscopy*, 2009, **109**, 1126–1143.

173 G. McMullan, A. T. Clark, R. Turchetta and A. R. Faruqi, Enhanced imaging in low dose electron microscopy using electron counting, *Ultramicroscopy*, 2009, **109**, 1411–1416.

174 J. Hattne, M. W. Martynowycz, P. A. Penczek and T. Gonen, MicroED with the Falcon III direct electron detector, *IUCrJ*, 2019, **6**, 921–926.

175 Y. Wang, T. Yang, H. Xu, X. Zou and W. Wan, On the quality of the continuous rotation electron diffraction data for accurate atomic structure determination of inorganic compounds, *J. Appl. Crystallogr.*, 2018, **51**, 1094–1101.

176 M. T. B. Clabbers, M. W. Martynowycz, J. Hattne, B. L. Nannenga and T. Gonen, Electron-counting MicroED data with the K2 and K3 direct electron detectors, *J. Struct. Biol.*, 2022, **214**, 107886.

177 P. P. Ewald, Introduction to the dynamical theory of X-ray diffraction, *Acta Crystallogr. A*, 1969, **25**, 103–108.

178 R. Henderson, The potential and limitations of neutrons, electrons and X-rays for atomic resolution microscopy of unstained biological molecules, *Q. Rev. Biophys.*, 1995, **28**, 171–193.

179 J. R. Helliwell, Protein crystal perfection and the nature of radiation damage, *J. Cryst. Growth*, 1988, **90**, 259–272.

180 M. T. B. Clabbers and J. P. Abrahams, Electron diffraction and three-dimensional crystallography for structural biology, *Crystallography Rev.*, 2018, **24**, 176–204.

181 P. Brázda, L. Palatinus and M. Babor, Electron diffraction determines molecular absolute configuration in a pharmaceutical nanocrystal, *Science*, 2019, **364**, 667–669.

182 P. B. Klar, Y. Krysiak, H. Xu, G. Steciuk, J. Cho, X. Zou and L. Palatinus, Accurate structure models and absolute configuration determination using dynamical effects in continuous-rotation 3D electron diffraction data, *Nat. Chem.*, 2023, **15**, 848–855.

183 L. Palatinus, P. Brázda, M. Jelínek, J. Hrdá, G. Steciuk and M. Klementová, Specifics of the data processing of precession electron diffraction tomography data and their implementation in the program PETS2.0, *Acta Crystallogr B Struct Sci Cryst Eng Mater*, 2019, **75**, 512–522.

184 V. Petříček, M. Dušek and L. Palatinus, Crystallographic Computing System JANA2006: General features, *Zeitschrift für Kristallographie - Crystalline Materials*, 2014, **229**, 345–352.

185 L.-M. Peng, Electron Scattering Factors of Ions and their Parameterization, *Acta Crystallogr. A*, 1998, **54**, 481–485.

186 X. Zou, S. Hovmöller and P. Oleynikov, in *Electron Crystallography: Electron Microscopy and Electron Diffraction*, Oxford University Press, New York, 2011, pp. 42–71.

187 D. A. Langs and H. A. Hauptman, Relaxation of the resolution requirements for direct-methods phasing, *Acta Crystallogr. A*, 2011, **67**, 396–401.

188 IUCr, IUCr checkCIF procedure PLAT089, https://journals.iucr.org/services/cif/checking/PLAT089.html, (accessed 14 October 2023).

189 IUCr, IUCr checkCIF procedure PLAT090, https://journals.iucr.org/services/cif/checking/PLAT090.html, (accessed 14 October 2023).

190 L.-M. Peng, Electron atomic scattering factors and scattering potentials of crystals, *Micron*, 1999, **30**, 625–648.

191 V. Vand, P. F. Eiland and R. Pepinsky, Analytical representation of atomic scattering factors, *Acta Crystallogr.*, 1957, **10**, 303–306.

192 P. A. Doyle and P. S. Turner, Relativistic Hartree–Fock X-ray and electron scattering factors, *Acta Crystallogr. A*, 1968, **24**, 390–397.

193 L.-M. Peng, G. Ren, S. L. Dudarev and M. J. Whelan, Robust Parameterization of Elastic and Absorptive Electron Atomic Scattering Factors, *Acta Crystallogr. A*, 1996, **52**, 257–276.

194 K. Yonekura, K. Kato, M. Ogasawara, M. Tomita and C. Toyoshima, Electron crystallography of ultrathin 3D protein crystals: atomic model with charges, *Proc. Natl. Acad. Sci. U. S. A.*, 2015, **112**, 3368–3373.

195 K. Yonekura, R. Matsuoka, Y. Yamashita, T. Yamane, M. Ikeguchi, A. Kidera and S. Maki-Yonekura, Ionic scattering factors of atoms that compose biological molecules, *IUCrJ*, 2018, **5**, 348–353.

196 T. Gruene and E. Mugnaioli, 3D Electron Diffraction for Chemical Analysis: Instrumentation Developments and Innovative Applications, *Chem. Rev.*, 2021, **121**, 11823–11834.

197 A. Thorn, B. Dittrich and G. M. Sheldrick, Enhanced rigid-bond restraints, *Acta Crystallogr. A*, 2012, **68**, 448–451.

198 M. T. B. Clabbers and H. Xu, Microcrystal electron diffraction in macromolecular and pharmaceutical structure determination, *Drug Discov. Today Technol.*, 2020, **37**, 93–105.

199 B. Gruza, M. L. Chodkiewicz, J. Krzeszczakowska and P. M. Dominiak, Refinement of organic crystal structures with multipolar electron scattering factors, *Acta Crystallogr A Found Adv*, 2020, **76**, 92–109.

200 L. R. Doyle, E. A. Thompson, A. L. Burnage, A. C. Whitwood, H. T. Jenkins, S. A. Macgregor and A. S. Weller, MicroED characterization of a robust cationic σ-alkane complex stabilized by the [B(3,5-(SF5)2C6H3)4]− anion, via on-grid solid/gas single-crystal to single-crystal reactivity, *Dalton Trans. J. Inorg. Chem.*, 2022, **51**, 3661–3665.

201 G. Winter, D. G. Waterman, J. M. Parkhurst, A. S. Brewster, R. J. Gildea, M. Gerstel, L. Fuentes-Montero, M. Vollmar, T. Michels-Clark, I. D. Young, N. K. Sauter and G. Evans, DIALS: implementation and evaluation of a new integration package, *Acta Crystallogr D Struct Biol*, 2018, **74**, 85–97.

202 H. Jenkins, process_datasets.py, https://github.com/huwjenkins/ed_scripts, (accessed 29 June 2023).

203 T. Gruene, H. W. Hahn, A. V. Luebben, F. Meilleur and G. M. Sheldrick, Refinement of macromolecular structures against neutron data with SHELXL2013, *J. Appl. Crystallogr.*, 2014, **47**, 462–466.

204 M. W. Martynowycz, M. T. B. Clabbers, J. Unge, J. Hattne and T. Gonen, Benchmarking the ideal sample thickness in cryo-EM, *Proc. Natl. Acad. Sci. U. S. A.*, 2021, **118**, e2108884118.

205 A. J. McEllin, PhD Thesis, 2022.

206 *CrysAlisPRO, version 1.171.41.122a*, Rigaku Oxford Diffraction, 2021.

207 O. V. Dolomanov, L. J. Bourhis, R. J. Gildea, J. A. K. Howard and H. Puschmann, OLEX2: a complete structure solution, refinement and analysis program, *J. Appl. Crystallogr.*, 2009, **42**, 339–341.

208 S. Smeets, X. Zou and W. Wan, Serial electron crystallography for structure determination and phase analysis of nanocrystalline materials, *J. Appl. Crystallogr.*, 2018, **51**, 1262–1273.

209 S. Smeets, J. Ångström and C.-O. A. Olsson, Quantitative phase analysis for carbide characterization in steel using automated electron diffraction, *Steel Res. Int.*, 2019, **90**, 1800300.

210 B. Wang, X. Zou and S. Smeets, Automated serial rotation electron diffraction combined with cluster analysis: an efficient multi-crystal workflow for structure determination, *IUCrJ*, 2019, **6**, 854–867.

211 Y. Luo, B. Wang, S. Smeets, J. Sun, W. Yang and X. Zou, High-throughput phase elucidation of polycrystalline materials using serial rotation electron diffraction, *Nat. Chem.*, 2023, **15**, 483–490.

212 T. Burden, PhD Thesis, University of York, 2023.

213 J. T. C. Wennmacher, C. Zaubitzer, T. Li, Y. K. Bahk, J. Wang, J. A. van Bokhoven and T. Gruene, 3D-structured supports create complete data sets for electron crystallography, *Nat. Commun.*, 2019, **10**, 3316.

214 G. McMullan, K. Naydenova, D. Mihaylov, K. Yamashita, M. J. Peet, H. Wilson, J. L. Dickerson, S. Chen, G. Cannone, Y. Lee, K. A. Hutchings, O. Gittins, M. A. Sobhy, T. Wells, M. M. El-Gomati, J. Dalby, M. Meffert, C. Schulze-Briese, R. Henderson and C. J. Russo, Structure determination by cryoEM at 100 keV, *Proc. Natl. Acad. Sci. U. S. A.*, 2023, **120**, e2312905120.

215 N. Jeddi, PhD Thesis, University of York, 2023.

216 G. Chen, S. Guo, H. Feng and Z. Qian, Anion-regulated transient and persistent phosphorescence and size-dependent ultralong afterglow of organic ionic crystals, *J. Mater. Chem.*, 2019, **7**, 14535–14542.

217 K. M. Appleby, E. Dzotsi, N. W. J. Scott, G. Dexin, N. Jeddi, A. C. Whitwood, N. E. Pridmore, S. Hart, S. B. Duckett and I. J. S. Fairlamb, Bridging the gap from mononuclear pd^{II} precatalysts to pd nanoparticles: Identification of intermediate linear $[pd_3(XPh_3)_4]^{2+}$ clusters as catalytic species for Suzuki–miyaura couplings (X = P, as), *Organometallics*, 2021, **40**, 3560–3570.

218 S. Kannan, A. J. James and P. R. Sharp, [Pd3(PPh3)4]2+, a new palladium triphenylphosphine complex, *J. Am. Chem. Soc.*, 1998, **120**, 215–216.

219 J. C. Goodall, M. A. Sajjad, E. A. Thompson, S. J. Page, A. M. Kerrigan, H. T. Jenkins, J. M. Lynam, S. A. Macgregor and A. S. Weller, In crystallo lattice adaptivity triggered by solid-gas reactions of cationic group 7 pincer complexes, *Chem. Commun.* , 2023, **59**, 10749–10752.

220 J.-D. Park, Y. Li, K. Moon, E. J. Han, S. R. Lee and M. R. Seyedsayamdost, Structural Elucidation of Cryptic Algaecides in Marine Algal-Bacterial Symbioses by NMR Spectroscopy and MicroED, *Angew. Chem. Int. Ed Engl.*, 2022, **61**, e202114022.

221 A. Brown and J. Clardy, Tiny crystals have big potential for determining structures of small molecules, http://dx.doi.org/10.1038/d41586-018-07756-5, (accessed 5 April 2024).

222 O. Sitsel and S. Raunser, Big insights from tiny crystals, *Nat. Chem.*, 2019, **11**, 106–108.

223 C. N. Filer, MicroED and cannabinoid research, *J Cannabis Res*, 2021, **3**, 14.

224 J. Heidler, R. Pantelic, J. T. C. Wennmacher, C. Zaubitzer, A. Fecteau-Lefebvre, K. N. Goldie, E. Müller, J. J. Holstein, E. van Genderen, S. De Carlo and T. Gruene, Design guidelines for an electron diffractometer for structural chemistry and structural biology, *Acta Crystallogr D Struct Biol*, 2019, **75**, 458–466.

225 P. Simoncic, E. Romeijn, E. Hovestreydt, G. Steinfeld, G. Santiso-Quiñones and J. Merkelbach, Electron crystallography and dedicated electron-diffraction instrumentation, *Acta Crystallogr E Crystallogr Commun*, 2023, **79**, 410–422.

226 ELDICO ED-1: THE ELECTRON DIFFRACTOMETER, https://www.eldico-scientific.com/product/, (accessed 5 April 2024).

227 S. Ito, F. J. White, E. Okunishi, Y. Aoyama, A. Yamano, H. Sato, J. D. Ferrara, M. Jasnowski and M. Meyer, Structure determination of small molecule compounds by an electron diffractometer for 3D ED/MicroED, *CrystEngComm*, 2021, **23**, 8622–8630.

228 XtaLAB Synergy-ED, https://www.synergy-ed.com/, (accessed 5 April 2024).

229 3DED/MicroED datasets, https://zenodo.org/communities/microed/records?q=&l=list&p=1&s=10&sort=newest, (accessed 17 April 2024).

230 XRDa microED search, https://xrda.pdbj.org/search/xrda?query=microED, (accessed 17 April 2024).

231 V. Corless, Scientists uncover a hepatitis C drug's hidden structures, https://www.advancedsciencenews.com/scientists-uncover-a-hepatitis-c-drugs-hidden-structures/, (accessed 8 April 2024).

232 M. O. Cichocka, J. Ångström, B. Wang, X. Zou and S. Smeets, High-throughput continuous rotation electron diffraction data acquisition via software automation, *J. Appl. Crystallogr.*, 2018, **51**, 1652–1661.

233 N. Devenish, DIALS 3.5.0, https://github.com/dials/dials/releases/tag/v3.5.0, (accessed 29 June 2023).

234 N. K. Sauter, R. W. Grosse-Kunstleve and P. D. Adams, Robust indexing for automatic data collection, *J. Appl. Crystallogr.*, 2004, **37**, 399–409.

235 W. Kabsch, Integration, scaling, space-group assignment and post-refinement, *Acta Crystallogr. D Biol. Crystallogr.*, 2010, **66**, 133–144.

236 U. W. Arndt, The optimum strategy in measuring structure factors, *Acta Crystallogr. B*, 1968, **24**, 1355–1357.

237 P. A. Karplus and K. Diederichs, Linking crystallographic model and data quality, *Science*, 2012, **336**, 1030–1033.

238 G. Assmann, W. Brehm and K. Diederichs, Identification of rogue datasets in serial crystallography, *J. Appl. Crystallogr.*, 2016, **49**, 1021–1028.

239 H. Jenkins, Joint refinement from biotin data (https: zenodo.org record 4895412), https://github.com/huwjenkins/ed_unit_cell/wiki/Joint-refinement-from-biotin-data-(https:-- zenodo.org-record-4895412), (accessed 30 June 2023).

240 P. Emsley and K. Cowtan, Coot: model-building tools for molecular graphics, *Acta Crystallogr. Sect. D*, 2004, **60**, 2126–2132.

241 A. J. C. Wilson, *International Tables for Crystallography, Volume C*, Springer, Netherlands, 1992.

242 E. Prince, *International Tables for Crystallography Volume C*, Wiley, 2006.

243 E. Tiesinga, P. J. Mohr, D. B. Newell and B. N. Taylor, CODATA Recommended Values of the Fundamental Physical Constants: 2018, *Rev. Mod. Phys.*, 2021, **93**, 025010.